Metal oxide catalysts for carbon nanotubes growth: The growth mechanism using NiO and doped ZnO.

Hassan Wahab

Submitted for the Degree of
Doctor of Philosophy

Department of Electronics
The University of York

April 2012

Abstract

The thesis describes the preparation and characterisation of novel oxide catalysts (NiO and doped ZnO) and catalyst free growth of carbon nanotubes (CNTs). Additionally a new growth mechanism has been proposed for these oxide catalysts, based on intra-granular charge transfer and lattice strain. The intra-granular charge transfer process is believed to help dissociate the hydrocarbon molecules and the lattice strain is believed to be responsible for the diffusion of carbon atoms through the catalyst nanoparticles. These two processes collectively give rise to CNTs growth. The materials were prepared through solid state reaction with a range of temperatures. The pellets were then thermally evaporated on to the substrates in order to use these catalyst nanoparticles for CNTs growth.

The chemical state and the chemical environment of the dopants (Ni, Cu, Sm, Tb and Ho) in the ZnO host material were identified through x-ray photoelectron spectroscopy (XPS). It was observed through XPS that the mixed oxidation state of the dopants in the ZnO gives rise to the intra-granular charge transfer process. The crystal structure and the lattice strain produced by the incorporation of dopant ions into the ZnO matrix were observed through x-ray diffraction (XRD). It was observed that dopant ions produce lattice strain and the extent of it, depends upon the ionic radii of the dopants. The higher the lattice strain the higher will be the diffusion of carbon atoms through the catalyst nanoparticles. The size and shape of the catalyst nanoparticles were obtained using scanning electron microscopy (SEM) and transmission electron microscopy (TEM). Energy dispersive x-ray spectrometry (EDS) in the TEM and SEM was applied to see the elemental composition of individual nanoparticles and the pellets respectively. After growth the CNTs were characterised through SEM and TEM to see the morphologies and EDS for the elemental composition of the particle at the tip of CNTs.

The study of these catalysts regarding the growth of CNTs showed that those catalyst nanoparticles with a strong intra-granular charge transfer mechanism and higher lattice strain gives rise to CNTs growth. The catalyst nanoparticles with dopants in their minimum or maximum oxidation states do not give rise to intra-granular charge transfer and hence no CNTs growth.

Chapter 5: Characterisation of rare earth doped ZnO

Chapter: 6: Growth of CNTs

Chapter 7: Field Emission Studies

List of tables

List of Figures

List of Figures

Acknowledgement

First I would like to express my deep appreciation to my supervisor, Professor Mohamed El-Gomati for his support, advice and encouragement during the project, which led to the submission of this thesis.

I would like to thank the Higher Education Commission (HEC) government of Pakistan particularly the Ex-chairman Dr Atta-ur-Rehman that has made all this possible. I would express my deep gratitude to the administrative staff of HEC especially Mr Rana Shafiq and Ms Madiha Anwar Butt.

I would like to offer special thanks to my friends and collogues especially to Dr Christopher Walker, Mr Torquel Wells, Dr Sharif Bakush and Mr Hamid Al-Garni and thanks to all those who encouraged my social life and kept me lively and spirited. I am also grateful to Mr Jonathon Cremer, Mr Ian Wells and especially to Malcome Law for their assistance in the clean room especially keeping the MPS1400 upto date. My many thanks to Ian Wright and Leonardo Lari of the York-JEOL Nanocenter for their support in using the TEM and SEM. In addition, my many thanks to Camilla Danese and Mrs Brenda Christmas for their support and help.

Finally and most importantly I would like to like to express my deep gratitude to my mum for her deep love, and my wife, my brothers and sisters for their encouragement and especially my deep love for Afnan, Ainan and my little Haula for their patience.

Thank you

Declaration

I declare that the work presented in thesis is based purely on my investigation, unless otherwise stated.

Signed

Hassan Wahab

Chapter: 1; Introduction

1.1): Introduction:

The history of the solid forms of the structures of carbon can be traced back to 1772, when Antoine Lavoisier proved that diamond is a form of carbon and produces carbon dioxide on combustion. In 1779 C. W. Scheele proved through combustion that graphite belongs to carbon family whereas before that time it was believed to be a form of lead. For the next two hundred years these were the only known forms of solid carbon. Hence it came as a considerable surprise when in 1985 it was observed the carbon has another allotrope which has been given the name fullerene[1] and the discovery of fullerene led to the discovery of carbon nanotubes (CNTs)[2] and monolayer graphene[3]. These new structures were most attractive for scientists and engineers because of their potential applications[4,5].

This thesis concerns mainly the development of new ways of growing CNTs, which have possible applications ranging from nano-electronics, quantum wire interconnects, field emitters to sensors[6]. Additionally growing CNTs at a desired position on a substrate is still a challenge for engineers. To address these challenges it is required to have synthesis techniques that could give rise to controlled growth. Chemical vapour deposition (CVD) appears to be the best option among the developed techniques for the CNT growth that is capable of addressing these requirements because CVD can grow CNTs at much lower temperature than arc discharge and laser ablation[7], which makes it suitable to grow CNTs on different substrates using a range of catalysts.

Growing CNTs through CVD on supported catalyst is a multi step process. First is the deposition of catalyst nanoparticles on a desired substrate. The substrate is then placed in a CVD chamber at some elevated temperature ranging from 500C to 1200C. Carbon containing gas is then allowed into the chamber for few minutes (10 to 20 min) to grow CNTs. The catalyst free growth of CNTs[8,9] has raised the very fundamental question that if CVD works properly then what is the role of catalyst. If we suppose that catalysts are used for the dissociation of carbon containing gas then again the dissociation of hydrocarbon does not mean the growth of CNTs[10,11].

For the catalytically grown CNTs there are two steps involved in the growth. The first and foremost step is to dissociate the hydrocarbon molecule upon the surface of the catalyst. For the dissociation it is essential to accept an electron from the adsorbates and must have the potential to give the electrons back to the antibonding orbitals of the adsorbates. The 2nd is

that the catalyst must have the property to allow the diffusion of carbon atoms through it; otherwise the amorphous carbon will cover the catalyst nanoparticles and will make it poisoned. Kim et al[12] associated the synthesis of CNTs with the wetting behaviour of the catalyst with the adsorbates, which depends upon the relevant interfacial energies. The lower the interfacial energy the stronger will be the interaction between the two materials. This interaction comes from the Van-der Waals forces or chemisorptions or the combination of both. The donation and back donation of electrons between the catalysts and that the adsorbates (hydrocarbon molecules) causes the weakening of the bonding strengths of hydrocarbon molecules (C_2H_2 in this study) up to an extent that they start dissociating into hydrogen and carbon[13].

Traditionally the 3d metal Fe, Ni and Co are used for the growth of CNTs and it was thought to be due to the unpaired d-orbitals that accept electrons from the carbon containing gas and helps in dissociating the carbon containing gas. After the dissociation of carbon containing gas the carbon atoms are then dissolved in the liquid droplet of the catalyst nanoparticles and when it becomes super saturated the carbon atoms start precipitating through the catalyst nanoparticles[14,15] and gives rise to CNTs growth. This type of growth is based on vapour liquid solid (VLS) theory of Wagner and Ellis[16]. However, if VLS based growth is supposed to happen then the very fundamental question regarding the driving force of carbon diffusion within the catalyst nanoparticles arises.

According to some of the authors[14,15] it is the temperature gradient that drives the carbon atoms through the catalyst nanoparticles. The front face of the catalyst nanoparticles is believed to behave as exothermic while the rear face behave as endothermic, this different behaviour gives rise to temperature gradient and results in carbon diffusion through the catalyst nanoparticles. Another group of researchers[17,18] believes that it is the concentration gradient that causes the carbon diffusion through the catalyst nanoparticles. It is because the basal planes of graphite have lower energy than the prismatic planes, and therefore the precipitation is more likely to occur through the low energy planes.

It was observed by Helveg et al[19] through an in-situ TEM experiment that during the growth of CNTs the catalyst (Ni) nanoparticles remains solid and the graphene layers terminate at the atomic steps on the surface of Ni nanoparticles. It was observed that an additional graphene sheet grows between the pairs of steps. These steps move towards the ends of the Ni surface and help in transporting the carbon atoms towards the graphene-Ni

interface. Additionally the melting point of the catalyst nanoparticles, even if the size effect is taken into account, is higher than the growth temperature[20,21] thus it seems unlikely that the growth of CNTs is governed by the VLS theory.

Dai et al[22] proposed another mechanism for CNTs growth, according to which first a graphene cap is formed on the surface of a catalyst. This cap in turn reduces the surface energy of the catalyst nanoparticles and makes it easy for other carbon atoms to get stabilised on it. Thus more and more carbon atoms accumulate on this graphitic cap and gives rise to a CNT. Uchino et al synthesised CNTs from Ge[23] and SiGe[24] islands and proposed that only nanoscale curvature is necessary for CNTs growth.

The noble metals with no unpaired d-orbitals like Cu were believed to show no catalytic activity towards the CNTs synthesis[25]. However, recent studies claimed the synthesis of multiwall and single wall CNTs using Cu[26,27] and Au[28] as catalyst through DC arc discharge and CVD, but did not mention any mechanism for the growth. The synthesis was just attributed to the reaction between the gaseous carbon specious and the copper nanoparticles. Zhou et al[27] argues that it is the low solubility limit of copper that causes an increased precipitation of carbon through the catalyst, which seems quite conventional.

There are two reasons for the catalytic activity of noble metal catalysts. One is that the fraction of low coordinated atoms increases with decreasing cluster size. These low coordinated atoms are believed to be the origin of the catalytic activity of noble metals[28]. Another possibility is that the catalyst support interface plays a key role in activating the noble metal catalyst through catalyst support interaction[13] (SiO_2 and Al_2O_3).

To understand the effect of oxide catalysts to grow CNTs the very fundamental question about the nature of the chemical state of the catalyst arises. After an attempt to grow CNTs through iron oxide it was observed that it is the reduced iron that catalyses the growth and not the oxides because these catalysts first reduces to metals and then catalyse the growth[29,30]. A range of papers[31,32,33] have shown that the catalytic activity (for CNTs growth) of Fe is better than metallic Ni and Co because of more unpaired d-electrons in the outermost shell. But how the unfilled 3d-orbitals give rise to CNTs growth has not been discussed[34]. Wong et al[35] (1990) studied the reaction between the copper and the acetylene molecules and attributed the dissociation of acetylene molecule to the ionic interaction between the acetylene molecule and the copper, which seems to be a quite suitable

mechanism if applied for the growth of CNTs. The growth of CNTs using metallic catalysts is a huge success, but despite the fact these metal catalyst have some drawbacks as well,

i): These metallic catalysts are believed to be toxic and are not appreciated in the clean room environment.

ii): For some applications of CNTs the catalyst particles are not desired and need to be removed. The removal process of catalyst particle quite often damages the CNTs.

Very recently it has been observed that oxide catalysts such as alumina (Al_2O_3)[36] and zerconia (ZrO_2)[37] as catalyst can actively grow CNTs. Liu et al[38] synthesised single wall CNTs using SiO_2 nanoparticles as catalyst and observed that SiO_2 nanoparticles can efficiently grow single wall CNTs while Si nanoparticles do not contribute towards the growth of CNTs. The author attributed the growth to the presence of oxygen ions that play an important role in the growth. These oxide catalysts have been used as support in the catalytic growth of CNTs. This has raised a serious question about the actual role of the support in the CNTs growth. Additionally it has posed a challenge of re-evaluating the growth mechanism. Although the CNTs formation using metallic catalysts have provided a wonderful insight into the growth mechanisms but it seems that there is still a gap in our understanding which could lead to other possible growth mechanisms.

This study reports on the growth of CNTs using novel metal oxide (NiO), doped ZnO with transition metals and rare earths (like Cu, Ni, Sm, Tb and Ho) and catalyst free growth on tungsten substrate through CVD and Direct Current-Plasma enhanced CVD (DC-PECVD) technique. The grown CNTs have been characterised for field emission properties. The main focus is the development of novel oxide catalysts for CNTs growth and the re-evaluation of a proper growth mechanism for these catalysts. According to an author[39] **"**there is an undeniable role outside the conventional thinking because their use enables the graphitization of carbon in scenarios beyond the norm**"**.

The main task was to deposit the catalyst nanoparticles on a desired substrate with narrow size and shape distribution. For this purpose pellets were prepared through solid state reaction and were thermally evaporated on tungsten and Si substrates.

The chemical state and the chemical environment (what are the other atoms attached to the dopant) of catalysts (pellets and thermally evaporated films) was investigated through x-ray photoelectron spectroscopy (XPS) in collaboration with the University of Surrey. The pellets were ground to powder form and were characterised through x-ray diffraction (XRD)

for phase identification and lattice strain. Additionally the pellets were characterised for elemental composition through energy dispersive spectroscopy (EDS) of x-ray in the scanning electron microscope (SEM). The size and shape distribution of grains were observed through SEM. The thermally evaporated grains were transported to transmission electron microscope (TEM) grid by scratching the sample through tweezers. The crystal structure of an individual grain was confirmed through high resolution transmission electron microscope (HRTEM) image and the elemental composition of the grain was confirmed through EDS in the TEM. After all these checks the sample was then put in the CVD chamber (MPS1400) to grow CNTs. MPS1400 is a high temperature chemical vapour deposition system and designed and manufactured by JLS design limited. Before growing CNTs a stable plasma, conditions are set up for the desired field. For a high field sufficient for the alignment of CNTs it is necessary to keep the chamber clean, otherwise it is very difficult to grow well aligned CNTs. DC voltage, DC current, gas flow rate, chamber pressure and the distance between the two electrodes are the important parameters to obtain a stable plasma.

After the growth process the samples were then characterised through SEM, TEM, electron diffraction (ED) and EDS. The structure and morphology of CNTs were carried out through SEM and TEM. The crystal structure of catalyst particles at the tip of CNTs was confirmed through HRTEM image and the elemental composition of the catalyst particle was observed through EDS in the TEM. In addition to the growth, the CNTs were characterised for field emission through triode and diode configuration. The field emission properties were observed in an ultra high vacuum (UHV) system. The current voltage (I-V) characteristics, field emission pattern and the emission current stability were observed for all CNTs grown by using various catalysts. It was observed that Holmium (Ho) doped ZnO grown CNTs show better emission current stability and good catalyst support interaction. Additionally the alignment of CNTs plays a key role in stability.

The thesis is structured in a way such that chapter 2 describes a literature review regarding the growth and applications of CNTs. Various growth models especially the effect of catalyst upon the growth will be described. Chapter 2 also covers the use of CNTs as an electron source. The conventional electron sources like thermionic electron sources, Schottky field emission sources and cold field emission sources are also described.

Chapter 3 is associated with different characterisation techniques like SEM, TEM, EDS, ED, XPS and XRD. These techniques have been briefly discussed to understand the working principle and the construction.

Chapter 4 deals with the preparation and deposition of transition metal (Cu and Ni) doped ZnO catalysts. These dopants are used to observe the intra-granular charge transfer mechanism and the effect of dopants on the lattice strain of the host material. These catalysts have been prepared through solid state reaction at 1200C for 14 hours. The effect of substrate surface and that of the buffer layer on the size and shape distribution of catalyst nanoparticles will be discussed briefly. The catalyst nanoparticles and the pellets have been characterised through XPS, SEM, TEM and EDS. Additionally the powder of the pellet has been characterised through XRD.

Chapter 5 is about the characterisation of rare earth (Sm, Tb and Ho) doped ZnO catalysts. These dopants are again used to see the intra-granular charge transfer mechanism and lattice strain and the effect of these characteristics on the growth of CNTs. The pellets and the thermally evaporated films have been characterised through a range of techniques like SEM, TEM, EDS, ED, XPS and XRD. These catalysts have been prepared through solid state reaction at various temperatures like 1000C, 1050C, 1150C and 1200C for
14 hours. The catalysts have been thermally evaporated like that of transition metal doped ZnO pellets. The nanoparticles have then been used for the growth of CNTs.

Chapter 6 is about the growth of CNTs using all these Transition metal doped and rare earth doped ZnO catalysts as well as metallic Ni and NiO nanoparticles as catalysts through DC-PECVD. Sm doped ZnO does not show any activity towards the growth of CNTs. This passiveness is attributed to the charge transfer mechanism that does not happen in these catalyst nanoparticles after thermal evaporation.

Chapter 7 describes to the field emission properties of the grown CNTs. It has been observed that the catalyst support interaction, residues and good alignment play an important role in the stable emission current. The design and set up of the triode configuration for the field emission will be discussed. Additionally the design and setup for the UHV system will be outlined.

Chapter 8 summarises the work that has been carried out in this thesis and suggests more future work.

2.1): Introduction to Carbon nanotubes (CNTs)

A carbon nanotube is a form of carbon with sp^2 bonding nature like that of graphite, in which a carbon atom is attached with three other carbon atoms making a hexagonal network. A sheet of this hexagonal network is rolled up to make the carbon nanotube. The graphene sheet is a single atomic layer of the hexagonal network. Single rolling of the sheet will give a CNT called as the single wall CNTs (SWCNTs), if two graphene layers are rolled up then it is called a double wall CNT (DWCNTs) and several concentric rollings will give multi-wall CNTs (MWCNTs). The structure of the CNTs depends upon the chirality (the way the graphene sheet is wrapped) of the graphene sheet. The chiral vector C_h can be represented as[40],

$$C_h = na_1 + ma_2 \qquad (2.1)$$

Where a_1 and a_2 are the unit cell vectors of the two dimensional lattice of graphene and *n* and *m* are the integers showing the number of unit cell vectors. For n = m & $\theta = 30^0$, the nanotube is called "armchair", if $n \neq m$ & $\theta = 0^0$ it is called as "chiral" and if m = 0 & $\theta < 30^0$ the CNTs are called "zigzag" as shown in figure (2.1).

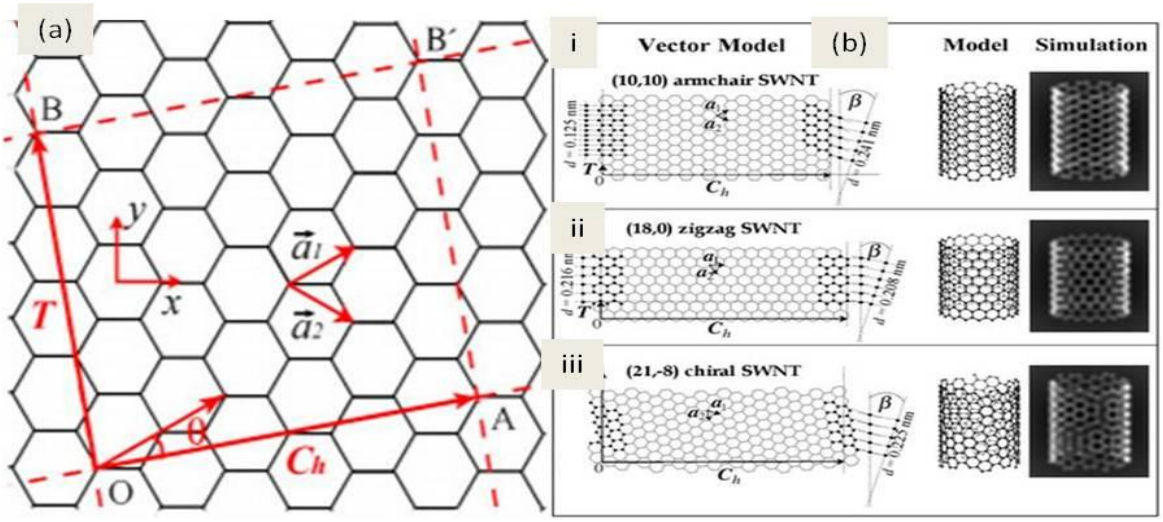

Figure 2.1[40] (a): Single layer of graphene (b): The corresponding rolling of the sheet with respect to different Chiral angles to form the three types of nanotubes like (i): shows the armchair tube (ii); Zigzag tube and (iii); Chiral tube:

The length "*L*" of the chiral vector C_h can be determined from the circumference of the CNT[40].

$$L = |C_h| = a\sqrt{n^2 + nm + m^2} \qquad (2.2)$$

Where "a" is the length of the unit cell vector either a_1 or a_2, and is equal to $a = a_{cc}\sqrt{3}$ where a_{cc} is the bond length between two carbons. The diameter of the nanotube is given by the following relation. Carbon nanotubes were first discovered by *Redushkevich and Lukenovich*[41] in 1952 as shown in figure (2.2). However, the importance of their result was not recognised.

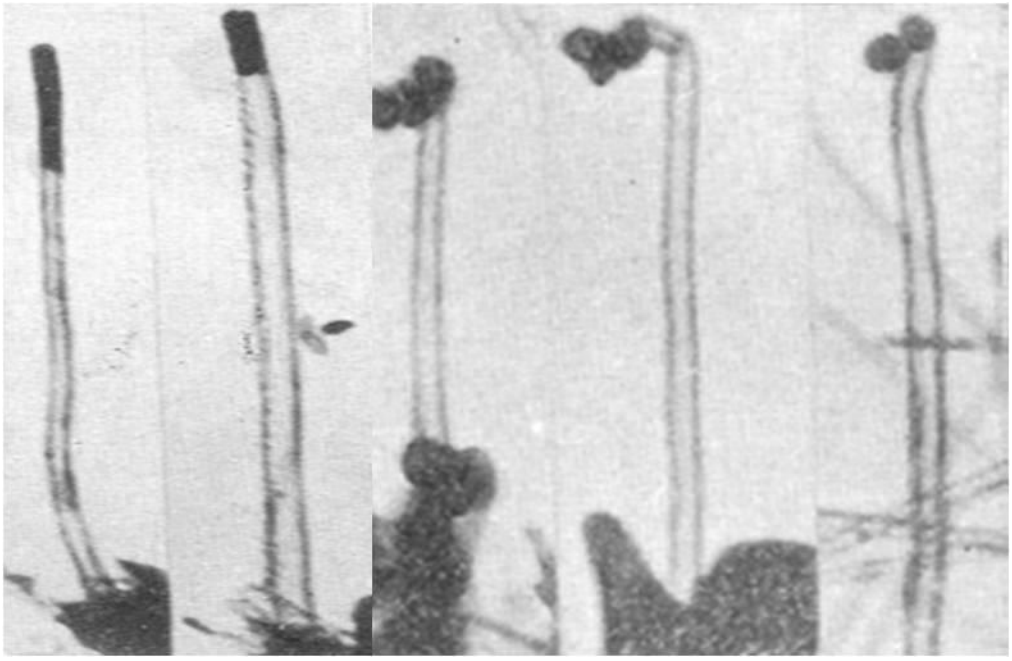

Figure 2.2[41]: TEM Images of CNTs first observed by Redushkevich and Lukenovich in (1952) .

These were then identified by *Iijima*[2] in 1991 and showed that the CNTs are concentrically a rolled up graphene sheet. Since then it has attracted more attention of the scientist and industries because of its potential for a range of applications.

The CNTs can be either metallic or semiconducting depending on the band structure of the CNTs. Saito et al[42] calculated the electronic density of states of CNTs and proposed that the tube indices (n & m) could be used to observe the electronic structure of CNTs. It has been shown that the band crossing the two degenerate points (Fermi level) during the rolling of 2D graphene sheet gives rise to a finite density of states and the CNTs are therefore metallic. Thus, all the armchair tubes have bands crossing the Fermi level and are metallic. There are two possibilities for the rest of the tubes (Chiral and zigzag), if n-m = 3q the CNTs are expected to be metallic and if $n - m \neq 3q$ (q is an integer) then the CNTs will be semiconducting, with a band gap of 0.5eV. The band structure defines the CNTs to be semiconductor or metallic, and this can be understood via the quantisation phenomenon. The wave vector perpendicular to the axis of a CNT is quantised and the parallel component is continuous because electrons are free in this direction. The band gap decreases with increasing the diameter of CNTs and could be observed from the relation below.

$$E_g = \frac{2\gamma_0 a_{C-C}}{d} \qquad (2.3)$$

Where a_{C-C} is the bond distance between the nearest neighbours, γ_0 is the overlap energy and d is the diameter of the tube. This clearly indicates that with increasing CNT diameter the energy gap decreases and approached to zero at some specific CNT diameter and hence defines the nature of CNTs that whether the CNTs are metallic or semi-conducting. From the figure (2.3a) it is clear that metallic CNTs have two conducting channels, which correspond to the number of sub-bands. The steps (spikes) represent the sub-bands and appear in pairs in CNTs because of the periodic boundary conditions. In fig (2.3a) there exists a finite density of states while in Fig (2.3b) there exists no density of states and hence it is considered semiconducting.

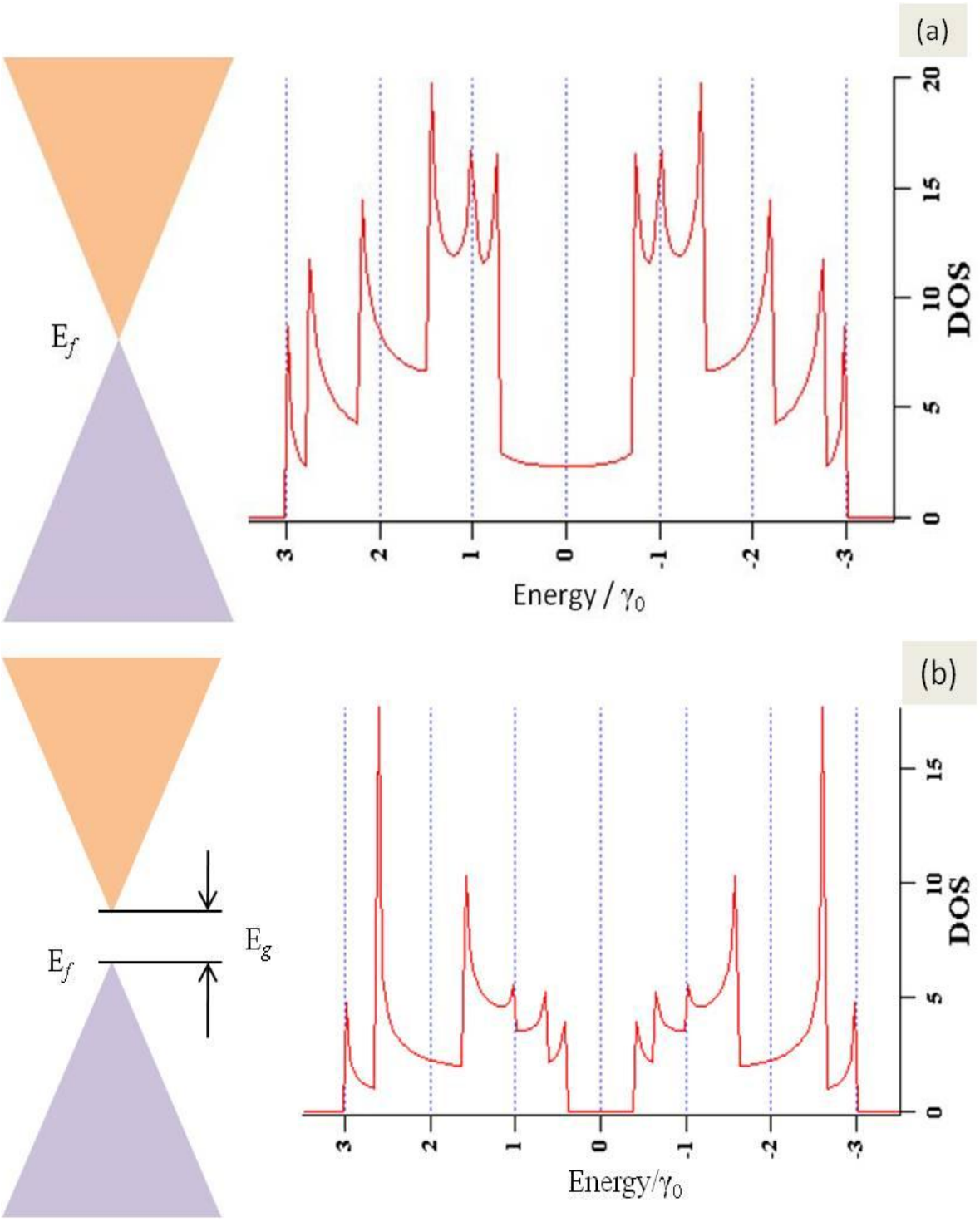

Figure 2.3[43] Characterisation of metallic and semiconducting nanotubes. (a): it is the band structure of (4,4) armchair metallic CNT, where the spikes represent the number of sub-bands. (b): is the band structure of (5,0) semiconducting zigzag tube showing that the energy gap at the Fermi level.

2.2): Properties and Applications of CNTs.

Since the discovery of CNTs[2], they have provided one of the most popular areas of research for Physicists, Engineers and Chemists[44,45]. Carbon nanotubes are ideal for both researchers and industrialists due to their unique properties and applications. The electrical properties of the CNTs are strongly associated with the structure of the CNTs, "whether the CNTs are semiconducting or metallic". They could be used for next generation devices, like field effect transistors[46] or sensors because of the high current density and conductivity, and could be used as the wiring leads in the future large scale integration circuits[47].

The Young's modulus is directly related to the chemical bonding of atoms in the material. It is believed that CNTs have high bending strength and this is associated with the flexibility of CNTs[48]. Lu et al[49] calculated the Young's modulus for a single wall CNTs using the tight binding model and found that CNTs with diameters in the range of 0.34nm to 13.5nm have a Young's modulus of 970GPa. A range of studies[50] have been carried out to calculate the Young's modulus for CNTs and the given range varies from 0.5 to 5.5TPa. Experimentally it was shown that a MWCNT have a tensile strength of 63GPa[51].

The high strength and low weight characteristics of CNTs are equally important for a range of composite materials used in sport and aircraft industries. The good load transfer capability between the matrix and CNTs makes them exceptionally mechanically strong material[52].

Carbon nanotubes are unique one dimensional systems that have potential applications in optics and photonics. The low work function, high aspect ratio and ballistic movement of electrons have made CNTs a promising candidate as a field emission electron source[53]. They could be used in light emitting diodes[54]. Absorption and emission of a beam of light or electrons describes the optical properties of CNTs and could be characterised by different spectroscopy like absorption and Raman spectroscopy.

It has been found that carbon nanotubes synthesised through arc-discharge have high thermal stability with thermal conductivity greater than 3000 Watt/meter.K at room temperature[55]. The heat conduction in nanostructures is considered to be quantised because at temperature near absolute zero, the number of active phonons in nanostructures remains very low[56]. A thermal rectifier has been fabricated, which is used in directing the heat flow in one direction by loading one end of the tube with high mass density material like trimethyl

cyclopentadienyle platinum[57]. Carbon nanotubes could also be used in super-capacitors because of the high aspect ratio (surface to volume ratio) and high specific capacitance[58]. In addition CNTs could be used in making loud speakers[59], hydrogen storage[60], Field emission displays and chemical sensors[61] and has a possible application as a spin polarized electron source.

2.3): Methods for the growth of CNTs

It has been well established now that carbon nanotubes can be synthesized through three different techniques. Although arc discharge[2] was the first successful technique to produce CNTs, laser ablation[62] and CVD[22,63] were also successfully used for their growth. All of these processes are used for the growth of multiwall and single wall CNTs and are described briefly here. The CNTs described in this study are grown by CVD technique.

2.3.1): Arc Discharge:

This technique is considered to be the easiest one to produce CNTs as it is quite simple to use. It was first used to produce fullerenes C_{60}. Iijima found that through the arc discharge that some of the evaporated anode redeposit on cathode with cylindrical geometries. The yield of CNTs strongly depends upon the gas pressure, and flow rate. A range of catalysts for the growth of CNTs using this technique have been employed like Fe[64], Co[65], Ni[66] and some rare earths[67,68]. The arc discharge reactor consists of a stainless steel vacuum chamber with a continuous supply of helium (H_e) gas. There are two electrodes i.e. cathode and anode, where the cathode is larger in diameter in comparison to the anode typically with a cathode to anode diameter ratio is 9 to 6. The cathode is kept fixed while the anode is adjustable from outside the chamber as shown in figure (2.4).

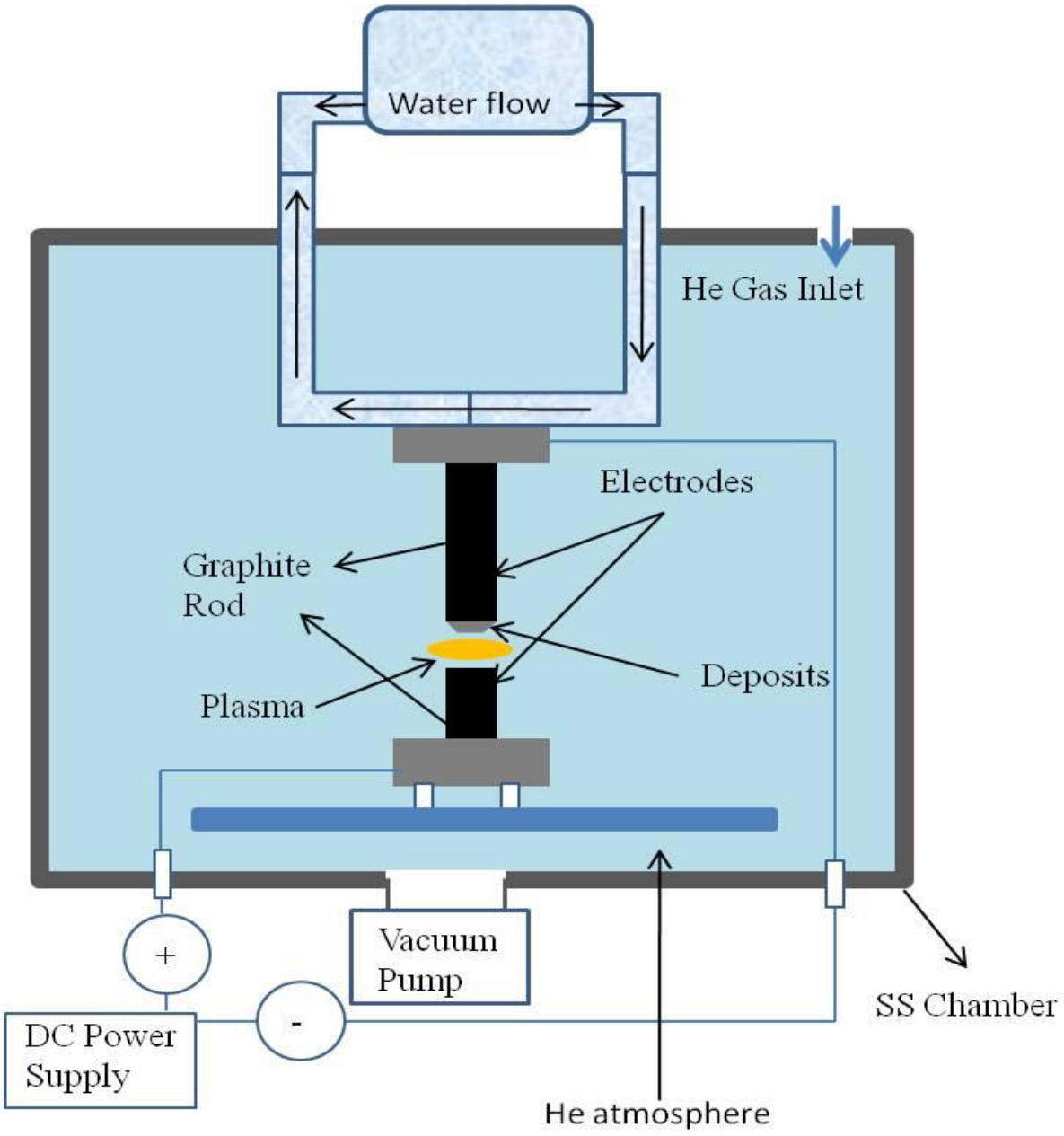

Figure 2.4 Schematic of arc discharge setup for CNTs growth

A DC voltage from a power supply is used to apply voltage across the electrodes. Usually 20V can produce a discharge. For a stable arc the electrodes are kept at a distance of 1mm or less. The voltage is applied after the pressure of the chamber is stabilized. A current in the range of 50 to 100A is produced as a result of the DC voltage and depends upon the diameter of the rods, the separation between them and the gas pressure. When the voltage is

applied the anode starts evaporating and gives rise to CNT formation on the cathode. After the anode is completely depleted the power is turned off.

The main factors affecting the yield and quality of CNTs are the gas pressure, current and cooling system. It has been observed by Ebbesen and Ajayan et al[69] that 500 torr is the optimum pressure for high yield and good quality CNTs. A stable plasma with current as low as possible is responsible for good quality and high yield CNTs, where high current has been reported to affect the yield and gives rise to hard and sintered material[70,71]. This method gives rise to a highly crystalline and almost with no defects or very few structural defects CNTs. Graphite is not necessary for the growth of CNTs, other material like coal can also be used for CNTs production which reduces the cost almost by tenfold.

The main problem with this technique, however, is: its need for a very high temperature for the growth than other methods that the produced CNTs are mixed randomly with a large amount of byproducts especially the one produced by the non-carbon constituents. Because of the higher temperature this method is not useful for metal oxides to be used as catalysts.

2.3.2): Laser Ablation

This technique was first used by Richard Smalley's group at Rice University. Both the continuous and pulsed laser modes are used to vaporise a metal graphite composite in the furnace at 1200C. The chamber pressure is kept at 500 torr using helium (He) or argon (Ar) as the environment[62].

The system consists of a furnace with quartz tube, metal graphite composite target, water cooling system and the gas flow system. The laser beam is focused onto the metal graphite composite target to produce CNTs. These CNTs are usually single wall (SWCNTs) and are collected by a copper collector. This copper collector is cooled down by water flowing through it, which causes condensation of carbon atoms and molecules thus gives rise to larger clusters. The carbon atoms then start diffusing through the catalyst particles until the catalyst particles are cooled sufficiently that prevent the further diffusion of carbon through its surface[72]. This has been shown schematically in figure (2.5).

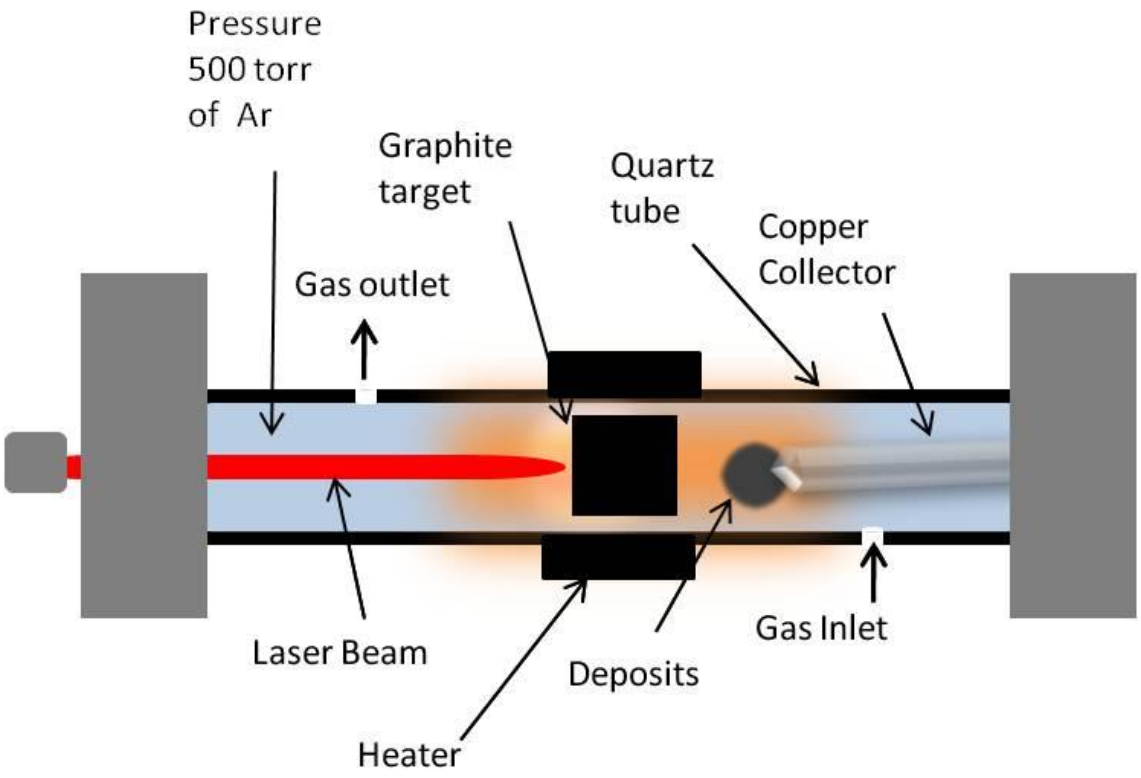

Figure 2.5 Schematic of Laser Furnace for CNTs growth

The diameter of SWCNTs is temperature dependent and could be controlled by varying the reactor temperature. This method is not so common for the growth of CNTs because it needs a quite expensive laser source.

2.3.3): CVD Method

Chemical vapour deposition (CVD) is considered a well-established method for producing CNTs in which organic precursors such as acetylene or methane etc; are used as the carbon source that are decomposed on the catalyst's surface. The choice of catalyst is important because it decomposes the carbon containing gas and has a strong effect upon the CNTs morphologies[33]. Although it has been observed that CVD can be used for catalyst free growth of CNTs[73], but usually this technique is used for catalytic decomposition of carbon containing gas, which decomposes on the catalyst surface and upon diffusion through the catalyst gives rise to CNTs formation. Koyama et al[74] (1972) reported the synthesis of carbon

filament through the catalytic decomposition of benzene at 1000C. The choice of the catalyst is the ultimate requirement for the low temperature CNTs growth through CVD. It has been observed by Deck and Vecchio[75] that only Fe, Ni and Co are active catalysts for the decomposition of hydrocarbon and diffusion of carbon through the catalyst particle. The other metals like Cr, Mn, Zn, Cd, Ti, Zr, La, Cu, V and Gd are non-active in growing CNTs. This is because, either they do not decompose the hydrocarbon or they form carbides with carbon after the decomposition of hydrocarbon and hinder the diffusion of carbon through it. Very recently this perception has been proved wrong by growing CNTs using Cu[76] and Gd[67] as catalysts for the growth of CNTs. In this study it has been shown that transition metals (Ni and Cu) and rare earths (Tb and Ho) doped ZnO could actively grow CNTs. Additionally undoped ZnO do not show in activity towards the CNTs synthesis.

The CVD system consists of a chamber with a stage for a sample, which is kept at a negative potential whilst the chamber's upper portion is kept grounded. The gas inlet is introduced through the upper part of the chamber. The chamber is connected with a turbo pump that creates a vacuum of about $1*10^{-7}$ Torr. The chamber is connected with a heater to provide a specific temperature for the growth of CNTs. Usually the growth temperature is kept between 500-800C and the chamber is kept cooled through water circulation as shown in figure (2.6).

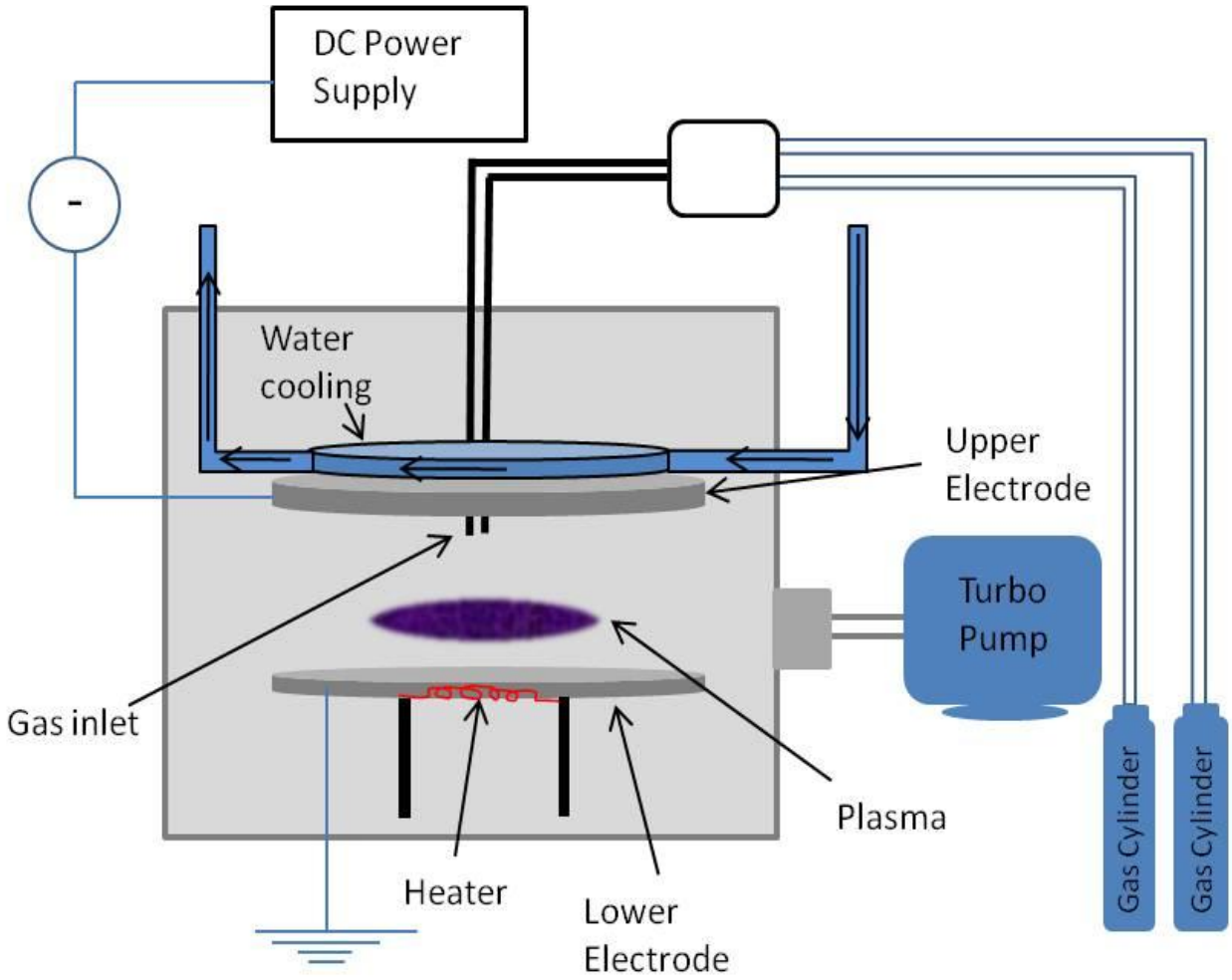

Figure 2.6 Schematic of CVD for CNTs growth

The main advantage of the CVD is that this technique shows high control over the growth process with a quite high yield. It offers a choice for the precursor and catalyst selection. The disadvantage of CVD is that it does not give high quality CNTs in comparison to laser ablation and arc discharge techniques, because of the amorphous carbon produced during the growth process. The amorphous carbon covers the catalyst particle and hinders the growth. The amorphous carbon is produced by the self decomposition of carbon containing gas during the thermal CVD process. In CNTs synthesis this is unwanted material and can lead to leakage current, which in result strongly affect the electrical and electronics properties of CNTs[77].

There are two types of CVD, one is thermal CVD and the other is plasma enhanced CVD (PECVD). In thermal CVD the hydrocarbon is decomposed via heating with catalysts

to promote growth. The growth temperature varies from 500 to 800C. The CNTs produced by the thermal decomposition of hydrocarbon are not aligned and are quite random. Although it has been reported that partially aligned CNTs can be grown through thermal CVD, which is attributed to the van der Waals forces and crowding effect where the neighbouring CNTs support each other[78]. In PECVD the plasma could be created through a range of ways e.g. by direct current (DC), by radio frequency (RF) and by microwave (MW) etc. In this study CNTs have been synthesised through thermal CVD and DC PECVD. Although the exact role of the plasma upon the CNTs growth is still unclear[79] the majority of views is that the electric field in the plasma is responsible for the alignment of CNTs[80,81,82,83]. Additionally it has been observed in this study that PECVD grown CNTs are well aligned while that of CVD is randomly oriented and curly.

2.3.3.1): DC PECVD:

Plasma could be generated when the gases are ionised by supplying energy to the neutral gasses to form the charge carriers like electrons, ions, atoms and reactive and non-reactive radicals with quite complex structures. The plasma is also referred to as electric discharge, glow discharge or gaseous discharge[84]. The energy supplied to the system through direct current is known as DC-Plasma. This is the most simple and common type of plasma in which a potential difference is created between two parallel plates and this can be accomplished by applying from several hundreds to few thousand volts across the two plates. The DC current from few mA to hundreds of mA could be obtained. The distance between the two electrodes could vary from 1mm to few cm, which depends upon the gas flow conditions and the amount of current[85]. The distance between the two electrodes are important for the DC-PECVD synthesis of CNTs, because it determines the field strength, which is believed to be responsible for the alignment of CNTs[80]. According to Tanemura et al[86]; for CNTs to be vertically aligned it is essential to produce excess of positive ions, because in DC-PECVD selective interaction of positive ions with the tip of a CNT is responsible for the alignment. The Schematic of DC glow discharge production is shown in figure (2.7).

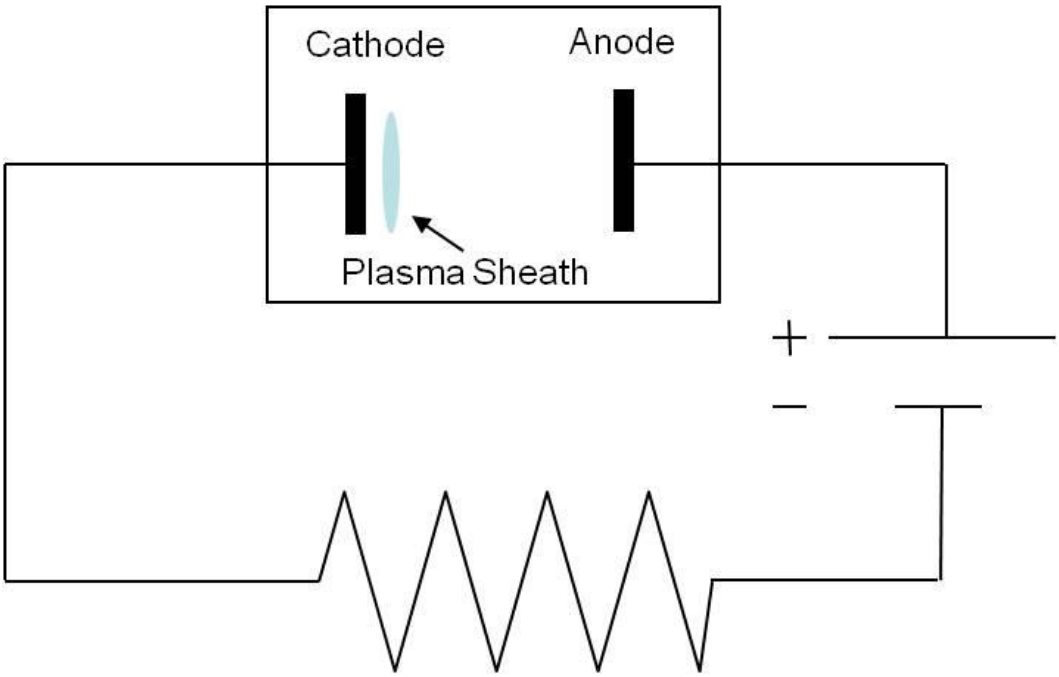

Figure 2.7 Schematic of DC plasma creation between two electrodes

The electrons are accelerated by the electric field with sufficient energy to ionize the rest of the gas molecules by collisions. The ions that are produced by these collisions are attracted towards the cathode, which upon striking the cathode gives rise to secondary electrons. These secondary electrons are accelerated towards the anode and cause further collisions and give rise to further ionization and continue until the potential difference is maintained.

2.3.3.2): DC Glow discharge**:**

Before the application of a potential the gas molecules remain electrically neutral. When a large potential difference in the range of few hundreds of volts is applied, the free electrons attain high kinetic energy and become quite hot because of their low mass. These electrons then collide with the gas molecules in the plasma giving rise to excitations, ionizations and dissociations of atoms and molecules, that result in a range of chemically

reactive species like ions and radicals. DC glow discharge consists of number of distinct regions like cathode sheath, negative glow and positive column etc, as shown in the figure (2.8).

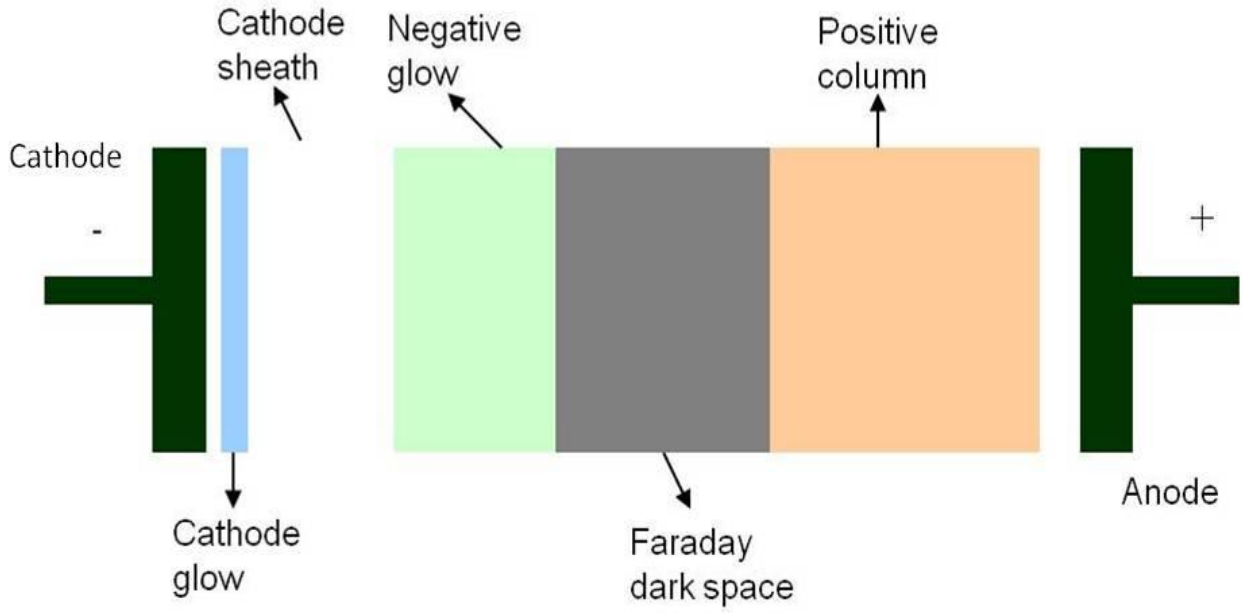

Figure 2.8 DC glow discharge diagram showing different regions of plasma.

The cathode and anode are the two plates that are kept at opposite polarity, the cathode is kept at negative potential while the anode is kept at positive potential. The cathode glow region is because of the excitation of neutral gas molecules by ions bombardment and has the higher ion density compared to other regions. The positive ions are accelerated towards the cathode and recombine. The excited ions fall to ground state with the emission of light and gives rise to the cathode glow. Most of the positive ions are coming from the negative glow region, where fast electrons collide the neutral atoms and causes ionisation and even excitation of ions as well.

The negative glow discharge region is the brightest region in the DC glow discharge volume. It contains almost equal number of electrons and ions. The ions are attracted towards the cathode from negative glow discharge and secondary electrons are attracted towards the negative glow discharge from the cathode. The space between the cathode glow and negative

glow is less luminescent, which is called as the cathode dark space. This region has the strongest electric field and is also called as the cathode sheath region consists of higher ion density and low electron density and most of the potential drops across this region.

The Faraday dark space has very low ion density and the electrons could be accelerated by a small field. Since electrons are moving slowly in this region therefore the chances of ion electron recombination is more likely. The electric field increases as we move towards the anode. The rise in electric field increases the kinetic energy of electrons. When the kinetic energy of an electron reaches the resonance energy then the electron can excite the neutral atom or molecule, which gives rise to light emission upon de-excitation[87].

2.4): Growth Modes of CNTs using CVD

The growth of CNTs by CVD is due to the decomposition of the carbon containing gas on the surface of the catalyst particle. The carbon atoms then diffuse through the catalyst particle and gives rise to CNTs formation. This process is divided into two parts, one is the decomposition of the carbon containing gas on the catalyst surface and the other is the diffusion or precipitation of the carbon atoms through the catalyst particle. The former is quite clear and mostly belong to the carbon deposition that strongly depends upon the surface morphology and chemical nature of the catalyst[101]. The later one is quite controversial but the most commonly held view is that the driving force for the carbon diffusion through the catalyst is the activation energy, because the activation for the CNTs formation is the same as that for the carbon diffusion through the catalyst material[88]. The diffusion of carbon through the catalyst particle could be divided further into two types, the surface diffusion and the bulk diffusion. In the surface diffusion process the carbon atoms diffuses through the catalyst surface and the CNT grows on the side of the catalyst particle. In this process the catalyst nanoparticles remains solid and is used to explain the low temperature growth[89]. This process was first shown by Tom Baired and his colleagues in 1974 [90]. The connection of the surface diffusion process with CNTs growth was first observed by Helveg[19] and Ajayan[91] through in-situ high resolution transmission electron microscope (HRTEM) experiment. They observed through high resolution images (atomic scale images) the reaction of methane (CH_4) on the

surface of Ni nanoparticles at 500C. It was observed that there are mono-atomic steps on the surface of the Ni nanoparticles and the graphene sheets terminate at these steps. These mono-atomic steps are believed to be responsible for the nucleation and growth of CNTs. As shown in figure 2.9.

Fig; 2.9[19]; HRTEM image of the catalyst nanoparticles during the in-situ CNTs growth process, the arrows show the mono-atomic steps in the catalyst nanoparticle , where the carbon atoms diffuse through and form a CNT.

The bulk diffusion is like that of the surface diffusion process but here it is believed that catalyst nanoparticle can either be a solid or become a liquid nano-droplet. In case the particle becomes a liquid droplet then it is necessary for it to be super saturated after which the precipitation of carbon will occur that causes the CNTs formation.

This is the basic assumption for vapour-liquid-solid (VLS) mechanism, which was first proposed in 1964 for the synthesis of Si and Ge whiskers[92,93] and *Saito et al*[94] extended the same model for the CNTs formation in 1995. The controversy with this process (VLS) appears to be that the temperature used for the MWCNTs ranges from 550C to 700C, while the melting point of the bulk material is too high above the temperature used for CNTs

synthesis. Like for Fe the melting point (MP) is 1536C and that for Ni is 1453C. However if the size effect is taken into consideration as shown by *Buffat*[95] and Mei[96], the melting point of the material could be depressed significantly if the particle size is reduced from bulk to nanoparticles, even though the melting point of 10nm Fe nanoparticle is shown to be about 940C and that of Ni is 1180C [97]. Therefore it seems quite difficult to believe that the melting of the catalyst particle occurs during the MWCNTs growth.

It was first proposed by *Baker and colleagues* in 1972[88] that the formation of a filament is the result of carbon deposition advancing behind the metal particle with the top surface of the metal particle remaining apparently clean. It was also observed that the activation energy required for the formation of a carbon filament is the same as that for the bulk carbon diffusion through a nickel particle. Using these, Baker proposed the tip growth and base growth mechanisms for the carbon filament and is briefly discussed below. Both the growth processes have been proposed for filaments, multiwall CNTs and single wall CNTs that largely depend upon the nature of the catalysts, carbon containing gas and the growth temperature. It is shown by *Huang et al*[98] that rapid heating of the substrate gives rise to tip growth while slow heating of the substrate results in the base growth process while keeping the other growth conditions constant.

2.4.1): Tip growth process

In this process the carbon containing gas (usually hydrocarbon) is decomposed on the front face of the catalyst nanoparticles and the carbon then diffused through the particle, which results in the formation of filament or nanotube. In this process the CNT remains stuck to the substrate and the catalyst particle is attached to the other end of the growing nanotube, as shown schematically in figure (2.10).

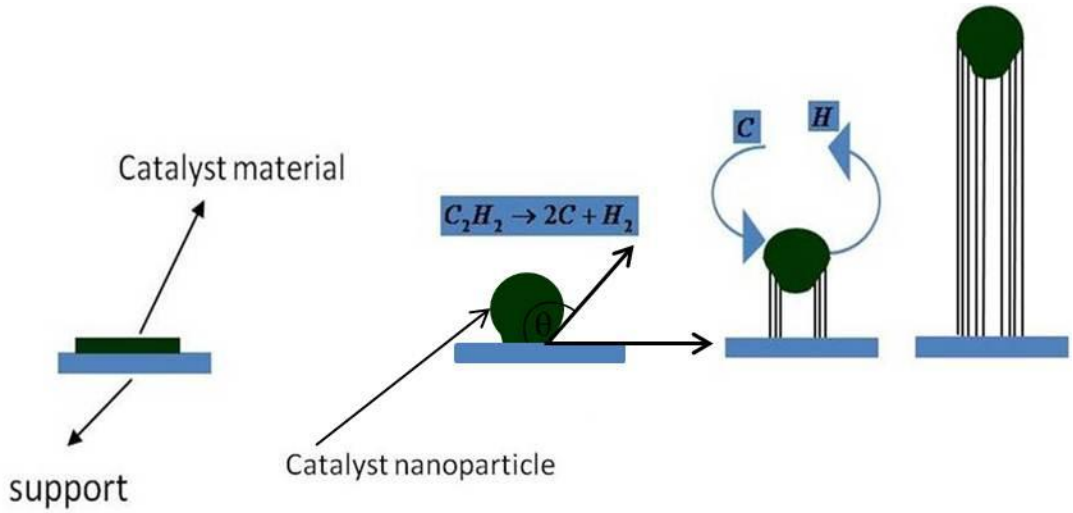

Figure 2.10 Schematic diagram of tip growth process, showing the nanoparticles formation from the evaporated continuous film at some elevated temperature. The angle between the catalyst and support defines the growth mechanism.

The main factors involved in the tip growth process are the temperature and concentration gradients. Additionally, the CNTs diameter is responsible for the growth mode, for larger diameter MWCNTs tip growth process is dominant while for MWCNTs with few shells or SWCNTs the base growth is the most favourable[99]. The formation of continuous film or islands upon physical deposition of a material on a substrate depends upon the surface energies of substrate and the depositing material. If γ_A is the interface energy of a substrate and γ_B is the energy of the depositing material then the contact between the two phases can be described as[100],

$$\gamma_A = \gamma_{AB} + \gamma_B cos\theta \qquad (2.4)$$

If $\theta = 0$ then the film will be continuous otherwise will give rise to islands. The higher the angle the higher will be the chances of tip growth process. According to *Dijon's et al*[101] there is a critical particle size limit and the chemical state of the catalyst particle that is responsible for the type of the growth mode. *Bower et al*[80] attributed the tip growth process to the weak catalyst support interaction using cobalt (Co) as catalyst.

2.4.2): Base growth Method:

In this process the catalyst particles remain attached to the substrate and the CNTs grow in the air with either the tip closed or open. The base growth process occurs because of the strong catalyst support interaction as shown schematically in figure 2.11.

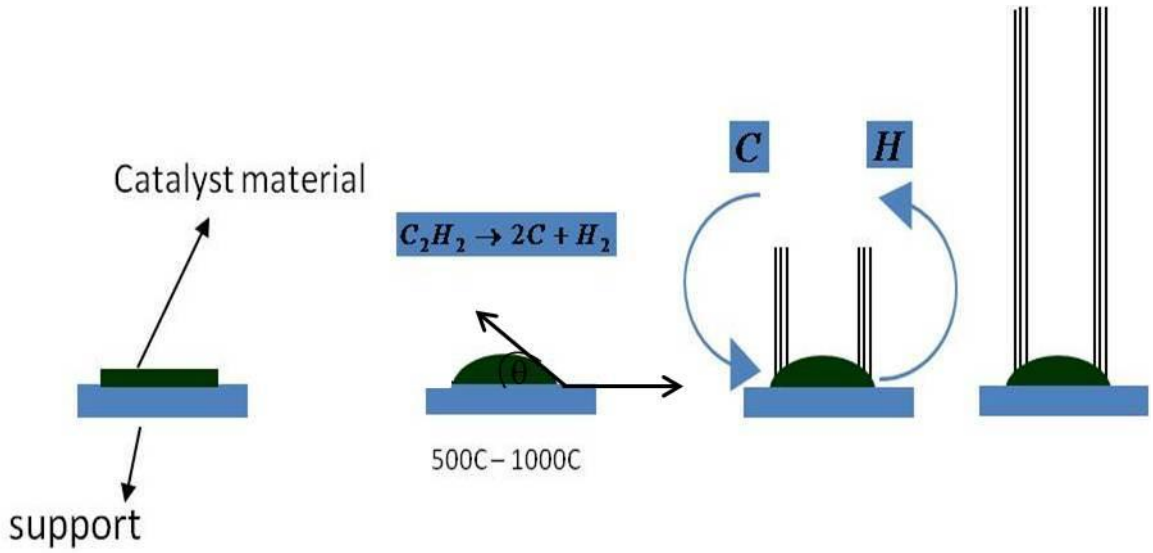

Figure 2.11 Schematic diagram of base growth process, showing that catalyst nanoparticles making smaller angle with the substrate gives rise to base growth process.

The CNTs will continue to grow until the carbon feedstock is stopped, or the amorphous carbon fully covers the catalyst particle. Actually there are two reactions that are taking place at the same time on the surface of the catalyst nanoparticle in CVD growth, one is the formation of amorphous carbon and the other is the formation of graphene layers. The amorphous carbon slowly and gradually covers the whole catalyst particle cutting off the carbon source and results in the termination of CNTs growth.

2.5): Electron sources

An electron beam is the collection of extracted electrons from a solid surface and it plays an important role in observing the fine details of mater. Electrons could be obtained

from the surface of a desired material by some physical emission processes. The electrons could be removed from the solid surface either,

i): By Exciting the electrons thermally to overcome the energy barrier of the solid surface, or

ii): By thinning and lowering the potential barrier through the external applied field, so that the electrons can tunnel through or pass over the potential barrier. The tunnelling of electrons through the potential barrier occurs in the cold field emission, while both the electron tunnelling and overcoming the barrier happens in Schottky field emission processes as discussed in the preceding sections of this chapter.

Electron beams have potential applications in microscopes, interferometers and field emission displays etc. A range of information could be obtained like topography, elemental composition and crystallographic information when an electron beam interacts with matter. The most important parameters for an electron source are the brightness, energy spread, stability and long life time. The brightness (B) of an electron source is the amount of current emitted per unit area (normal to the beam) per solid angle as defined by Hawks et al[102] (1989) and is measured in $A/cm^2\ sr$.

$$B = \lim_{\Delta a \to 0} \lim_{\Delta \Omega \to 0} \left(\frac{\Delta I}{\Delta a \Delta \Omega} \right) \tag{2.5}$$

The final beam diameter (d_T) of an electron source is affected by two main factors. One is because of the nature of the electron source and the other is the lenses of the electron optical system. The final; beam diameter could be described as[103],

$$d_T = \sqrt{d_0^2 + d_s^2 + d_c^2 + d_d^2} \tag{2.6}$$

Where

$$d_d = \frac{0.61\lambda}{\alpha_i} \tag{2.7}$$

$$d_s = 0.5 C_{si} \alpha_i^3 \tag{2.8}$$

$$d_c = 2C_{ci}\alpha_i \, {\Delta V}/{V_i} \qquad (2.9)$$

Where d_0, d_d, d_c and d_s are the contribution of the diameter of the emitted beam from the electron source, the diffraction effect, chromatic aberration and spherical aberration respectively, λ is the electron wave length, α_i is the beam angle in the image side, C_{ci} and C_{si} are the co-efficients of chromatic and spherical aberrations respectively and ΔV is the energy spread of the electron source. Here it is worth noting that d_c and energy spread (ΔV) are directly related to one another and it is the full width at half maximum (FWHM) of the total energy distribution as shown schematically in figure 2.12.

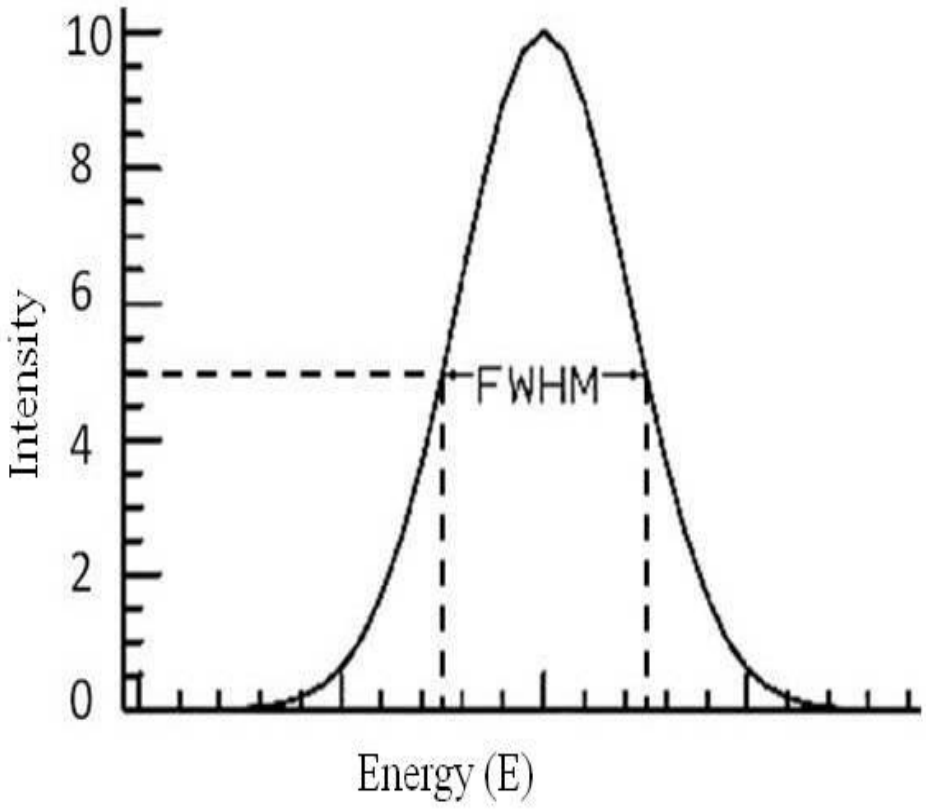

Figure 2.12 Schematic of the total energy distribution of the emitted electrons. The energy spread is the FWHM of the total energy distribution curve.

Emission current stability is the emission current fluctuations, which arises either from the variations in the work function or from the variation of applied field. Variation in

the work function usually happens because of the adsorption and desorption of gasses, and the applied field fluctuation which arises from the geometric fluctuations. An electron source is said to be ideal if it exhibits high brightness, low energy spread, small source size, high stability and longer life. The most commonly used electron sources are the thermionic sources, cold field emission sources and Schottky field emitters. These three sources are described briefly below.

2.5.1): Thermionic emission

It is the process in which electrons cross the potential barrier and escape into the vacuum by gaining sufficient thermal energy. The potential barrier also known as the work function is different for different materials. The work function is the potential energy barrier between the Fermi level and the vacuum and the Fermi level in metals lies in the conduction band. If the temperature is increased to some finite value T, then the energy distribution function for an electron to occupy higher energy levels is given by the Fermi-Dirac distribution function as,

$$n(E) = \frac{1}{exp\left(\frac{E - E_f}{kT}\right) + 1} \qquad (2.10)$$

Where *n(E)* is the density of states with energy *E* and E_f is the Fermi energy. k is the Boltzmann constant and T is the temperature in Kelvin. This equation indicates that the difference in energy decreases with increase in temperature. More and more electron will overcome the potential barrier and will escape into the vacuum. The minimum amount of energy required for the escape of electrons would be of the order of [104]

$$E_{min} = E_f + e\emptyset \qquad (2.11)$$

Where $e\emptyset$ is the work function of the metal. The current density of thermally emitted electrons with work function $e\emptyset$ at any temperature T is given by the Richardson-Dushman equation[105].

$$J(T) = \frac{4\pi mek^2T^2}{h^3} e^{\left(-e\emptyset/kT\right)} = AT^2 e^{\left(-e\emptyset/kT\right)} \qquad (2.12)$$

Where T is the temperature, $e\emptyset$ is the work function, k is the Boltmann constant and A is the Richardson constant $= 120\ Amp/cm^2K^2$ [105]. It is evident from the above equation that the current density of the thermally emitted electrons depends strongly upon the temperature and the work function of the cathode material. These two characteristics define a basis for the thermionic source. A material with low work function and high melting point can be a good thermionic electron source.

A thermionic electron gun consists of a cathode, anode and a Wehnelt. The cathode is usually made in a hairpin shape and is kept at negative potential. The filament current is responsible for the temperature of the cathode and hence controls the beam current. A wehnelt is a cylindrical shaped electrode near the cathode and is kept at less negative potential relative to cathode. It is used to control the electron beam and focus it. The anode is held at strong positive potential that causes electrons to accelerate. The beam of electrons passes through a small opening at the centre of the anode as shown in figure 2.13.

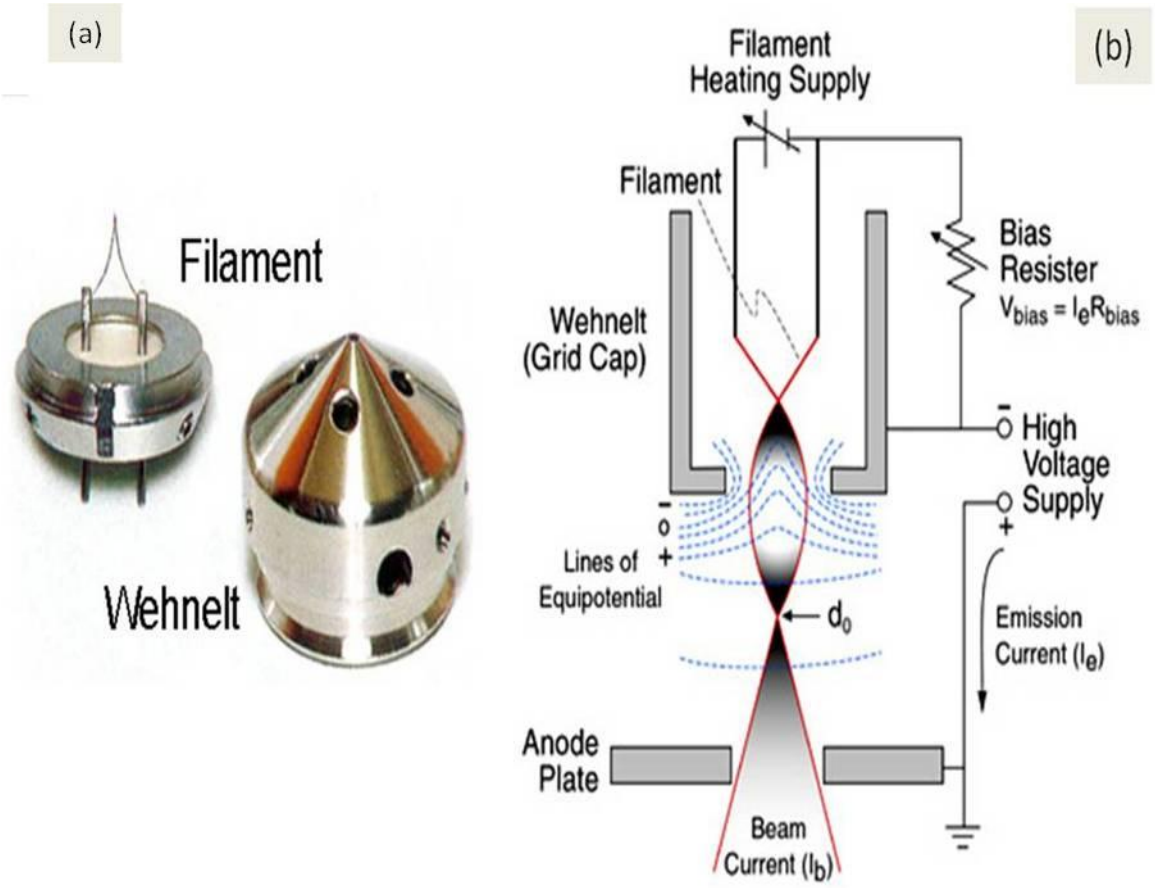

Figure 2.13[106] (a): tungsten filament with corresponding Wehnelt (b): Schematic of thermionic emission along with the electrode configuration.

Usually a tungsten hairpin is used as a thermionic electron source with a work function of 4.5eV and melting point around 3650K. The tungsten hairpin is usually operated as thermionic electron source in a pressure of about 1×10^{-5}mbar or lower. Another widely used thermionic electron source for microscopy is the single crystal of lanthanum hexaboride (LaB_6) with a work function of about 2.5eV [107]. The operating pressure for LaB_6 cathode is about 1×10^{-6} mbar and has 10 times higher brightness than Tungsten filament.

2.5.2): Schottky Field Emission:

In this process the electrons are emitted from the metal surface with the combination of both the temperature and that of the electric field. The electric field is used to make the potential barrier thinner and the temperature provides the electrons an extra energy to escape from the metal surface. The energy diagram for the Schottky emission is given in figure 2.15. If F is the applied electric field, then the work function will be reduced by the amount of [108].

$$\acute{\phi} = \phi - e^{\frac{3}{2}} F^{\frac{1}{2}} \qquad (2.13)$$

The total emission current density of the Schottky emitter will be [108,109],

$$J_s = 120T^2 \exp\left(\frac{-\phi}{kT}\right) \exp\left(\frac{(e^3F)^{1/2}}{kT}\right) \quad Amp/cm^2 \qquad (2.14)$$

This equation shows that the Schottky emission depends upon the applied electric field, the temperature and that of the work function of the tip material. The electric field has two effects on the emission process[110]. One effect is that it lowers the potential barrier and makes it easier for electrons to overcome the barrier with increasing the temperature. It is because at higher temperatures, electrons occupy the higher energy levels near the top of the potential barrier. The other effect is that it reduces the width of the barrier (thinning) so that electrons could tunnel through the barrier. The total emission current is then the combination of both the thermionic electrons and the field emitted electrons this is usually called extended Schottky emission.

The Schottky emitter is usually a single crystal tungsten wire with one end etched down to tip and the other end is spot-welded to polycrystalline tungsten wire. The single crystal tungsten wire with (100) plane normal to the axis of the tip is coated with ZrO, which is used to lower the work function from 4.5eV to 2.8eV. The ZrO coating lower the work function of (100) plane more, than the other orientations like [111] or [110] etc[111]. The Zr

and O_2 ratio plays a critical role in defining the work function, because the excess amount of oxygen may increase the work function, however it is reversible if the emitter is operated below 1850C [112] as shown in figure 2.14. The Schottky emitter is operated at 1800K with a relatively poor vacuum of about 10^{-8} to 10^{-9} mbar in comparison to the cold field emitter. The electric field of about 1V/nm is required at the tip to get emission from the source.

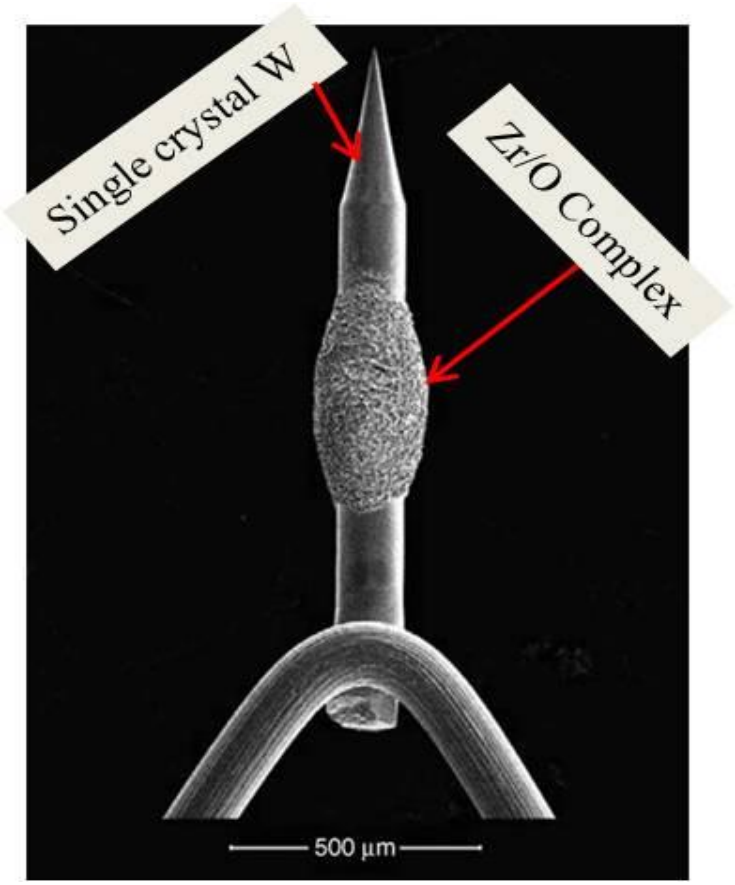

Figure 2.14[112]: Single crystal W tip with Zr/O complex.

The essential parameters for an electron source are the brightness, energy spread and the stability. The brightness determines the amount of current, energy spread is involved in the probe diameter and the stability of the shape of the emitter specifies the stability of the beam. The shape of the emitter is not thermodynamically stable because of the applied field and the temperature that causes surface diffusion.

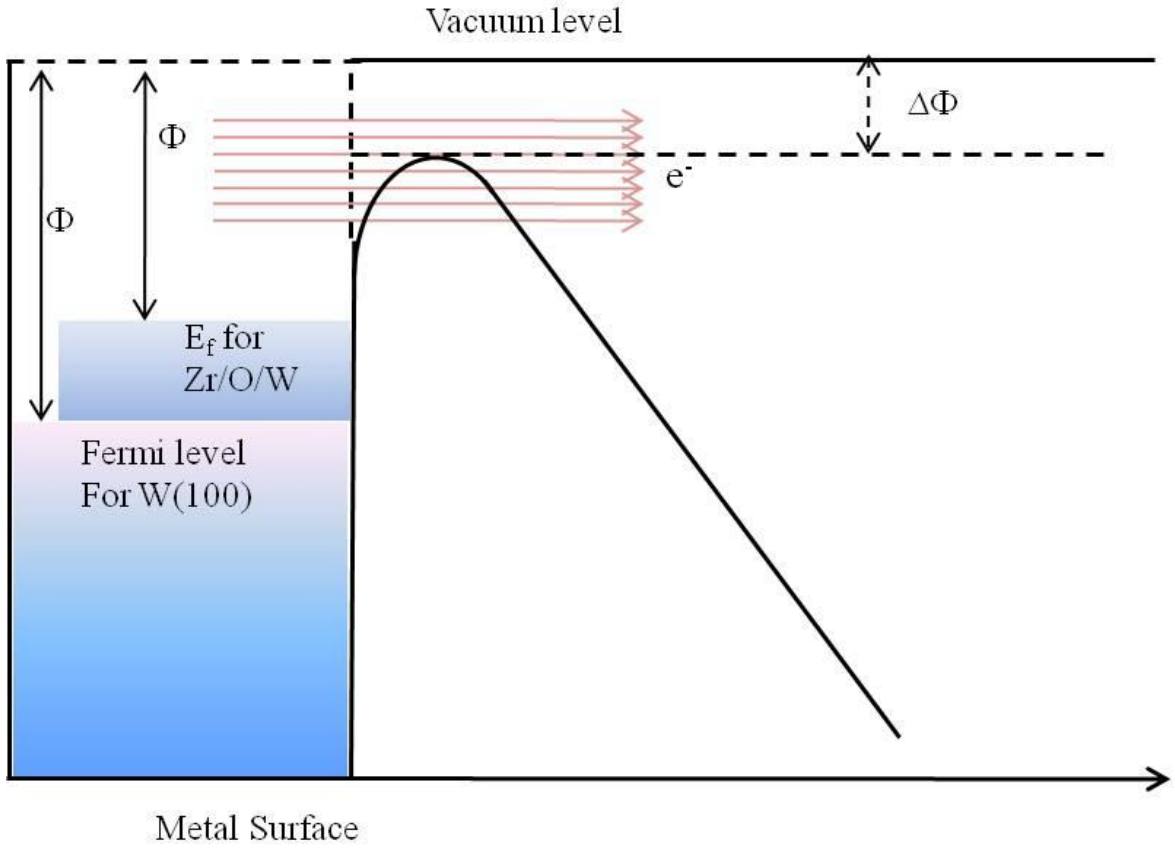

Figure 2.15[110] Potential energy diagram showing the lowering and thinning of the potential barrier. The potential barrier is lowered by an amount of Δϕ. Some of the electrons acquire enough energy and overcome the barrier while some of the electrons tunnel through the potential barrier.

The main advantages of the Schottky emitter is, it has a longer life, small source size, high brightness and high emission stability.

2.5.3): Field Emission Mechanism

In the cold field emission process, electrons are extracted from a material (metals and semiconductors) with the application of a very high electric field (of the order of several KV/μm)[113], which is used for thinning the potential barrier. The electrons then tunnel through the barrier quantum mechanically, according to wave mechanics there is always a probability for the electron to tunnel through the potential barrier. At low temperatures the electrons tunnel through the potential barrier from around the Fermi level because the high energy

levels are empty and electrons are not available above the Fermi level. Therefore the field emission process could be treated as one dimensional potential barrier, as shown by the potential energy diagram in figure 2.16.

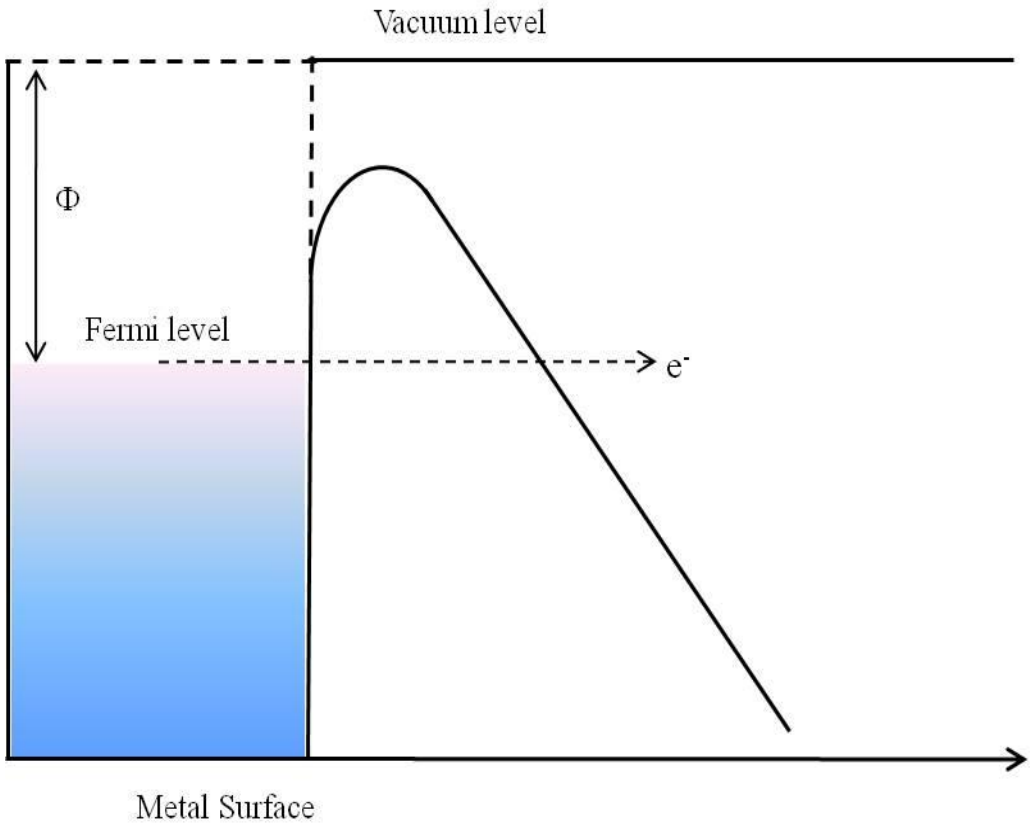

Figure 2.16 Potential energy diagram showing emission mechanism of field emitted electrons. Electrons are emitted through tunneling from the Fermi level.

The cold field emitters have a longer life compared to other emitters but have lower emission stability. It is the high electric field around the tip that causes in the ion formation which attacks the tip and causes instability. To minimize the back ion bombardment, it is necessary for the field emitter to operate in the ultra high vacuum, in the range of about 10^{-10} mbar. But even at ultra high vacuum some of the adsorbates contaminate the tip and it needs flashing after successive usage to restore the emission current[103]. Field emission electron sources are generally made of a single crystal tungsten wire because of its high melting point and its ability to withstand with high electrostatic stress.

In a field emission system, there are two anodes, one is called the extractor that regulates the field at the tip and the other anode is responsible for accelerating the electrons. The cold field emitter has a very sharp tip in comparison to the thermionic emitter. It is because the electric field around the tip increases with decreasing the radius of the tip. Therefore the sharper the tip the higher will be the field enhancement factor β (where $F = \beta F_0$ and $\beta = h/r$) where h is the height of the tip and r is the radius of the tip[114]. As shown schematically in figure 2.17

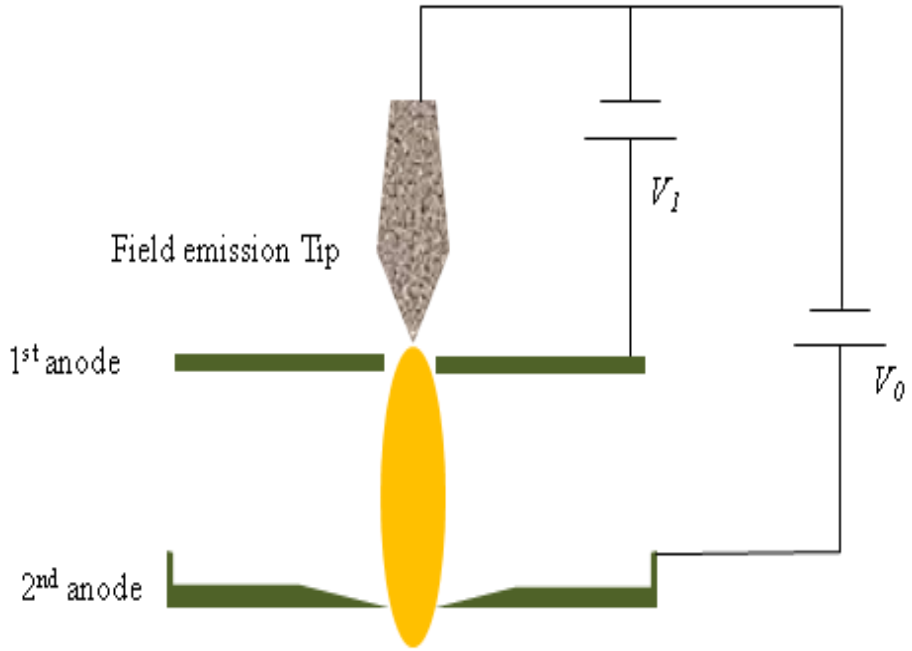

Figure 2.17 Schematic for the field emission along with the corresponding electrode configuration.

The tip is made sharp to obtain a high electric field, because the smaller the radius of curvature the higher will be the electric field. The field emission mechanism is described by the Fowler-Nordheim model for the electron tunnelling to vacuum from the metal surface. The relation between the applied electric field and the emission current density at T=0 is given as[115] ,

$$J = 1.42 \times 10^{-6} \frac{F^2}{\phi} \exp\left(\frac{10.4}{\phi^{1/2}}\right) \exp\left(\frac{-6.44 \times 10^7 \phi^{3/2}}{F}\right) \quad (2.15)$$

Where J(Acm^{-2}) is the current density, F(V/cm) is the applied electric field, Φ(eV) is the work function of the metal. For field emission the shape and the work function of the cathode plays an important role. A smaller change in the shape or in the chemical state of the cathode has a strong impact on the emission current because it ultimately changes the field strength or the work function[116].

The main advantage of the field emission electron source is the high brightness of about 10^8 to 10^9 Amp/cm^{2}sr. The energy spread for the cold field emitter remains in the range of 0.2 to 0.3eV. The stability of the field emitter can be improved by improving the vacuum conditions and having properly cleaned electrodes. The tip can be cleaned through moderate heating. For carbon nanotubes the applied potential is quite small and remains in the range of 1.5KV to 2KV[117] for typical systems employing the Schottky emitter.

2.6): Carbon Nanotubes as an Electron Source:

Electron sources are the main focus of research and industry, and there is still a huge appetite of field emission sources in cathode ray tubes and in flat panel displays. The work function of CNTs is an important physical property for the field emission and can be determined from the electronic structure of CNTs. It has been focused on the investigation of the localized states near the Fermi level during emission process and has been understood that the work function of CNTs depends upon the tip geometry[118]. The voltage, current stability and the energy spread are the important parameters for the electron emission sources. The energy spread and the reduced brightness affect the resolution of the equipment, and depend upon the angular current density and the virtual source size. Carbon nanotubes have shown a high degree of coherence, a small value of virtual source size and a small energy spread[119]. An individual CNT emits most of the current in a single beam, which shows a round spot along with some wide visible patterns which contain a minor fraction of total current[120], which is attributed to be the magnified image of the capping of the emitting nanotube[121]. This

single spot brightness (as shown in the figure 2.18) is more desirable as a source in an electron microscope, but again it depends upon the band structure of a CNT which alters with the way it is synthesised.

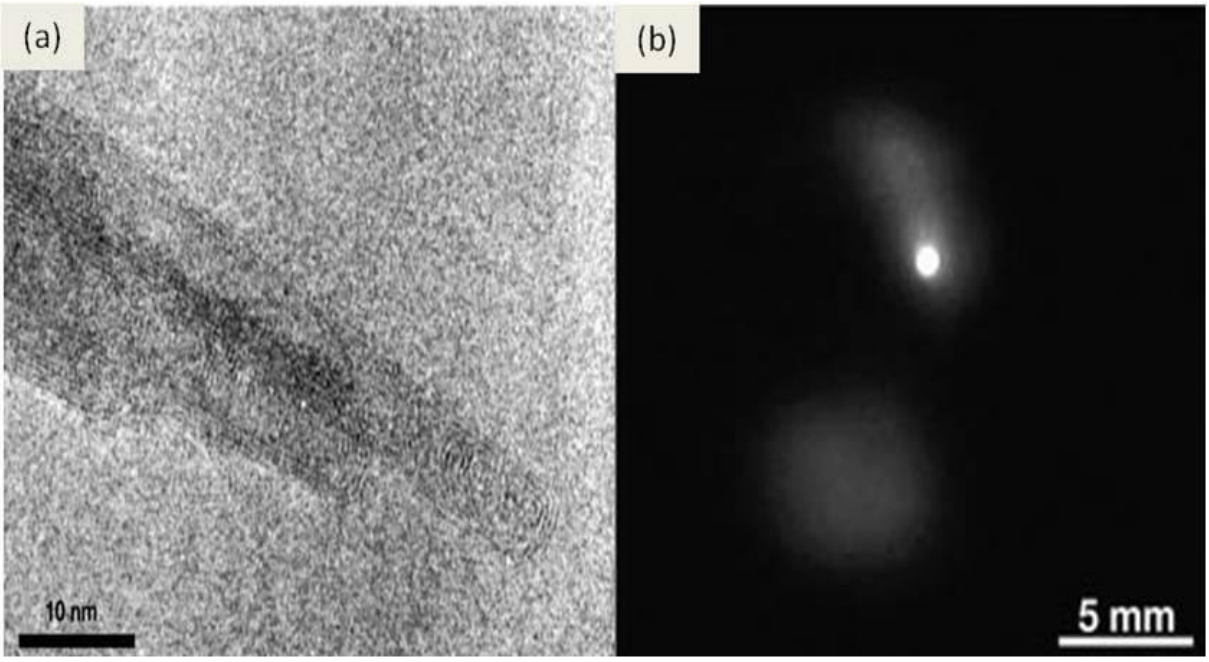

Figure 2.18[120] (a); A single CNT (b); the corresponding emission pattern.

Carbon nanotubes are considered to be an ideal field emitter because of the high aspect ratio, small radius of curvature at the tip, high electrical conductivity and high mechanical strength. For aligned CNTs it is believed that maximum field emission can be obtained if the ratio of inter-tube distance to the height of a CNT is kept at approximately 2. This is because of the reduced the screening effect in the nearest neighbour CNTs[122]. It has been shown by Bonard et al[123] that a maximum current of about 0.2mA can be drawn from one CNT, and the greatest part of the emitted current comes from the localized states that lie near the Fermi level. The localized states have a great impact upon the emission mechanism because of high density of states. Simulations show that at the tip of CNTs the local density of states is higher (almost 30 times higher) than the rest of the CNT, which is why the field emission current in CNTs is far higher because of the carrier density at the tip[123]. Fujii et al[124]

characterised the aligned CNTs bundle for emission current, and showed that it is the edge effect that is responsible for high field emission in CNT bundles, while the electric field remains constant for CNTs flat film. Also it was shown that the CNT bundles are highly stable, and this is because of the high density structure and low per CNT current in the bundle[124] as shown in figure 2.19.

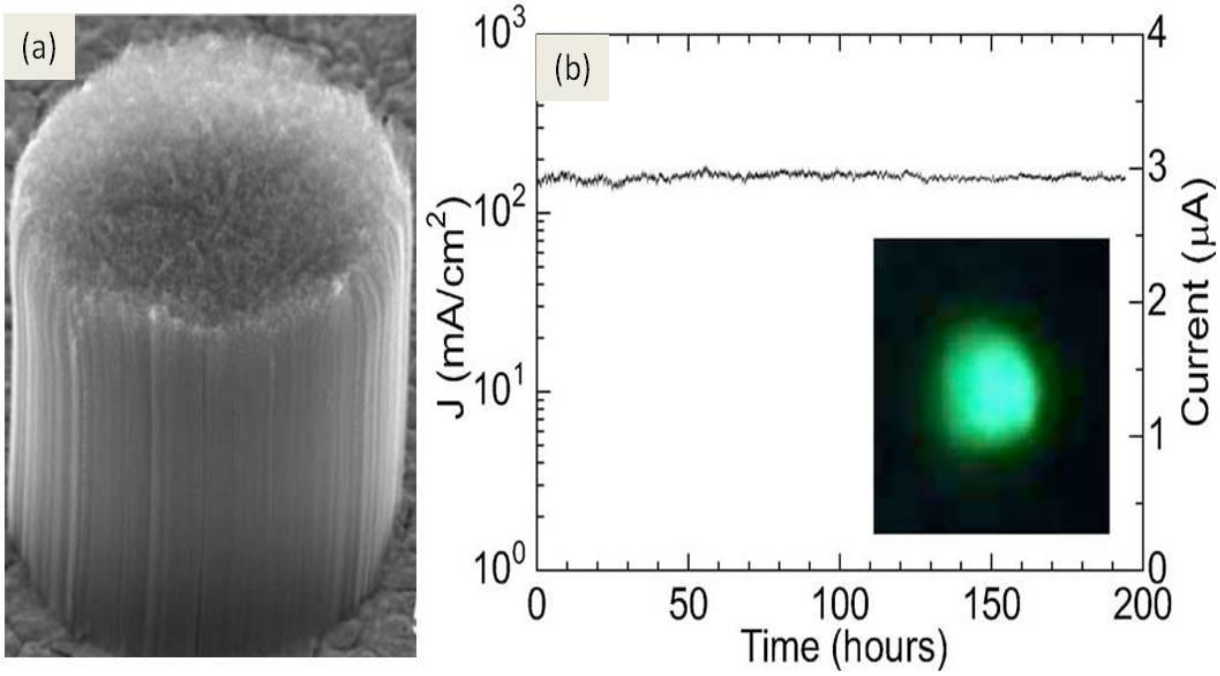

Figure 2.19[124] (a); CNTs bundle (b); the corresponding emission stability for 200 hours and field emission pattern that shows a single spherical spot.

Baik et al[125] (2007) tried to improve the emission characteristics of CNTs with electrical treatment and showed that non-stationary electric field is more effective in enhancing the emission characteristics of CNTs than direct current and square-pulsed electrical treatment. The ac treatment activates the emitter and also suppresses the abnormal emitting spots.

2.7): Crystal structure of ZnO

It crystallizes in three different phases' i.e hexagonal wurtzite, sphalerite (zinc blend) and cubic rock salt. In each phase each anion or cation is surrounded by four other cations or

anions respectively. The wurtzite phase of the ZnO remains stable under ambient conditions, while the other structures could be obtained by applying specific conditions, like strain and high external pressure. The wurtzite structure is an example of hexagonal crystal system, where two tetrahedrally packed sublattices are joined together to form a wurtzite structure. In wurtzite phase each sublattice has four atoms per unit cell and every atom of Zn is surrounded by four O atoms and in similar way an O atom is surrounded by four Zn atoms. For an ideal wurtzite structure the atoms are displaced along the c-axis by an amount of u =3/8 = 0.375, Where, *u* is the bond length parallel to c-axis[126]. The schematic of the unit cell is given in figure 2.20.

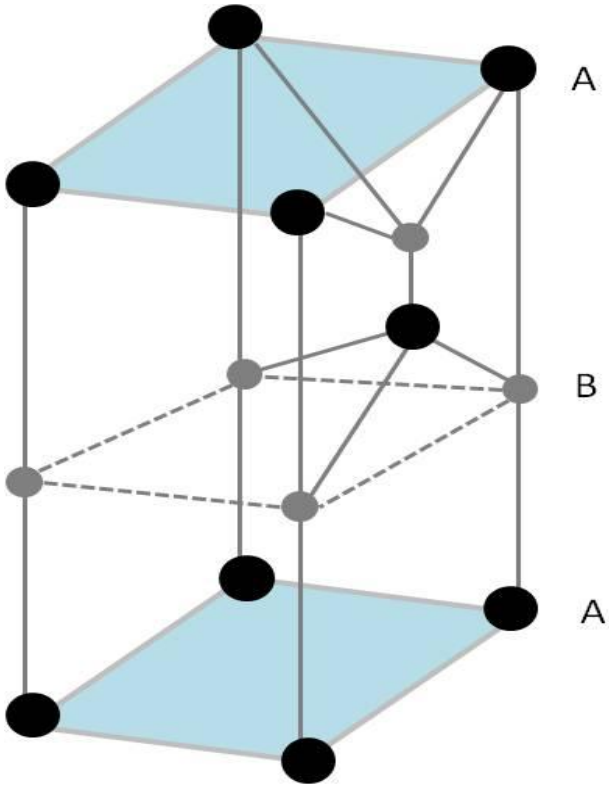

Figure 2.20: Schematic representation of one of the tetragons of Wurtzite crystal structure of ZnO. The gray spheres represent the Zn atoms while the grey spheres represent the oxygen atoms.

The lattice parameters for wurtzite phase observed experimentally through various techniques are in good agreement with the theoretical calculations. The experimentally observed values by *Karzel et al*[127] through x-ray diffraction (XRD) and Desgrenier et al[128] through energy dispersive x-ray diffraction (EDXD) are a =0.3247nm, c =0.5204nm and a

=0.3249nm, c= 0.5207nm respectively, while Catti et al[129] calculated the lattice parameters for the ZnO through ab-ibintio calculation using linear combination of atomic orbitals theory and found a = 0.3286 nm and c =0.5241nm.

The wurtzite structure belongs to the symmetry group of $P6_3mc$. Since each Zn atom is surrounded by four O atoms, therefore each atom (Zn or O) will be coordinated at the edges of a tetrahedron. If a wurtzite structure in ZnO is disturbed from its ideal atomic arrangements through a distortion of tetrahedral angles, the *c/a* ratio will decrease and the parameter *u* will increase in such a way that the four tetrahedral distances remain constant. The parameters u and c/a ratio are inversely related to one another by a relation below[126].

$$u = \left(\frac{1}{3}\right)\left(\frac{a^2}{c^2}\right) + \frac{1}{4} \qquad (2.16)$$

ZnO could also be crystallized in sphalerite (zinc blende) phase and this happens because of high strain. This phase is not stable and could be stabilized if grown hetroepitaxially on cubic substrates such as GaAs[130]. Like that of wurtzite phase, the unit cell in sphalerite phase consist of four atoms in which every cation is surrounded by four anions and vice versa, but here two face centred sublattices are joined together to form a sphalerite phase instead of tetrahedral sublattices. The two sublattices are shifted along the body diagonal by one fourth (1/4) of the body diagonal. Both the wurtzite and sphalerite phases have the same tetrahedral coordination and the same bond length between the nearest and next nearest neighbours. There are four nearest and twelve next nearest neighbours in both the wurtzite and sphalerite phases. The only difference between both the structures is the stacking sequence of the closed packed diatomic planes. The stacking sequence in sphalerite structure takes place in AaBbCcAaBbCc…….. manner, along (111) plane in the <111> direction, as shown in the figure 2.21.

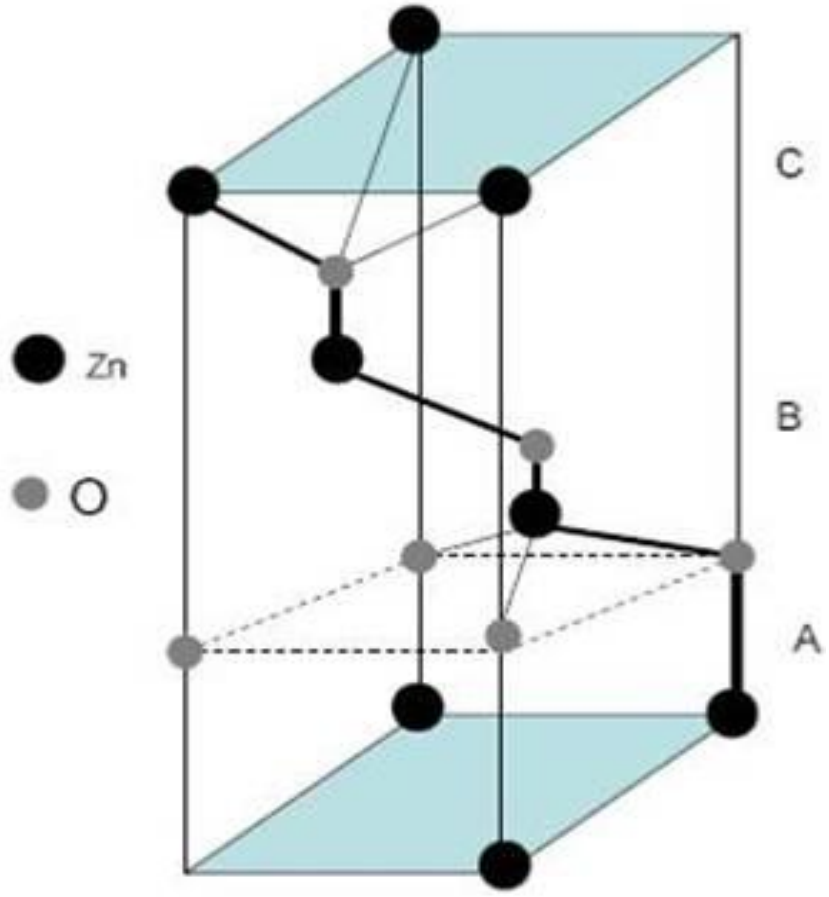

Figure 2.21 Schematic reperesentation of sphelerite crystal structure of ZnO. The black spheres represent the Zn atoms while the gray spheres represent the oxygen atoms. The crystal is arranged in ABCABCABC …….. packing.

While the stacking sequence in wurtzite structure is in AaBbAaBb…… manner along the (0001) plane in the <0001> direction. The lattice parameters calculated through the ab-initio calculations were found to be a^{131} = 0.460nm and a^{129} =0. 4619 nm and belongs to the space group $F\bar{4}3m$.

The third form in which the ZnO could be crystallized is the rock salt structure, which takes place when an external pressure is applied on wurtzite ZnO shown in figure 2.22. It happens because of the reduced lattice dimension that breaks the covalent nature of the bonds and become more ionic. This structure has a face centred cubic array of anions with an interpenetrating array of cations and specified by *Fm3m* symmetry group. In the rock salt structure each atom is coordinated with six other atoms at the edges of an octahedron. The term octahedron is because it makes eight different sites with six atoms. The lattice constant

for the rock salt structure was found by Karzel et al[127] to be 0.4271nm using XRD while by Desgrenier et al[128] through energy dispersive x-ray diffraction (EDXD) the lattice constant was observed to be 0.4283nm. The lattice constant for the rock salt structure of ZnO was calculated by Recio et al[132] using density functional theory and was found to be 0.4058nm and 0.4316nm using various techniques like Hartree Fock perturbed ion (HF-PI), generalized gradient approximation (GGA) and Local density approximation (LDA), which is either smaller or greater than the than the experimentally observed values.

This cubic phase of ZnO is meta-stable and cannot be stabilized by epitaxial growth like that of sphalerite structure. According to Bates et al[133] the phase transition in ZnO from wurtzite to rock salt cubic occurs at approximately 10GPa and this was taken further by *Gerward*[134] and *Recio et al*[132] and explained that the phase transformation completes at 15GPa.

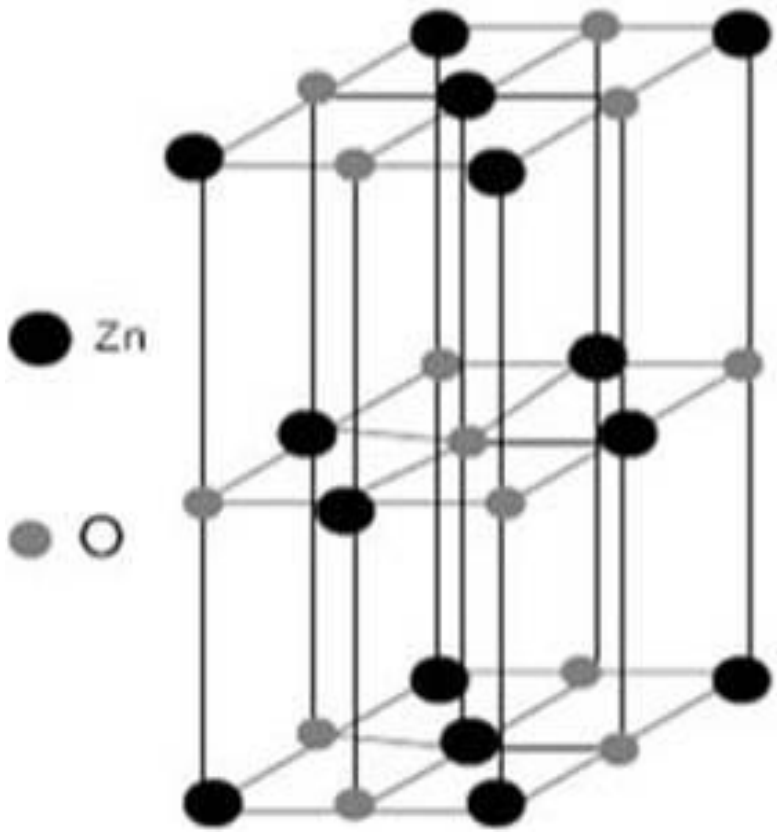

Figure 2.22 Schematic representation of the rock salt cubic structure of ZnO. The black spheres represent the Zn atoms while the gray spheres represent the oxygen atoms.

The (111) plane in sphalerite and in rock salt structure and the (0001) in wurtzite structure are different from their corresponding inverse $(\bar{1}\,\bar{1}\,\bar{1})$ and $(000\bar{1})$ planes, which shows that these structures possess crystallographic polarity. This would either be Zn polarity or O polarity, i.e if the bond along the c-direction is from Zn to O then this is called Zn polarity and vice versa. This crystallographic polarity is responsible for a range of ZnO properties like defect generation, plasticity and spontaneous polarization.

2.8): Doping of ZnO

ZnO has a wurtzite structure in the ambient condition as discussed in the previous section, which is a form of hexagonal crystal system. This system of unit cells is highly anisotropic which leads to wider energy gap and strongly dependent upon the direction of force. ZnO is naturally n-type semiconductor because of the non-stoichiometric nature. The non-stoichiometry in ZnO mostly arises from oxygen vacancies and gives rise to vary high n-type conductivity of about $10^{21}cm^{-3}$ [135]. It has a large exciton binding energy, where some of the rare earth or transition metal ions can replace the Zn ions and because of its wide band gap it could be manipulated for any desired hetrostructure with the addition of any impurity. It has a strong potential in optoelectronic devices, chemical sensor as well as luminescent devices such as transparent conductors, optical wave guides, acousto-optic modulators / deflectors, ultra violet laser source and detectors[136,137].

2.8.1): Transition metal (TM) Doped ZnO

ZnO is a wide band gap semiconductor and can be doped with transition metals and rare earths through a range of techniques like solid state reaction, physical layer deposition (PLD), sputtering and molecular beam epitaxy (MBE). In this study the ZnO has been doped through solid-state reaction method with various metal oxides (transition metal oxides and rare earths). Although this technique requires high temperature for the process, which is not cost effective but the thermal evaporation of pellets seems very helpful in complete doping of the ZnO grains. In wurtzite structure the cations and anions are bonded tetrahedral with sp^3

nature and TM ion shares its 3d electron to the sp^3 bonding to form TM^{+2} charge state and replace Zn^{+2} ion upon doping, as shown by blue spheres in the figure 2.23.

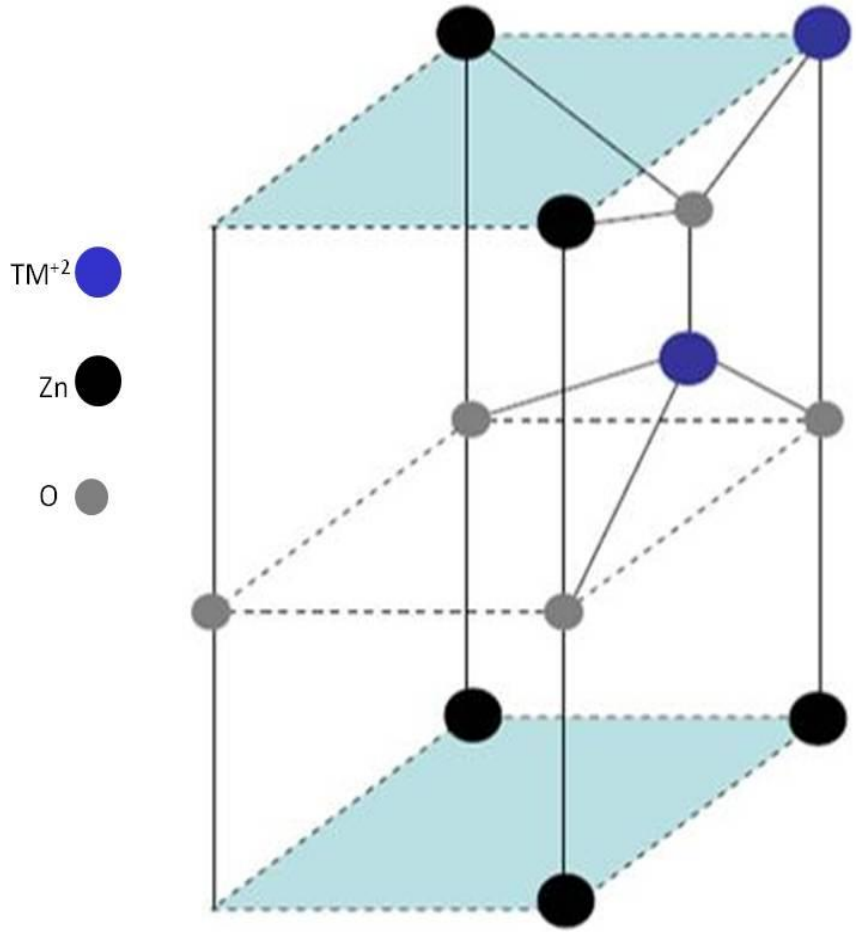

Figure 2.23 Schematic representation of the replacement of Zn atoms in Wurtzite crystal structure of ZnO. TM^{2+} ions (Cu and Ni) replace Zn^{2+} ions in wurtzite phase. Blue spheres are TM^{2+} ions.

In transition metals s and d orbitals are considered as valence orbitals, where the 3d-orbitals have lower energy than 4s. The 3d band of the transition metals of spin up or spin down states always remain partially filled and hybridize with the p-orbital of the host material, which gives rise to exchange interaction between the localized 3d spin and the carrier in the valance band of the host material[138]. In case of Cr and Cu one 4*s* electron and one 3*d* electron participate in bonding as they have one *s* electron in their outer orbital. It is because of the fact that empty, half-filled and completely filled orbital are more stable,

therefore Cr remains in $4s^1 3d^5$ state rather than $4s^2 3d^4$ and the same happens with Cu that completes its d orbital first rather than to complete s orbital as shown in the figure 2.24.

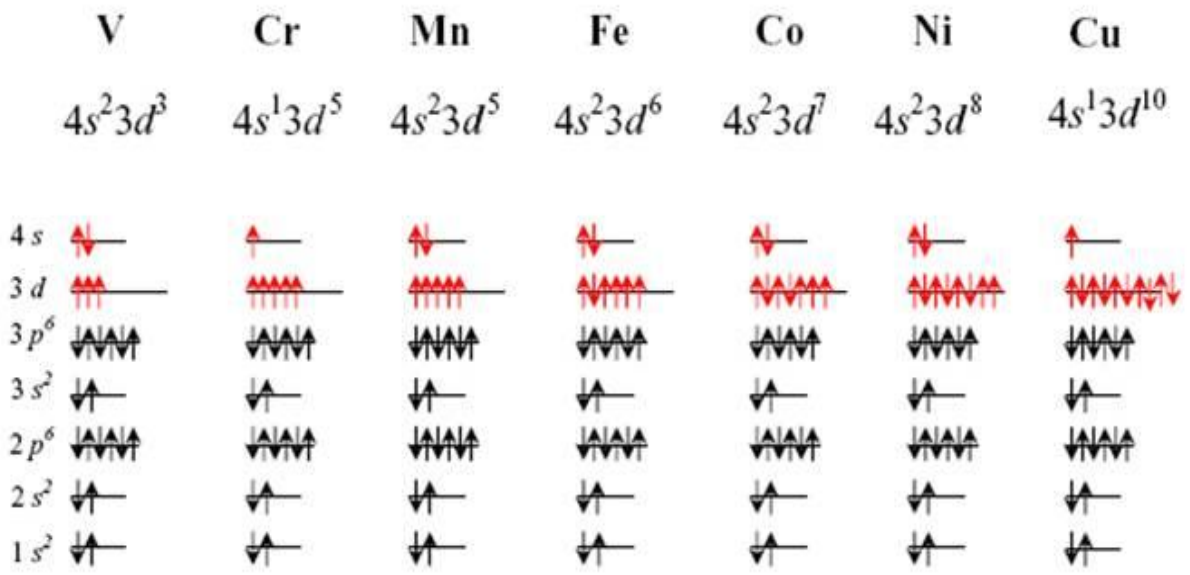

Figure 2.24[138] Electronic configuration of the transition metal elements showing the 3d and 4s occupation of electrons.

In ferromagnetic material (like Fe, Ni, and Co) the d-band is divided into two sub-bands, one is filled with spin up electrons and the other is occupied by spin-down electrons. The sub-band with spin up electrons is first filled and then if there are some electrons remaining are adjusted in the spin down sub-band according to Hunds rule of maximum multiplicity.

The doping of ZnO strongly depends upon the dopant and the doping level, because the overlapping of the states and the splitting of the energy levels are dopant and doping level dependent. It has been found that different transition metals have different effects if used as dopant in ZnO. For example Ti, V, Cr, Fe, and Ni-doped ZnO behave as metals while Mn, Co and Cu doped ZnO behave as ferromagnetic semiconductor and Sc doped ZnO is non magnetic, which are attributed to the difference in the band gap of spin up and spin down electrons. For example the band gap in spin up and spin down electrons for Mn, Co and Cu are (0.26eV, 0.93eV), (0.76eV, 0.92eV), (0.81eV and 0.53 eV) respectively[139].

The magnetic behaviour of TM doped ZnO depends upon the concentration of the TM ions in the semiconductor crystal, the carrier density, and the crystal quality of ZnO. The electronic structure of the TM doped ZnO is governed by two competing processes. One is the strong overlapping of the d-orbitals of the TM ion with the p-orbital of the neighbouring atoms and the other is the strong coulomb interaction between the d-electrons of the impurity atoms. The 3d-host overlapping is responsible for the multiplet splitting[140] observed in the 3d XPS spectra of TM ions. This multiplet splitting gives rise to metal-ligand or ligand-metal charge transfer transition.

The foremost requirement for the catalyst to be used for the growth of CNTs is to accept electrons from the carbon containing gas molecules and have the potential of back donating the electrons to the anti-bonding orbitals of carbon containing gas molecules. In case of transition metals like (Fe, Ni and Co) it is highly expected that the unfilled d-shells of the transition metal would adsorb hydrocarbon on its surface by accepting electrons. This electronic interaction is believed to dissociate the hydrocarbon molecule and this property of the transition metals is believed to be due to their electronic structures, which discriminates the efficiency of various catalyst for growing carbon nanotubes (CNTs), like Fe, Ni and Co[31,32,33,141]. In case of metal oxides or doped metal oxides it has been observed for the first time experimentally in this study that it is the intra-granular charge transfer transition and lattice strain that gives rise to CNTs growth. The intra-granular charge transfer transition is responsible for the dissociation of hydrocarbon molecules because it strengthens the back donation of electrons to the anti-bonding orbitals of the hydrocarbon molecules and the lattice strain is believed to be responsible for the diffusion of carbon atoms through the catalyst surface.

3.1): Introduction:

In the previous chapter the methods and modes of CNTs growth mechanism have been briefly described. This chapter is dedicated to the characterisation techniques, where the construction and working principle will be described. These techniques include the SEM, TEM, EDS, ED, XRD and XPS. SEM and TEM are used to see the morphology and structure of grains and CNTs, while the EDS is used to determine the elemental composition of the catalysts nanoparticles before and after the growth. ED is used to see the crystallinity of grains, XRD analysis has been carried out for the phase identification and XPS describes the chemical state and chemical environment of the catalyst nanoparticles.

3.2): Scanning Electron Microscope

It is high magnification electron microscope where a focused electron beam is used to image a specimen. SEMs have higher depth of field, higher resolution and larger magnification. The beam of electrons is produced by an electron source that can be made of many different materials depend upon the nature of the source (like thermo-ionic or field emission source). The beam of electrons is then attracted by the anode, which is put at higher positive potential. In the case of thermionic source there is a cloud of electrons in the vacuum because the electrons are given high energy to overcome the work function of material and then accelerated by the anode, while for field emission (FE) source the electrons are extracted from the material through a high electric field and the tunnelled electrons are then accelerated by the anode. This beam is then passed through a condenser lens to demagnify the beam and then to make the beam smooth and parallel. The highly scattered electrons from the beam are removed through the condenser aperture. The beam is then passed through a set of coils that is used for scanning the beam. The scanning beam is then passed through the objective lens, which focuses the beam further and then the beam is finally passed through the objective aperture to remove the high angle scattered electrons as shown in figure 3.1.

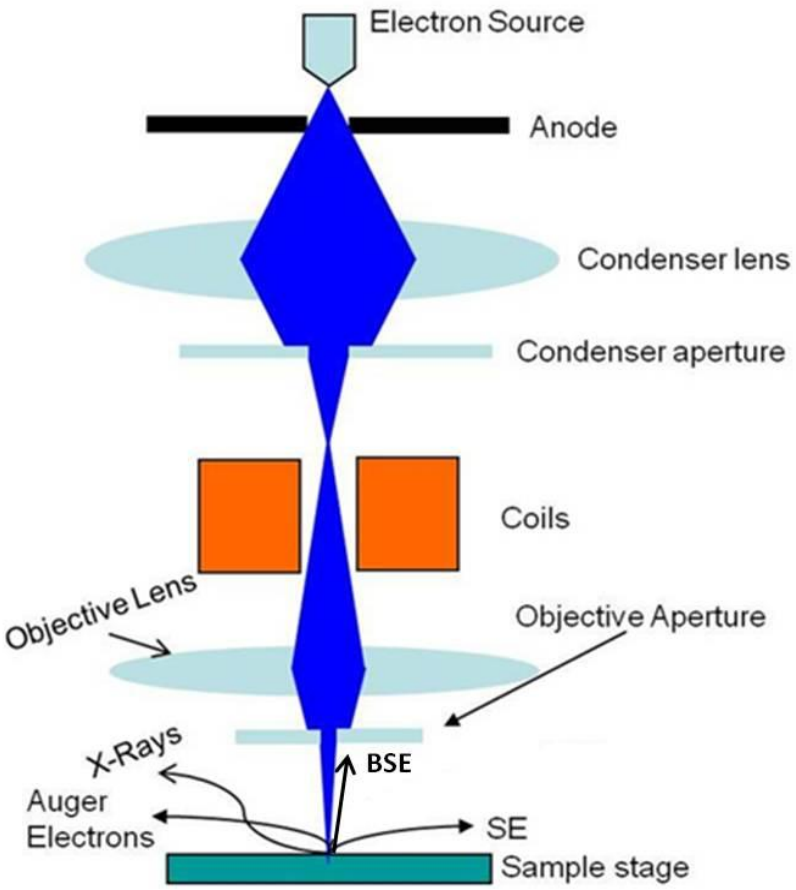

Figure 3.1 Schematic of scanning electron microscope (SEM), showing the emission of various types of electrons like secondary electron (SE), back scattered electrons (BSE), Auger electrons and x-rays photons during the beam sample interaction.

When the beam hits the sample, it gives rise to electrons (secondary, backscattered and Auger electrons) and x-rays and is detected by various detectors. All these electrons and x-rays collect different information from the sample underneath. For example the secondary electrons are used for surface topography, backscattered electrons (BSE) have the information about the atomic number and surface topology because they interact with the nucleus of the atom. The atoms with larger nuclei will yield high BSE. Auger electrons are used for surface elemental composition and the x-rays have information about the elemental composition of the bulk of the sample. The SE and BSE are used to image the sample and the x-rays and Auger are normally used for spectroscopy.

3.3): Transmission Electron Microscope (TEM):

The principle of operation of transmission electron microscope is the same as that of the optical microscope, but here a beam of electrons is used instead of light. Electron microscope has a very high resolution than the optical microscope, because of the very short wave length of electrons. Resolution of a microscope is different from the magnification in a sense that it the beam property, while magnification corresponds to the power of lens. It is based on de Broglie's hypothesis, which states that the wavelength is inversely proportional to momentum. For higher resolution the wavelength needs to be very short. Resolution is the power of microscope that enables an operator to see the fine details separately. The resolution of an optical microscope estimated from Abbe's equation,

$$d = \frac{0.612\,\lambda}{(2nsin\theta)} \qquad (3.1)$$

Where d is the separation between two different objects, n is the refractive index of the medium, λ is the wavelength and θ is the half angle of the cone of light from specimen plane accepted by the objective. Equation (3.1) can be extended for TEM using De Broglie's hypothesis as,

$$\lambda = \frac{h}{mv} \qquad (3.2)$$

Where h is the Plank's constant, m is the mass of an electron and v is the velocity of an electron. Since the kinetic energy of an electron is directly proportional to the applied voltage (V), therefore it can be written as,

$$eV = \frac{1}{2}\,mv^2 \qquad (3.3)$$

$$\Rightarrow \qquad \lambda = \frac{1.23\,nm}{\sqrt{V}} \qquad (3.4)$$

$$\Rightarrow \qquad d = \frac{0.753}{aV^{\frac{1}{2}}} \qquad (3.5)$$

Every electron microscope has an electron gun. This source produces a beam of electrons, which are controlled by the voltage applied to the filament. High voltage TEM requires ultra high vacuum (UHV) in the range of 10^{-9} to 10^{-11} mbar to avoid any arcing[142]. Usually the electron gun is isolated from the main chamber by use of a gate valve. The electron gun consists of an electron source, which might be thermionic or field emission source. The TEM used in this study is JEOL 2011F with LaB_6 thermionic source. The electron source is heated to obtain an electron beam. The beam of electrons is then passed through a strong magnetic field that acts as a lens. The lens converges the beam to the second condenser lens to make it parallel at the output. The beam of electrons is then focused on the sample through an aperture which eliminates high angle scattered electrons as shown in figure 3.2. Apertures are of different sizes, but the selection of an aperture is made by the operator to balance the intensity and filtering effects of the aperture.

When an electron beam strikes the sample, some of the electrons are scattered and some are transmitted. These transmitted electrons are then passed through an objective lens which gives an inverted image. An objective aperture is placed at the back of the objective lens to form an image. The first image generated by the objective lens is magnified by an intermediate lens, which is further magnified by the projector lens. The function of an objective lens can be estimated from the quality of an image, which should be magnified and as exact as the object. This works well for less transparent objects and as the transparency of an object increases the quality of an image decreases. It is because of the constant intensity of the transmitted electrons.

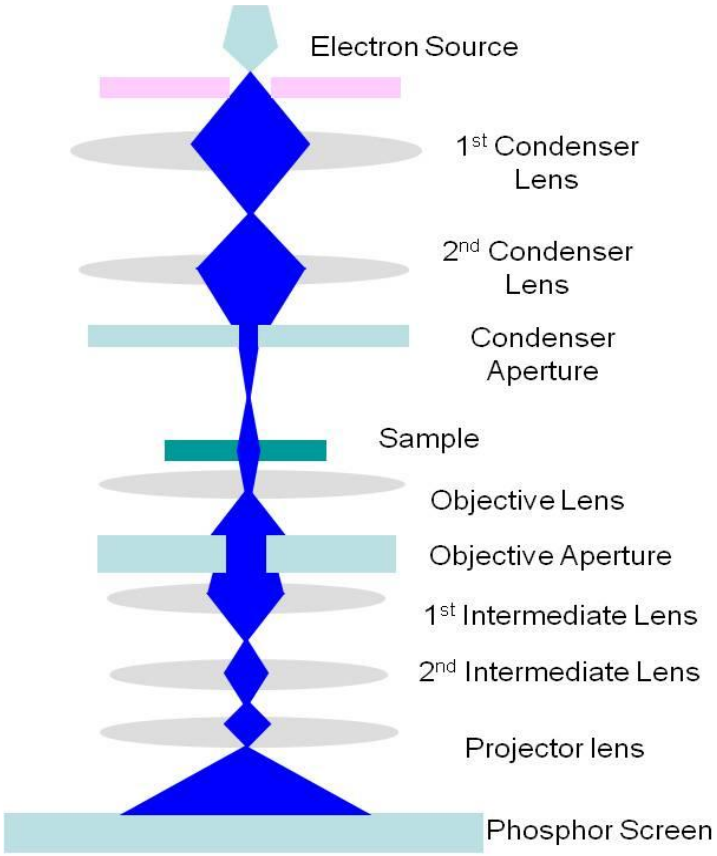

Figure 3.2 Schematic of Transmission electron microscope (TEM).

There are three types of contrast mechanisms: mass contrast is the interaction of the electron beam with the atoms of the particle. For a particle with heavy atoms the interaction will be strong in comparison with a particle with light atoms. Thickness contrast depends upon the thickness of the sample. A thicker particle will appear darker than the thinner one. Third is diffraction contrast that depends upon the crystallinity of the particle. Highly crystalline particle will scatter the electrons and will appear darker if the planes are at the Bragg angle as shown by equation (3.7).

3.4): Selected Area Electron Diffraction (SAED):

It is a technique that is used for the identification of solid material regarding the lattice parameter measurement, disorder and defect identification. When a beam of electrons

strikes the sample they are scattered and gives rise to interference. The scattered electrons will interfere constructively if the path difference between the diffracted electronic waves is an integral multiple of wavelength and will give rise to bright sharp spots for single crystals or bright rings for polycrystalline material. The diffraction rings are because of the random orientation of single crystals in a polycrystalline grain. Each ring consists of a large number of bright spots that corresponds to a specific plane of a single crystal as shown in figure 3.3.

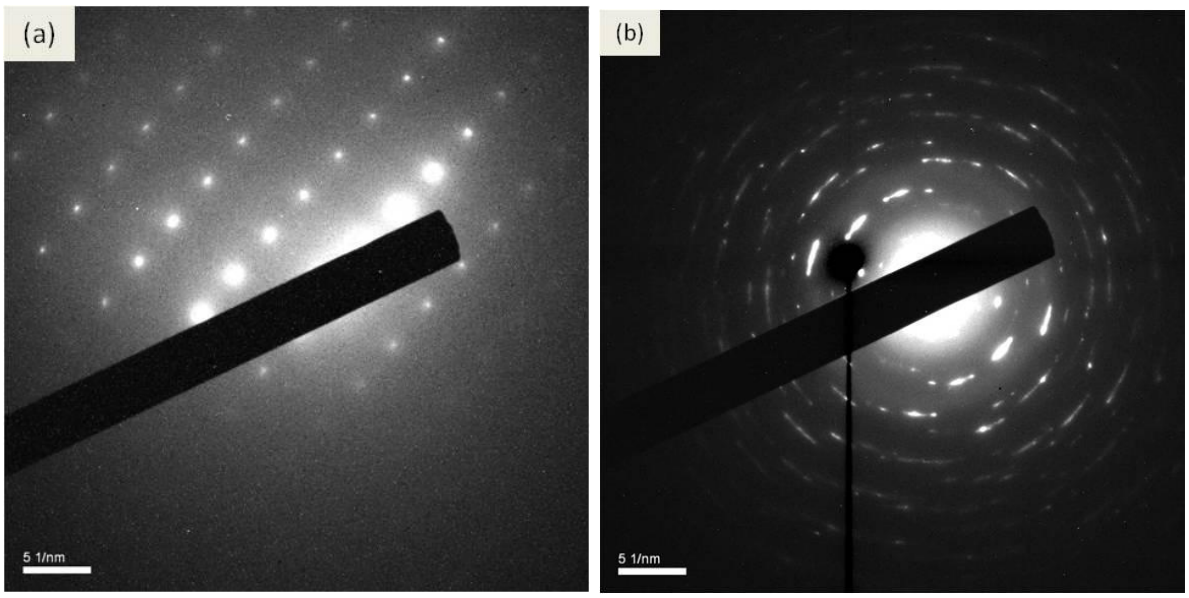

Figure 3.3 SAED pattern for (a) Single crystal (b) polycrystalline

To obtain SAED pattern through TEM an area of interest is selected by inserting a selected area aperture in the first image plane. The spot size is reduced to minimum and the brightness is lowered to avoid any damage to the CCD camera. Sharp spots or continuous rings will appear on the screen upon switching to the diffraction mode. The diffraction pattern is then focused and saved. SAED pattern is helpful if we are interested in the area of constant orientation, or to find a relation between two different crystals or we are interested in a very small particle. The radius (R) of each ring depends upon the scattering angle (θ) and the camera length (L), mathematically[143],

$$R = Ltan\theta \qquad (3.6)$$

By tilting the specimen with respect to the electron beam direction can give rise to a recognisable diffraction pattern that might correspond to a specific pattern like phase contrast, defects in the crystal structure (atomic dislocation) or chemical composition of grains etc.

For amorphous material the diffraction patterns are fuzzy rings because of the disordered atomic arrangements. The diameters of these rings correspond to the average nearest neighbour distance in the material.

3.5): Energy dispersive x-rays spectroscopy

It is a technique used for the elemental composition of materials. It is based on the principle that when an inner core electron is knocked out by electron beam interaction with the sample, an electron from the higher energy level jumps to the lower level to occupy the inner shell electron space and releases energy, which corresponds to the energy difference between the two energy levels. The characteristics x-rays of the element is also a form of this energy and is shown schematically in figure 3.4.

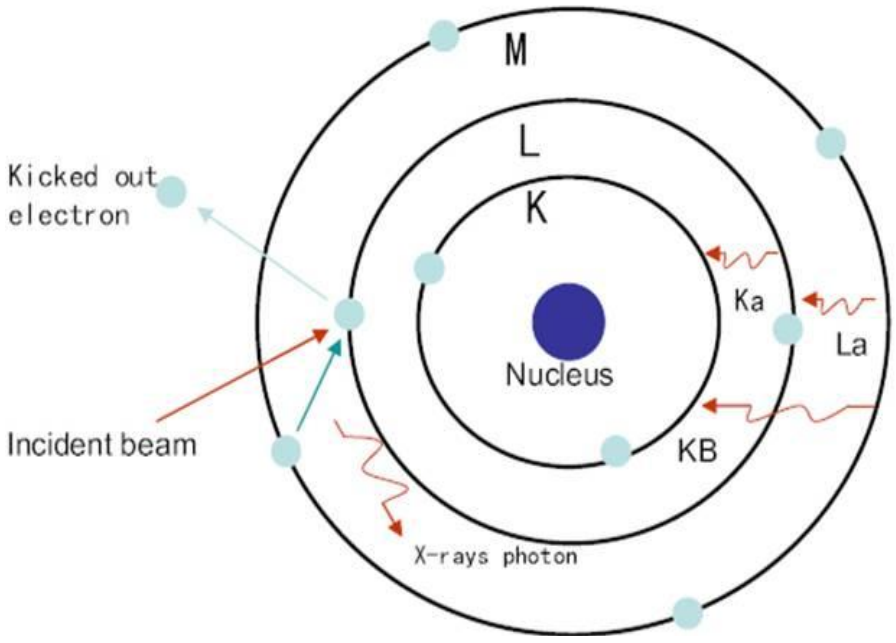

Figure 3.4 Schematic of the EDS phenomenon, showing that an incident beam kicks out an electron and gives rise to photon emission when an electron in the higher energy level jumps to the lower level

Every element emits a specific characteristic x-rays and can be used to identify which specific element is actually present in the specimen. A particular area or spot of a specimen is selected for EDS analysis. The x-rays emitted from the selected area are analysed through energy dispersive spectrometer for different energies. When an x-ray photon strikes the Lithium-drifted silicon detector it generates photoelectrons. This causes an electron hole pair in the reverse biased diode and is converted to voltage pulse by a charge sensing amplifier. The pulse is then analysed through a multichannel analyser and is sent to the computer. The software then displays the peak after identification and quantifications as shown in the figure 3.5.

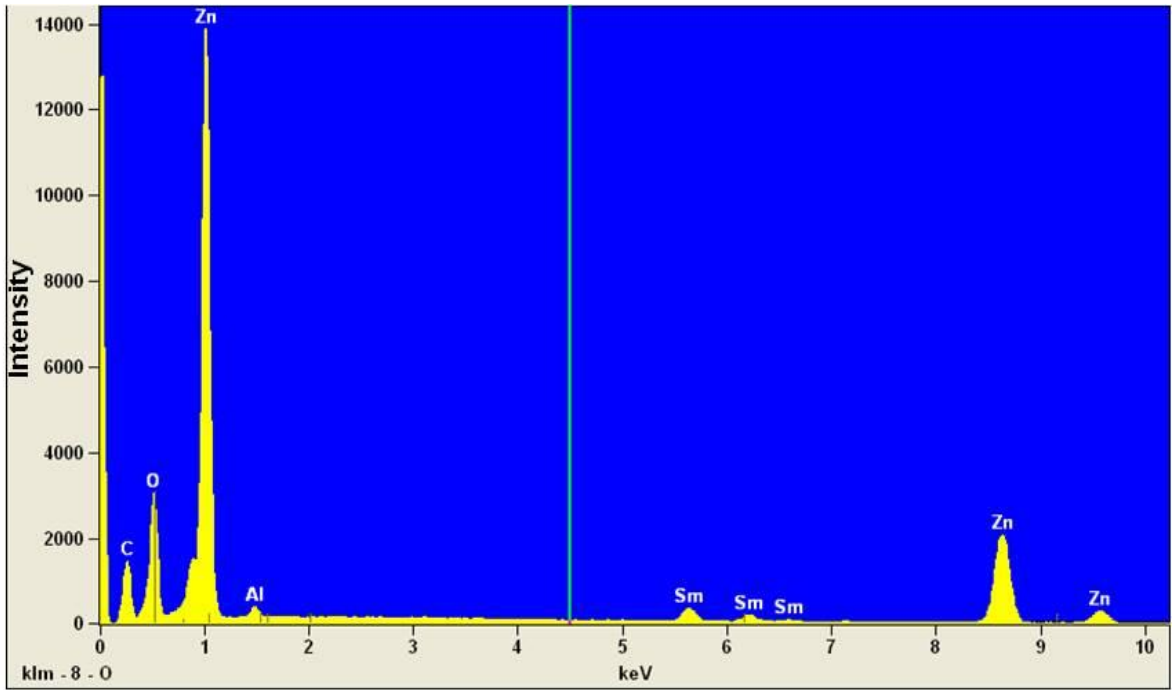

Figure 3.5 EDS spectrum for Sm doped ZnO pellet prepared through solid state reaction

The quantification of the peak [shown in table 3.1] is a complicated process, it is because of the background and overlapping effects and especially it depends upon the operating conditions of SEM. There following few steps are considered necessary for better quantification like, i): Removal of the background ii): Identification of the peak and iii): the peak resolution.

Element Line	*Weight %*	*Weight % Error*	*Atom %*
C K	13.22	+/- 0.17	33.35
O K	19.35	+/- 0.19	36.65
Al K	0.96	+/- 0.05	1.08
Zn K	59.28	+/- 0.61	27.47
Zn L	---	---	---
Sm L	7.19	+/- 0.29	1.45
Sm M	---	---	---
Total	100.00		100.00

Table 3.1 quantitative analysis of the EDS spectrum.

Despite the fact that EDS provides a better chemical analysis, however the technique has got some draw backs related to the detection process like, x-ray escape peaks, peak distortion and peak broadening. The escape peak is because of the interaction between the x-ray photon with the detector, which ionizes the Si and results in Auger emission. Some of the Auger electrons recombine in the detector and some of the electrons escape. Therefore the probability of making an electron hole pair is negligibly small. This phenomenon gives rise to escape peak and is equal to the energy of the parent line minus the energy of the Si x-rays.
The non-uniformity of the detector near the faces and edges gives rise to recombination and trapping of electrons. This in turn causes the peak distortion. The peak broadening is the result of variation in the number of charge carriers and thermal noise during amplification. This could be overcome only by increasing the collection time.

The EDS data in this study was obtained using an Oxford INCA analysis system equipped with 30mm 2 light element capable ATW detector. The system is capable of analysing element with $Z \geq 5$. The spectrum consists of energy along the x-axis and the counts/intensity along the y-axis, which gives rise to peaks where each peak corresponds to a specific element. Quantitative information about an element in the specimen could also be obtained, which show what weight per cent and what atomic per cent of an individual element does exist in the sample.

3.6): X-Ray Diffraction (XRD):

It is a non destructive technique used for the phase identification of materials. The crystal lattice is a three dimensional array of atoms in space with the lattice planes separated by a distance d. When a monochromatic x-rays fall on the crystalline surface they are scattered and gives rise to interference phenomenon. The diffracted x-rays from various planes with integral multiple (*n*) of wavelength (λ) will interfere constructively and results in a large output signal at the corresponding angles in the spectrum. The diffraction with half integral multiple of wavelength will interfere destructively and will cancel each other's effect. By changing the angle (θ) the lattice spacing (*d*) varies to satisfy the Bragg's law, as shown schematically in figure 3.6.

$$2dsin(\theta) = n\lambda \qquad (3.7)$$

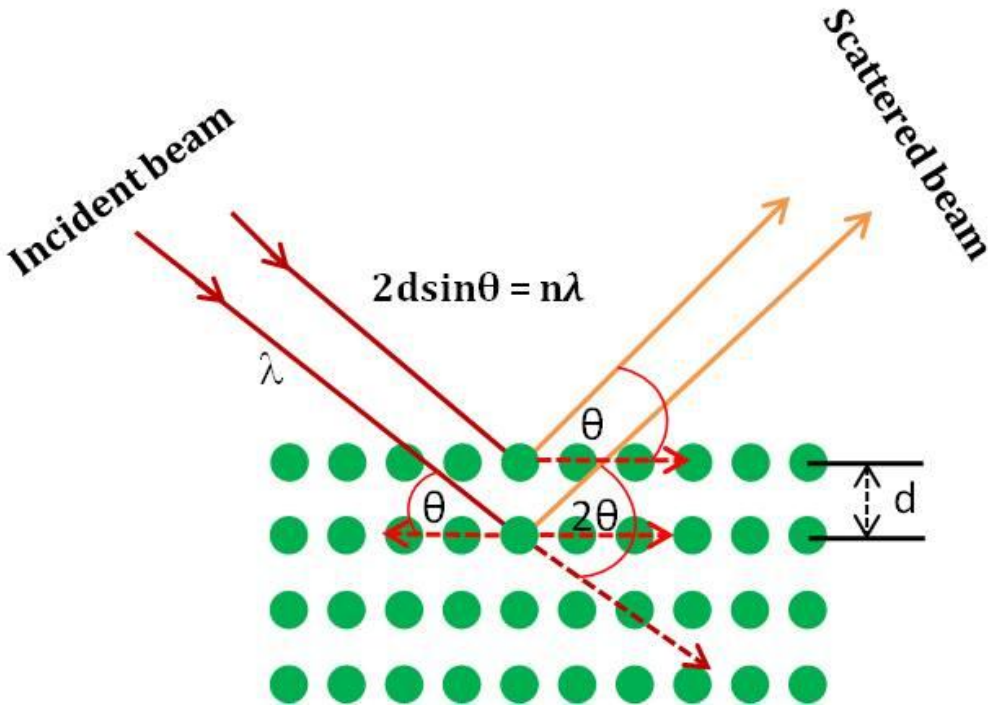

Figure 3.6 Bragg's scattering from lattice planes with spacing "d" with the same angle of incidence and the angle of reflection.

XRD pattern plays an important role in determining the lattice parameter and the number of planes with various orientations for powder samples. The grains in the powder samples are randomly oriented and the peak positions are used to identify the planes. The wave length of an x-ray source is known and the angle (θ) can be estimated from the XRD spectra and hence the lattice spacing (d) can be calculated using Bragg's law (equation (3.7)). Since the powder samples used in this study are doped ZnO belonging to *hcp* crystal family, therefore the lattice parameter can be calculated from equation (3.8). The lattice spacing (d) can be calculated by using Miller Indices that describes the orientation of planes with respect to different crystal axis and the lattice spacing d_{hkl} for *hcp* crystal is given by the equation[143]

$$\left(\frac{1}{d_{hkl}}\right) = \frac{2}{a\sqrt{3}\sqrt{(h^2 + hk + k^2) + \frac{l^2}{c^2}}} \qquad (3.8)$$

Where '*a*' and 'c' are the lattice constants and *h*, *k*, *l* are the Miller indices along x, y, and z-axis respectively.

3.7): X-ray Photoelectron Spectroscopy (XPS):

XPS is a spectroscopic technique that is used to measure the elemental composition and chemical state of elements. The working principle of this technique is based on the principle of photoelectric effect. A material is irradiated by a beam of x-rays, which causes to eject a core electron from the sample atom. The energy of a core level electron is a function of its binding energy which is different for different elements and helps identify the elemental composition in a sample up-to the depth of 1 to 10nm. The binding energy of an atom depends upon the formal oxidation state and the chemical environment. The higher oxidation state of an atom will shift the photoemission peak towards a higher binding energy side because of the smaller ionic radii, which gives rise to a higher coulomb attraction between the nucleus and the surrounding electrons. The binding energy of a photo emitted electron can be represented mathematically as,

$$E_B = h\upsilon - E_{k.E} - \phi \quad (3.9)$$

$$\phi = E_f - E_v \quad (3.10)$$

Where E_B is the binding energy of a photoelectron, $h\upsilon$ is the energy of the incident x-ray beam, $E_{k.E}$ is the kinetic energy of the photo emitted electron and ϕ is the work function of the spectrometer. The core level photoemission peak corresponding to certain element can be grouped into three categories. i): the peak corresponding to the core level, ii): the Augur transition, iii): the valance level transition at low energies. The emission of photoelectron is shown schematically as in figure 3.7.

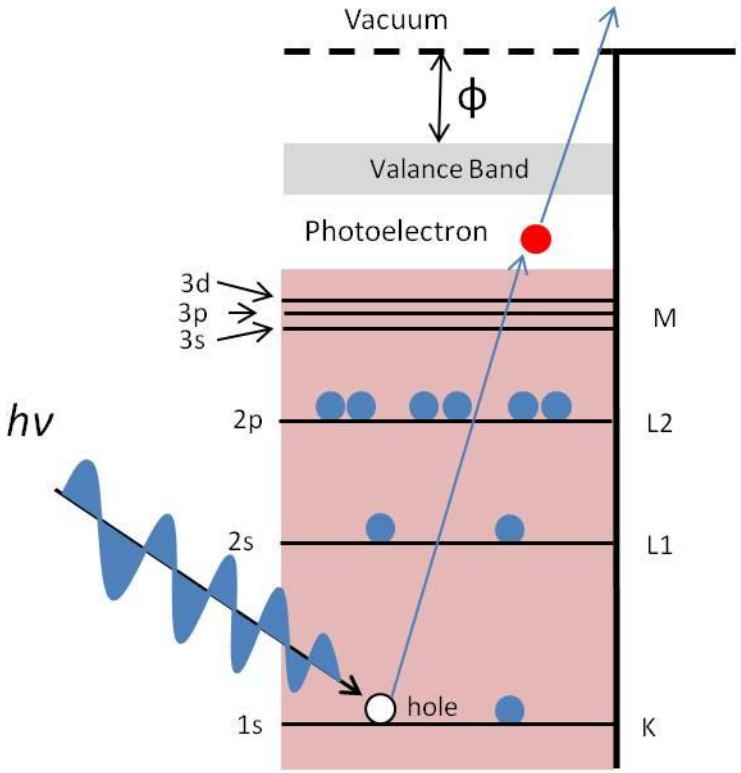

Figure 3.7 Schematic of the photoelectric effect.

The main source of information is the core level peaks and is the main focus of this study. Although the importance of the processes (ii) and (iii) cannot be underestimated, however they contribute little in this study therefore will not be discussed. XPS spectra is

described in terms of the angular momenta, which are described by the quantum numbers like *n* (principal quantum number), *l* (orbital angular quantum number), *S* (spin quantum number) and *J* (total angular momentum quantum number). For all non s orbitals the core level peak appears as doublet, which arises from the spin orbit coupling. For example the removal of a d electron from the core level gives rise to two 3d peaks, one corresponds to $3d_{5/2}$ and the other corresponds to $3d_{3/2}$. It is because for d-orbitals the orbital angular momentum is 2 ($l = 2$) and $S = 1/2$ so $J = 5/2$ and 3/2. Since the former is more than half full therefore appears at lower binding energy and the later appears at higher binding energy with respect to the former photoemission peak. The intensities and the widths of the photoemission peaks are different for different materials and are strongly dependent on the ionization potential of different core levels.

The XPS system consists of a vacuum chamber with a sample stage, electron energy analyser and x-ray source. The x-ray source used in this study is the Al K_α. XPS is operated in ultra high vacuum (UHV) of the order of 10^{-8} to 10^{-10} mbar to obtain high signal to noise ratio. Additionally a low vacuum also causes a monolayer deposition on the surface of the sample. The fact that XPS is a surface technique with a depth resolution of up to 10nm for Al K_α source clearly requires a UHV system. To characterise a sample through XPS the sample is first cleaned through Ar ions sputtering to remove the adsorbates like amorphous carbon from the sample surface. After proper cleaning, the sample is further characterised in two steps. First a broad survey spectrum is taken and then the detected desired elements are characterised through the core level spectra. All the spectra are scanned from 30 to 50 times to improve the signal to noise ratio. After that the peaks are corrected with respect to the carbon peak at 284.6eV.

4.1): Introduction:

Better activity and selectivity of catalysts for a process is the ultimate goal of the catalyst research. In this regard the catalyst-support interaction is an important issue in all technological areas especially in the growth of CNTs through CVD where the catalyst determines the morphology and the growth modes i.e (CNTs are grown through tip growth or base growth mode). Novel oxide catalysts have been used for the first time to grow CNTs. Their preparation and deposition methods and the factors affecting the size and shape of grains upon thermal evaporation will be discussed in this chapter. The characterisation of catalysts is carried out through a range of techniques like SEM, TEM, EDS, ED, XRD and XPS and will also be briefly discussed in this chapter.

4.2): Catalyst preparation through solid state reaction

In solid state reaction the reactants react with one another to form a new substance without dissolving in any appropriate solvent. It takes place under specific conditions. In one such method, referred to as the oven technique, a high temperature is used to cause a reaction between the reactants to form a new desired substance. Another way is that the reactants are melted together and are then allowed to interact with each other to form a new substance, this new substance is then cooled down to solid state. A third method, called gas reaction in which the reactants are exposed to gases, in the presence of which they react and form a new substance. In this study the first condition is used for producing the catalysts. The reaction chamber used for the sample preparation is shown in figure 4.1.

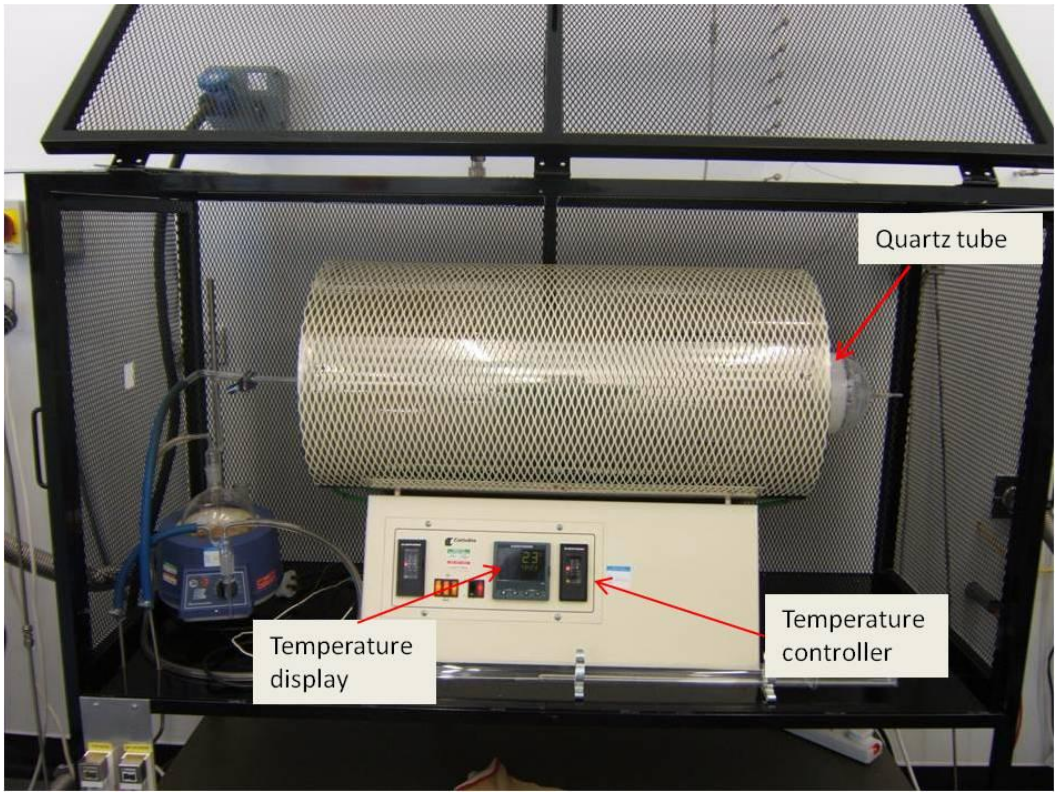

Figure 4.1 Carbolite furnace used for samples preparation through solid state reaction

For solid state reaction to take place the reactants have to be mixed vigorously either by mortar and pestle or by ball milling for about an hour. After this vigorous mixing the reactants were placed in furnace at some specific temperature for hours. In this study ZnO powder from sigma Aldrich was obtained and was mixed with transition metal oxides (like NiO and CuO) and rare earth oxides (SmO, Tb_2O_3 and Ho_2O_3) with 5 wt%. All oxides used has purity levels of 99.99%. The mixed powder was then ground for about an hour with mortar and pestle. The powder was then annealed for about 7 hours at 700C and then let to cool down to room temperature in the furnace. The annealed samples were again mechanically ground for about half an hour to ensure complete mixing of host and dopants. Pellets were then made through the presser and put in the furnace for sintering for 14 hours at 1200C, 1150C, 1050C and 1000C. The pellets were then slowly cooled down to room temperature in the furnace and then were imaged under the SEM to obtain the grain morphologies. The pellets were then evaporated on the substrates for further use as catalyst for the growth of CNTs.

4.3): Catalyst deposition

Thin films can be deposited in two ways i.e. Physical deposition that consists of thermal evaporation, sputtering, electron beam deposition and pulsed layer deposition, while the chemical deposition consists of chemical vapour deposition and plasma enhanced chemical vapour deposition. The technique for the buffer layer deposition and for the deposition of catalyst used in this study is the thermal evaporation. The thermal evaporation process consists of three basic steps,

i): Sublimation of the source material.

ii): Transportation of the material from the source material to the substrate.

iii): Condensation of the material on the substrate.

The thermal evaporator is used for the buffer layer and catalyst deposition. It consists of rotary and backing pump with two gauges and two valves and an in-situ film thickness monitor. The source material is placed in a tungsten boat that is connected across the two terminals of the electrode. The substrates are placed at the same distance as that of the thickness monitor. The shutter is kept upon the tungsten boat to avoid deposition of the adsorbates on the substrate at the beginning of the evaporation and after one minute the shutter is removed and the thickness is monitored through the in-situ thickness monitor. After obtaining the desired thickness the shutter is closed and the filament is switched off. The samples are kept under vacuum for some time and removed when the samples are cool.

Novel oxide catalysts for the growth of CNTs have been prepared through solid state reaction. According to this process first a pellet of the desired material was made and was then evaporated thermally on the substrate. Unlike metals the pellet of doped ZnO evaporates in the form of nano-grains instead of continuous film. There is a distribution of grain sizes and shapes, which is attributed to the catalyst support interaction. The effect of substrate surface morphology and buffer layer deposition upon the size and shape distribution and the density of grains are discussed briefly in this section, because these are the possible factors that seems to be responsible for the size and shape distribution of grains and hence the growth of CNTs.

4.3.1): Effect of substrate and surface roughness:

Three parameters have been chosen to understand the effect of substrate upon the deposited material.

i); The size and shape distribution of grains

ii): Density of grains

iii): Crystallinity of grains

After the thermal evaporation of the transition metal and rare earth doped ZnO pellet it was observed that the above parameters are a function of substrate surface roughness and that of the nature of material used. The surface morphology of the substrate defines the size and shape of the grains because of the residual stress of the individual substrate [144]. Pellets of transition metal and rare earth doped ZnO were evaporated thermally on a tungsten (W) substrate and was observed that rough surfaces gave rise to elongated and non-uniform grains with large grain size distribution. The high residual stress is because of the high lattice mismatch of the substrate and that of the deposited material, which gives rise to elongated and non-uniform grains. The high surface stress gives rise to higher lattice energy that lowers the mobility of atoms and molecules and ultimately yields low density[145]. SEM studies of all materials confirm these previous observations as shown in the figure 4.2.

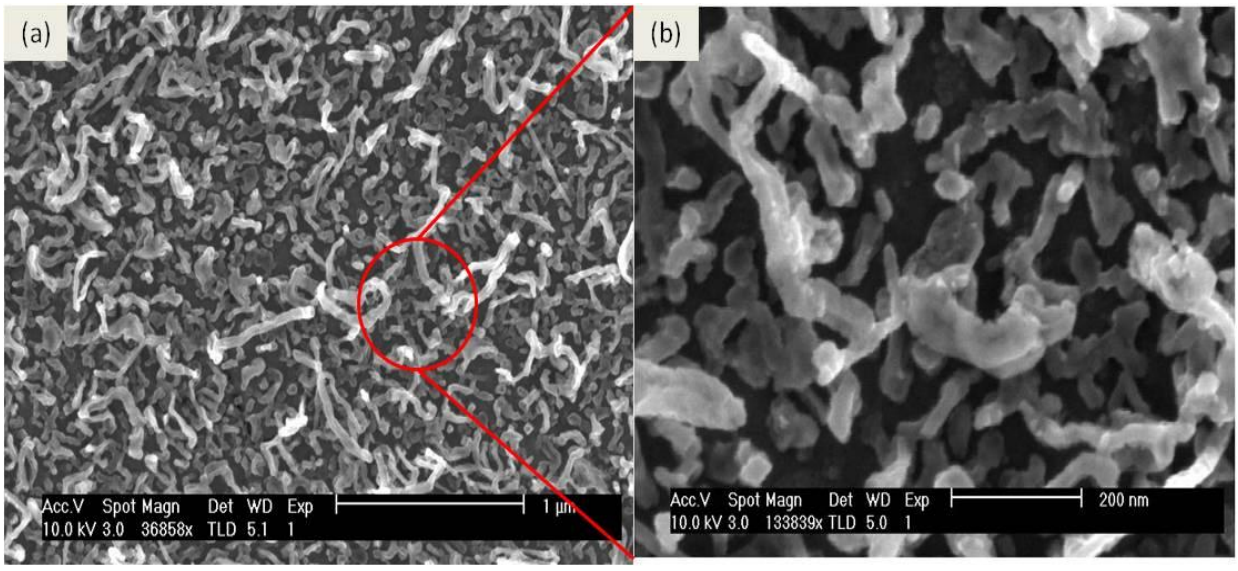

Figure 4.2 (a) low magnification image of thermally evaporated SmZnO pellet on bare W substrate (b) High magnification image of the circled area.

Another important factor affecting the size and shape distribution of grains is the lattice strain. It is widely believed[146,147] that the doped material builds a charge field at the grain boundaries, which results in a reduced mobility and pinning of the grain boundaries, which eventually affects the growth of grains. The doping of ZnO with rare earth especially Sm produces relatively high lattice strain [table 5.4 chapter 5], which might be a reason for the anisotropic grain growth upon thermal evaporation on rough surfaces like bare tungsten. This is because of the fact that added rare earth oxides might change the chemical character of the point defects in the lattice[148] and hence affect the grain growth and make it anisotropic. The transition metal doped ZnO like Cu and Ni produces relatively low strain, which might be because of the comparable ionic radii of Cu and Ni that replace Zn in the ZnO matrix and produces relatively isotropic grains as shown in the figure 4.3. The Cu doped ZnO pellet produces well crystalline grains with proper hexagonal geometry. Therefore it could be concluded that the lattice strain of the material also play a key role in defining the size and shape of the grains.

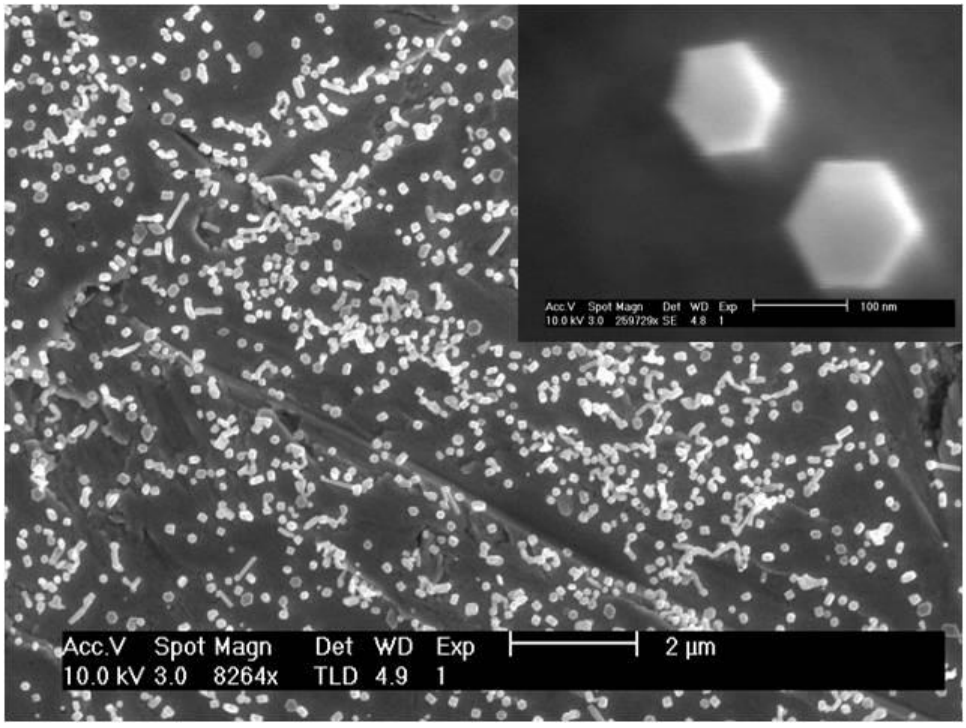

Figure 4.3 Cu doped ZnO pellet evaporated on bare W surface. In the inset is the high magnification image of the grains showing the proper hexagonal geometry and the scale bar is 100nm.

4.3.2: Buffer layer deposition:

To avoid the undesired chemical reaction between the catalysts and support (substrate) a buffer layer is usually deposited onto the substrate before the deposition of any catalyst material. Additionally it is highly desirable to control the size and shape of the catalyst nanoparticles through manipulation of the supporting substrate. For this purpose Cr, and Al were used as buffers layer in this study. The buffer layer controls the polarity of the ZnO film as shown by Park et al[149] and this strongly depends upon the thickness of the buffer layer.

The crystallinity and crystal structure of the catalyst nanoparticles upon thermal evaporation strongly depends upon the nature of the substrates. For example the crystallinity of grains will be different if deposited on W and Cr coated W substrate. This might be because of the electrostatic interaction between the two different materials as observed by Ricci et al[150]. The catalyst support interface can be used to control the shape of the catalyst, because the electronic and magnetic properties of the nano-materials are strongly size and shape dependent[151]. Furthermore the size and shape of the catalyst nanoparticles defines the CNTs morphologies.

An aluminium (*Al*) layer was employed on the substrate both on the Si and W. It was observed that the Al buffer layer does not gives rise to isotropic grain growth as shown in figure 4.4. However when Cr was used as buffer layer there was a narrow distribution of grain sizes and shape as shown in figure 4.5. This might be because of the following reasons,

i); one might be the high lattice mismatch between the ZnO nanoparticles and Al buffer layer, which gives rise to needle like structures.

ii): the other might be the low interfacial charge of the Al-ZnO interface, which gives rise to strong adhesive bonding between the two materials and controls the growth[150].

iii): The third probable reason could be the ZnO polarity, which could be explained on the base of surface bonding Model[152]. According to which the ZnO has two polar surfaces one is Zn-polar surface and the other is O-polar surface. The O-polar surface is more reactive than Zn polar surfaces because of the two dangling electron per oxygen atom. Since there is significant difference in the electronegativity of O and Zn

atoms, therefore the covalent nature of ZnO becomes partially covalent and the electrons are more attracted towards the O. The Zn surface becomes more positive while the O surface becomes more negative. Because of these two electrons per oxygen atom the O surface is more reactive than Zn surface. Since Al reacts with oxygen more quickly than Cr therefore it is more probable that the needle like structure in figure 4.4 is because of the O-polar surface of the doped ZnO material. Because it is the believed[149] that it is the buffer layer that defines the O-polar or Zn-polar growth of ZnO. Additionally the needle like structures are quite shiny and white, which might be because of the Zn termination of the ZnO[153].

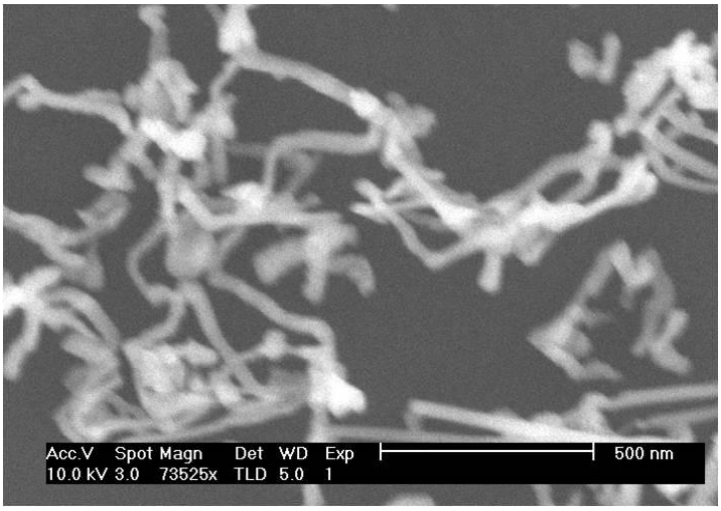

Figure 4.4 CuZnO pellet thermally evaporated on Si substrate with Al as buffer layer

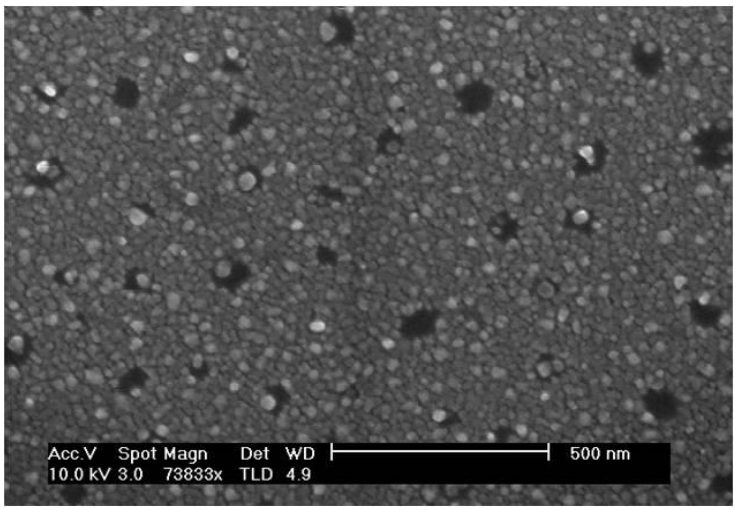

Figure 4.5 CuZnO pellet thermally evaporated on Si substrate with Cr as buffer layer

It has become quite clear that lattice mismatch of the catalyst and support, lattice strain of the catalyst nanoparticles and substrate roughness play a key role in controlling the size, shape and density of the catalyst nanoparticles upon thermal evaporation.

4.3.3): Substrate cleaning

Carbon nanotubes were grown on two substrates insulator (SiO_2 coated *Si*) substrates and metallic substrates (tungsten *W*). The Si was cut from a 6 inch diameter wafer and for W, the tungsten boat was used as the substrate. The substrates are expected to have two types of contamination i.e. organic and in-organic contamination. A couple of steps were taken to clean the substrates.

1): To remove the organic contamination a solution of H_2O_2 / H_2SO_4 with 50wt% were mixed in a glass beaker and then the samples were put into the solution using tweezers and left for about 20 minutes

2): Again there is always a chance of in-organic contamination especially that of the sodium (*Na*) as human being are the biggest source of *Na*. To remove this inorganic contamination the substrates are then put for just one second in the 0.01wt% *HCl* added to water. It removes immediately the inorganic contamination[154].

3): Flush the beaker containing the substrates several times using DI water and take the substrates out of the beaker and blow the substrates with the filtered nitrogen gun.

4): The substrates were then put on the hot plates at a temperature 100C for about a minute to completely dry the substrate.

4.4): SEM and EDS Studies of CuZnO:

Scanning electron microscope (SEM) studies were carried out on the sintered pellets and after thermal evaporation of the pellet on the Cr coated W substrates. The SEM images of the pellets show that the grains of the CuZnO have quite distinctive boundaries. The results obtained display a large distribution of grain sizes and shapes in the pellet as shown in figure 4.6. It is found that the grain size of the pellet depends upon the sintering time, sintering

temperature and the nature of dopant. Higher temperature and longer sintering time will give rise to larger grains due to grain growth[155], because the smaller grains will diffuse with one another at high temperature if the latter persists for a long time. Since all the pellets (TM doped as well as RE doped ZnO) have been sintered for 14 hours. Hence the time dependence of sintering was not considered in this study.

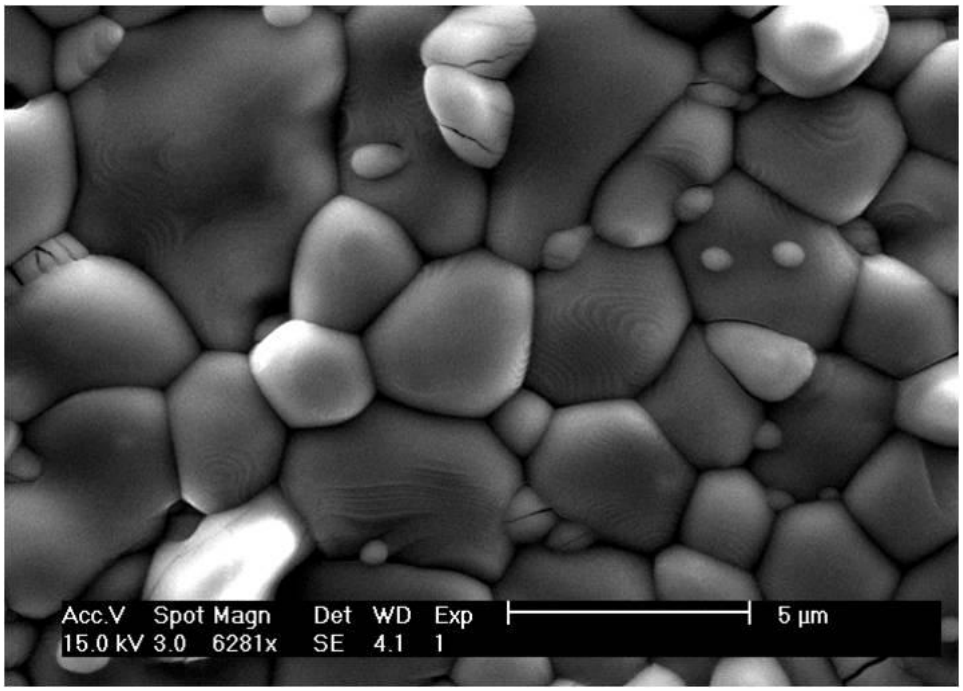

Figure 4.6 SEM image of CuZnO Pellet

After the thermal evaporation of the pellet on Cr coated W substrate it was observed that the material deposits on the substrate in the form of grains. These grains are quite uniform in size with well defined shapes as shown in figure 4.7. This is more likely for two reasons.

i): since the copper produces very low strain in the ZnO lattice (observed through the XRD analysis of CuZnO powder), therefore it seems likely that it produces very small lattice mismatch with the support and hence gives rise to isotropic grain growth with well defined shapes[156].

ii): Since the buffer layer is believed to control the polarity of ZnO grains[149], therefore it is more likely that Cr coated W substrate gives rise to Zn-polar growth of grains. The Zn polar surfaces are not as reactive as O-polar surfaces, because of the lower electronegativity than oxygen[153].

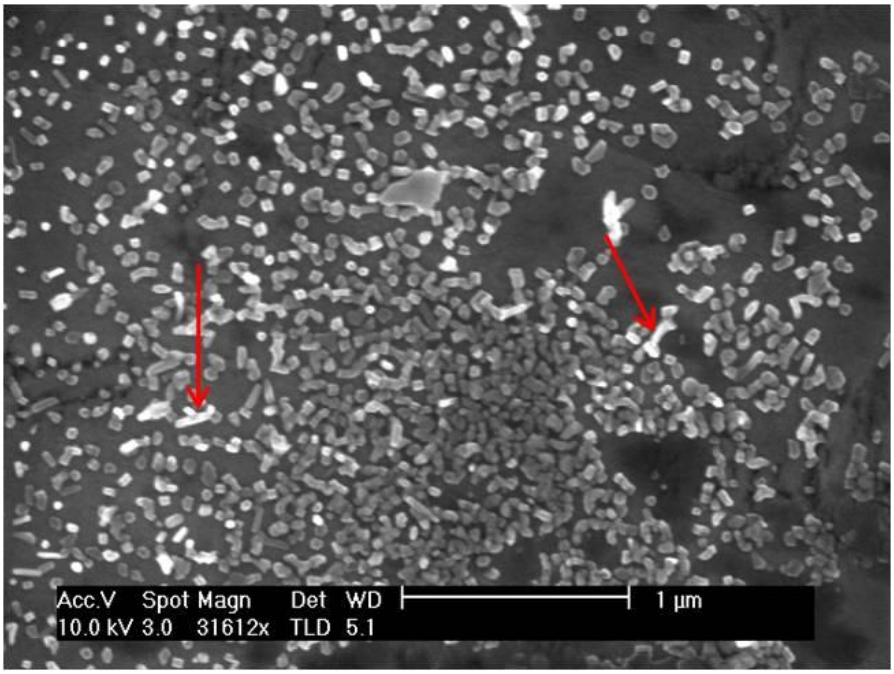

Figure 4.7 SEM image of a thermally evaporated CuZnO pellet, the red arrows show the needle like structures that are believed to be non-active for the CNTs growth.

The elemental composition and the quantitative analysis of the CuZnO pellet were carried out through EDS. The spectrum was taken from the whole surface of the pellet as shown in figure 4.8. Because of the varying morphology of the pellets, the pellet was characterised through EDS in the SEM at three different points to see the uniformity of the dopant ions across the pellet. All the three point analysis shown in figure 4.9 confirms the presence of Cu, Zn and O. the quantitative analysis of the figure 4.6 is given table 4.1 and the corresponding EDS is given in figure 4.8.

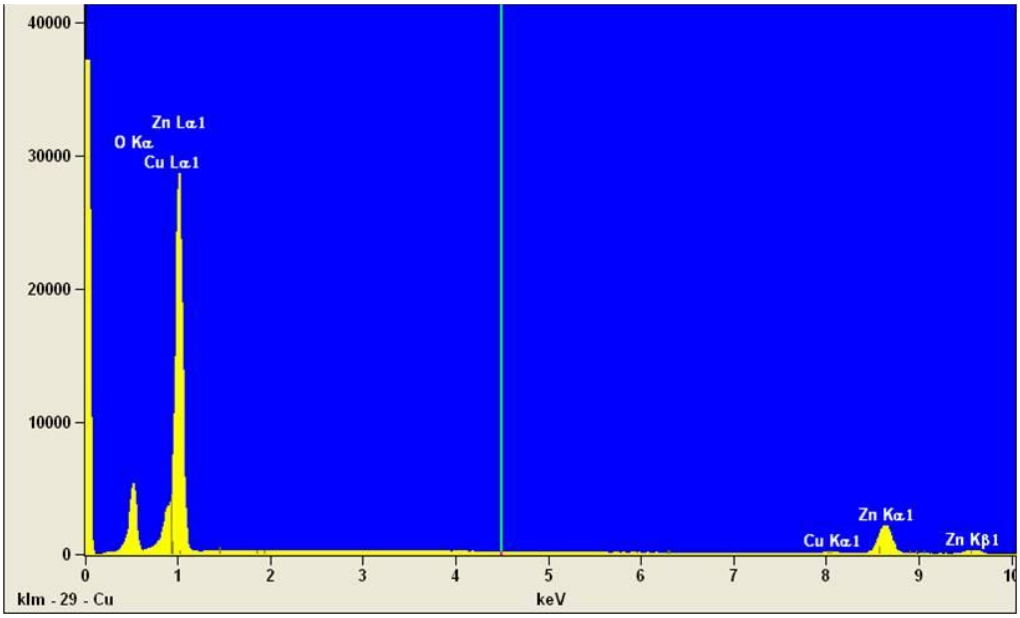

Figure 4.8 EDS spectra for CuZnO pellet

Quantitative Results

Element Line	*Weight %*	*Weight % Error*	*Atom %*
O K	14.7	+/-0.08	41.2
Cu K	4.4	+/-0.67	2.4
Zn K	80.9	+/-0.53	56.4
Total	100.0	+/-0.43	100.0

Table 4.1 Quantitative analysis of the CuZnO pellet.

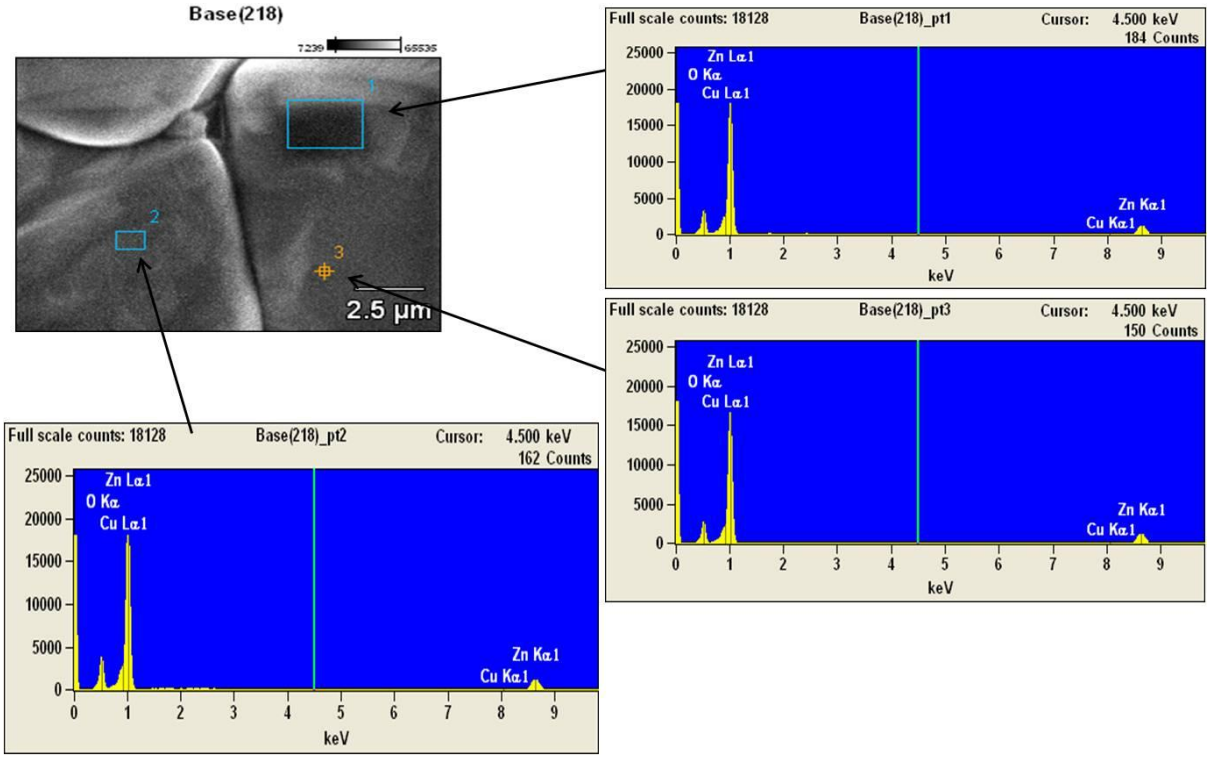

Figure 4.9 EDS analysis of grains in the pellet at three different points

The quantitative results of the pellets show that the dopant (Cu) is uniformly distributed within the pellet.

4.5): Electron Diffraction Studies

An electron diffraction pattern is the result of the interference of the two electronic waves scattered from two crystalline planes. The Selected Area Electron Diffraction (SAED) pattern of the particles was taken using a JEOL 2011 transmission Electron Microscope (TEM) with the beam parallel to (0002) zone axis. The observed SAED pattern was used to see the crystalline nature of the catalyst before using it for the CNTs growth. The pattern shows that the catalyst particles are highly crystalline with hexagonal crystal structure. It is evident from the pattern below that there exists no secondary phases as shown in figure 4.10.

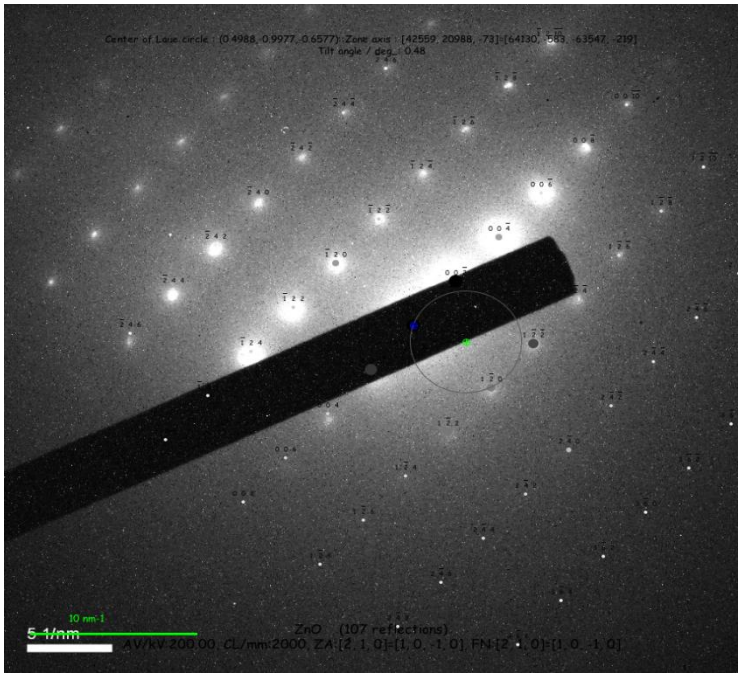

Figure 4.10 Selected area electron diffraction (SAED) pattern collected in TEM from the CuZnO catalyst particle showing the crystallinity of the catalyst nanoparticles.

The contrast of the spots varies from sharp to an elongated spots with tilting the sample along any axis (X or Y). The elongated spots show that the beam is diffracted from larger angle and the intensity of the spots increases towards the axis as shown in figure 4.11.

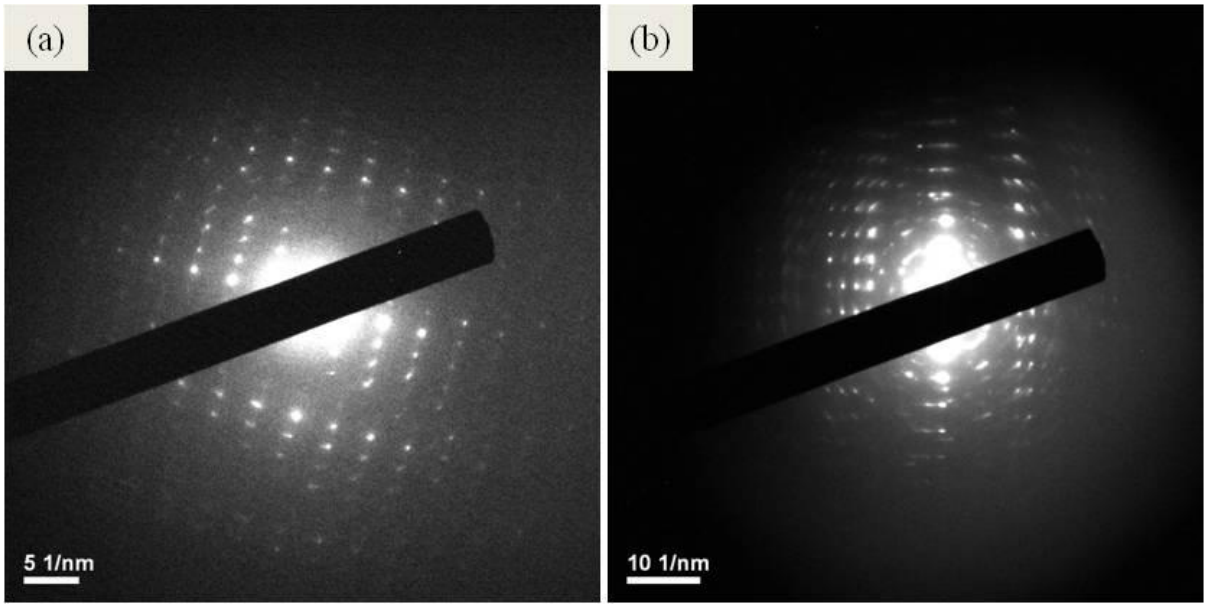

Figure 4.11 SAED patterns of the CuZnO grains after tilting the sample along the x-direction at (a) 3.5 and (b) 6.5 degrees

4.6): XRD analysis of the CuZnO powder

X-ray diffraction was carried out to investigate the phase of the CuZnO powder and the lattice strain due to the incorporation of Cu ions into the ZnO matrix. Data were collected using Cu K_α as an x-ray source at room temperature. The analysis of the data indicates that there is no secondary phase and the only phase that has been observed corresponds to ZnO wurtzite structure, as shown in the figure 4.12.

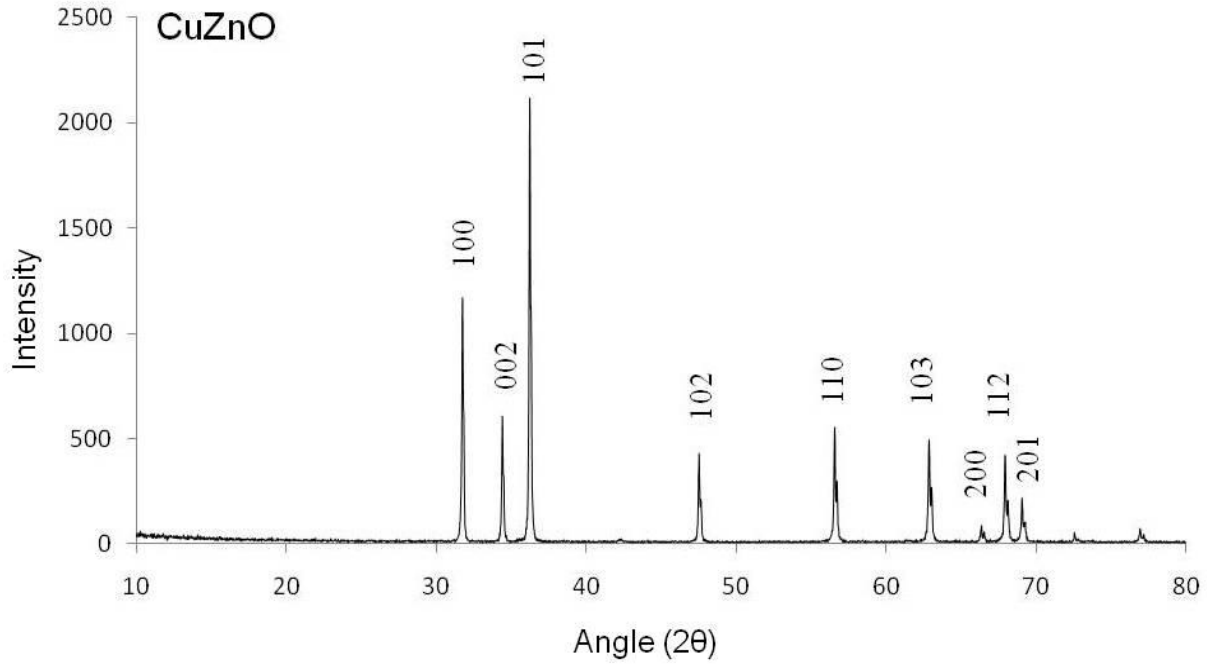

Figure 4.12 XRD pattern of CuZnO pellet ground to powder

The incorporation of dopants changes the lattice strain and the lattice constant of the host material and usually depends upon the ionic radii of the dopant ions[157]. The lattice parameters were calculated as a = 0.3252nm and that for c = 0.5202nm from the XRD peaks using the formula for a hexagonal structure as[143],

$$\left(\frac{1}{d_{hkl}}\right) = \frac{2}{a\sqrt{3}\sqrt{(h^2 + hk + k^2) + \frac{l^2}{c^2}}} \qquad (3.8)$$

Where *a* and *c* are the lattice parameters for the hexagonal crystal system, h, k, and l are the Miller indices and d_{hkl} is the spacing between the planes. Crystalline material contains a range of crystal imperfections and distortions that affect the properties of the material[157]. The factors affecting the properties of doped materials are the reaction temperature and the chemical reaction between the impurity and the host material. The lattice strain can be estimated using the Williamson-Hall model[158].

$$\beta\,(rad)cos\theta = \frac{0.9\,\lambda}{D} + 4\varepsilon\, sin\theta \qquad (4.1)$$

Where β is the full width at half maximum (FWHM) of the individual peak, λ is the wave length of the x-ray source which is 0.154nm for CuK_{α}. The estimated crystallite size from 101 peak is of the order of 73nm. The data observed from the XRD analysis is given in the table 4.2.

β(deg)	*β(rad)*	*θ*	*cosθ*	*sinθ*	*4*sinθ*	*β(rad)*cosθ*
0.11	0.00192	15.87	0.96188	0.27346	1.09384	0.00185
0.11	0.00192	17.22	0.95518	0.29604	1.18417	0.00183
0.114	0.001989	18.12	0.95041	0.31101	1.24404	0.00189
0.13	0.002269	23.77	0.91517	0.40307	1.61226	0.00208
0.136	0.002373	28.29	0.88056	0.47393	1.89572	0.00209
0.153	0.00267	31.44	0.85319	0.52161	2.08644	0.00228
0.161	0.002809	33.97	0.82933	0.55876	2.23504	0.00233

Table 4.2 angular parameters observed from the XRD pattern of CuZnO powder in figure (4.12)

Since the plot of *β(rad)*cosθ vs 4*sinθ* gives rise to a straight line therefore the microstrain due to the incorporation of Cu ions into the ZnO matrix could be estimated from the slope of the line as shown in the figure 4.13. The estimated strain is of the order of 4.3 x 10^{-4}.

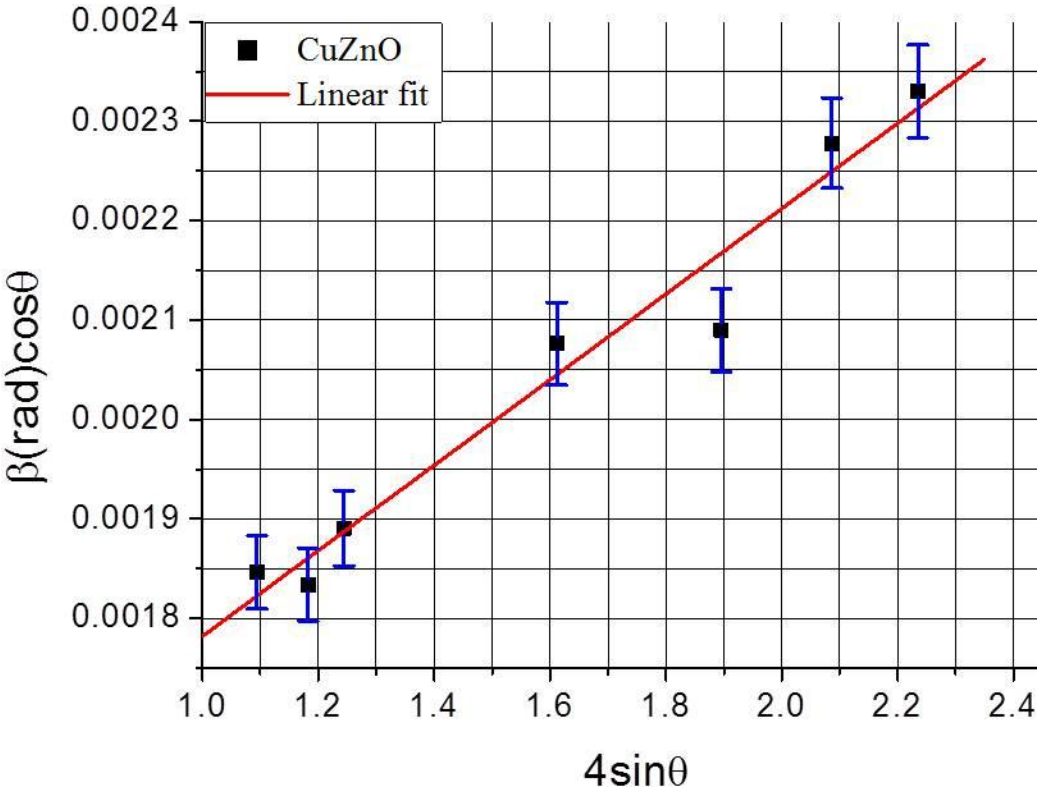

Figure 4.13 Williamson-Hall plot of the CuZnO powder and the lattice strain is calculated from the slope of the straight line.

The average crystallite size [using Scherer's formula (equation (4.2)], lattice strain and lattice parameter of the CuZnO powder is given in table 4.3.

Crystallite size (D)	Microstrain (ε)	Lattice constants (nm)
73nm ±1.5 nm	$4.3 \times 10^{-4} \pm 0.2 \times 10^{-4}$	a = 0.3252 ± 0.02 c = 0.5202 ± 0.02

Table 4.3 crystallite size, lattice strain and lattice constant of the CuZnO powder

4.7): XPS analysis of the CuZnO catalyst.

XPS is a powerful technique for studying the oxidation state for a range of materials and especially the transition metal compounds having localized valence d-orbital. The XPS studies were carried out in order to understand the bonding state of $Cu_{0.05}(ZnO)_{0.95}$ and to study the possible changes in the chemical composition of this material when it is thermally evaporated on a substrate. Usually copper in the divalent state has d^9 character with an unpaired electron, whilst Cu_2O and metallic copper Cu^0 is expected to have d^{10} character with no unpaired electron[159].

The Cu doped ZnO was characterised through XPS, which is a representative of several Cu oxidation states as shown in figure 4.14. The XPS detects the core level and shake up satellites for $Cu2p_{3/2}$ and $Cu2p_{1/2}$ in the pellet. While no shake-up satellite were observed in the film. The core level lines of $Cu2p_{3/2}$ and $Cu2p_{1/2}$ correspond to the binding energy of 933eV and 953eV respectively, while the shakeup satellites are revealed at 940.7eV and 943eV for $Cu2p_{3/2}$ and 961.7eV for $Cu2p_{1/2}$. The core level spectrum at 933eV along with the shake-up satellites at higher energies correspond to the mixed oxidation states of Cu^{+1} and Cu^{+2} ions[160], which gives indication that there is no metallic copper on the surface of the pellet or in the film.

The satellites in the higher binding energy sides show that the material has a d^9 character in its ground state, which corresponds to the Cu^{2+} ions in the ZnO matrix[159]. The satellites are considered to be due to the transition from the valence band to the un-occupied states in the conduction band as discussed by Kim et al[161]. The structure of satellites is due to the multiple splitting of the $2p^5 3d^9$ final state and a range of transitions of a second electron during the photo-ionisation. After the thermal evaporation of the pellet the satellites disappear and two very striking peaks are observed, that correspond to the $Cu2p_{3/2}$ and $Cu2p_{1/2}$ at 933.7eV and 953.7eV, respectively, which is because of the spin orbit splitting. The peaks have been shifted by 0.7eV to the higher binding energy side. This indicates that after thermal evaporation of the pellets the Cu^+ ions are further oxidized to form Cu^{2+} ions. The peak for $Cu2p_{3/2}$ at 933.7eV and the absence of the shake-up satellites in the Cu2p spectra is attributed to the charge transfer transition from metal (Cu) to ligand (O), because the satellites will appear in the core electron spectra of the acceptor species[162]. It can be concluded that after

thermal evaporation of the pellet, the concentration of the Cu^{+2} species increases, which has a d^9 character and is used to trap an electron in its active d-shell[163].

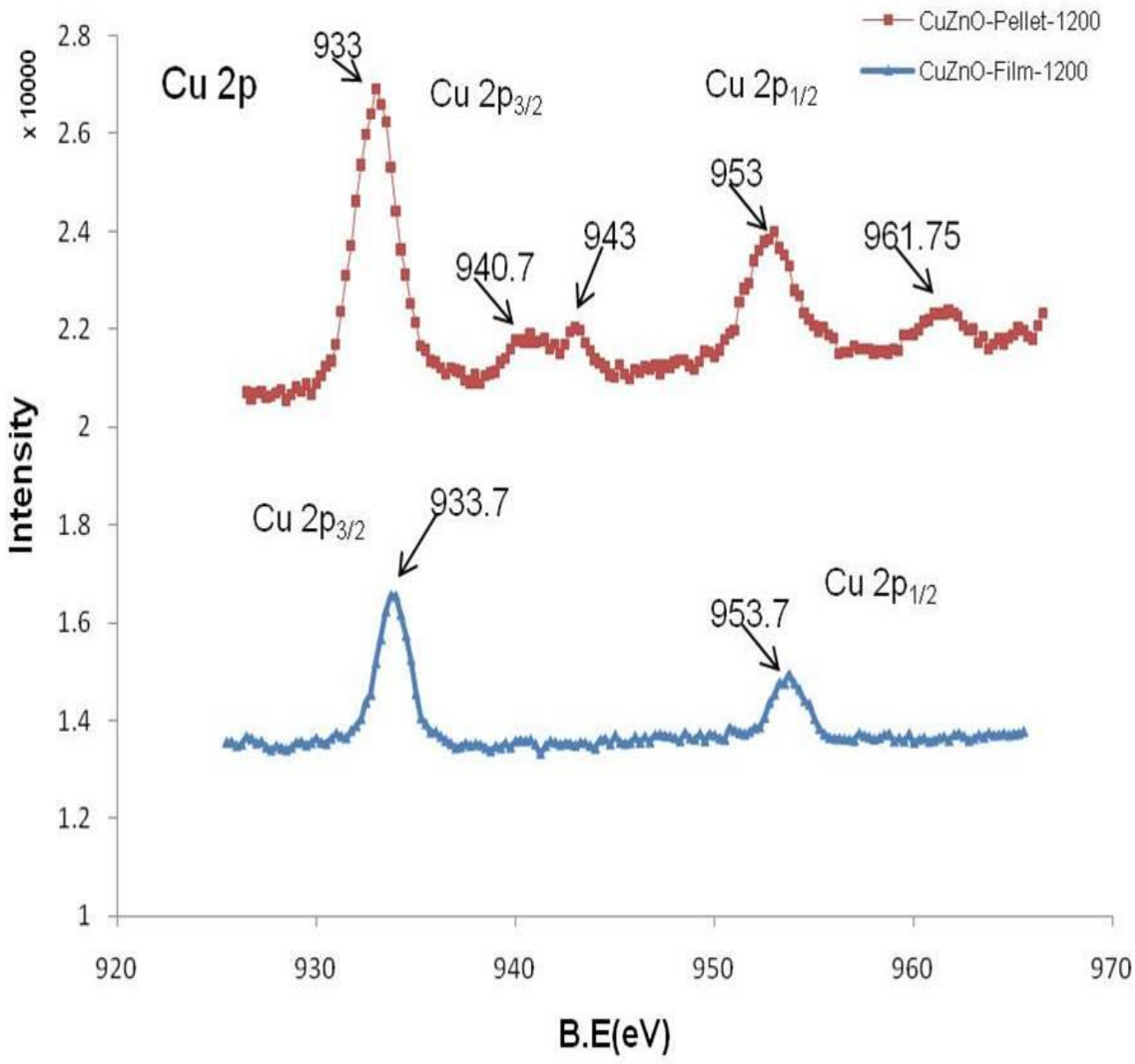

Figure 4.14 XPS spectrum of Cu 2p for pellet (red) and thermally evaporated film (blue). The peak at B.E=933eV and 933.7eV represent the $2p_{3/2}$ for the pellet and film respectively. The satellite structure only appears in the pellet spectra at 940.7eV and 943eV. The Cu $2p_{1/2}$ peak appears at B.E = 953eV and 953.7eV for both pellet and film respectively. The corresponding satellite peak for the pellet appears at B.E = 881eV.

The broadness (FWHM) of the Cu2p3$_{/2}$ peak for cuprous oxide (Cu_2O) is of the order of 1eV and for that of the metallic copper Cu^0 is about 0.8eV[164]. In comparison to these values the observed peak from the evaporated CuZnO material is much broader than the combination of both, which indicates that there is neither Cu_2O nor metallic copper Cu^0 that resides on the surface of the film. Here it could be expected that the dopant has taken some interstitial lattice positions as well that resulted in the broadening of the spectrum[165].

Two peaks have been observed for O1s core level spectrum in the pellet. One peak is at the binding energy of 530.3eV and the other is at 531.5eV. The peak at 530.3eV is considered to be the lattice oxygen corresponding to Cu_2O[159,166], while the other peak at 531.5eV corresponds to O^{-2} in the oxygen deficient regions within the matrix of ZnO[168]. If the two earlier studies[159,166] is considered a base for the XPS analysis of the bulk CuZnO (pellet) then the Cu2p core level and O1s spectra are quite controversial with one another. The authors attributed the Cu2p$_{3/2}$ peak at 933.2±0.2 to the presence of CuO with the corresponding O1s peak at 529.2±0.3. Again if the O1s peak at 530.3eV is associated with the presence of Cu_2O then the FWHM of the Cu2p$_{3/2}$ peak does not support, which is quite higher than the corresponding FWHM (~1eV)[164] of Cu_2O. Additionally no secondary phase corresponding to CuO or Cu_2O has been observed through the XRD analysis of the CuZnO powder [section (4.6)]. Therefore it can be deduced that the binding energy corresponding to O1s core level in bulk is different from that of the film. This behaviour is quite evident in rare earth doped ZnO samples (discussed in section 5.3 and 5.9) as well. Thus it is believed that the O1s peak at 530.3eV correspond to the oxygen in the bulk ZnO.

However after thermal evaporation the O1s core level XPS peak shifts towards the higher binding energy and appears at 530.9eV. This is believed to correspond to O^{-2} on wurtzite structure of ZnO matrix[167], as shown in figure 4.15 (blue spectrum). The intensity of the O1s peak of the thermally evaporated film is quite high in comparison to that of the pellet, which is attributed to the variations in the oxygen vacancies. A small kink at 531.3eV shows that there still exist some oxygen deficient areas[168]. It is evident now that after thermal evaporation most of the oxygen deficient regions have been recovered. Additionally there is dispersion in the O1s core level on the higher binding energy side for the thermally evaporated sample, which clearly identifies the Cu (2p) to O (1s) charge transfer transition[169]. This intragrannular charge transfer transition from Cu2p to O1s is believed to play a critical role in dissociating the hydrocarbon molecule during the CNTs growth.

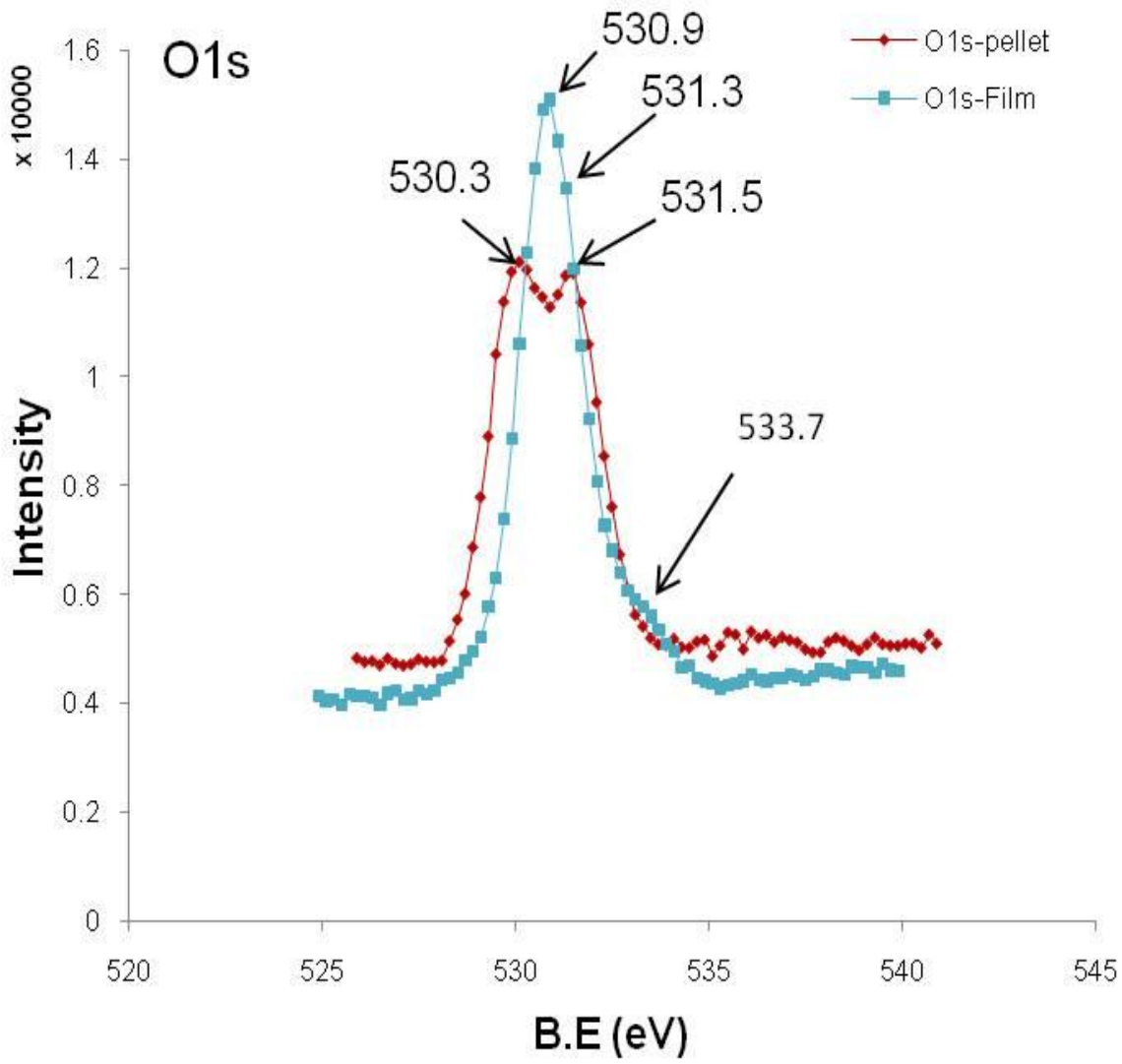

Figure 4.15 XPS spectra of O1s in the CuZnO pellet (red) and film (blue). The pellet spectrum has two well defined peaks at B.E = 530.3eV and 531.5eV. The film spectrum has a well defined peak at B.E = 530.9eV with two other shoulders at 531.3eV and 533.7eV.

The core line spectra for the Zn from the pellet and that of the film are different as shown in figure 4.16. Both of the samples do not exhibit the same character. The core level XPS spectrum of the pellet for the Zn2p3/2 seems to be a convolution of two peaks and appear at 1021.3eV and 1021.7eV showing the existence of the Zn in metallic and in the first oxidation state[170]. But after thermal evaporation of the pellet on the substrate the main peak shifts towards the higher binding energy side and appears at 1022.1eV. This confirms that the metallic Zn or Zn^{+1} have been transformed into Zn^{2+} oxidation state[170].

It is obvious from the results shown in figure 4.16 that the intensity and the width of the $Zn2p_{3/2}$ peak for the film decreases after evaporation which is suggested as being due to the decrease in Zn concentration with copper doping in the ZnO matrix. The shoulder peak on the lower binding energy side at 1020.9eV corresponds to the Zn—Cu bonding. It is because the electronegativity of Cu (1.9) is less than that of oxygen (3.44) therefore the Zn—Cu bonding will appear on the lower binding energy side than Zn—O [171]. This further confirms that copper has successfully been incorporated into the ZnO matrix.

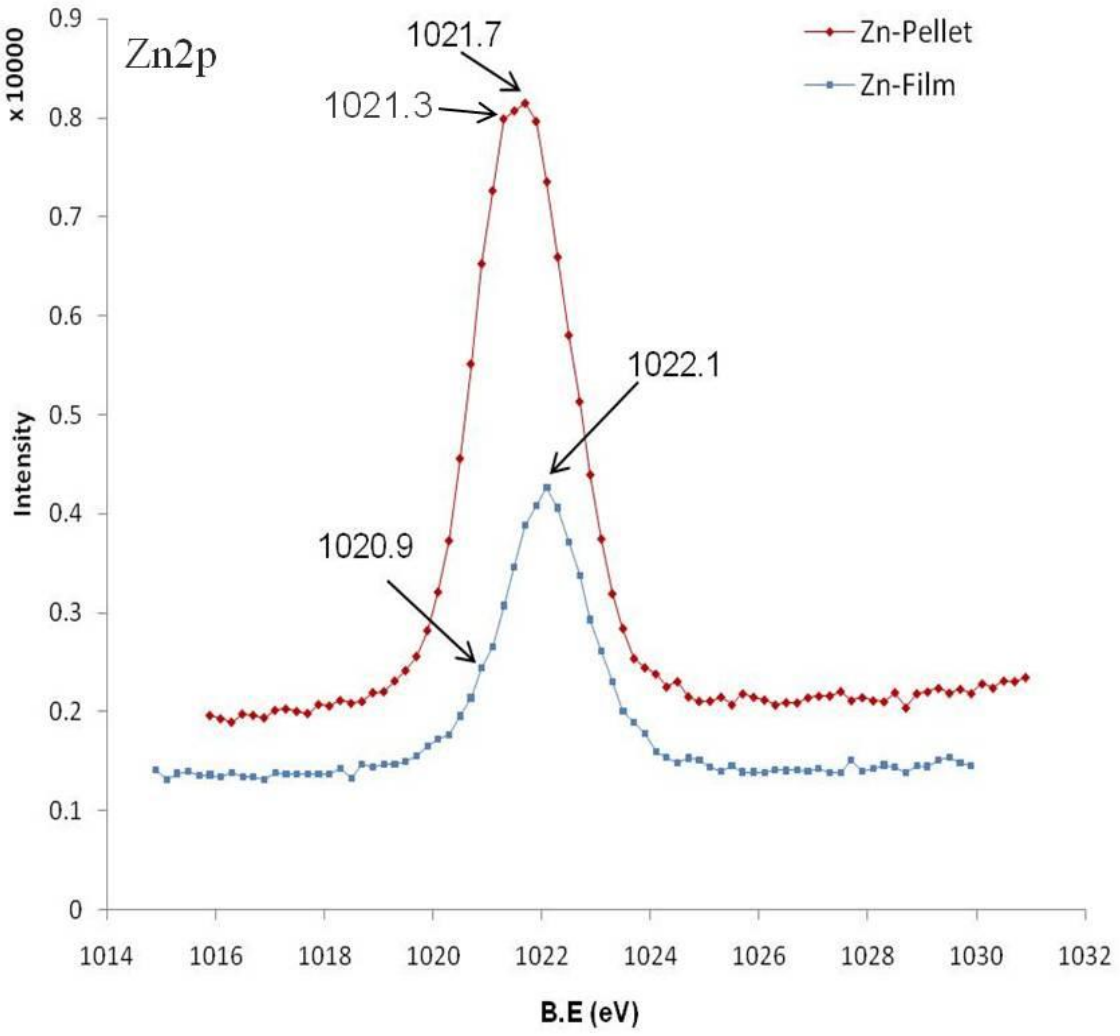

Figure 4.16 XPS spectra for Zn2p. The red spectrum is for the pellet showing a peak at B.E=1021.7eV and the blue is for the thermally evaporated pellet at B.E=1022.1eV. The shoulder at 1020.9eV corresponds to the Cu—Zn bonding.

4.8): SEM and EDS Characterisation of NiZnO

Nickel doped zinc oxide (NiZnO) pellets were prepared through solid state reaction. The pellet was then evaporated thermally on Cr coated W substrates in view to using the material for the growth of CNTs. The pellet was characterised through the SEM for the grain morphology. It is obvious that there is large distribution of grain sizes and shapes with sharp grain boundaries, and is shown in the figure 4.17.

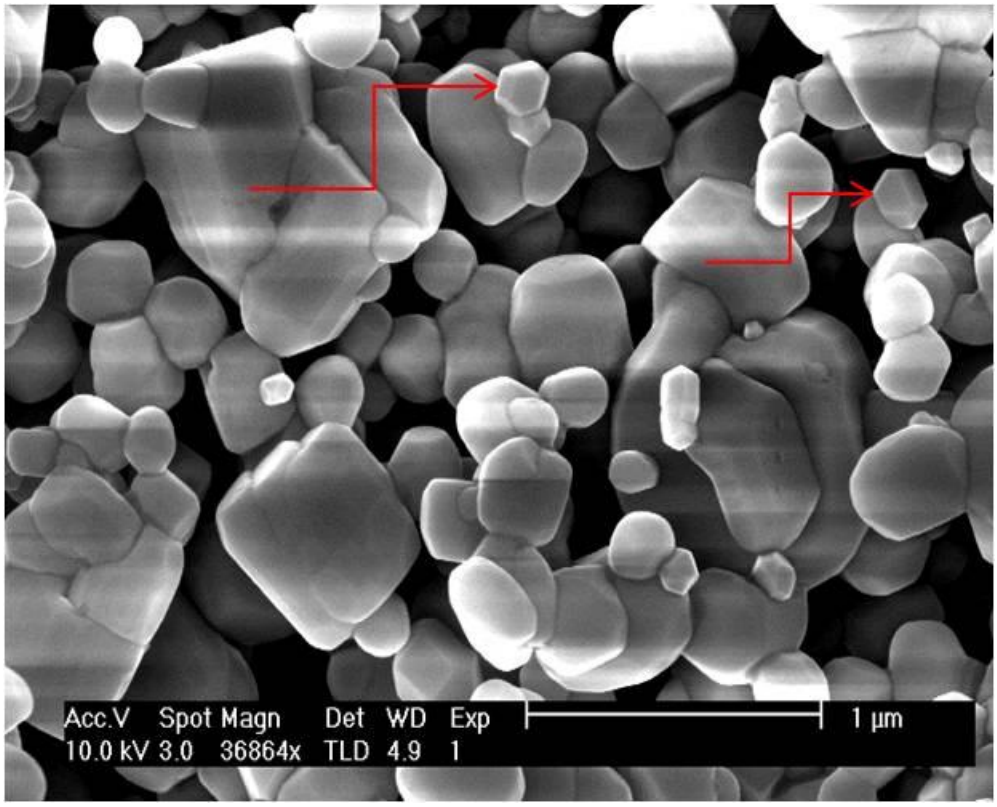

Figure 4.17 NiZnO pellet prepared through solid state reaction. The arrows showing grains facets and sharp geometry.

The elemental analysis of the pellet was carried out through EDS, which confirms the presence of all the three elements Ni, Zn and O and is shown in figure 4.18. The quantitative results obtained from the EDS are given in the table 4.4, which confirms the added quantity of 5wt% Ni.

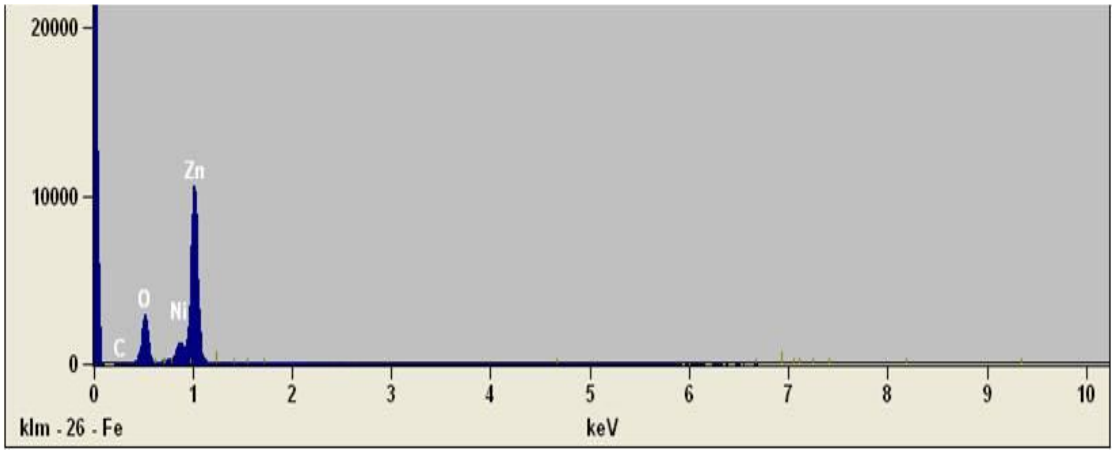

Figure 4.18 EDS spectrum for NiZnO pellet

Element Line	Weight %	Weight % Error	Atom%
C K	0.5	+/- 0.06	1.7
O K	17.4	+/- 0.15	45.5
Ni L	4.8	+/- 0.20	3.3
Zn L	77.3	+/- 0.42	49.5
Total	100.0		100.0

Table 4.4 quantitative analysis of NiZnO pellet

After the thermal evaporation, the sample was imaged under the SEM for the grains morphology. The grains have quite irregular shapes but with sharp grain boundaries and some of the grains have diffused with one another and have become elongated, which might be because of the lattice mismatch arises from the Ni doping of ZnO. It is observed in section (4.9) through XRD that the doping of Ni produces higher strain in the ZnO lattice and increases the lattice parameter more than Cu doping of ZnO. Therefore it is more likely that NiZnO will produce higher lattice mismatch with support than CuZnO. This higher lattice mismatch will give rise to higher surface stress and will result in anisotropic grain growth[156]. It has been observed in this study that smaller grains are more favourable for CNTs growth. This may be because the smaller particles have high surface to volume ratio and the surface atoms of smaller nanoparticles are more active than bulk.

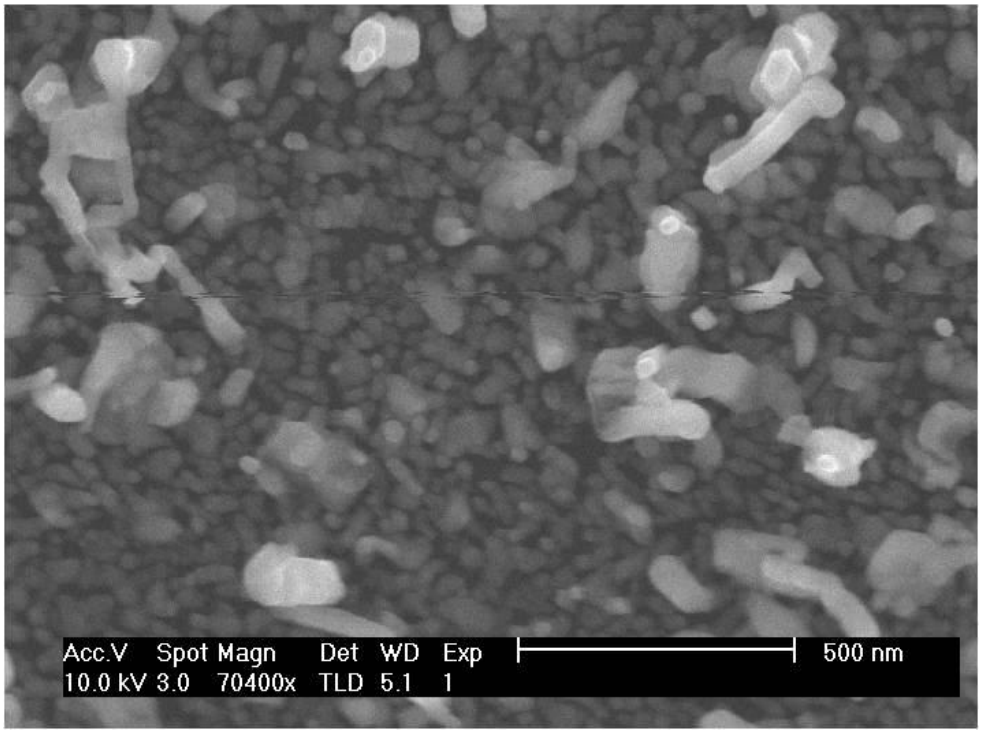

Figure 4.19 thermally evaporated pellet of NiZnO upon W substrate with Cr as buffer layer

4.9): X-ray diffraction studies of the NiZnO powder

The ZnO powder doped with 5wt% NiO through solid state reaction was analysed through XRD to see the phase of the powder after heating it up-to 1200C for 14 hours. The sample was then let to cool down to room temperature. From the analysis of the XRD data it is found that the sample is crystalline and the main peaks correspond to the ZnO wurtzite crystal structure. A secondary phase of NiO has been observed, as shown in figure 4.20.

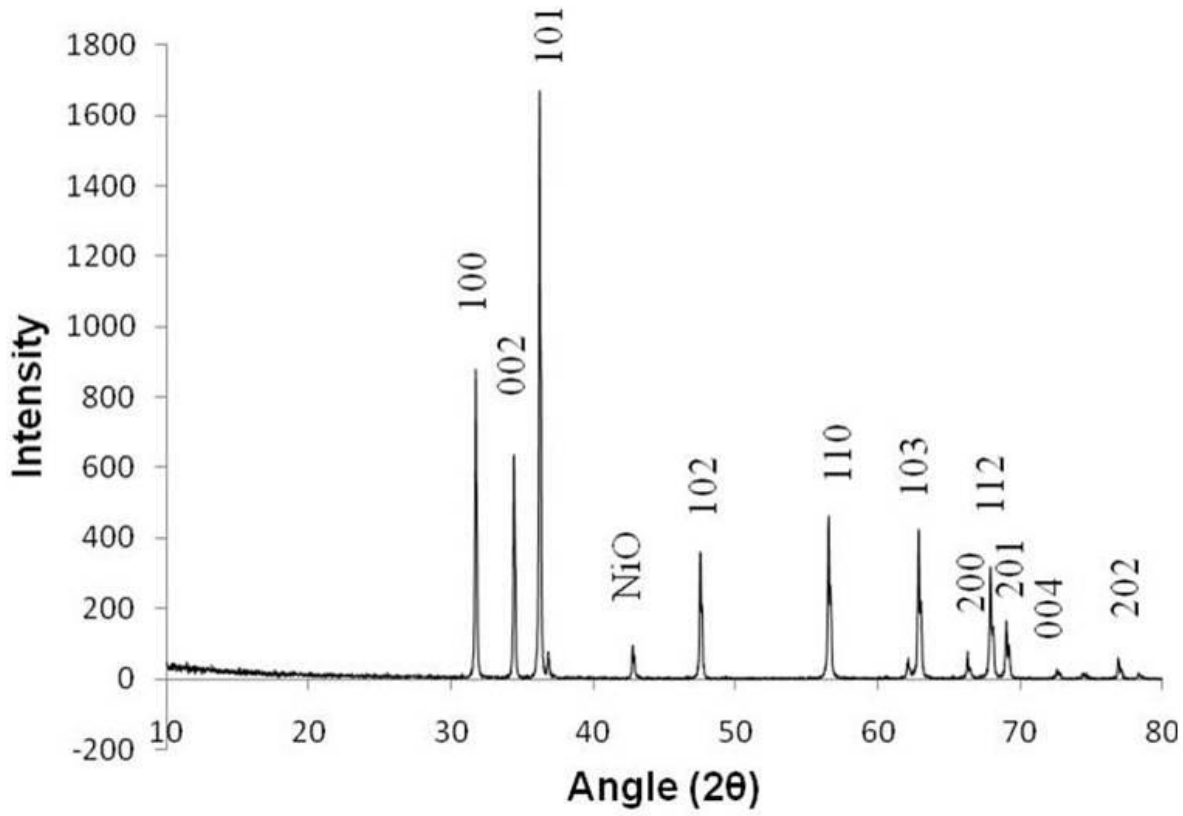

Figure 4.20 XRD spectra of NiZnO powder

The XRD analysis of NiZnO powder shows that there is a small angular deviation of the peaks to the lower angle in comparison to the CuZnO material. This indicates that some of the Ni ions have been incorporated into the ZnO matrix and have changed the lattice parameter of the host material as shown in table 4.6. However the only secondary phase observed is that of the NiO, which shows that some of the NiO have been accumulated in separated and have not been incorporated into the ZnO matrix. This indicates that the sintering temperature of 1200C for 14 hours is not sufficient for the complete incorporation of Ni ions into the ZnO matrix, which might be because of the different crystal structures of NiO and ZnO. Since NiO crystallises in rock-salt structure while ZnO belongs to hexagonal crystal family, therefore it seems difficult to accommodate Ni ions in the ZnO host lattice[157]. There is no direct evidence of metallic Ni or clusters of Ni atoms. The data for the peaks (100), (002), (101), (102), (110), (103) and (112) have been analysed and are given in the table 4.5.

$\beta(deg)$	$\beta(rad)$	θ	$cos\theta$	$sin\theta$	$4*sin\theta$	$\beta(rad)*cos\theta$
0.142	0.002478	15.87	0.96188	0.27346	1.09384	0.00238
0.148	0.002583	17.2	0.95518	0.29604	1.18416	0.00247
0.151	0.002635	18.11	0.95046	0.31084	1.24336	0.00250
0.169	0.002949	23.76	0.91524	0.40291	1.61163	0.00270
0.185	0.003228	28.28	0.88064	0.47378	1.89512	0.00284
0.194	0.003385	31.45	0.85309	0.52175	2.087	0.00289
0.199	0.003473	33.98	0.82923	0.55891	2.23564	0.00288

Table 4.5 angular parameters observed from the XRD pattern of NiZnO powder in figure 4.20.

To see any structural modification due to the incorporation of Ni ions into the ZnO matrix through solid state reaction it was necessary to go through an in-depth analysis of the XRD pattern. The change in the microstrain or in the lattice constant of the ZnO indicates that some impurity has been incorporated into it. The microstrain was obtained from the slope of the linear fit of the plot of $4*sin\theta$ vs $\beta(rad)*cos\theta$ as shown in figure 4.21.

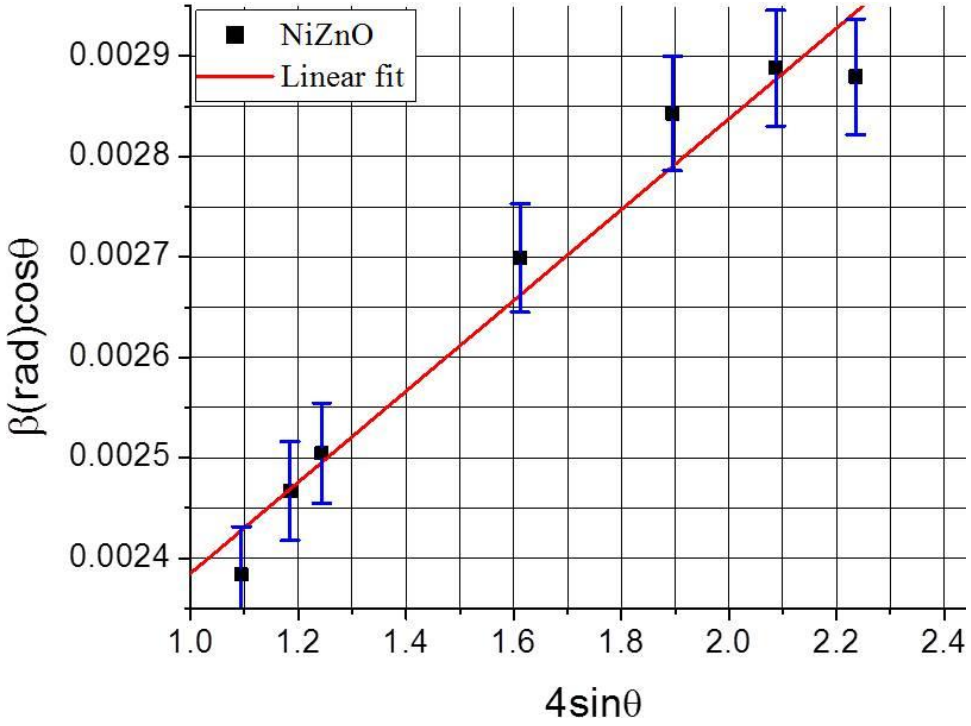

Figure 4.21 Williamson-Hall plot for the NiZnO powder and the lattice strain is calculated from the slope of the straight line. The error bars represent the 2% error in the FWHM of each diffraction plane.

The microstrain observed from the slope of the linear fit is of the order of 5×10^{-4}. The crystallite size for (101) planes was calculated using Scherer's formula,

$$D = \frac{0.9\lambda}{\beta(rad)cos\theta} \qquad (4.2)$$

The average crystallite size, the microstrain and the lattice parameters for the NiZnO powder are given in the table 4.6.

Crystallite size (D)	Microstrain (ε)	Lattice constants (nm)
55.4 +/- 5nm	5×10^{-4} +/- 0.1×10^{-4}	a = 0.3252 +/-0.02 c = 0.5210 +/-0.02

Table 4.6 crystallite size, lattice strain and lattice constant of the NiZnO powder in table.

There is a small increase of the order of 0.06nm in the value of the lattice constant 'a' that might be the cause of slight increase in the lattice strain in comparison to that of the CuZnO. This increase in the lattice constant in the (101) plane shows that some Ni ions have been incorporated into the ZnO matrix.

4.10): XPS analysis of NiZnO catalysts

After the thermal evaporation of the NiZnO pellet onto the Cr coated W substrate it was characterised through XPS to see any possible changes in the chemical composition of the sample. The XPS spectrum gives information about the oxidation state of the Ni on the substrate. The XPS spectrum for NiZnO shows a doublet with binding energies at 855eV and 873.75eV that correspond to Ni $2p_{3/2}$ and $2p_{1/2}$, respectively. The corresponding satellite peaks for $2p_{3/2}$ and $2p_{1/2}$ are observed at 862.25eV and 880.5eV, respectively. The binding energy for metallic Ni is 852.6eV[172]. This indicates that no metallic (Ni) exists; additionally the absence of the metallic Ni on the surface of the substrate could be supported from the energy difference between the $2p_{3/2}$ and $2p_{1/2}$ peaks, which is 17.4eV for metallic Ni and 18.4eV for NiO[173]. The observed binding energy difference in our case is 18.75eV, which rules out the existence of metallic Ni and NiO. The shoulder on the higher binding energy side of the main peak (855eV) at 856.25eV shows that there is a combination of Ni^{+2} and Ni^{+3} ions in the nanoparticles. The presence of the mixed valance state of the metal ions also gives rise to charge transfer transitions[174]. This shows that Ni has been incorporated in the ZnO matrix. This has been confirmed from the oxygen (O1s) core level electron spectra [figure 4.24] where the O1s peak appears at 530.9eV that corresponds to the oxygen in the ZnO matrix[167]. It has been observed from the XRD pattern of the NiZnO powder that there exist NiO phase and also shows an increased lattice constant along the (100) plane, that is mainly because of the incorporation of Ni ions into the ZnO matrix. Therefore it is strongly believed that after thermal evaporation of the pellet the ZnO has been doped with Ni. The satellite peaks in the Ni2p spectra correspond to the charge transfer transition from O2p to Ni3d, because the shakeup satellites appear in the core level electron spectra of the acceptor species[162].

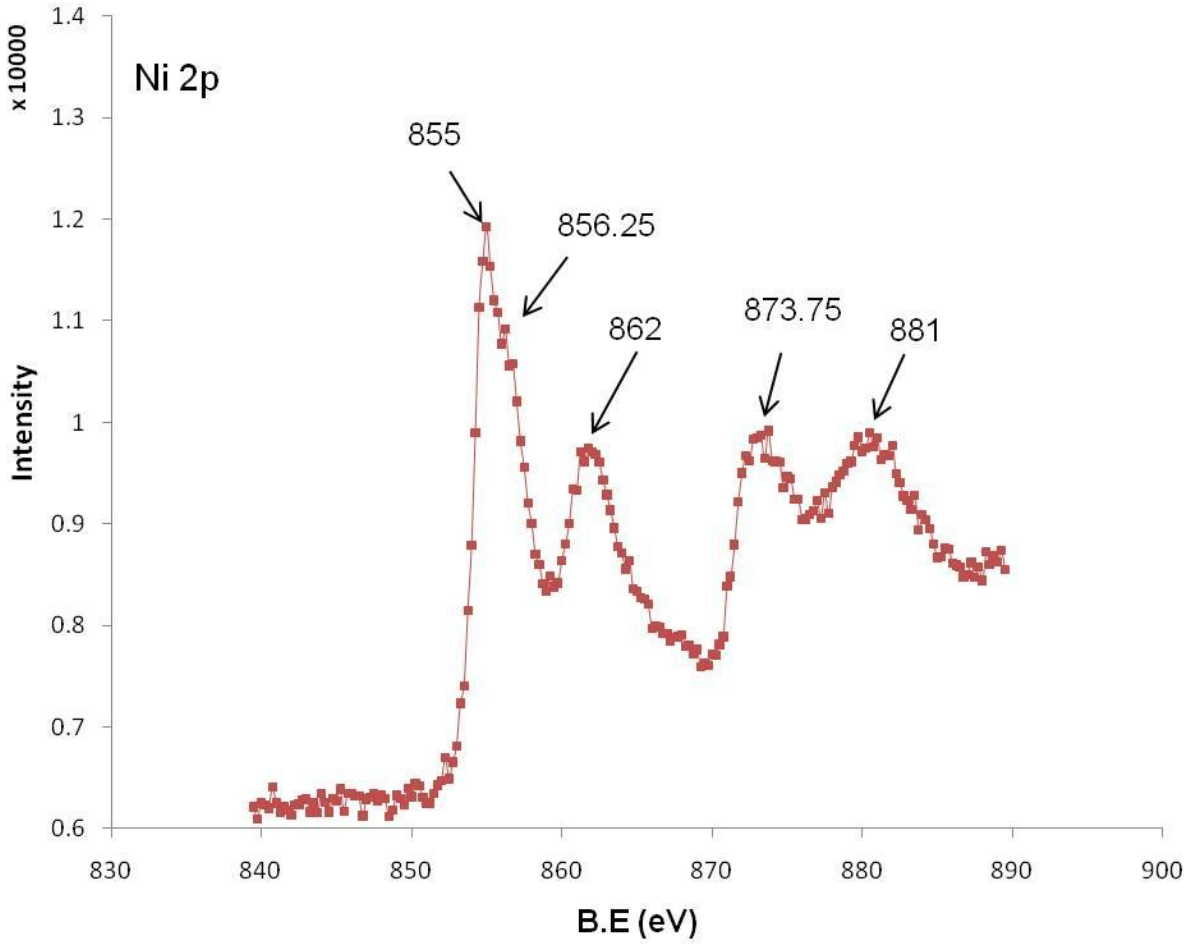

Figure 4.22 XPS spectrum of Ni 2p for thermally evaporated pellet. The peak at B.E=855eV represent the $2p_{3/2}$ with corresponding satellite structure at 862eV. The Ni $2p_{1/2}$ peak appears at B.E = 873.75eV with corresponding satellite peak at B.E = 881eV.

The Zn2p spectrum is a representation of multiple components. There are two peaks observed, one at 1022.1eV and the FWHM is 1.75eV, which corresponds to the Zn — O bonding. This shows that Zn is in the 2+ oxidation state and there is no effect of doping upon the oxidation state of Zn. The other peak is in the lower binding energy side at B.E=1020.5eV, that corresponds to Zn—Ni bonding. Since the electronegativity for both elements Zn (1.65) and Ni (1.91)) is lower than oxygen (3.44) therefore the peak for Zn and Ni will appear in the lower binding energy side[171]. Additionally this peak has a quite low intensity indicating that a small number of Ni ions are bonded to Zn and that the bonding strength is quite low. This gives clear evidence that Ni has been incorporated into the ZnO matrix.

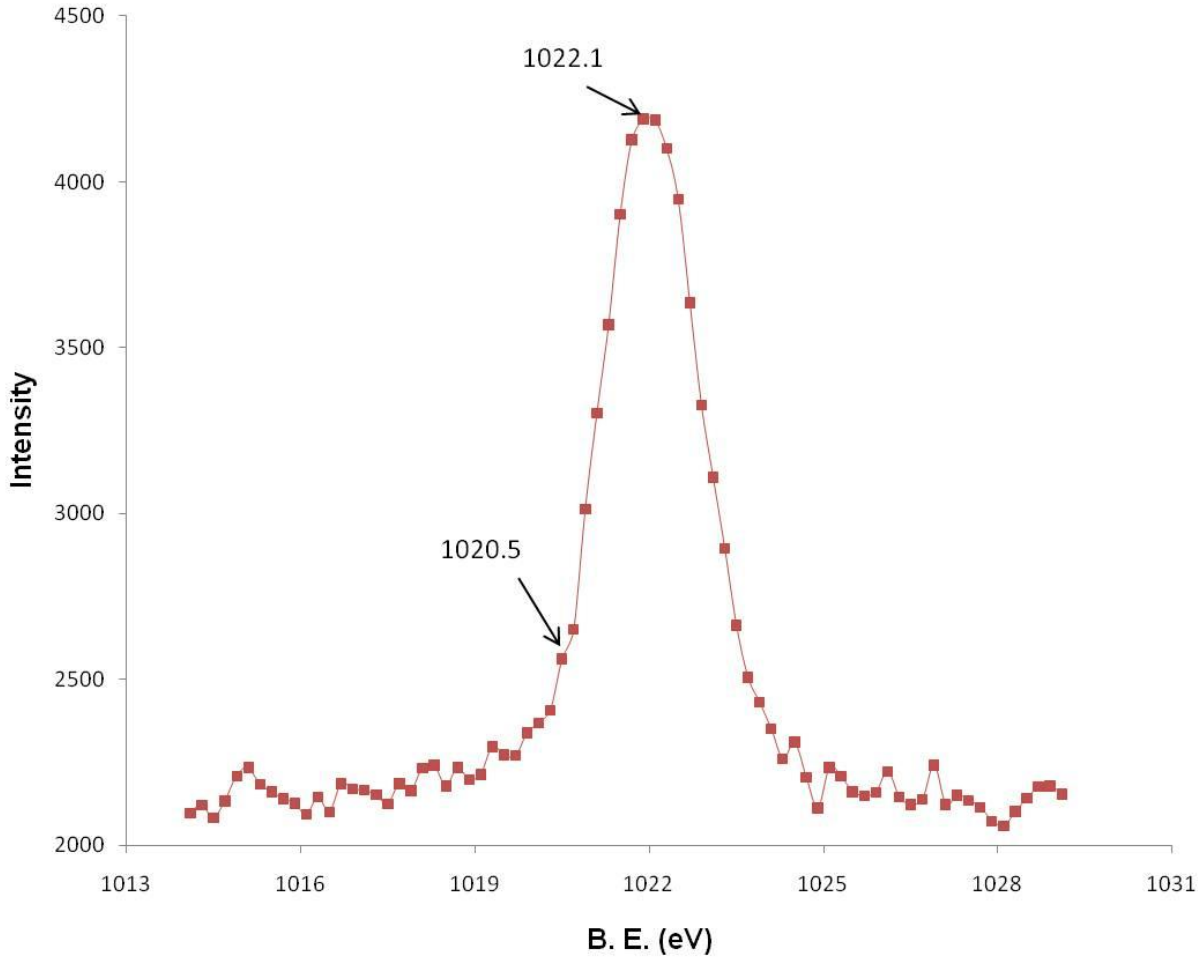

Figure 4.23 XPS spectrum of Zn 2p. The peak at B.E=1022.1eV represent the Zn2$p_{3/2}$ another small shoulder in the lower binding energy side represent the Zn—Ni bonding.

The photoemission spectrum for O1s is not symmetric. The main peak was observed at 530.9eV and the other at 532.1eV. The main peak corresponds to the Oxygen in the ZnO matrix, while the other peak on the higher binding energy side at 532.1eV corresponds either to the oxygen deficient regions [161] or to the hydrogen bonding[175,176]. It is worth mentioning that some of the species cannot be removed completely from the surface of the thermally evaporated pellet. Adsorbed hydrogen on the ZnO surface may give rise to Zn—H or OH species that results in passivation of the surface and protects it from reduction during hydrogen plasma or heat treatment and increases its thermal stability[177].

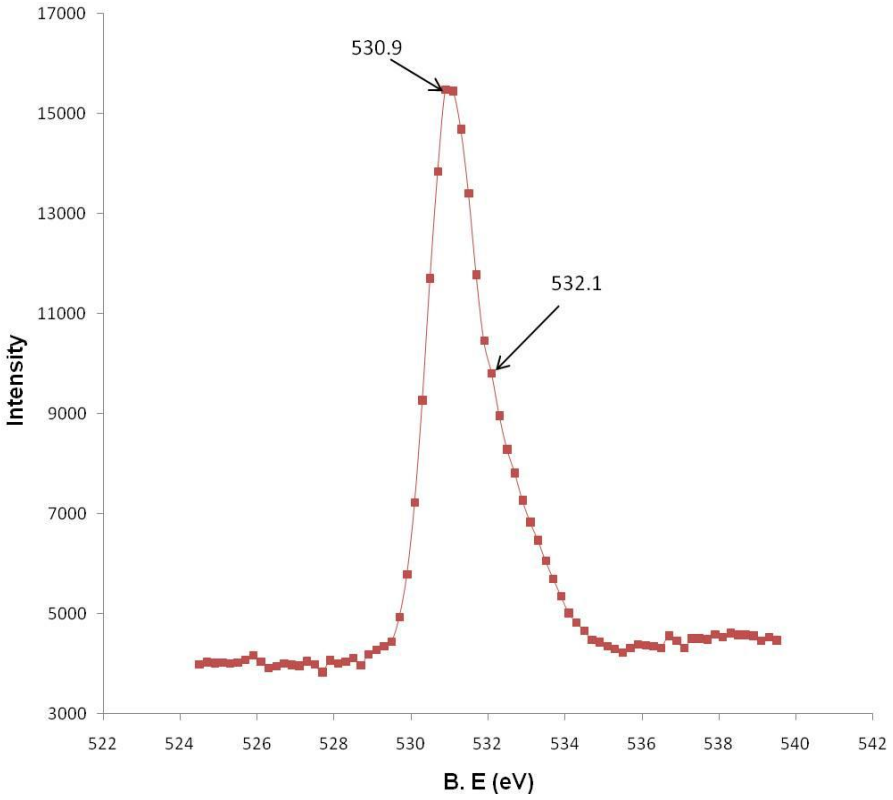

Figure 4.24 XPS spectrum of O1s. The peak at B.E=530.5eV represent the lattice oxygen and the shoulder at 532.1eV corresponds to the oxygen in the oxygen deficient regions.

4.11): Conclusion

This chapter describes the preparation (in general) and characterisation of transition metal (Cu & Ni) doped ZnO prepared through solid state reaction. The CuZnO nanoparticles show well the crystalline nature and quite narrow distribution of particle sizes when thermally evaporated upon Cr coated W substrate. Additionally it has been observed through XPS [section (4.7)] that charge transfer transition occurs from metal to ligand (from Cu to O) in CuZnO nanoparticles when thermally evaporated. While the NiZnO nanoparticles are quite irregular in shape and have a wide distribution of particle sizes. The charge transfer transition occurs from ligand to metal in NiZnO nanoparticles upon thermal evaporation.

5.1): Introduction:

Catalysts play a key role in synthesising the carbon nanotubes through CVD. Novel rare earth doped ZnO catalysts have been prepared through solid state reaction and the pellets have been thermally evaporated on W and Si substrates. The catalysts have been characterised through various techniques such as SEM, EDS, HRTEM, XRD and XPS. The effect of dopants and the sintering temperature upon the doping of ZnO and that on the size and shape distribution of grains will be briefly discussed in this chapter.

5.2): SEM and EDS studies of TbZnO

Pellets of Tb_2O_3 mixed ZnO were prepared through solid state reaction and sintered through a range of temperatures: 1000C, 1050C, 1150C and 1200C and were named after the sintering temperature such as T1000, T1050, T1150 and T1200. The pellets were then imaged under the SEM for the grain morphology and it was observed that there is a large distribution of grain sizes ranging from 200nm—3.5µm, as shown in figure 5.1.

To observe the elemental composition and the quantity of each element present in the pellet, it was characterised through EDS. The EDS spectra confirm the presence and the stoichiometry of all the elements Tb, O and Zn in the pellet as shown in the table 5.1.

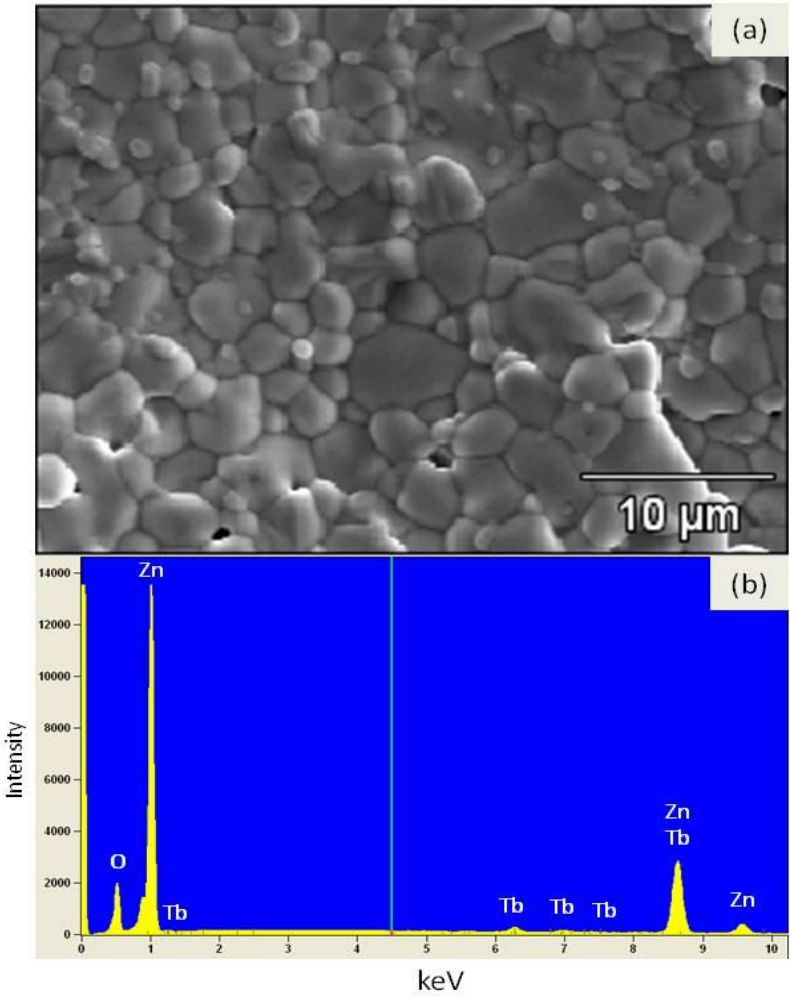

Figure 5.1 SEM image of $Tb_{0.05}$ $ZnO_{0.95}$ pellet sintered at 1200C showing the grains size and shape and in the inset is the EDS spectrum representing the elemental composition of the pellet.

Element Line	*Weight %*	*Weight % Error*	*Atom %*	*Formula*
O K	16.7	+/- 0.17	44.3	O
Zn K	78.1	+/- 0.74	53.9	Zn
Zn L	---	---	---	
Tb L	5.2	+/- 0.41	1.8	Tb
Tb M	---	---	---	
Total	100.0		100.0	

Table 5.1 quantitative analysis of the $Tb_{0.05}ZnO_{0.95}$ pellet sintered at 1200C.

The pellets were then thermally evaporated onto a Cr coated tungsten (W) substrate (after that will be described as W) to use the material for the growth of CNTs afterwards. All the samples accumulated on the W substrate in the form of grains as shown in figure 5.2.

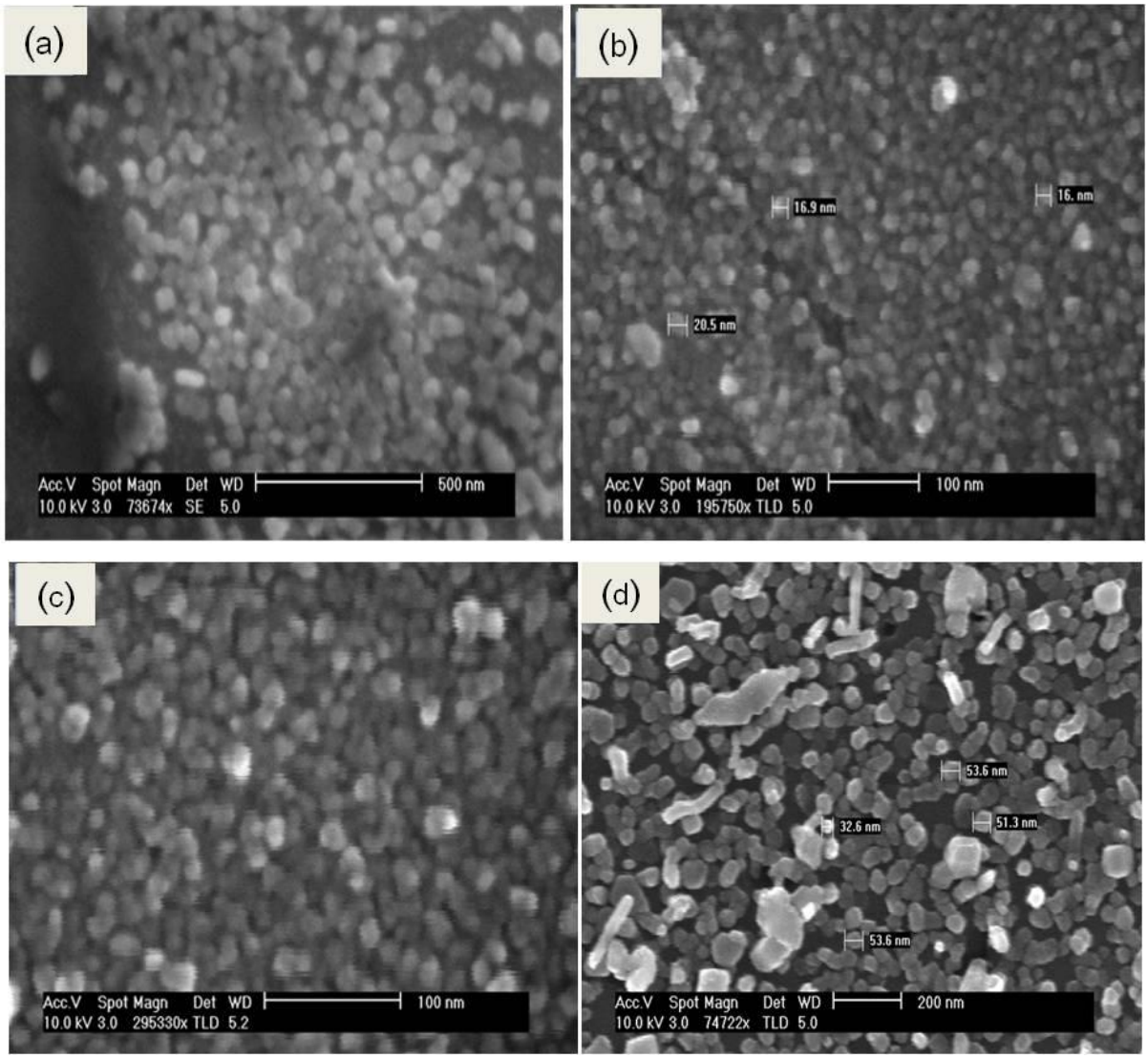

Figure 5.2 SEM image of the thermally evaporated pellets (a) sintered at 1000C, (b) sintered at 1050C, (c) sintered at 1150C and (d) sintered at 1200C on W substrate.

The pellets sintered with different temperature behave differently regarding the grain size and density upon thermal evaporation. The grains of the pellets with lower temperatures show more coalescence and have smaller particle sizes while the sample sintered at 1200C the grains are sharper with definite boundaries and with near hexagonal structure. The

increased coalescence is because of the strong interaction between the particles, which arises from the large amount of defects present in the particles[155]. The thermal evaporation of the pellets exactly follows the trend what has been observed from the XRD analysis regarding the average particle size as given in table 5.2, which might be because of the different composition of dopant ions in individual particle. It is quite clear from figure 5.2 that the thermal evaporation of the TbZnO pellets gives rise to a very narrow distribution of sizes. It seems more likely that the grain deposition on Cr coated W substrate is governed by the vapour solid process[178], in which the oxide vapours evaporates from the high temperature zone and deposits on the substrate at lower temperature and gives rise to grain growth.

After thermal evaporation the grains were further characterised through HRTEM. The W substrate was scrapped through a tweezers to eliminate grains and was put over a copper grid. The copper grid was then examined through TEM to observe the grains morphology and structure. It was observed that the grains correspond to the ZnO with a lattice parameter of 0.5196nm as shown in the figure 5.3.

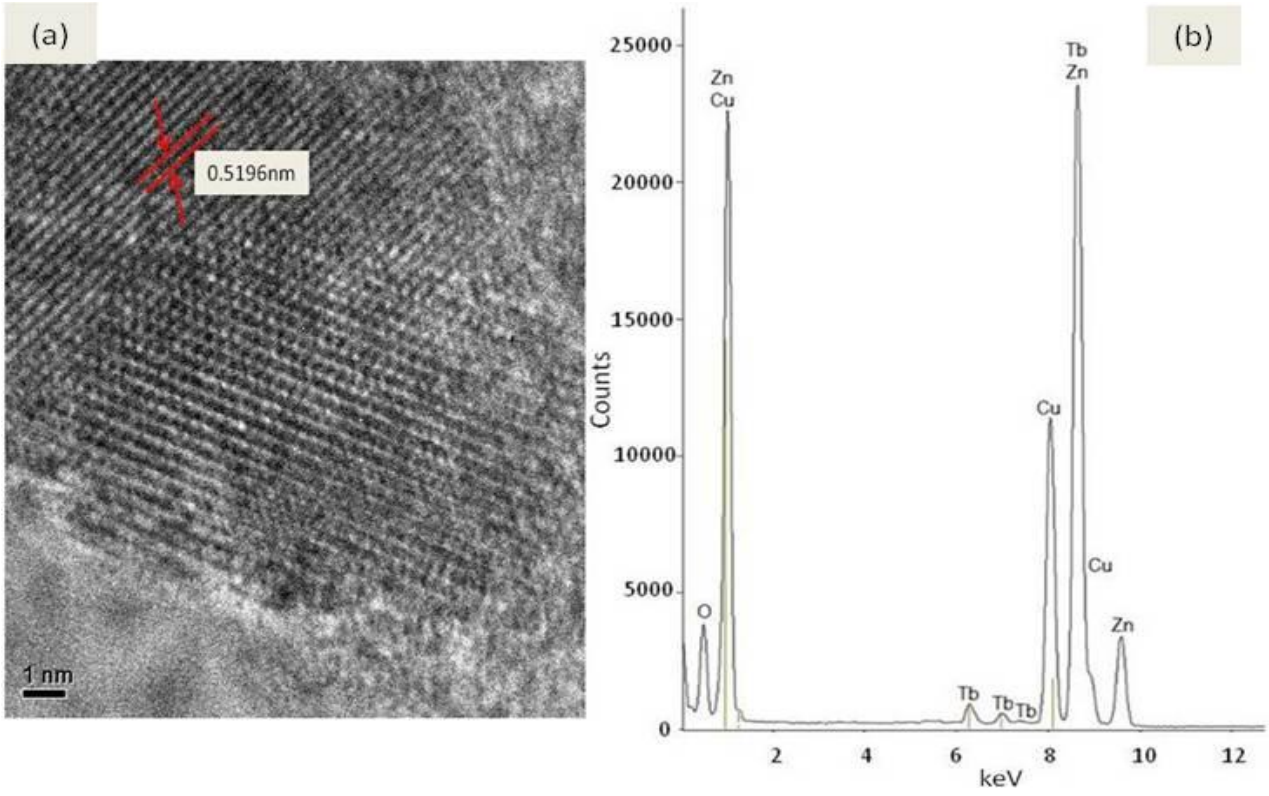

Figure 5.3 (a) HRTEM image representing the lattice parameter of about 0.5196nm that correspond to ZnO structure. (b); EDS analysis through TEM showing the elemental composition of the grain.

The HRTEM image shows that the grains are highly crystalline with c-axis as the preferred orientation of growth. This value is a bit smaller than the corresponding value observed through the XRD analysis (shown in table 5.2) of the same sample (T1200), which might be because of the smaller grain size with less strain. Elemental analysis of the grain was carried out through the EDS in TEM which confirms the presence of Tb in the ZnO matrix as shown in figure 5.3b. There is a peak for Cu in the EDS spectrum that is because of the copper grid.

5.3): XPS analysis of TbZnO

The doping of ZnO with terbium (Tb) was investigated through XPS. The binding energy shift due to relative surface charging was corrected with respect to C1s of binding energy 284.6eV. Three samples of TbZnO were characterised through XPS. Two of them were pellet sintered at 1000C and 1200C and the third sample was the thermally evaporated film on the tungsten substrate and the samples are named after that as T1000, T1200 and TW1200 respectively. The 3d core level spectra for all the three samples were obtained. The characteristic peaks for $Tb3d_{5/2}$ and $Tb3d_{3/2}$ for all the samples are shown in figure 5.4. It is quite evident that the $Tb3d_{5/2}$ peak is a convolution of different peaks and this behaviour appears for all the samples. There is a steep increase from 1240.75eV to 1242.5eV. This happens when the Tb^{+3} and Tb^{+4} ions are present together[179]. According to Sarma et al[180]; the change of oxidation state from +3 to +4 does not shift the peak significantly towards the higher binding energy side. This clearly indicates the presence of more than one oxidation state of Tb on the surface of the sample.

The corresponding satellite structures become prominent as the temperature increases and become more visible after the pellet is thermally evaporated. Interestingly the shakeup satellite structure for the pellet samples is a convolution of two different peaks that appears at 1250.75eV and 1251.5eV. The former correspond to the Tb^{+3} and the later correspond to the Tb^{+4} ions[179]. After thermal evaporation of the pellet the peaks for the $Tb3d_{5/2}$ and $3d_{3/2}$ appears at the same binding energy with the same behaviour as that for the pellets. The only difference is that the satellite gets sharpened in comparison to the structures for pellets. The

sharpening of the satellite structure is due to the increased oxidation state of Tb in the sample[181].

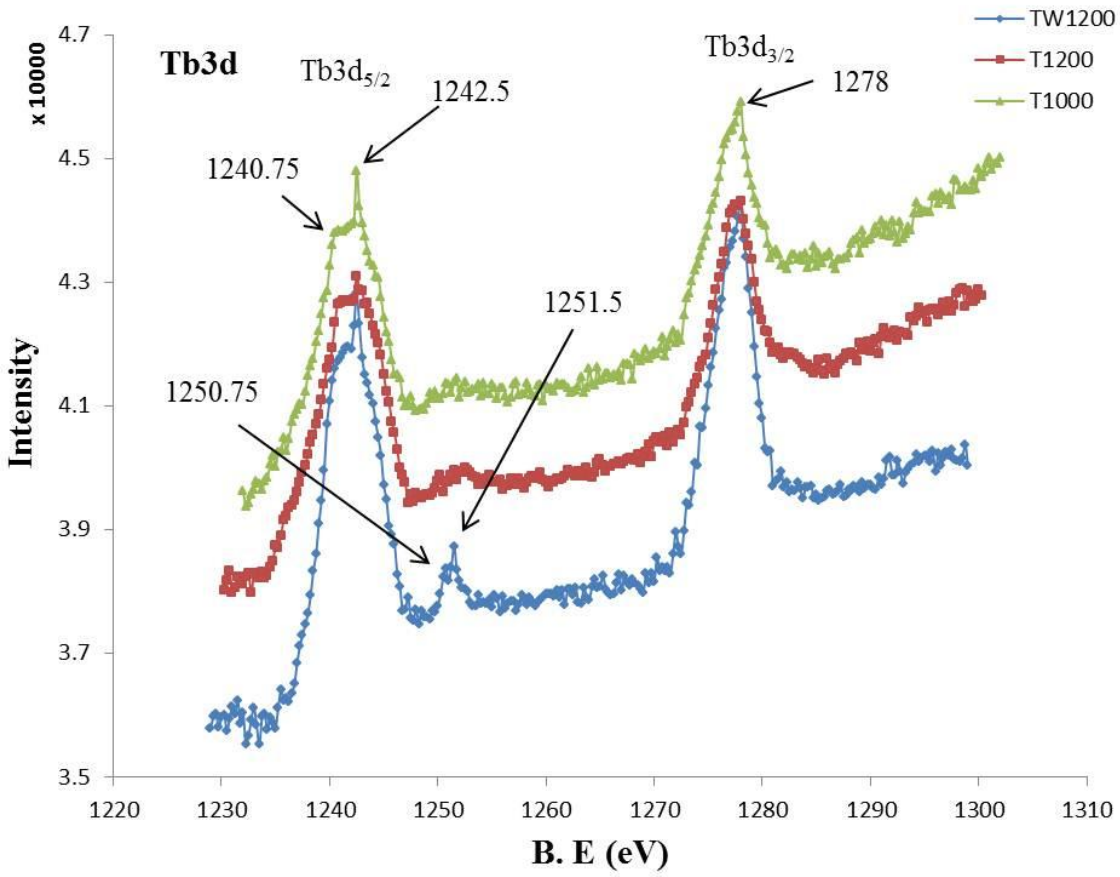

Figure 5.4 XPS spectra of $Tb_{0.05}(ZnO)_{0.95}$ representing the $3d_{5/2}$ and $3d_{3/2}$ core level peaks for the pellets (red and green spectra) and thermally evaporated (blue) samples. The satellite structures appears at 1250.75 and 1251.5eV, which correspond to the presence of Tb^{+3} and Tb^{+4} oxidation states respectively.

The appearance of shakeup satellite structure in the Tb3d core level spectra shows a ligand to metal charge transfer. This happens when an electron from the O2p transfers to the unoccupied 4f level of the rare earth (Tb)[162]. Although the binding energy of the $3d_{5/2}$ (1242.5eV) is still higher from the standard peak for $Tb3d_{5/2}$ that appears at 1241.2eV in Tb_2O_3 where Tb ions exists in the +3 oxidation state. This is because the distance between the Tb—O in Tb_2O_3 is different from that of Tb—O in ZnO. The appearance of $3d_{5/2}$ peak on the higher energy side seems more likely because of the Tb^{+4} ions in the ZnO matrix, which is in complete accordance with the earlier study[182].

Since the XPS analysis of Tb is very rare and also there is no unique agreement on the oxidation states of Tb that correspond to a certain unique value. For example Rodrigo et al[183] doped gadolinium oxide with Tb and obtained the peak at 1242eV for $Tb3d_{5/2}$ and attributed the peak to the +3 oxidation state of Tb. The $Tb3d_{5/2}$ peak for Tb^{+3} ions appears at 1239.1eV if used as an external dopant in $LiAl_5O_8$ [179] and if it is used as a dopant in ZnO nanorods synthesised through electrochemical deposition the peak for $Tb3d_{5/2}$ appears at 1242.4eV[184], which shows that it behaves differently if used as an extrinsic dopant in different host materials. Therefore it is necessary to make an analysis of the Tb4d spectrum, which is considered one of the most important parameter to distinguish the oxidation state of Tb in a host material[185].

The Tb4d spectra for all the three samples show very interesting features as shown in figure 5.5, such as for the sample T1000 there appears a single peak at 149eV, which confirms the +3 oxidation state of Tb. For the pellet sintered at 1200C (T1200) the main peak appears at the same binding energy of 149eV along with another peak on the higher binding energy side at 157eV. The appearance of the high binding energy peak at 157eV clearly indicates the trend of incorporation of Tb^{+4} species into the ZnO matrix. This is because usually Tb^{4+} ions have two photoelectron peaks at 150.5eV and at 157eV and Tb^{3+} ions have a single peak at 149 eV[185]. This shows that increase in annealing temperature increase the Tb^{4+} content in the ZnO matrix. After thermal evaporation of the pellet the peak shifts towards a higher binding energy side and appears at 150.5eV. The intensity of the peak at 149eV has significantly reduced, which shows that the Tb^{+3} species decreases. Additionally the peak at 157eV is more visible, which confirms the existence of both +3 and +4 oxidation states of Tb in the ZnO matrix[181].

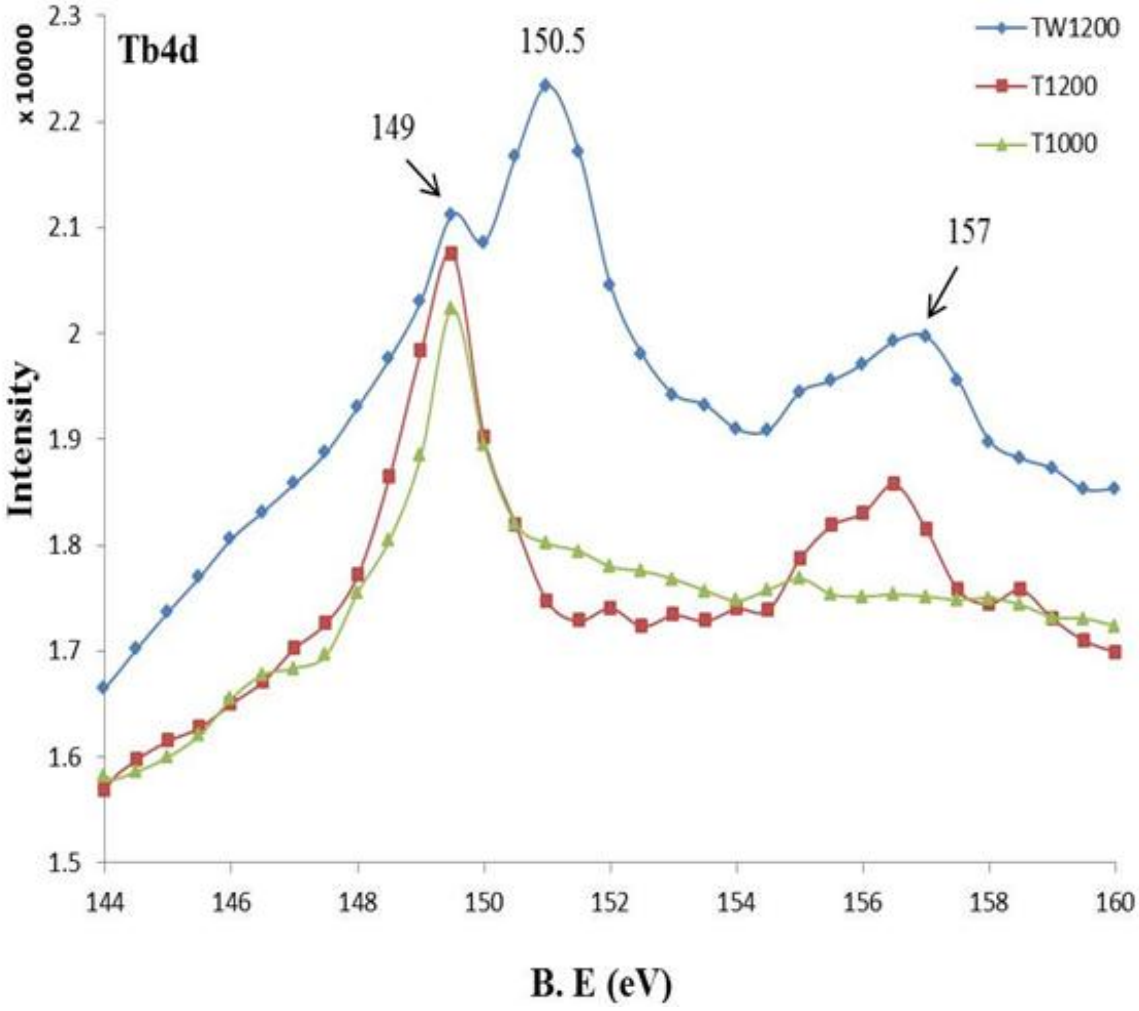

Figure 5.5 XPS Tb4d spectra for the pellets (red and green) and thermally evaporated (blue) samples. The blue spectrum clearly indicates the existence of Tb in both +3 and +4 oxidation state.

It is now well established from the analysis of the Tb3d and Tb4d core level XPS spectra that Tb exists in the sample in mixed oxidation states (+3 & +4). It has been observed through the XRD analysis for the samples T1000, T1050 and T1150 in section (5.4) that there exists a secondary phase of Tb_4O_7, which is a mixed valance oxide. To confirm that the mixed oxidation of Tb exists in the ZnO matrix rather than in the form of Tb_4O_7 it is necessary to carry out the XPS analysis of O1s core level spectra.

The XPS core level spectra for O1s were observed for all the three samples. The spectra are asymmetric with a peak for both the samples T1000 and T1200 appears at 530.1eV, but the shoulders appear at different binding energies, which are at 531.3eV for

T1000 and 530.9eV for T1200. This indicates that the sintering temperature of 1000C show somehow clustering behaviour that has been agglomerated on the surface and remained unreacted with ZnO. The sample T1200 shows a visible shoulder at 530.9eV that correspond to the oxygen in the ZnO matrix[186] as shown in the figure 5.6.

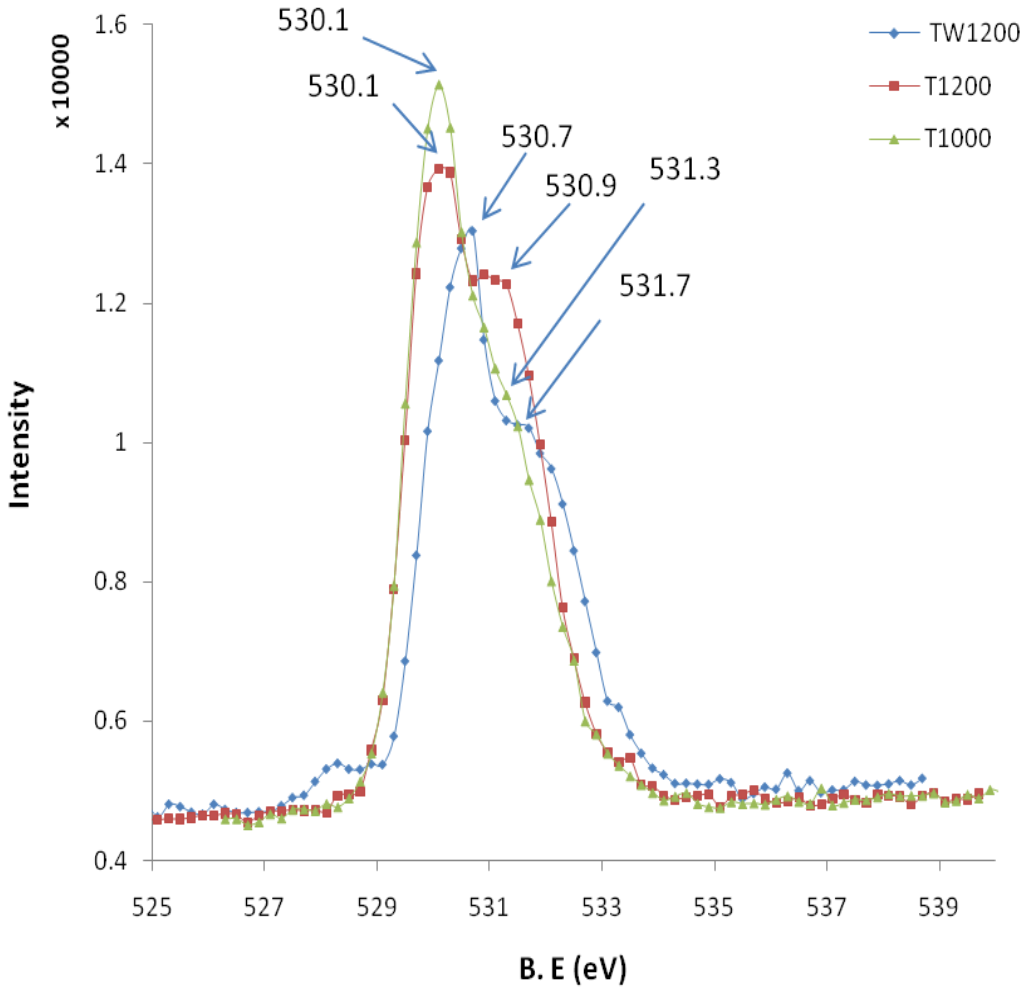

Figure 5.6 O1s core level XPS spectra for $Tb_{0.05}(ZnO)_{0.95}$. The spectrum represent a main peak at B.E=530.1eV and at 530.7eV for the pellet (red and green) and thermally evaporated (blue) samples respectively.

From both the peaks (530.1eV and 530.9eV) of the sample T1200 it is hoped that some Tb ions have been incorporated into the ZnO matrix and some of the terbium oxide still remain in the separate form, which correspond to the Tb_4O_7. This has not been detected by

XRD for the sample T1200 as discussed in section (5.4). This means that either this amount is too low for the XRD to detect or it exists just on the surface of the pellet. This shows that sintering temperature of 1200C increases the incorporation of Tb contents into the ZnO matrix. After thermal evaporation the behaviour of oxygen changes and the main peak shifts towards the higher binding energy side and appears at 530.7eV with the shoulder at 531.7eV. The main peak is attributed to the lattice oxygen in normal wurtzite structure[167] and that the shoulder peak of the sample TW1200 that appears at 531.7eV correspond to oxygen ions in the oxygen deficient regions[168]. The low intensity peak in the sample TW1200 at 528.5eV correspond to the surface oxygen, while the shoulder at higher binding energy side at 533.3eV correspond to the OH group attachment[208].

The XPS core level spectra for the $Zn2p_{3/2}$ were observed for all the three samples. For T1000 the peak appears at 1021.5eV, while for T1200 the peak shifts towards the lower binding energy and appears at 1021.3eV. The peak at binding energy of 1021.5eV corresponds to the Zn^{+1} state, while the peak at lower binding energy for T1200 corresponds to metallic Zn[170]. This confirms that when annealing at higher temperature the dopants replace the Zn in the ZnO matrix and because of the oxygen deficiencies the Zn remain in metallic form and lies on the surface of the pellet. After thermal evaporation of the pellet the peak for $Zn2p_{3/2}$ shifts towards the higher binding energy and appears at 1022.1eV, which shows the +2 oxidation state of the Zn in the ZnO matrix[170].

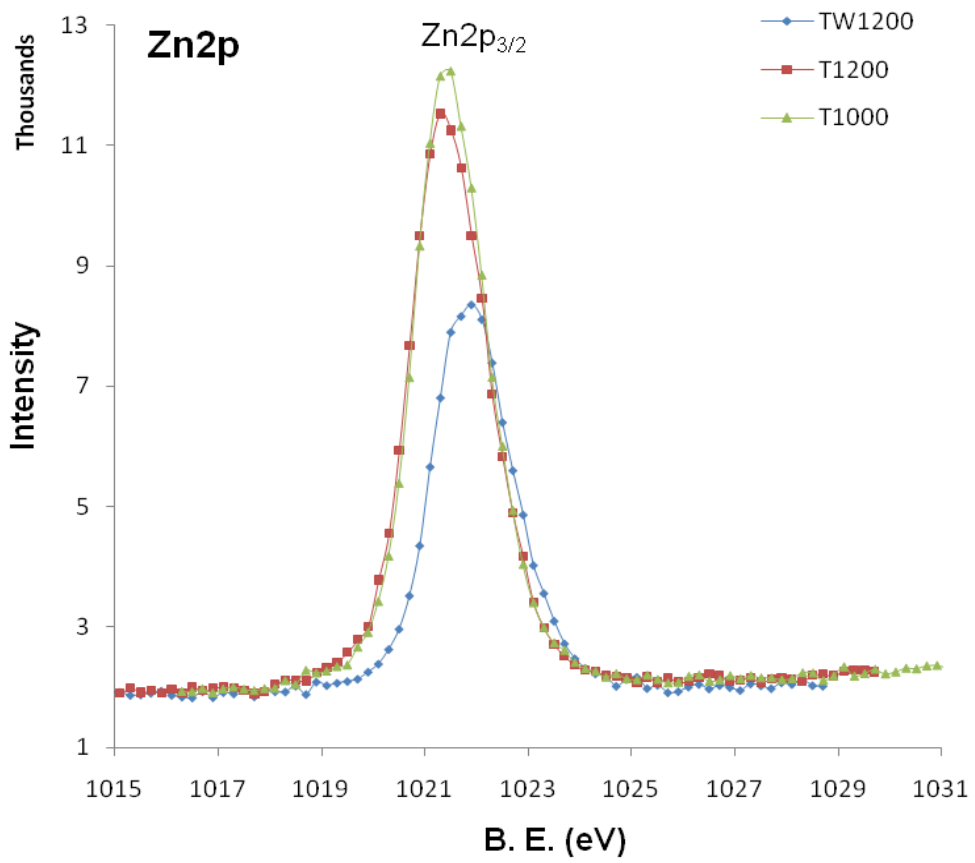

Figure 5.7 XPS core level spectra for Zn2p representing the main peak at B.E=1021.1eV, 1021.5eV and 1022.1eV for the samples T1000, T1200 and TW1200 respectively

From the XPS analysis of all the three samples for TbZnO, it can be concluded that the pellets prepared through solid state reaction are not completely doped. Because sintering at lower temperature the doping does not occur properly while at higher temperature clusters are formed and the material behave independently. However after thermal evaporation the doping is very successful and no clustering has been observed. Additionally the dopant ions in the ZnO matrix remain in the mixed oxidation states.

5.4): XRD analysis of TbZnO powder

All the four samples T1000, 1050C, 1150C and T1200 were then characterised through XRD with the XPERT-PRO diffractometer using Cu K_α source, to estimate some of the most important parameters of the mixed material such as the phase of the material,

crystallite size, lattice strain and the effect of doping upon the lattice constant of the ZnO. From the XRD pattern it has been observed that at lower sintering temperature a secondary phase corresponding to Tb_4O_7 appears but as the sintering temperature increases the peak that corresponds to Tb_4O_7 loses its intensity and disappears for the sample sintered at 1200C (T1200). There is only one phase detected that corresponds to the ZnO wurtzite structure in the sample T1200 and the other complex Tb_4O_7 gets incorporated into the ZnO matrix. This shows that the Tb_2O_3 is first converted into the Tb_4O_7 and then dissolved into ZnO to form a single phase solid sample of TbZnO, as shown in the figure 5.8.

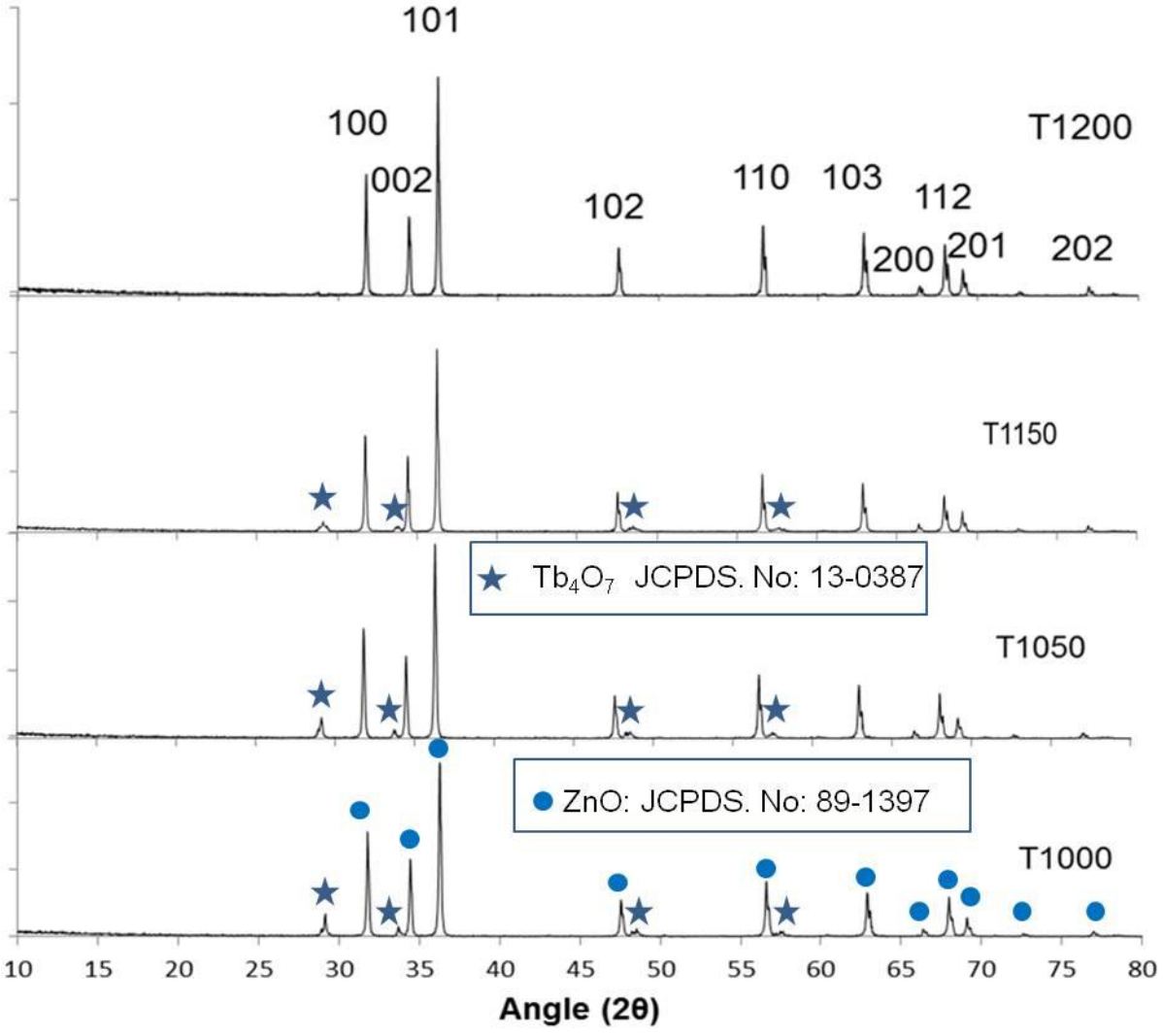

Figure 5.8 XRD spectra representing the phase of the $Tb_{0.05}(ZnO)_{0.95}$ powder sintered at various temperatures. The secondary phase is evident at lower temperatures and loses its intensity with increasing sintering temperature and completely vanishes at sintering temperature of 1200C.

The appearance of secondary phase at low temperature is because of the relatively higher ionic radii Tb^{+3} ions than that of the Zn^{+2} and causes a limited amount of ions to go into the ZnO matrix and some of the Tb_2O_3 remains unreacted which forms a complex of Tb_4O_7. This type of behaviour has been observed by Kim et al[187] and Cheng et al[188] and showed that the degree of replacement of the cation in the host material strongly depends upon the radius of the impurity ion. This secondary phase persists up to 1150C. This indicates that 1150C is not a sufficient temperature for 5wt% Tb_2O_3 to be incorporated fully into the ZnO matrix. Additionally at a sintering temperature of 1150C the crystallite size decreases, which confirms the incorporation of Tb ions into the ZnO matrix. This is because the incorporation of Tb ions inhibits the grain growth[191].

The lattice parameter for the sample T1000 and T1050 remains unchanged, while it increases for the other samples (T1150 & T1200). Furthermore the large crystallite size of the sample T1050 seems to be because of the diffusion of smaller crystallites into one another to form larger grains[155]. Upon further increasing the sintering temperature the ZnO lattice accommodates further Tb ions thereby increasing the lattice parameter[189]. The lattice parameter of a semiconductor usually depends upon[190].

(i): The concentration of free electrons present in the conduction band minimum acting via deformation potential.

(ii): The presence of defects and the concentration of impurity atoms and the difference between the ionic radii of the impurity atom and that of the host material.

(iii): External strain usually produced by a substrate on which the material is deposited.

(iv): Temperature

Interestingly at sintering temperature of 1200C the two parameters (crystallite size and the lattice strain) decreases, while the lattice constant increases. This might be because, the higher sintering temperature of 1200C further oxidises the Tb^{+3} ions into Tb^{+4} ions, which have relatively smaller ionic radii and it is easier for the ions to inter the ZnO matrix. Additionally the incorporation of Tb ions with increased oxidation state inhibits the grain growth and results in smaller crystallite size[191]. This is why the lattice strain and the crystallite size decreases for the sample T1200. The increase in the lattice constant might be because of the excess oxygen absorbed due to the higher sintering temperature[192] or it might be because of the excess presence of dopant ions in the matrix[190]. This is in complete

accordance with the XPS analysis described in section (5.3). The XPS analysis of the samples shows the existence of both the +3 and +4 oxidation state of the Tb ions in the ZnO matrix and the +3 content of Tb decreases with increase in sintering temperature, and because of the smaller ionic radii of the later produces less strain and less polarity. The behaviour of the samples as a function of temperature and dopant ions signals towards two very interesting points.

(i): The crystallite size will increase and the lattice strain will decrease with increasing sintering temperature if the oxidation state of dopant ions remains unaltered.

(ii): The smaller crystallite size and the smaller lattice strain at higher sintering temperature of 1200C correspond to the presence of the large amount of Tb ions with +4 oxidation state in the ZnO matrix.

These points could be supported with two arguments. One is that if we look at the XRD pattern [figure 5.8] the extra peak that corresponds to the Tb_4O_7 phase disappears at a temperature of 1200C, which means that the sample corresponds to a material with one crystal structure. The other is that the contraction of Tb ions inhibits the crystallite size[193]. Therefore it is strongly believed that majority of the dopants have a +4 oxidation state in the ZnO matrix. The lattice parameters *a* and *c* were calculated from the XRD pattern using the equation[194].

$$\frac{1}{d^2} = \frac{4}{3}\left[\frac{h^2 + hk + k^2}{a^2}\right] + \frac{l^2}{c^2} \qquad (3.8)$$

The full width at half maximum (FWHM) of the diffraction peaks decreases at 1050C and then increases with sintering temperature. The broadening of XRD lines, i.e. FWHM is mainly caused by microstructural imperfections that diffract the x-ray beam incoherently. These microstructural imperfections give rise to microstrain, which is mainly because of the stacking fault or any impurity in the crystal lattice[194]. Additionally the incorporation of bigger ions into the ZnO host material causes an increase in the lattice strain[157]. The change in the FWHM of the XRD lines might be because of the two reasons,

i): One is that at 1050C the Tb_2O_3 just transforms into Tb_4O_7 without going into the ZnO matrix. So this temperature is used to improve the crystallinity of the ZnO powder.

ii): The other is that the increase in the FWHM at higher sintering temperature (at 1150C and 1200C) is because of the incorporation of dopant ions into the ZnO matrix. The intensity of the secondary phase corresponding to Tb_4O_7 decreases and vanishes at 1200C, which is quite evident from figure 5.8.

Williamson-Hall model was used to estimate the microstrain from the graph of $4sin\theta$ *vs* $\beta cos\theta$ observed from the seven different orientations of the ZnO crystal planes, like (100), (002), (101), (102), (110), (103) and (112). A straight line was then fitted to the data and the slope of the linear fit then gives rise to lattice strain as shown in following figure 5.9.

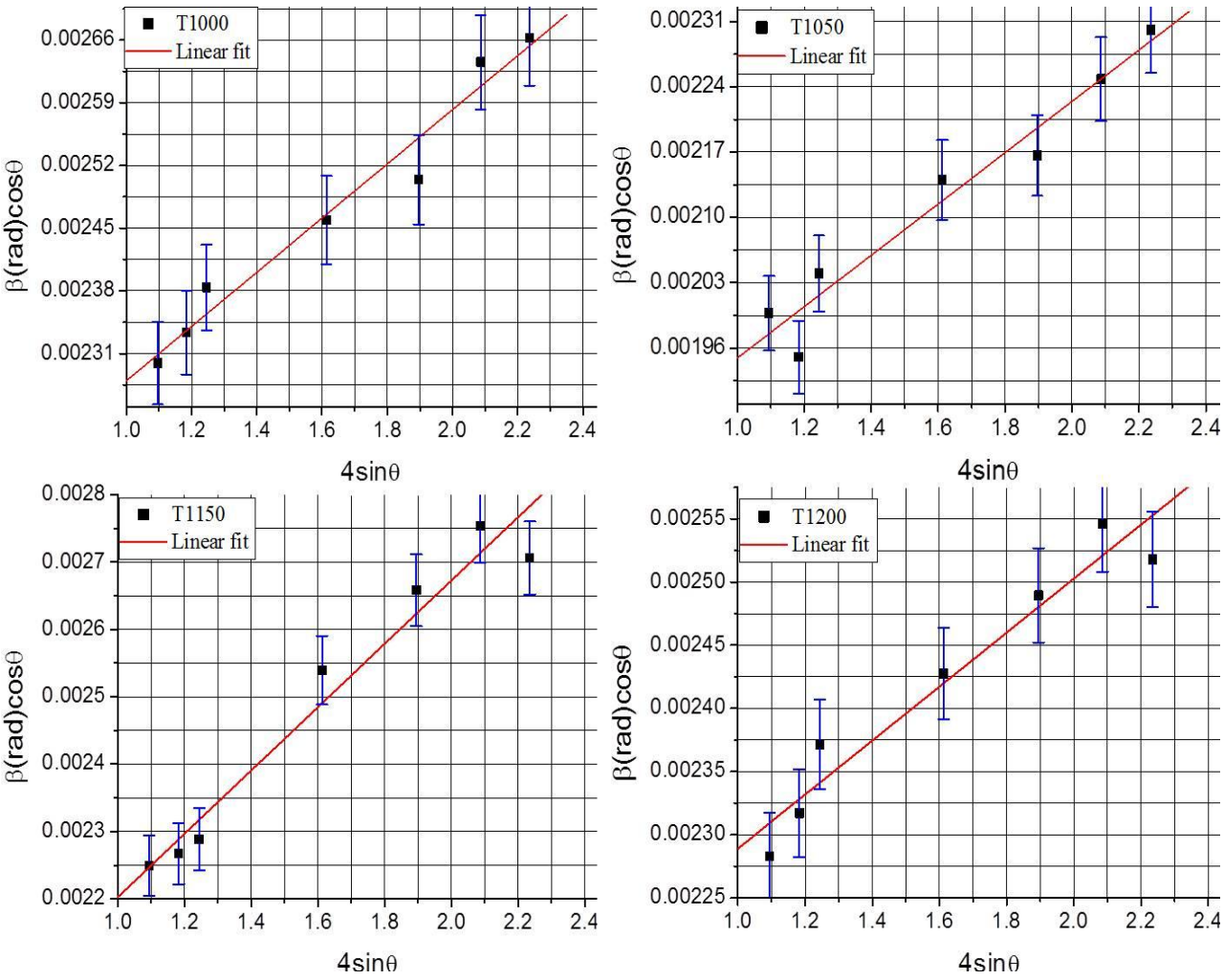

Figure 5.9 Williamson-Hall plots obtained from $Tb_{0.05}ZnO_{0.95}$ powders sintered at different temperature.

The crystallite size for the dominant peak representing the (101) plane of the XRD spectra in figure 5.8 were calculated using the Scherer's formula given by Eq (4.2) and has been given in table 5.2.

$$D = \frac{0.9\lambda}{\beta(rad)cos\theta} \qquad (4.2)$$

The crystallite size increases with temperature but reduces for the sample T1200. This shows that the crystallite size is more dopant dependent rather than temperature dependent.

Sintering temperature	Lattice strain	Crystallite Size	Lattice constant (nm)
1000C	3×10^{-4}	59.23nm +/-5nm	a = 0.3245 c = 0.5199
1050C	2.8×10^{-4}	68.27nm +/-5nm	a = 0.3245 c = 0.5199
1150C	5×10^{-4}	60.52nm +/-5nm	a = 0.3249 c = 0.5205
1200C	2.3×10^{-4}	58.35nm +/-5nm	a = 0.3251 c = 0.5208

Table 5.2 lattice strain, crystallite size and lattice parameter of $Tb_{0.05}ZnO_{0.95}$ samples sintered at 1000C, 1050C, 1150C and 1200C.

5.5): SEM and EDS studies of SmZnO

The powders of SmO and ZnO were mixed and were pressed to make pellets and were then sintered through a range of temperatures like 1000C and 1200C and were named after the sintering temperature e.g. Sm1000 and Sm1200. The pellets were then characterised through SEM to observe the surface morphology and the size distribution of grains. The

grains are quite huge with sizes up to 10µm with various shapes. The grain sizes of T1200 pellet are much smaller than that of Sm1200 although both were sintered at 1200C for 14 hours, which shows that crystallite size is not the only function of temperature but strongly depends upon the dopants as well. The surface of the pellet were then characterised through EDS to see the elemental composition and the quantity of each element present. The analysis confirms the existence of Sm, Zn and O. Clusters of Sm complexes are observed on the surface of the pellet, which clearly indicates that Sm has not been fully incorporated into the ZnO matrix.

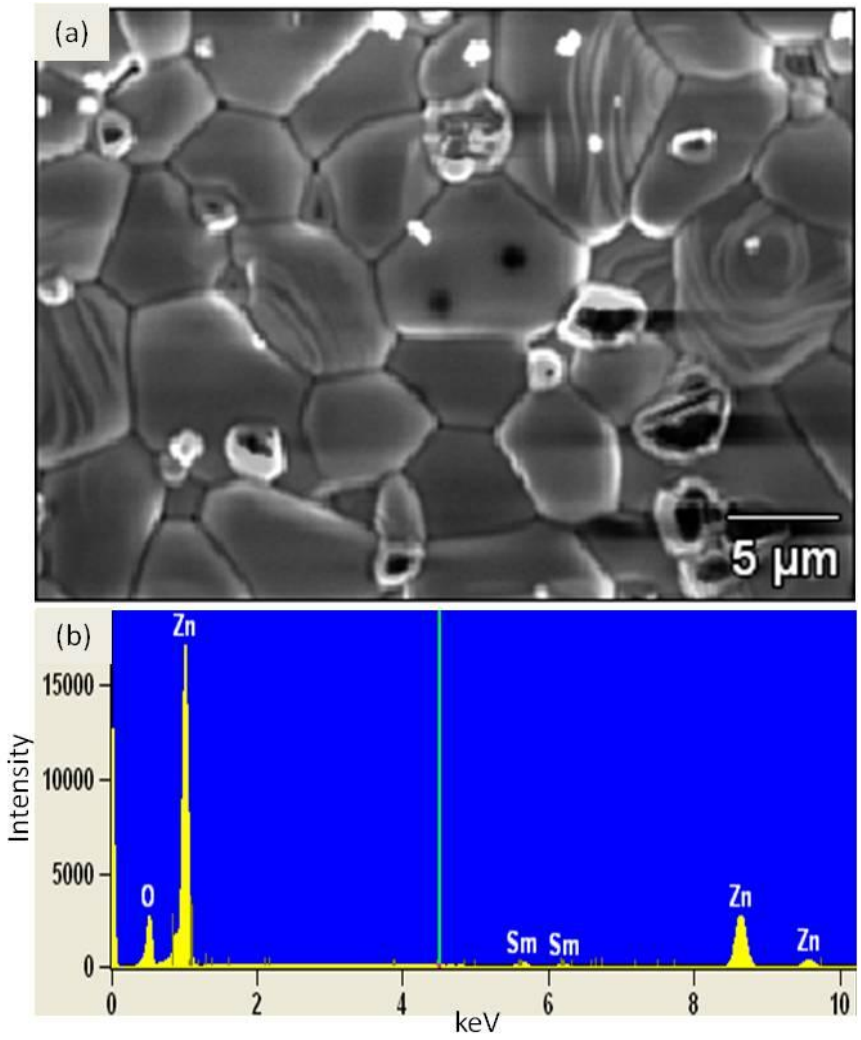

Figure 5.10 (a) SEM image of the pellet S1200. The image shows the size and shape distribution of grains of $Sm_{0.05}(ZnO)_{0.95}$. (b) The corresponding EDS spectra indicating the elemental composition of the pellet sintered at 1200C.

Element Line	Weight %	Weight % Error	Atom %	Formula
O K	23.3	+/- 0.2	55.7	O
Zn K	71.9	+/- 0.7	43.8	Zn
Sm L	4.8	+/- 0.3	0.5	Sm
Total	100.0		100.0	

Table 5.3 Quantitative analysis of $Sm_{0.05}(ZnO)_{0.95}$ pellet sintered at 1200C.

The pellets were then thermally evaporated on a Cr coated W substrate and it was observed that the pellets evaporate in the form of grains. These grains are of uniform sizes and shape of all the pellets. The grains in both the samples are quite mixed with one another and do not show any sharp geometry. The grains of the pellet sintered at 1200C gives rise to clusters upon thermal evaporation while that of the pellet sintered at 1000C are still uniform with less coalescence as shown in figure 5.11. The coalescence is because of the strong interaction between the smaller crystallites with large amount of defects[155].

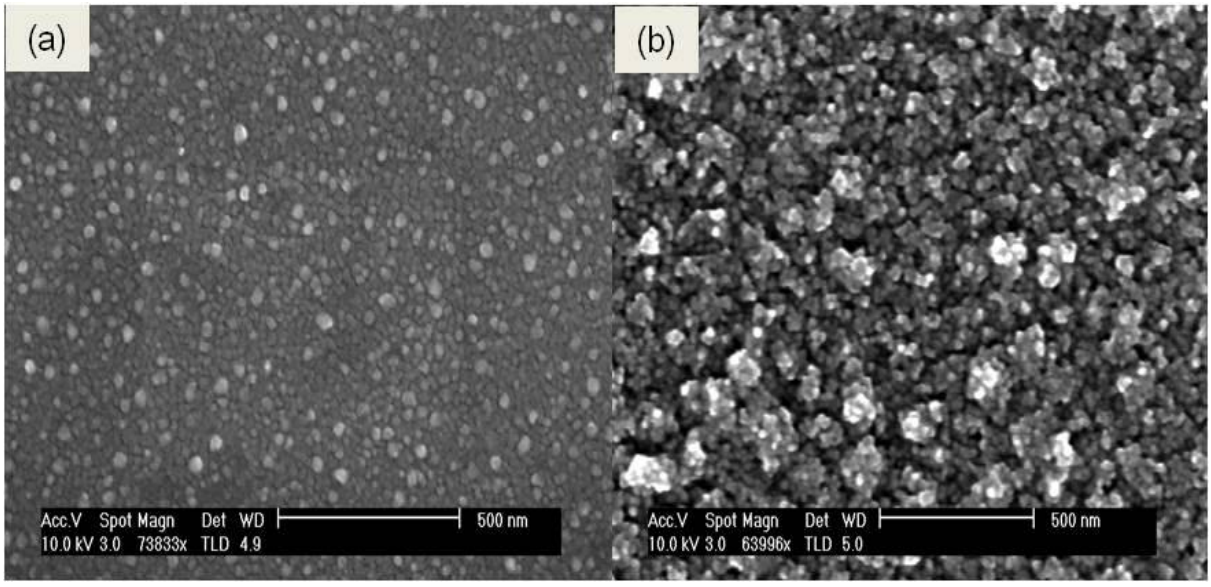

Figure 5.11 SEM image showing the size and shape distribution of grains of the thermally evaporated pellets on the W substrates (a) sintered at 1000C (b) sintered at 1200C

The grains were then characterised through TEM to confirm the nature of grains. These were scrapped from the W substrate through tweezers and put on the copper grid. The TEM analysis shows that the grains are highly crystalline with the lattice parameter of about 0.5206nm that correspond to the c-axis of the ZnO. This is shown in the figure 5.12.

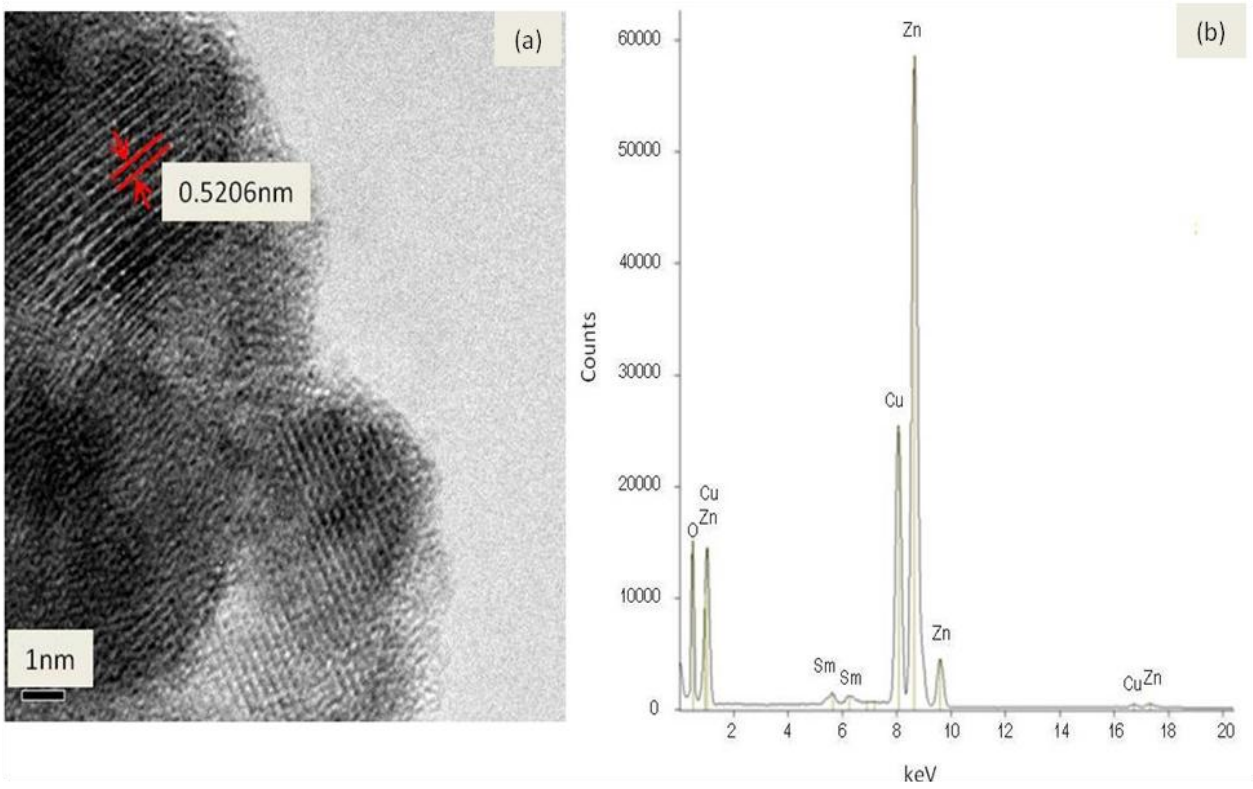

Figure 5.12 HRTEM image of grains taken from a thermally evaporated pellet sintered at 1200C indicating the lattice parameter of about 0.5206nm. (b); EDS spectrum showing the presence of Sm ions in the grain.

The existence of the dopant was then investigated through EDS in the TEM. The EDS analysis of the grain shows that Sm ions have been incorporated into the ZnO matrix. This confirms that after the thermal evaporation the SmZnO pellet the dopants have been incorporated into the ZnO matrix. The copper peak observed in the EDS spectrum is because of the copper grid. It could be concluded that ZnO grains have been successfully doped with Sm ions.

5.6): XPS analysis of SmZnO catalysts.

The analysis of Sm3d was carried out to observe the oxidation state of Samarium in the ZnO. It was observed that the $Sm3d_{5/2}$ peak for the samples sintered at 1000C and that at 1150C appear at the same binding energy of 1083.6eV, which corresponds to Sm^{+3} oxidation state [195] and the $3d_{3/2}$ peak for both the samples appear at 1110.6eV. This is very similar behaviour for the Sm in the Sm_2O_3 compound. But here the observed difference is the energy difference between the two peaks, which is 27eV while that for Sm_2O_3 is 27.6eV[196]. The peaks shift towards the higher binding energy side for the samples sintered at 1200C and appear at 1083.8eV and 1110.8eV respectively. But the energy difference for both the peaks remains constant (i.e 27eV). This indicates a strong spin orbit splitting, but the multiplets are not resolved properly, which shows a weak exchange interaction between the d—f orbitals in Sm doped ZnO. The other is that for charge transfer transition to happen [either from metal to ligand or from ligand to metal] the energy difference between the two 3d peaks should be constant[197]. The energy difference between the two 3d peaks is quite constant for the pellet samples (S1000, S1150 and S1200), which is 27eV.

There is a different trend observed for the thermally evaporated sample. The $3d_{5/2}$ peaks shifts more towards the higher binding energy with no peak on the lower binding energy side, indicating the full contribution of Sm^{+3} ions in the ZnO matrix. This effect has been confirmed by XRD analysis of the samples discussed in section (5.7), where it shows that the microstrain decreases and the crystallite size increases with increasing sintering temperature [table (5.4)]. This clearly confirms that the higher sintering temperature does not change further the oxidation state of Sm ions and these dopant ions remain in the +3 oxidation state in the ZnO matrix.

The very interesting behaviour observed from the spectra in figure (5.13a) is the peak broadening with the increase in sintering temperature, The full width at half maximum (FWHM) for the sample Sm1000, Sm1150, for Sm1200 [figure 5.13a] are 3.7eV, 3.86eV and 4.2eV respectively and that for SW1200 [figure (5.13,b)] is 4.4eV. This clearly shows the oxidative behaviour and especially the sample SW1200 confirms that the nanoparticles have not been reduced after thermal evaporation[164]. The intensity ratio of the $3d_{3/2}$ to $3d_{5/2}$ almost remains constant at 0.5 for all the samples. The FWHM for the metallic Sm is 2.8eV[198] and that the ratio of $3d_{3/2}$ to $3d_{5/2}$ remains at about 0.67[198]. Additionally the binding energy peak

of Sm $3d_{5/2}$ for metallic samarium appears at 1081.1eV[199]. These effects clearly rule out the possibility of the existence of metallic Sm on the surface.

The most important behaviour of all the pellet samples is the appearance of the peak at the lower binding energy side. The peak on the lower binding energy side from the main $3d_{5/2}$ peak has two possibilities, either it corresponds to the Sm^{+2} oxidation state or is the shake-down satellite peak. The intensity of this peak remains the same for the pellet sintered at 1000C and at 1150C but loses its intensity in the sample sintered at 1200C and completely vanishes after the thermal evaporation. In this study the peak is attributed to the shake-down satellite structure, because of the two reasons.

(i) This behaviour appears in the pellet samples that behaves like a bulk of Sm doped ZnO material. It is believed that Sm atoms in the bulk remain in trivalent state[200].

(ii) (ii): The core-level separation between the divalent and trivalent states of Sm remains of the order of 7.6eV[201], while the observed difference in our case between the main peak and that the peak on the lower binding energy side is 11.4eV.

With the belief that the peak on the lower binding energy side corresponds to the shake down satellite structures, there are two possible mechanisms for their description. One that is proposed by Burroughs et al[202] according to which the shake-down satellite structures are due to the energy gain process, when an electron transfer occurs from the ligand to the metal 4f ion. But this mechanism does not seem to be applicable here because if the electron transfer occurs from O_{2p} (which is the valance band of oxygen) to the 4f of Sm the energy difference between the main peak and shake-down peak should not exceed 3.0eV—5.0eV[203]. Where the energy difference between the Sm3d main peak and that the shake down satellite in our case is 11.4eV.

Another mechanism is proposed by Crecelius et al[204], according to which the shake down satellite structures are due to the jump of an electron from the 5d conduction band to the 4f level. This mechanism seems quite suitable because the amount of energy required to remove an electron from the 4f level to Fermi energy level is comparable to the electron energy that jumps from 5d to 4f level. This clearly shows that there is no Sm in the +2 oxidation state.

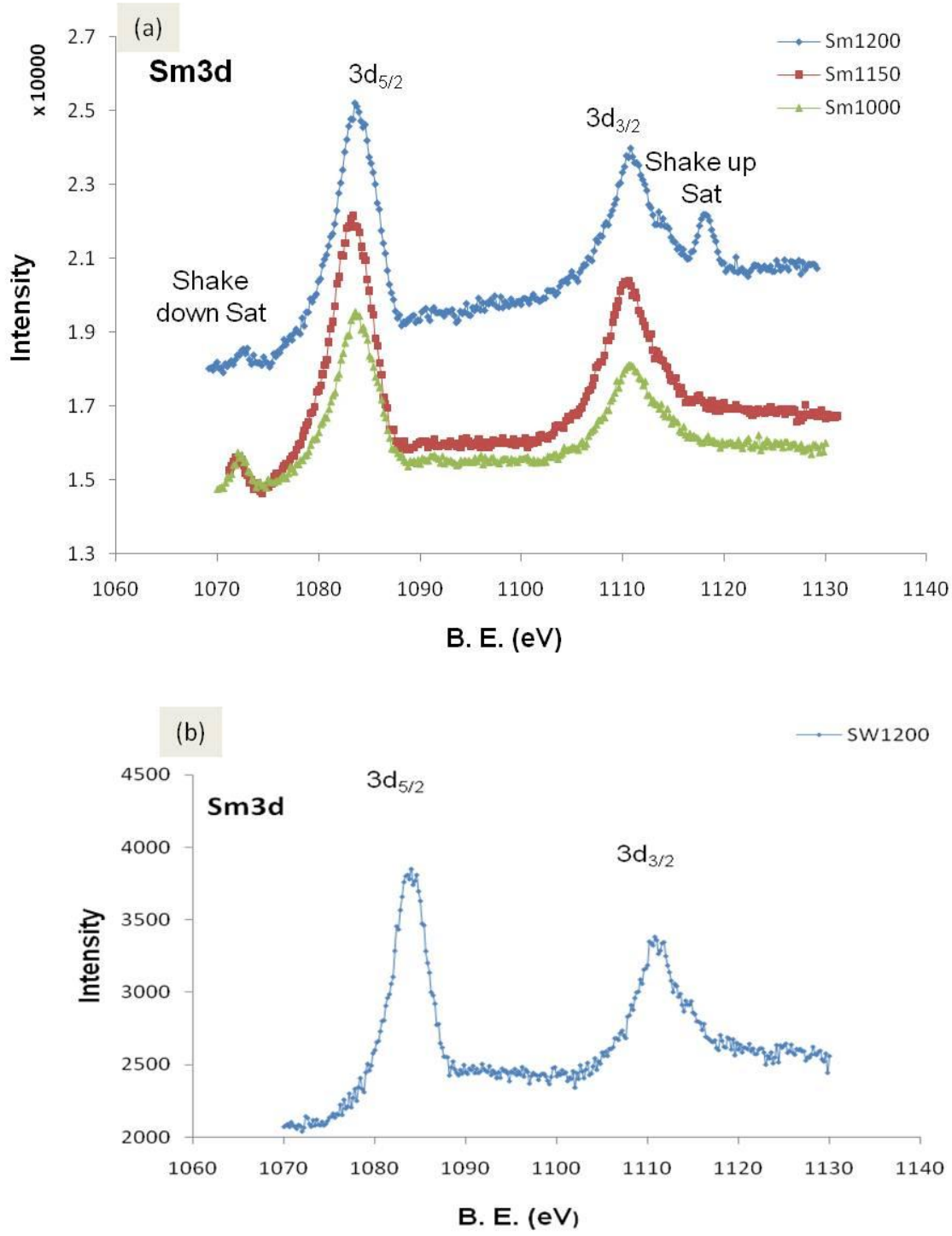

Figure 5.13 (a): 3d core level XPS spectra of $Sm_{0.05}ZnO_{0.95}$ pellets sintered at 1000C (green) at 1150C (red) and 1200C (blue). The main peak corresponds to $3d_{5/2}$ and the smaller peak corresponds to $3d_{3/2}$. The smaller peak at the very left correspond to the shake down satellite (represented as shake down sat). The shakeup satellite (represented as shake up sat) only appears in the sample sintered at 1200C at the very right of the $3d_{3/2}$ peak. (b): 3d core level XPS spectra for the thermally evaporated pellets sintered at 1200C. The two main peaks at B.E=1084eV correspond to $3d_{5/2}$ and the smaller peak correspond at B.E= 1110.8eV corresponding to $3d_{3/2}$.

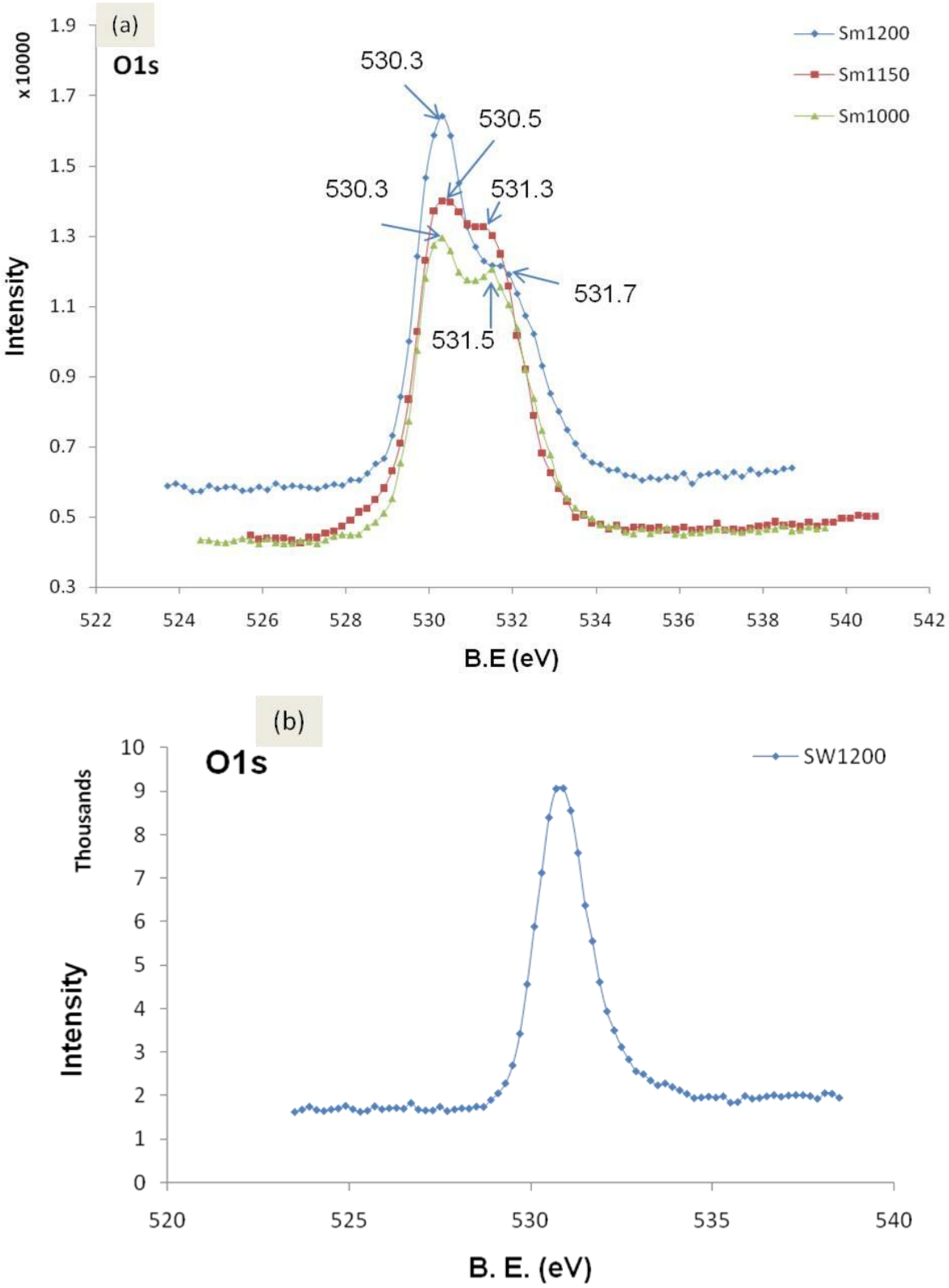

Figure 5.14 (a): O1s core level XPS spectra for the pellets sintered at 1000C, 1150C and 1200C. The main peaks correspond to the lattice oxygen and the shoulders correspond to the Oxygen ions in the oxygen eficient regions. (b): XPS core level spectra of O1s for the SW1200. The peak corresponding to B. E. = 530.9eV

O1s core level XPS spectra were obtained to understand the oxidation state of the Sm in the ZnO matrix. It was observed that O1s spectra for all the three samples is a convolution of two peaks that appears at 530.3eV and 531.5 for the sample Sm1000, at 530.5 and 531.3eV for the sample Sm1150 and that for the Sm1200 it appears at 530.3eV and 531.7eV. The main peak corresponds to the lattice oxygen in the bulk ZnO and the shoulder at higher binding energy is attributed to the Sm^{+3} — O[205]. After thermal evaporation of the pellet the O1s peak shifts towards the higher binding energy and appears at 530.9eV, which clearly corresponds to the oxygen in the ZnO matrix. The shift in the lower binding energy side is quite understandable, with the addition of Sm atoms into the ZnO matrix the O1s photoemission peak for Zn—O—Zn would be replaced by Zn—O—Sm and would lead to a lower binding energy. It is because the ionic radii for the Sm ions are larger than that of the Zn, which will lead to higher screening effect that result in lower binding energy[206].

The Zn core level peak profile of the XPS spectra for all the three samples are quite symmetric and show some reversible behaviour in their peak widths as shown in figure (5.15a). The FWHM for the sample sintered at 1000C is 1.55eV and that for the sample sintered at 1200C reduces to 1.45eV. After the thermal evaporation of the pellet the FWHM for the Zn spectra increases to 1.5eV. This shows that the pellet sintered at 1200C shows more metallic behaviour than the one sintered at 1000C for the same time. Additionally the thermal evaporation helps in doping the material and getting the oxidative behaviour back again[164]. All the three samples show photoemission peaks at different binding energies. The sample sintered at 1000C show a peak at 1021.5eV, the sample sintered at 1150C show a peak at 1021.3eV while that for the sample sintered at 1200C appears at 1021.7eV. This might be because of the existence of metallic Zn (Zn^0) and Zn^{+1} oxidation state on the pellet surface.

After thermal evaporation the peak shifts towards the higher binding energy and appears at 1022.3eV and also gets broadened that corresponds to the Zn in the +2 oxidation state as shown in figure 5.15b. Another interesting behaviour is the appearance of the shoulder at 1020.9eV that correspond to the Sm—Zn bonding. It is because the electronegativity of Sm (1.17) and Zn (1.65) is lower than oxygen (3.44)[207] therefore the bonding between these two elements will appear at the lower binding side. This clearly indicates that Sm ions have been successfully incorporated into the ZnO matrix. Similar behaviour has been observed by Huang et al[171] while doping ZnO with Ni.

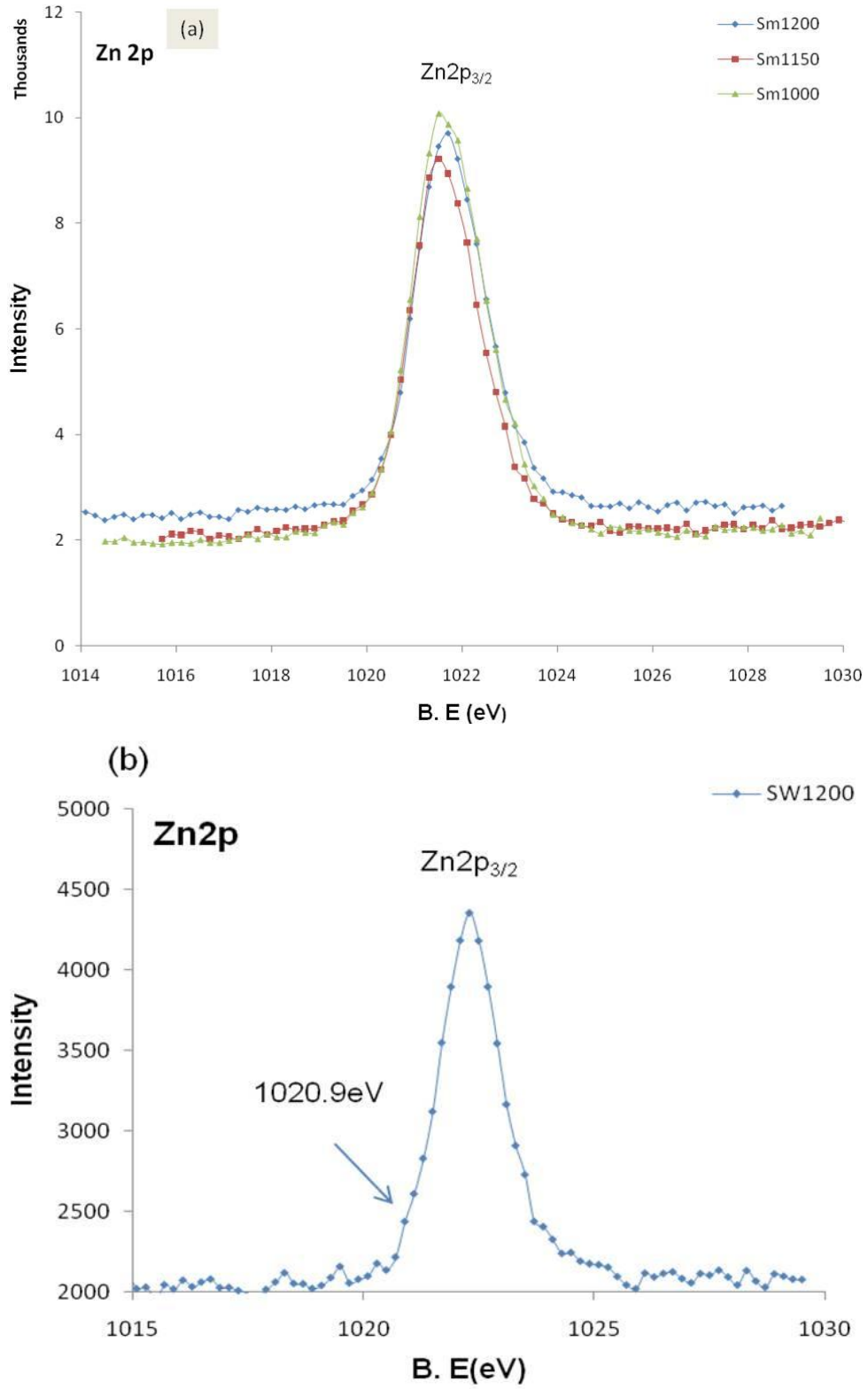

Figure 5.15 (a): XPS core level spectra of Zn2p for the samples sintered at 1000C (green), at 1150C (red) and sintered at 1200C (blue). (b): XPS core level spectra of Zn2p for the samples SW1200. The main peak for $Zn2p_{3/2}$ appears at 1022.3eV and the shoulder at 1020.9eV is attributed to the Sm—Zn bond.

5.7): XRD analysis of SmZnO

The Samarium doped ZnO was characterised through XRD for the phase identification and the behaviour of Samarium through solid state reaction. Two samples Sm1000 and Sm1200 that are named after its sintering temperature were characterised through XRD as shown in the figure 5.16.

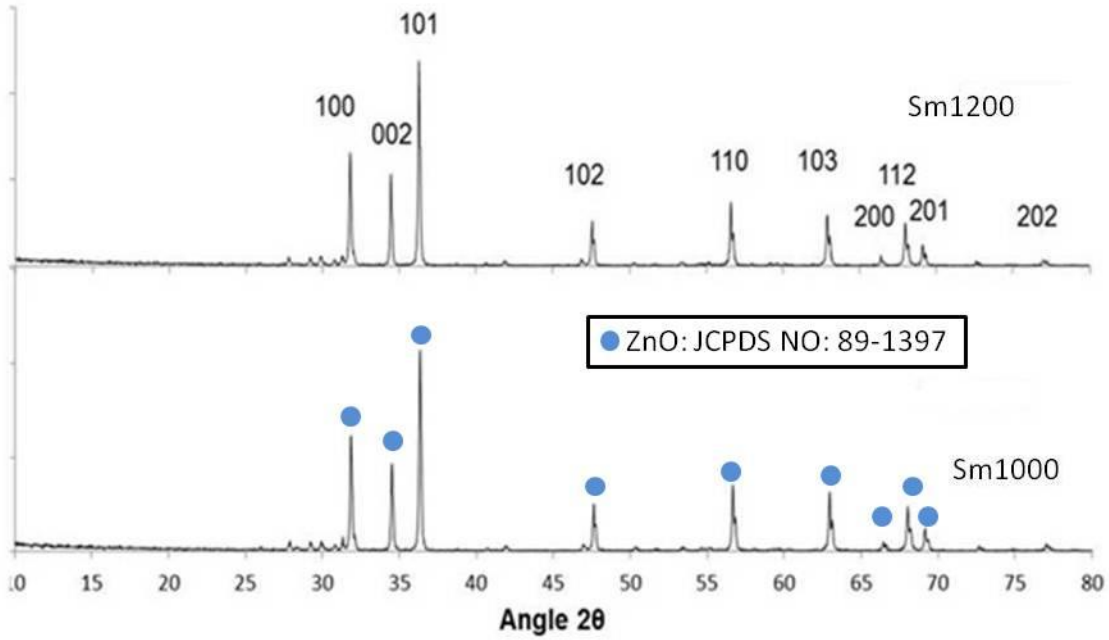

Figure 5.16 XRD analysis of the $Sm_{0.05}ZnO_{0.95}$ powder representing the phase identification of the powder sintered at 1000C and 1200C

Two phases have been observed from the XRD pattern, one that correspond to the wurtzite ZnO structure and the other correspond to the Sm_2O_3 phase. The XRD pattern indicates that Sm shows a very complex behaviour if sintered at 1000C and at 1200C with ZnO. At these temperatures the Sm ions do not go into the ZnO matrix completely and some of the SmO remains unreacted and appear in a separate phase and might form other Sm complexes like Sm_2O_3. It might be because of the bigger ionic radii of Sm^{+3} ions than Zn^{+2} and is hard for the ZnO to accommodate these ions. Lattice strain was calculated using the Williamson-Hall model (shown in figure 5.17) and it was observed that the incorporation of

Sm ions increases the lattice strain and also the lattice constant at 1000C. After increasing the sintering temperature to 1200C the crystallite size increases but the lattices strain decreases. This seems to be because of the two processes;

i): One is that there is no change in the oxidation state of the Sm ions at 1200C that could inhibit the grain growth and result in smaller crystallite size. This is because the increased oxidation state of dopants inhibits the grain growth[193].

ii): The other is that there is no further incorporation of Sm ions into the ZnO matrix that could increase the lattice strain. The increase in temperature from 1000C to 1200C seems to reduce the defects density thereby improving the crystallinity.

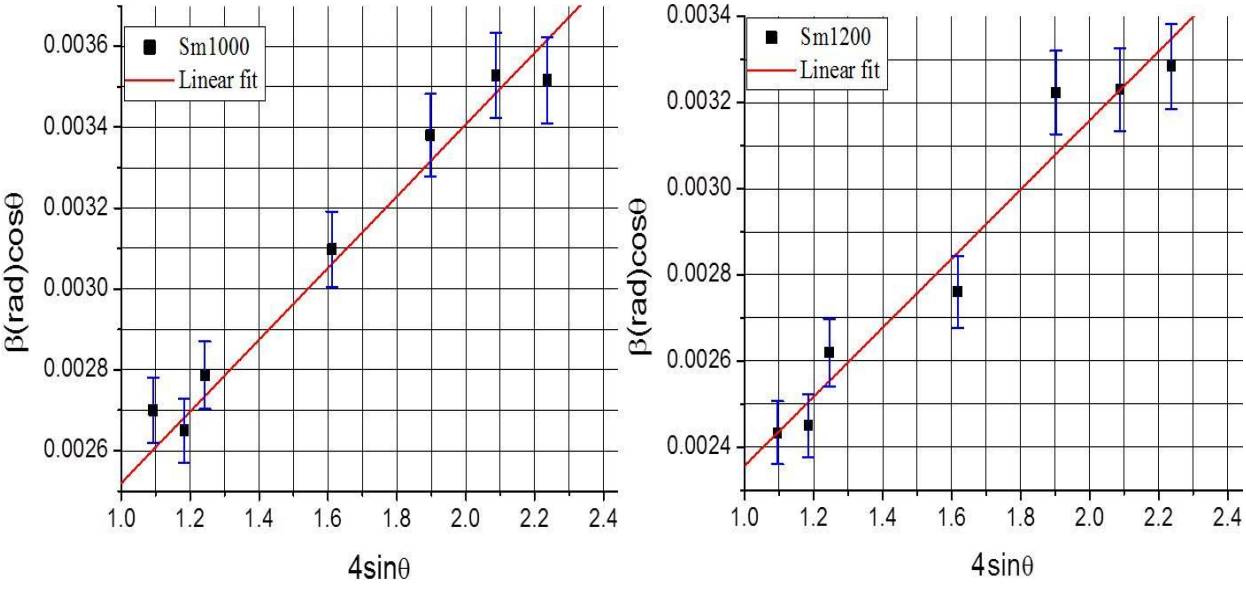

Figure 5.17 Williamson-Hall plot for the sample Sm1000 and Sm1200 obtained from the XRD peaks corresponding to seven different planes. The error bars correspond to 3% error in the FWHM of individual diffraction peak.

The particle size was calculated from the XRD peak of (101) plane using Scherer's formula and the lattice constant was calculated from the XRD pattern using Eq (4.2) and are summarised in table 5.4.

Sintering temperature	Lattice strain	Crystallite Size	Lattice constant (A^0)
1000C	8.75×10^{-4}	49nm +/-1nm	a = 3.2557 c = 5.2081
1200C	8×10^{-4}	53nm +/-1nm	a = 3.2456 c = 5.1992

Table 5.4 lattice strain, crystallite size and lattice parameter of $Sm_{0.05}ZnO_{0.95}$ samples sintered at 1000C and 1200C.

5.8): SEM and EDS studies HoZnO

The Ho_2O_3 with 5wt% was mixed with ZnO powder and four samples were prepared through solid state reaction with a range of sintering temperature of 1000C, 1050C, 1150C and 1200C. The samples sintered at 1000C are named as Ho1000, at 1050C as Ho1050, at 1150C as Ho1150 and at 1200C is named as Ho1200. The pellets were characterised through SEM to see the grain morphologies in the pellet. It was observed that there is no uniformity in shapes and in the sizes of the grains. No clusters corresponding to Ho were found on the surface of pellets as shown in the figure 5.18. The large distribution of grain sizes show that smaller crystallites have been diffused with one another to form bigger grains, which is believed to be due to the large amount of defects. These defects cause a strong interaction between the smaller crystallites and gives rise to bigger grains[155].

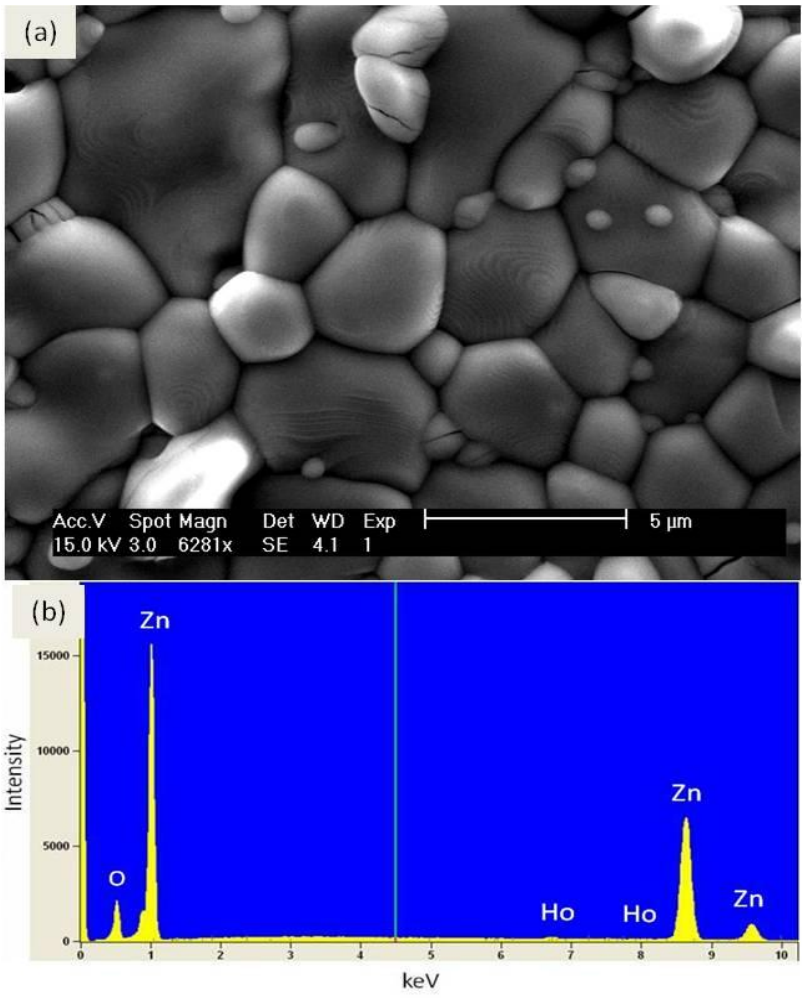

Figure 5.18 (a); SEM image of the $Ho_{0.05}ZnO_{0.95}$ pellet sintered at 1200C, indicating the size and shape distribution of grains. (b) The corresponding EDS spectra of the pellet for the elemental composition confirming the presence of Ho ions in the pellet.

Element Line	*Weight %*	*Weight % Error*	*Atom %*	*Formula*
O K	15.2	+/- 0.17	44.3	O
Zn K	80.1	+/- 0.48	55.	Zn
Zn L	---	---	---	
Ho L	4.7	+/- 0.27	0.6	Ho
Ho M	---	---	---	
Total	100.0		100.0	

Table 5.5 Quantitative analysis of $Ho_{0.05}ZnO_{0.95}$ pellet sintered at 1200C.

EDS analysis of the pellet confirms the presence of Ho, Zn and O. The observed quantity of Ho in the pellet is 4.7wt % ± 0.27%, which corresponds to the quantity that have been added to the ZnO powder. The quantity of each element present in the pellet is given in the table 5.5 with respect to its atomic and weight percent.

After the thermal evaporation of the pellets on Cr coated W substrate, no clusters of Ho were found on the surface and this has been confirmed through XPS as discussed in section (5.9). The grains of the pellet sintered at 1000C have very poor geometry, while the grains morphology improves with increasing sintering temperature. All the samples show almost similar behaviour regarding the grain size distribution upon thermal evaporation on the W substrate. The samples have some needle like structures (shown by red arrows) which usually happens because of the Zn termination and excess oxygen[153].

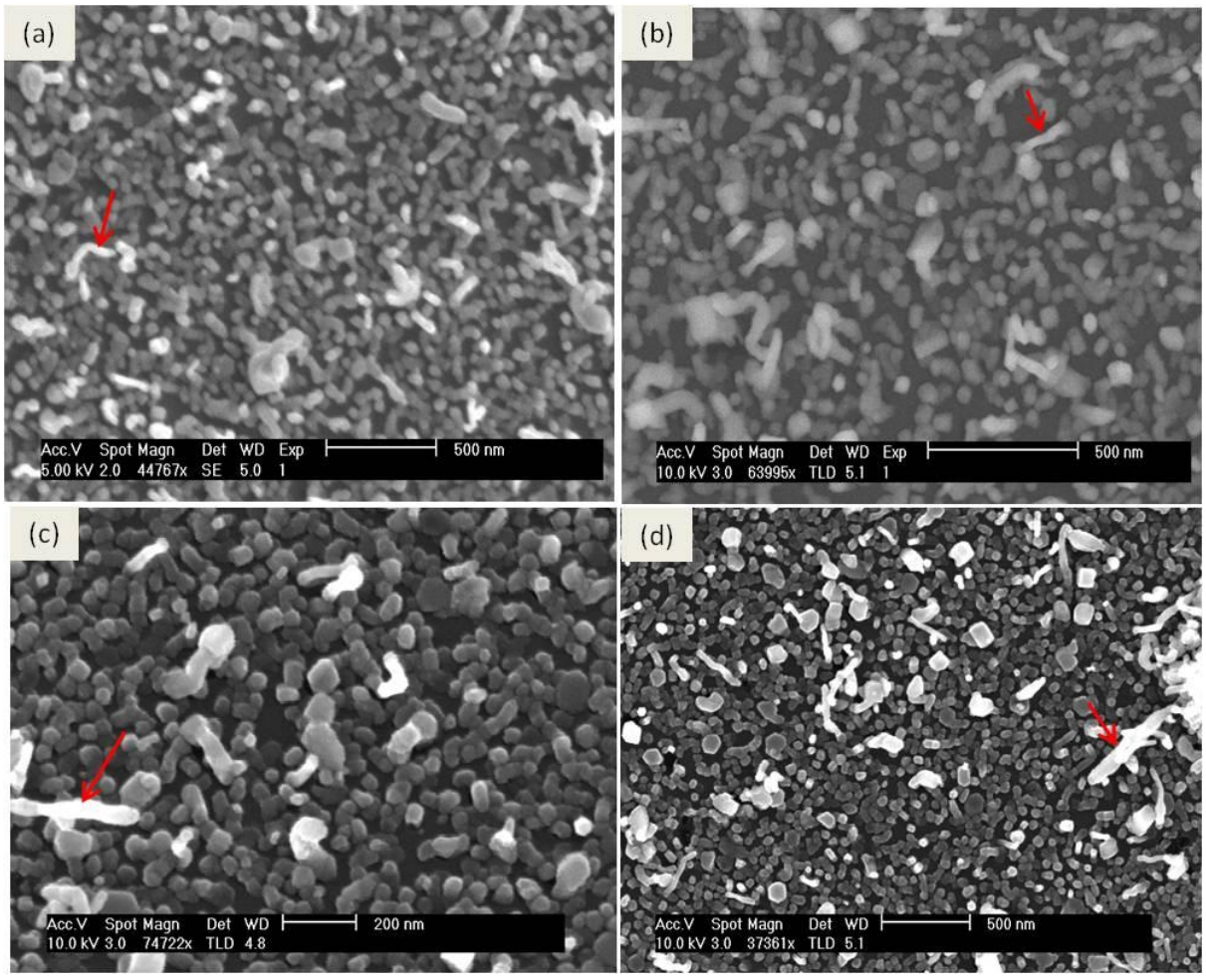

Figure 5.19 thermally evaporated pellets of HoZnO (a) sintered at 1000C and (b) sintered at 1050C (c) at 1150C and (d) at 1200C.

After thermal evaporation of the pellets the grains were scratched through tweezers to make a TEM sample. The grains were then examined through TEM (JEOL 2011) and are shown in the figure 5.20.

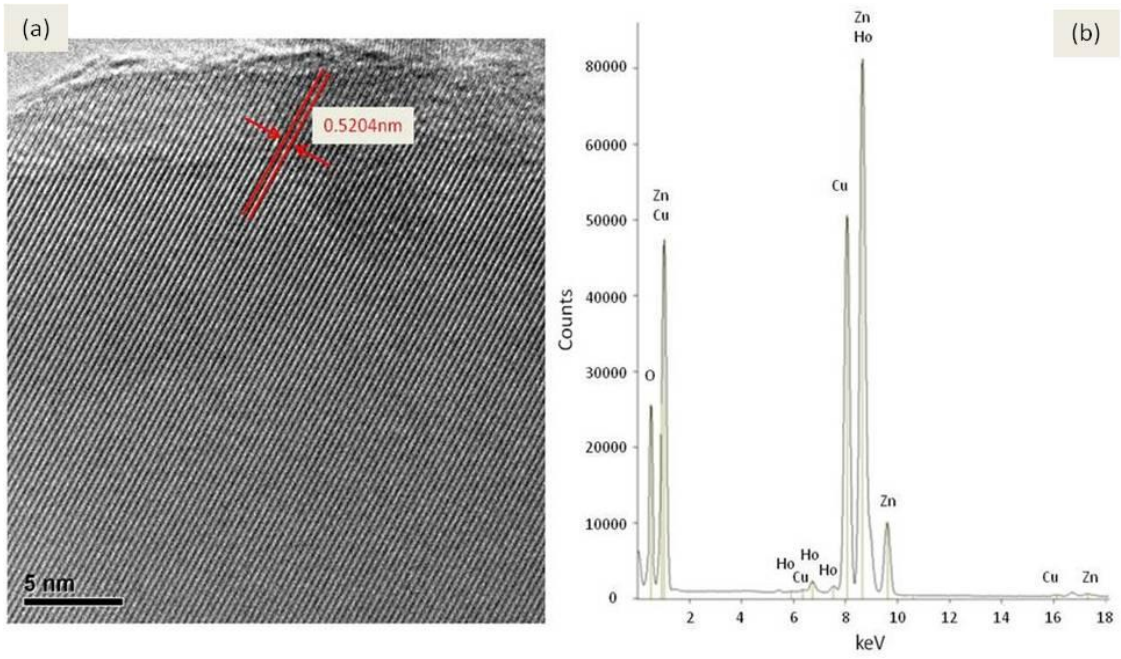

Figure 5.20 (a) HRTEM image of the thermally evaporated grain of HoZnO, showing the lattice parameters of about 0.5204nm, which corresponds to ZnO crystal lattice. The pellet was sintered at 1200C. (b); EDS spectrum that confirms the presence of Ho ions in the grain

The HRTEM image shows that the grains correspond to ZnO structure with lattice parameter of 0.5204nm, which correspond to the lattice constant *c* of ZnO, which is in good agreement with the lattice parameters observed from the XRD pattern shown in table 5.6. The grains were then analysed through EDS in the TEM to observe the elemental composition of the grains. It was observed that Ho ions have been incorporated into the ZnO matrix upon thermal evaporation.

5.9): XPS Characterization of HoZnO

ZnO was doped with 5wt% Ho_2O_3 through solid state reaction as discussed in section (4.2). Three samples were characterised through XPS to see the chemical state and chemical

environment of dopants in the ZnO matrix. Two of the samples are pellets and the third one is the thermally evaporated pellet on Cr coated W substrate.

The core level 4d peak for Ho was observed at the binding energy of 161.2eV for both the samples Ho1000 and Ho1200. After the thermal evaporation the peak shifts towards a higher binding energy and splits into doublet. One peak appears at 161.8eV and the other at 163.8eV as shown in figure 5.21. Usually Ho exists in the trivalent state, however the removal of one 4d electron causes perturbation and gives rise to multiplet structure in the XPS spectra, where the peaks appear at different energies. This is because of the various possible states of the $4d^9$ configuration. The splitting of the 4d peak into doublet therefore seems to be due to the multiplet splitting that occurs because of the interaction between the 4d holes and the 4f shell electrons and gives rise to $4d^9 4f^n$ final state configuration[208]. This multiplet splitting gives rise to a charge transfer process[162] that plays a key role in dissociating the hydrocarbon molecules.

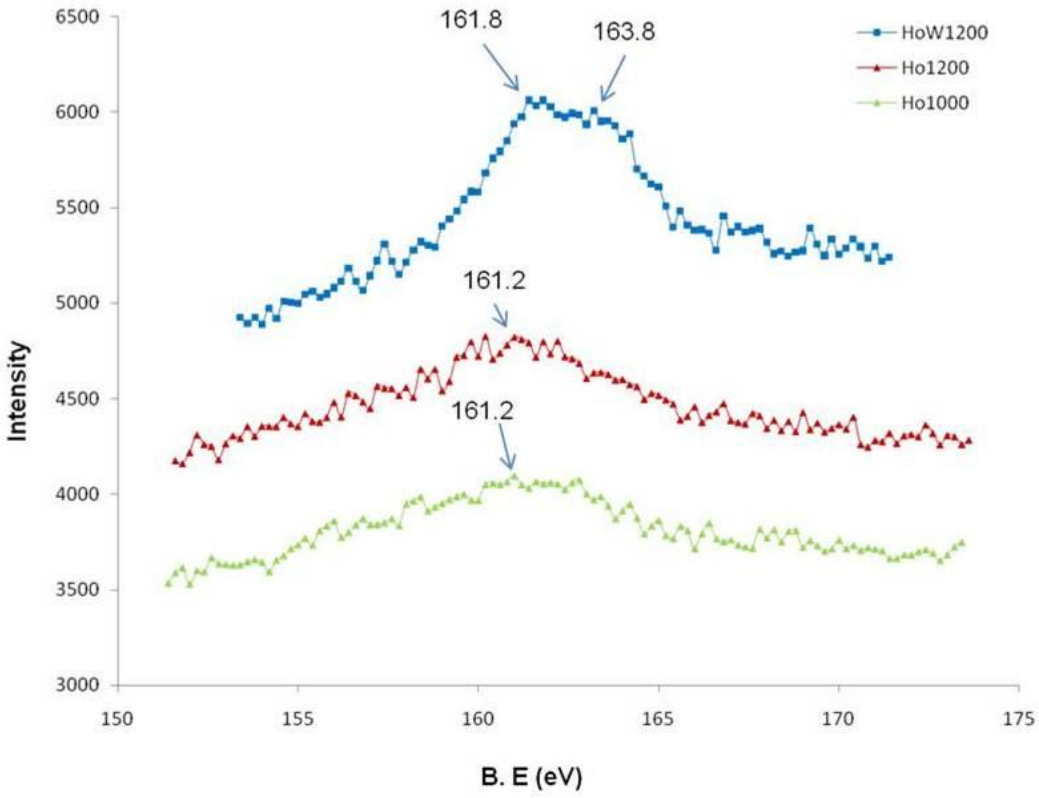

Figure 5.21 Ho4d spectra for the pellets sintered at 1000C and 1150C (green and red) and for the thermally evaporated sample (blue)

The Ho 4d spectra containing the un-paired 4f electrons are expected to exhibit multiplet splitting[209,210]. The interaction between the 4d and 4f is more complicated because of the coupling nature[203].

The O1s core level spectra for all the three samples is a convolution of two peaks as shown in figure 5.22. For the sample Ho1000 the main peak for O1s appears at 530.1eV. The peak shifts towards the higher binding energy side and appears at 530.5eV for the sample Ho1200. This shows that oxygen corresponds to two different compounds within the pellets. The peak at 530.1eV has two possibilities either it corresponds to $Ho(OH)_3$ as observed by Milligan et al[203], or it corresponds to Zn—O—Ho bonding in the bulk. The former has a very low probability because the XRD analysis of HoZnO powder [section 5.10] shows a secondary phase that corresponds to the hcp phase of Ho_2O_3. The latter seems more likely because the Ho has larger ionic radii than Zn and the Ho substitution of Zn will result in lower binding energy[206].

For the sample Ho1200 the main peak of O1s shifts towards the higher binding energy side and appears at 530.5eV. Singh et al[208] attributed the peak to the formation of Holmium oxide, which does not seem probable because the XRD analysis does not show any secondary phase for the sample Ho1200, even if it exists then the amount is negligibly small and it resides on the surface of the pellet. The following two seem to be the most likely reasons for the shift towards the higher binding energy (B.E) side,

i): One is that the higher sintering temperature decreases the covalent nature of the pellet, which results in higher binding energy[206].

ii): The other is that the higher sintering temperature increases the Ho^{+4} species in the ZnO matrix, which have relatively smaller ionic radii than Ho^{+3} and shifts the peak towards the higher binding energy[206]. This is quite evident from the Ho4d spectrum (blue spectrum) in figure 5.21.

The peaks at the higher B.E energy side at 531.5eV for both the samples are attributed to the formation of a surface hydroxyl group[206] or to the oxygen deficient regions[168]. After thermal evaporation of the pellet the main core level XPS peak for O1s shifts more towards a higher binding energy side and appears at 530.7eV, which corresponds to the oxygen in the ZnO matrix[167] and the shoulder peak corresponds to the oxygen ion in the oxygen deficient region[168]. This indicates that the grains on the Cr coated tungsten substrate have been properly doped.

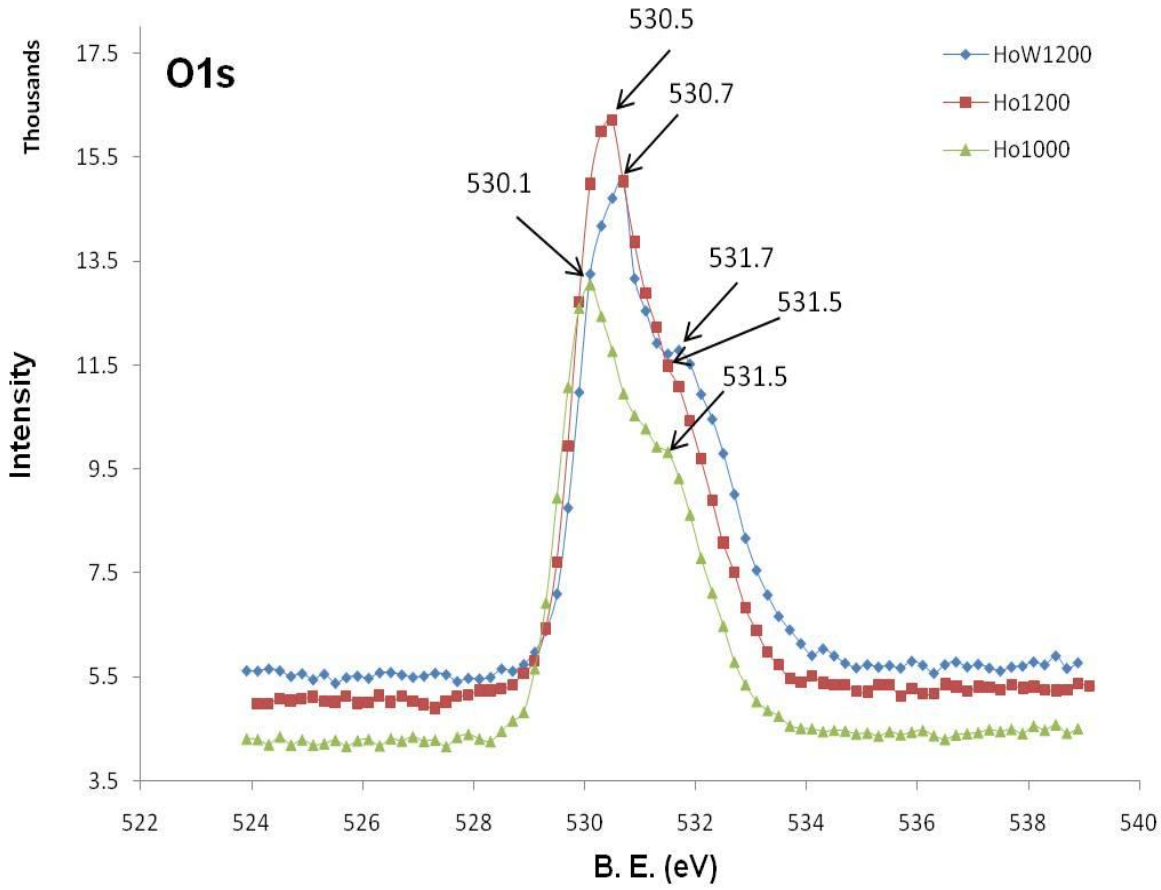

Figure 5.22 O1s XPS spectra for the pellets sintered at 1000C and 1150C (green and red) and for the thermally evaporated sample (blue). The main peaks correspond to the lattice oxygen and the shoulders correspond to the Oxygen ions in the oxygen deficient regions.

Core level XPS were performed for Zn2p to understand the chemical state of Zn in the Ho doped ZnO as shown in figure 5.23. It is observed that for the sample annealed at 1000C the peak for the Zn 2p is shifted towards the lower binding energy and appears at 1021.5eV, which shows that more Zn atoms are attached to oxygen and the sample is more Zn rich than oxygen rich[211]. The trend of the Zn2p peak changes with sintering temperature. The sample sintered at 1200C the peak appears at 1021.7eV and after thermal evaporation the peak appears at 1021.9eV, which corresponds to ZnO. The peak shift towards a higher binding energy side is a finger print towards +2 oxidation state of Zn.

A reversible behaviour in the FWHM has been observed. The Zn2p spectra for all the three samples sintered at 1000C, 1200C and thermally evaporated one the FWHM is 1.55eV, 1.53eV and 1.58eV respectively. This clearly indicates that after thermal evaporation of the

pellet that the Zn remain in oxide form. This rules out the possibility of the existence of the metallic Zn on the surface of the tungsten substrate[164].

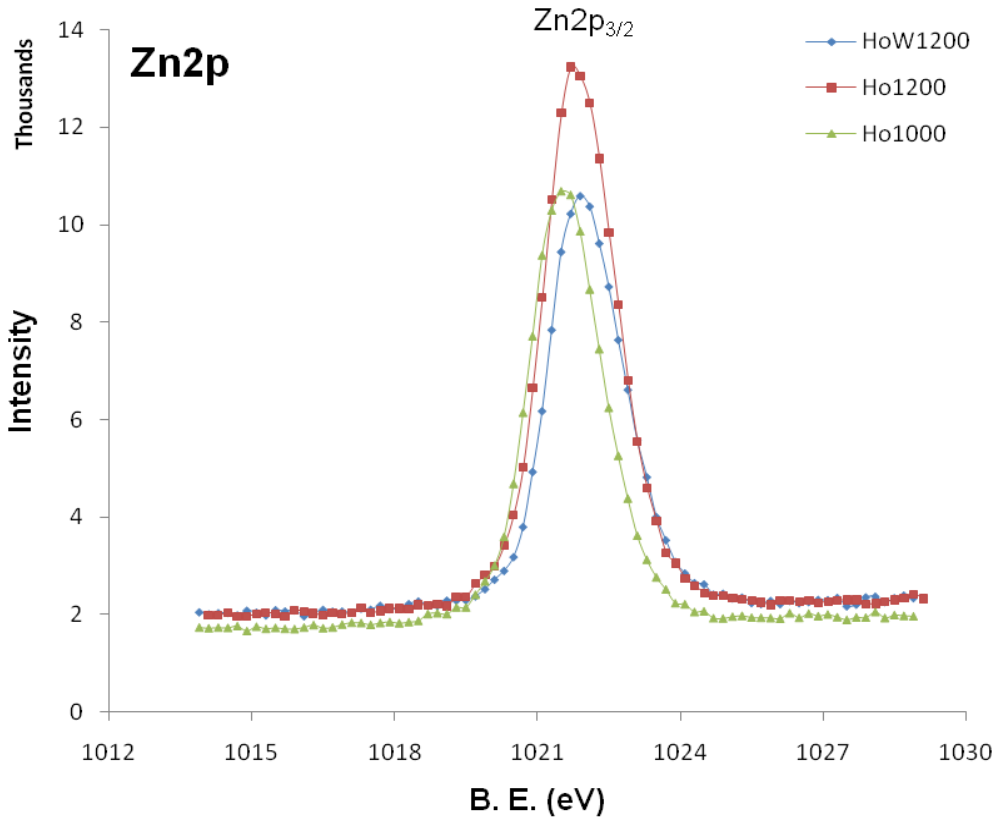

Figure 5.23 XPS core level spectra of Zn2p for the samples $Ho_{0.05}ZnO_{0.95}$ sintered at 1000C (green), at 1200C (red) and thermally evaporated pellet sintered at 1200C (blue).

5.10): XRD of HoZnO

The ZnO powder with 5wt% Ho_2O_3 was added and the doping was carried out through solid state reaction. Four samples were prepared through a range of temperatures in order to setting up the optimal temperature for complete incorporation of the dopants into the ZnO host material. The samples were named after the sintering temperature like the sample sintered at 1000C is named as Ho1000 and similarly Ho1050, Ho1150 and Ho1200. The pellets were ground down to powder and were analysed through XRD as shown in the figure 5.24.

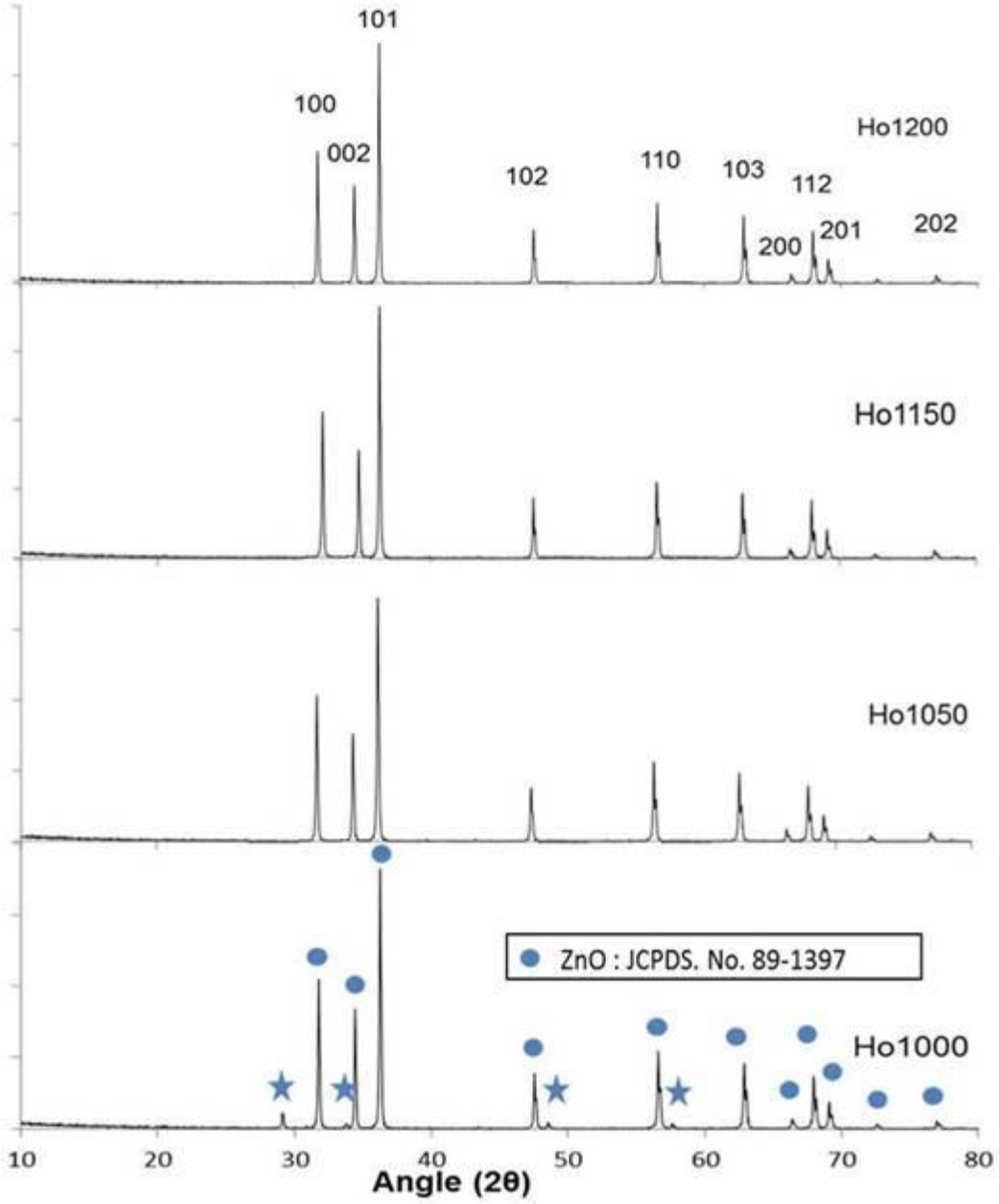

Figure 5.24 XRD spectra of the $Ho_{0.05}(ZnO)_{0.95}$ powder sintered at various temperatures.

The XRD pattern of HoZnO powder shows two different crystal structures. One that represents the ZnO wurtzite structure and the other correspond to the hcp phase of Ho_2O_3. The secondary phase exists at 1000C and vanishes for higher sintering temperature. This behaviour is quite similar to that of the Tb doped ZnO pattern discussed in section (5.4), where the secondary phase exists up to 1150C. This might be because of the fact that dopant ions with smaller ionic radii could easily be adjusted in the ZnO matrix[187,188]. This confirms

that 1050C is the sufficient temperature for 5wt% Ho to be completely incorporated into the ZnO matrix. The FWHM of the diffraction peaks increases at 1050C and then decreases with increasing sintering temperature. According to Bayan et al[157], the main reason for broadening the XRD lines is the microstructural imperfections that cause an incoherent diffraction of the x-ray beam. These microstructural imperfections arise mainly from the stacking faults or any dopant ions in the host material. Additionally the incorporation of dopant ions with bigger ionic radii causes an increase in the lattice strain[187]. The lattice strains for all the four samples were observed through the Williamson-Hall model and are given in the figure 5.25.

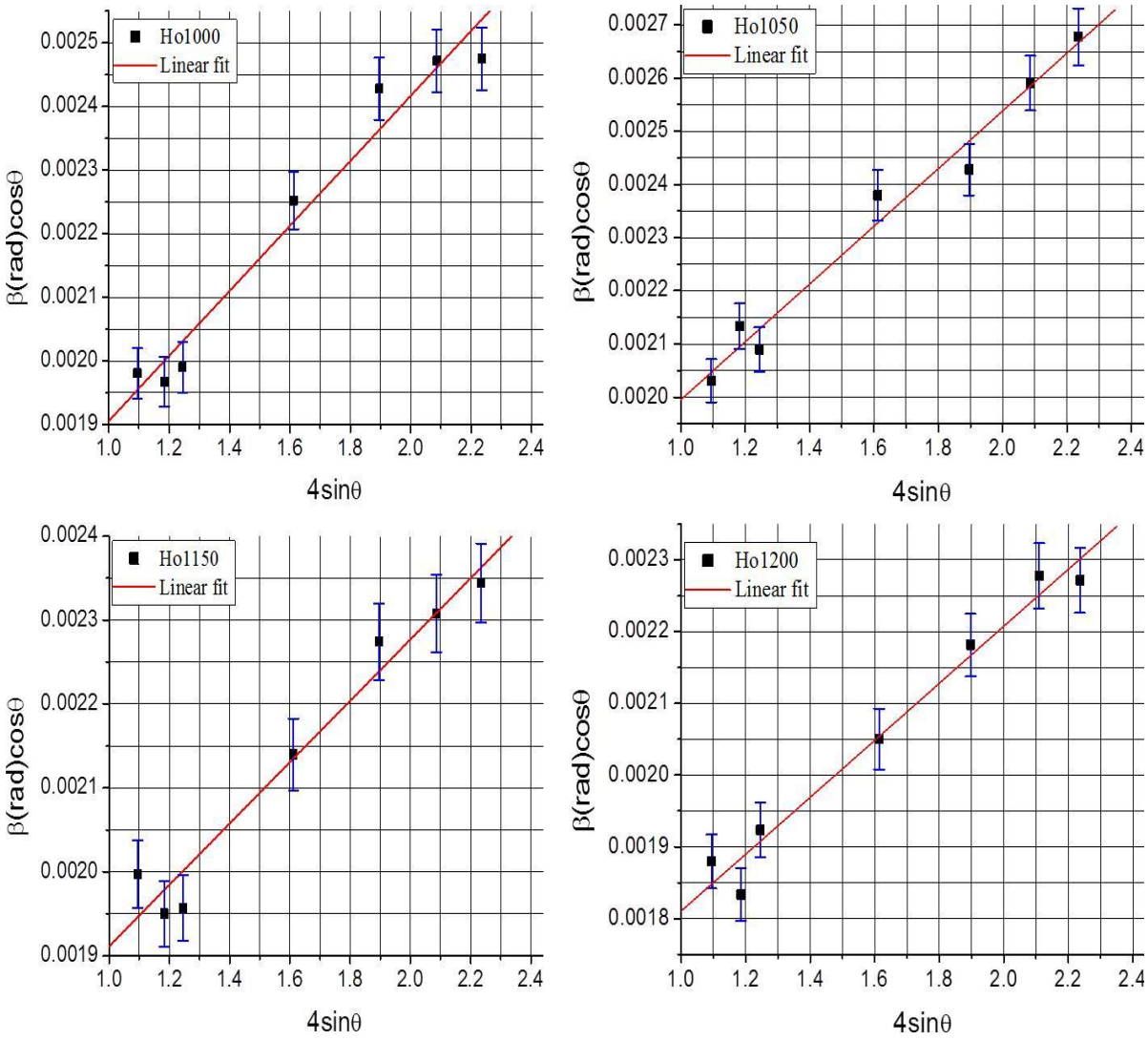

Figure 5.25 Williamson-Hall plots of the $Ho_{0.05}ZnO_{0.95}$ samples sintered at various temperatures like 1000C, 1050C, 1150C and 1200C obtained from the XRD analysis of seven different peaks. The lattice strain was calculated from the slope of the straight line.

The three most important parameters (lattice strain, crystallite size and lattice constant) of the Ho doped ZnO powder have been calculated from the XRD pattern and are summarised in table 5.6.

Sintering temperature	Lattice strain	Crystallite Size	Lattice constant (nm)
Ho1000C	5.17×10^{-4}	72nm +/- 2nm	a = 0.3246 c = 0.5199
Ho1050C	5.45×10^{-4}	61.59nm +/-2nm	a = 0.3249 c = 0.5205
Ho1150C	3.75×10^{-4}	66.521nm +/-2nm	a = 0.3248 c = 0.5203
Ho1200C	3.33×10^{-4}	69.29nm +/-2nm	a = 0.3249 c = 0.5202

Table 5.6 lattice strain, crystallite size and lattice parameter of $Ho_{0.5}ZnO_{0.95}$ samples sintered at 1000C,1050C, 1150C and 1200C

From the table 5.6 it evident that the lattice strain for the sample Ho1050 is higher than all the other samples. This means that, either there are more defects or there is a higher concentration of Ho ions in the ZnO host material. In this study the latter seems more probable because of the two reasons. One is that the Ho ions as a dopant act as a grain growth inhibitor and give rise to a smaller crystallite size upon incorporation into a host material[212]. Another is that, peaks of the sample Ho1050 have been slightly shifted towards the lower angle, which is a clear indication of the incorporation of impurity ions in the ZnO host material[213]. It is because the ionic radii of the Ho ions are bigger than that of the Zn ions therefore upon replacement of Zn ions by Ho ions the distance between the adjacent crystal planes increases and results in the shift towards a lower diffraction angle. Furthermore the lattice parameter for the sample Ho1050 increases, which seems to be because of the high concentration of Ho ions in the ZnO matrix. Therefore it is more likely that the higher lattice strain, smaller crystallite size and larger lattice constant at 1050C is because of the higher concentration of Ho ions in the ZnO matrix.

For the other two samples Ho1150 and Ho1200 the lattice strain decreases, and the crystallite size increases, which shows that a sintering temperature above 1050C can be used to improve the crystallinity by reducing the imperfections. The larger particle size at low sintering temperature (Ho1000) is because of the slow doping of the host material[214]. The earlier study by Kakazey et al[155] shows that higher amounts of defects give rise to a strong interaction between the particles and hence a strong coalescence between the nanocrystallites and results an increased crystallite size. It is quite clear from the XRD pattern that the host material can accommodate some proper amount of foreign atoms at some specific temperature and after that it gets saturated.

5.11): Conclusion:

This chapter describes the analysis of rare earth doped ZnO material prepared through solid state reaction with a range of temperatures. The effect of sintering temperature upon the incorporation of dopants into the ZnO matrix is different for different dopant materials. The ionic radii and the crystal structure of dopants seem to be the most important parameters for incorporation into the ZnO matrix. It was concluded from characterisation of these samples that size and shape distribution of grains depend upon the sintering temperature and the nature of dopants if the sintering time is kept constant. Additionally the doping of ZnO with rare earths seems quite successful after thermal evaporation.

6.1): Introduction

There has been a lot of work published regarding the synthesis of CNTs through CVD in the last one and a half decade. But still a very fundamental question remains unanswered: what is the actual role of catalyst in the synthesis of CNTs through CVD? In the last few years the growth of CNTs using ceramics and particularly the oxides as catalyst has completely changed the scenario of conventional thinking. This has raised the question again: How to understand the actual role of a catalyst regarding the growth of CNTs as we are still lacking a proper understanding of the role of a catalyst. In this chapter the synthesis procedure of CNTs through DC-PECVD using novel metal oxide nanoparticles as catalyst has been described. These new oxide catalysts lead towards very exciting and contemporary concepts, which need re-evaluation of the growth mechanisms. A new growth mechanism regarding the synthesis of CNTs has been proposed.

6.2): Proposed growth mechanism using metal oxide catalysts

The chemical state of the oxide catalyst nanoparticles plays a key role in the growth of CNTs. After an attempt to grow CNTs through iron oxide it was observed that it is the reduced iron that catalyse the growth and not the oxides[29,215] because these catalysts first reduces to metals and then catalyses the growth. ZnO is a direct band gap semiconductor with large exciton binding energy of about 60meV. It is usually used for device application like light emitting diodes[216] and lasers[217]. Since ZnO is intrinsically n-type because of the defects regarding the oxygen deficiencies on its surface and the probability of high recombination rate[218] makes it unfavourable for CNTs growth. After doping the ZnO with some transition metals like Cu and Ni and some rare earths like Tb and Ho, it was observed that it can catalyse the growth of CNTs quite efficiently. This shows that the incorporation of dopants into the ZnO matrix changes the catalytic activity of the intrinsic ZnO. The use of dopants makes two very prominent changes in the electronic properties of ZnO. One is that it changes the lattice strain of ZnO nanoparticles, and the other is that it enhances the charge transfer transition, (either from ligand to metal or from metal to ligand) which produces a non-radiative relaxation channels[219,220].

Here we propose a mechanism for the synthesis of CNTs using the metal oxide or doped metal oxide nanoparticles. Since the catalytic growth of CNTs through CVD involves two steps, one is the dissociation of carbon containing gas and the other is the diffusion of carbon through the catalysts. There are two different processes involved with these two steps, one is the intra-granular charge transfer transition that is responsible for the dissociation of hydrocarbon molecules and the other is the lattice strain that is responsible for the diffusion of carbon atoms through the catalyst nanoparticles. The intragrannular charge transfer transition in metal oxides is believed to be responsible for the change in activation energy which lowers the activation barrier and helps to dissociate the hydrocarbon molecules[221]. The energy required for this transition depends upon the ionization potential of the donor and the electron affinity of the acceptor. Additionally the charge transfer process opens additional non-radiative channels for the defects relaxation[219,220]. The charge transfer rate is temperature dependent and can be written as[222,223]

$$k_{transfer} = \sqrt{\frac{\pi}{\lambda k_B T}}\ \frac{V^2}{\hbar}\exp\left(-\frac{\lambda}{4k_B T}\right) \qquad (6.1)$$

Where k_B is the Boltzmann constant, T is the temperature, $\hbar$ is the Plank's constant, λ is the hopping energy accompanying geometric relaxation associated with the charge transfer and V is the electronic coupling matrix element between the neighbouring ions.

The lattice strain arises from the stretched side of a dislocation and the edge dislocations have higher adsorption energy than the rest of the surface[224]. Since after the dissociation of hydrocarbon molecules the resultant carbon atoms are more energetic therefore the edge dislocations are the most favoured place for these carbon atoms to get stabilised. Additionally it has been observed experimentally[225] that the lattice strain considerably modifies the chemisorptions properties of the catalyst nanoparticles. Thus this ability of lattice strain could also be used to manipulate the reactivity of the catalyst nanoparticles. Although the role of defects cannot be underestimated, it could not be solely considered responsible for the growth using transition metal oxides. Therefore it could be concluded that the intragrannular charge transfer transition and the lattice strain of the catalyst nanoparticles play together important roles in the growth of CNTs. The charge transfer mechanism is shown schematically in the figure 6.1.

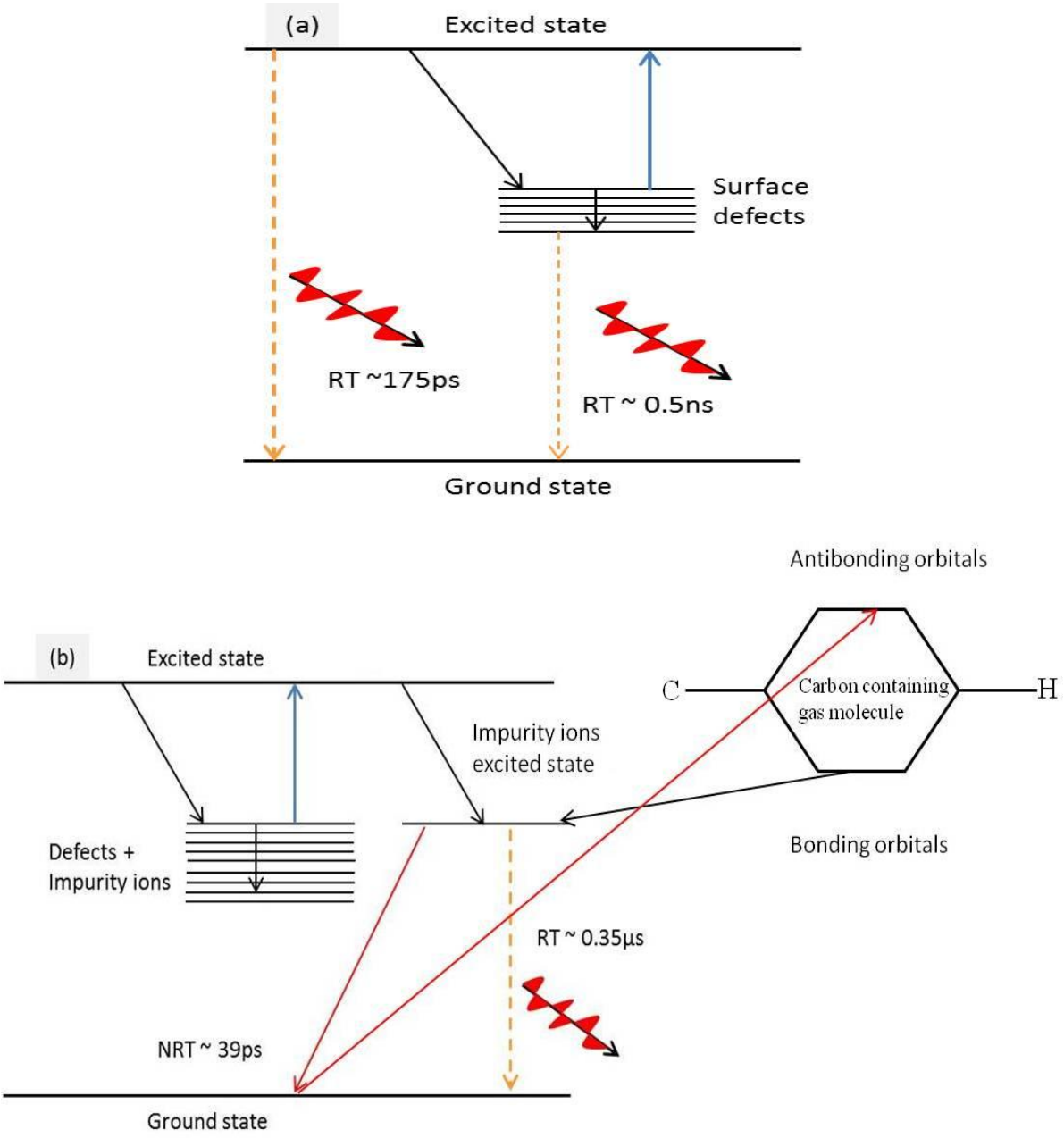

Figure 6.1[163]; Charge transfer mechanism in doped ZnO: (a); showing the recombination time (RT) of electron-hole pairs in undoped ZnO, where the electron relaxes to the ground state through radiative recombination in ~175ps. (b): in doped ZnO, the electron trapped by the impurity ions relaxes to the ground state non-radiatively via phonon mode in ~ 39ps. This is because the impurity ions produce non-radiative relaxation channels. The radiative relaxation in doped ZnO is very rare and takes place in ~0.35µs. The electrons in the bonding orbitals of the carbon containing gas are trapped by the impurity ions in the ZnO matrix and are sent back to the antibonding orbitals of the carbon containing gas molecules, where temperature plays a key role. This back donation of electron density causes dissociation.

6.3): CNTs with NiO as Catalyst

The sample was carefully prepared to prevent it from any possible transition metal contamination. The sample was prepared in clean room while using a clean glass and plastic tools. The SiO_2 substrate was put in 50% hydrogen peroxide and sulphuric acid solution and was placed in ultrasonic bath for about 20min. After 20min the substrate was then placed in de-ionised (DI) water for about 15min in ultrasonic bath and was dried with dry nitrogen afterwards. The SiO_2 substrate was then dipped in DI water with 0.1% added *HCl* to remove any possible sodium contamination. The sample was then dried with dry nitrogen and was put in a heater for 1min to make it completely dry. After that the sample was put in IPA and was cleaned ultrasonically for about 20min. The sample was then dried with dry nitrogen. The NiO powder was treated ultrasonically with IPA through ultrasonic bath for about an hour to make the particles smaller and remove the agglomeration. A drop of NiO nanoparticles mixed with IPA was then put on the SiO_2 substrate and left for about an hour to dry it completely under a glass cover. The SiO_2 substrate with NiO particles was then put into the chamber of PECVD reactor (MPS1400).

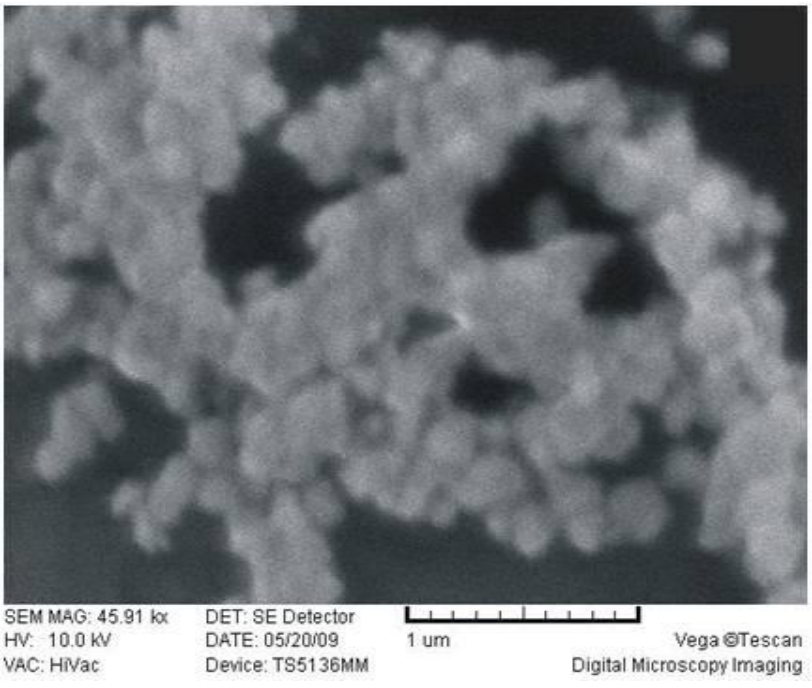

Figure 6.2 SEM Images of NiO nanoparticles

The substrate temperature was measured by a thermocouple attached to the substrate heater. As soon as a vacuum below 4×10^{-6}Torr was achieved; the process was activated with a flow rate of nitrogen (N_2) as 80 sccm (standard cubic centimeter per minute) with chamber pressure kept at 2.5Torr. After the attainment of this pressure, the heater was switched on in order the growth temperature is reached. It normally took two minutes to get to 650C and that the acetylene (C_2H_2) was allowed into the chamber with a flow rate of 20 sccm. Both the electrodes (anode and cathode) were separated by about 18mm with the chamber pressure set around 1.2 Torr. The DC power was applied to generate the plasma, which was obtained with a stable state at 442V and at a current of 65 mA. The growth process was carried out for 20minutes at a temperature of 650C. After this time the process was de-activated and the sample was allowed to cool down below 100 ^{0}C. This process produced CNTs with a range of diameters from 20nm to 70nm, as shown in figure 6.3.

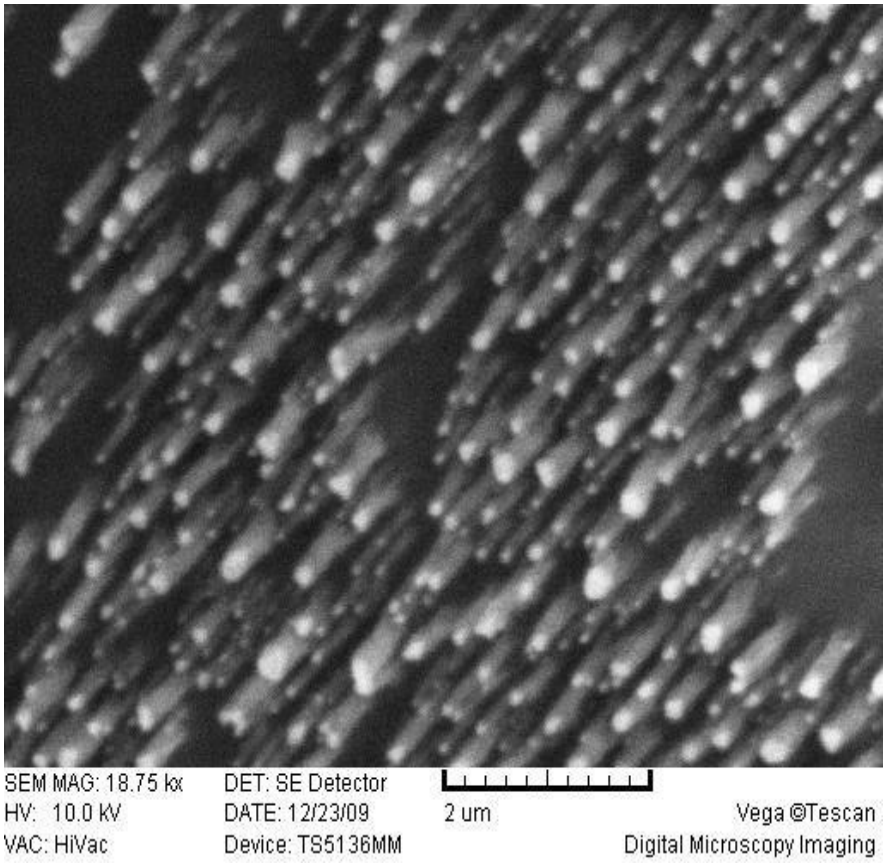

Figure 6.3 SEM Images of CNTs using NiO as catalyst showing the good alignment of CNTs and indicates the tip growth mode.

The SEM images show two well established phenomena, one is that the DC-PECVD grown CNTs are quite well aligned and the second is that the growth is not uniform with respect to the height and diameter of CNTs. The wide distribution in the diameters of CNTs is because of the wide range of particle size distribution that plays a main role in controlling the diameter of CNTs. The particles of the same size, shape and composition will produce CNTs of the same diameter and height; because the decomposition of the carbon feed gas and diffusion of carbon atoms occur at the same time on the surface of catalyst particle, which in turn will yield a uniform growth[226,227]. Additionally the composition of catalyst nanoparticles is believed to affect the lattice strain, which controls the diffusion of carbon atoms through the catalyst nanoparticles[228]. The density of CNTs is quite high, almost every particle is catalysing the growth and it is clear from the SEM images shown in figure 6.3 that the CNTs are grown where a catalyst particle exists. Additionally the SEM images show that tip growth is the dominant mode for the CNTs grown through DC-PECVD using NiO as a catalyst because the majority of CNTs have the catalyst particle at the tip. This usually happens when there is a weak interaction between the support and catalyst[80]. Additionally the chemical state of the catalyst nanoparticles also plays an important role in defining the growth modes as shown by Dijon's et al[101]. Usually the base growth is identified from the curvature of compartments that would be directed towards the tip of CNTs and that for the tip growth the compartments are directed towards the substrate[229].

The sample was scrapped using plastic tweezers and rubbed with copper grid of TEM to prepare the sample for TEM analysis. The transmission electron (TEM) micrograph of the NiO grown CNTs shows that all the CNTs are multiwall with diameter ranging from 50nm to 70nm. The CNTs that have a particle at the tip showing a tip growth process as shown in figure 6.4 a & b.

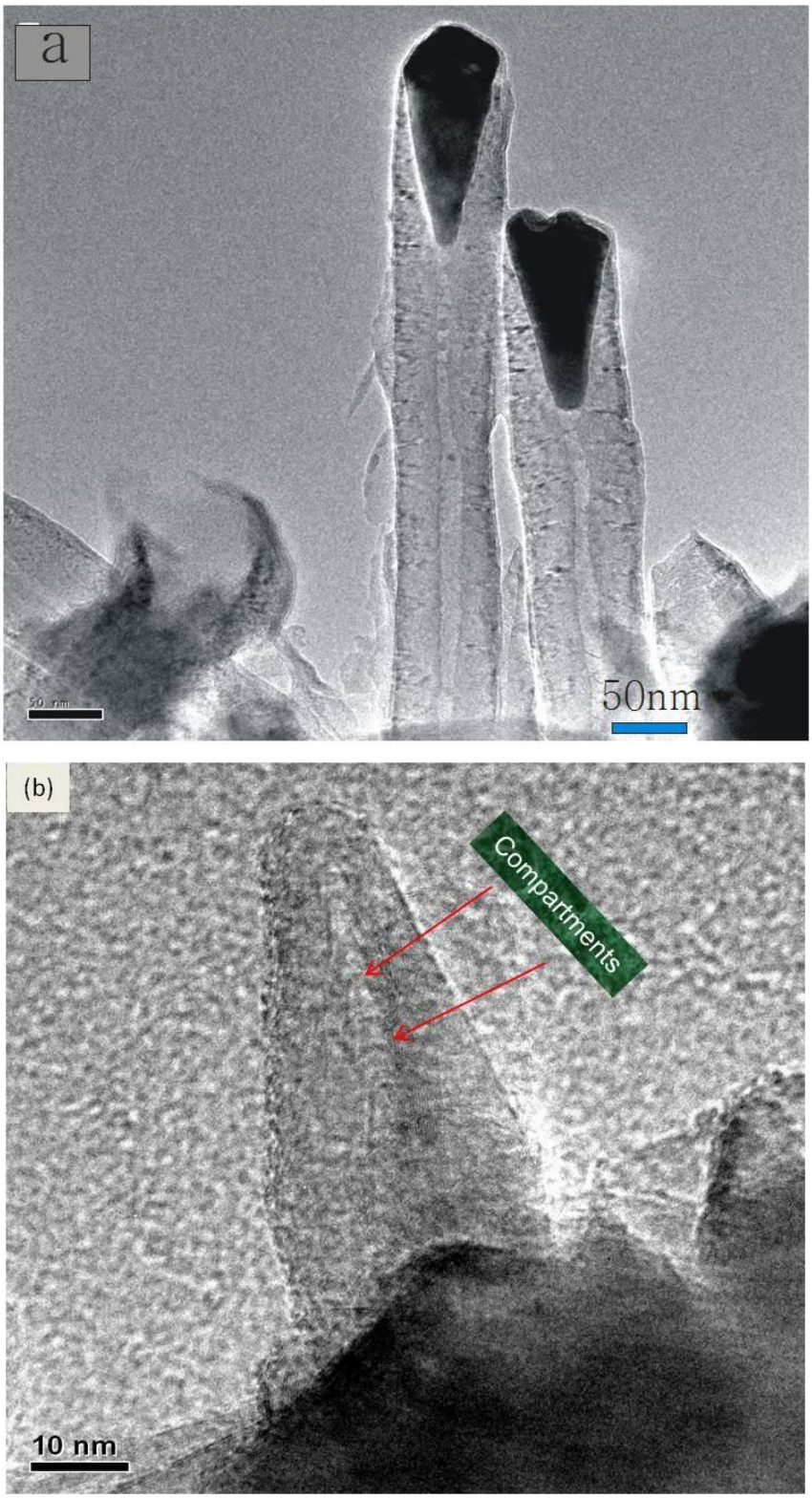

Figure 6.4 TEM Images of the NiO/CNTs (a): a straight CNT with particle at the tip showing the tip growth process (b): is a closed cap CNT with the compartments directed towards the cap indicating the base growth process.

The TEM images show that NiO grown CNTs have different carbon morphologies depending on whether they have been grown through tip growth or base growth mechanisms as shown in figure (6.4a &b). The arrows show the direction of the curvature of compartments that are directed towards the tip indicating the CNTs that have been grown through base growth mechanism. The figure (6.4a) shows a multi-walls CNTs with quite tabular morphology, while in figure (6.4b) the CNTs is bamboo shaped with very narrow compartments (shown by the arrows).

The different CNTs morphologies seem to be because of the large particle size and shape distribution and varying composition of the catalyst nanoparticles. Lee and Park (2001)[229], have suggested that the bamboo structure of the nanotubes is because of the base growth process and could be recognised from the direction of the compartments. The compartments are directed towards the tip which favours the Lee and Park model. The shape of the compartments is due to the surface geometry of the catalyst particles and these compartments will appear periodically as long as the carbon is supplied continuously and steadily. Also the catalyst composition is believed to be a factor that affects the CNTs morphologies[230] . The catalyst nanoparticles with varying compositions of elements give rise to CNTs with different morphologies. It has been observed in this study that varying the composition of the catalyst nanoparticles may affect the lattice strain of the grains and hence the non-uniform extrusion of carbon through the catalyst nanoparticles, which might lead to a non-uniform growth.

When NiO nanoparticles are used as catalyst, the charge transfer process from O2p to Ni3d plays an important role because it strengthens the back donation of electron density to the anti-bonding orbitals of the adsorbates[13]. Acquisition of the negative charge of Ni from the O enhances its catalytic activity. It is because the Ni becomes more negative, where the Fermi level gets raised and the electron transfer occurs from Fermi level to the lowest unoccupied molecular orbitals, which might widen the band gap[231]. But, according to Blazy et al[232] the charge transfer in NiO (either from metal to ligand or ligand to metal) does not affect the band gap but it is strongly dependent upon the valency of the metal ion. Since NiO remains non-stoichiometric and 1:1 ratio does not usually hold[233], therefore it is strongly believed that in NiO there is always present excess oxygen, which results in the Ni^{+3} oxidation state and these ions act as electron acceptor. This behaviour pins the Fermi energy at the top of the valance band, which is also the O2p band[234].

The mechanism for accepting electrons from acetylene molecules and the potential of back donating the electron to the acetylene antibonding orbitals causes weakening of the bonding strength of C_2H_2 to an extent that they start dissociating into hydrogen and carbon[13]. The charge transfer transition between the O2p and Ni3d is believed to be responsible for the change in activation energy which lowers the activation barrier and help dissociating the acetylene molecules[235]. After dissociating the acetylene molecules the atomic carbon then start diffusing through the atomic steps at the grain boundaries of the catalyst nanoparticles as proposed by Helveg et al[19]. The atomic steps or vacancies or any imperfections at or near the grain boundaries will be different from that at the centre of the grain, which gives rise to lattice strain gradient[236,237]. This lattice strain gradient is believed to be responsible for the drift velocity of the diffusion of carbon through the catalyst[228]. It could be inferred that the charge transfer mechanism help in dissociating the acetylene molecules and lattice strain controls the carbon diffusion through the catalyst.

The nature of the particle at the tip of CNTs was verified through line spectrum EDS in the scanning transmission electron microscope (STEM) to verify the elemental composition of the particle at the tip of a CNT. The line spectrum obtained shows the presence of Ni and O. The STEM EDS analysis verifies the existence of ~52% oxygen and ~48%Ni, which correspond to the NiO stoichiometry. In order to avoid the Cu contribution, the spectra was taken from a particle of interest away from the grid. This clearly indicates that NiO does not reduce if used as catalyst for the dissociation of hydrocarbon (acetylene) at 650C in N_2 environment.

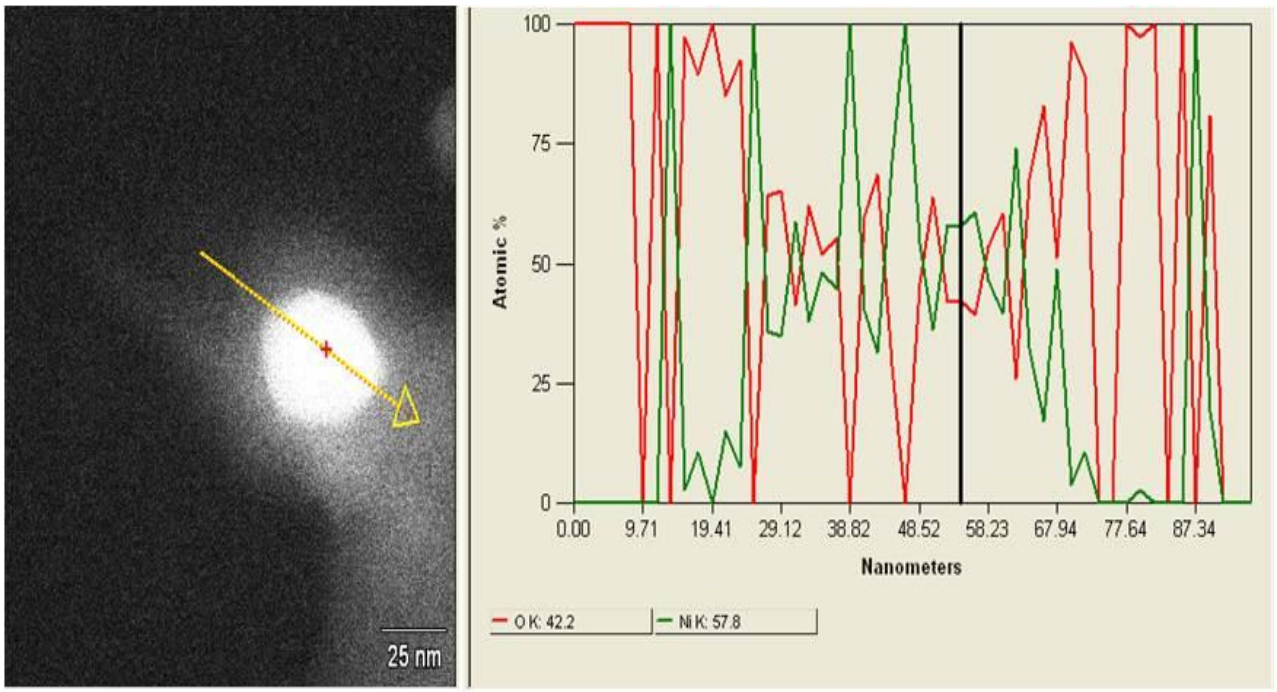

Figure 6.5 Line scan EDS spectrum of the NiO nanoparticles at the tip of a CNT taken with the scanning transmission electron microscope (STEM), showing the elemental composition of the catalyst particle. The EDS spectrum was taken at the accelerating voltage of 200kV.

Element Line	*Weight %*	*Weight % Error*	*Atom %*	*Atom % Error*	*Formula*
O K	22.78	+/- 8.12	51.99	+/- 13.00	O
Ni K	77.22	+/- 17.57	48.01	+/- 10.84	Ni
Ni L	---	---	---	---	
Total	100.00		100.00		

Table 6.1 quantitative analysis of the line scan spectrum in figure 6.5.

The diffraction pattern from a particle at the tip of a CNT was observed through TEM. The spot pattern shows that the particle at tip of the CNT is single crystal and is in the form of square arrays that correspond to a rock salt structure of NiO.

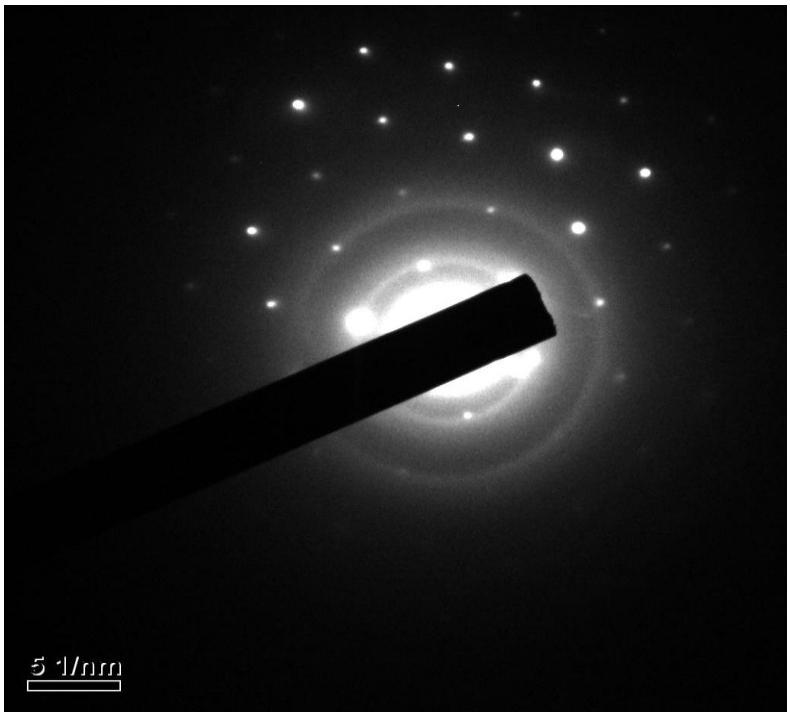

Figure 6.6 selected area electron diffraction pattern of a NiO particle at the tip of CNT confirming the rock salt structure of NiO catalyst.

6.4): Growth of CNTs using Ni as Catalyst

CNTs were grown using Ni as catalyst. A layer of Ni film of thickness 7nm was thermally evaporated on a SiO_2 substrate. The thickness of the film was controlled through a crystal monitor. The SiO_2 sample was then put in the MPS1400 and was heated to 700C under hydrogen atmosphere to make nanoparticles of the film. The hydrogen is used to remove any amorphous carbon if does exist on the sample surface.

The sample was then put back in the chamber of the MPS1400 for growth of CNTs. The sample was heated up to 750C. After the pressure below $4*10^{-6}$ Torr was obtained, ammonia was introduced in the chamber with a flow rate of 100 sccm followed by acetylene with a flow rate of 20sccm. Acetylene is used as a carbon source and ammonia as an etchant, which is used for the removal of amorphous carbon produced during the growth process. The process was continued for about 25minutes in stable DC plasma with the DC voltage of 460V and a current of 95mA giving rise to a net power of about 44W. The process was then

stopped and the sample was taken out when the temperature of the chamber comes down to room temperature. The sample was then investigated through the SEM to see the CNTs growth as shown in figure 6.7.

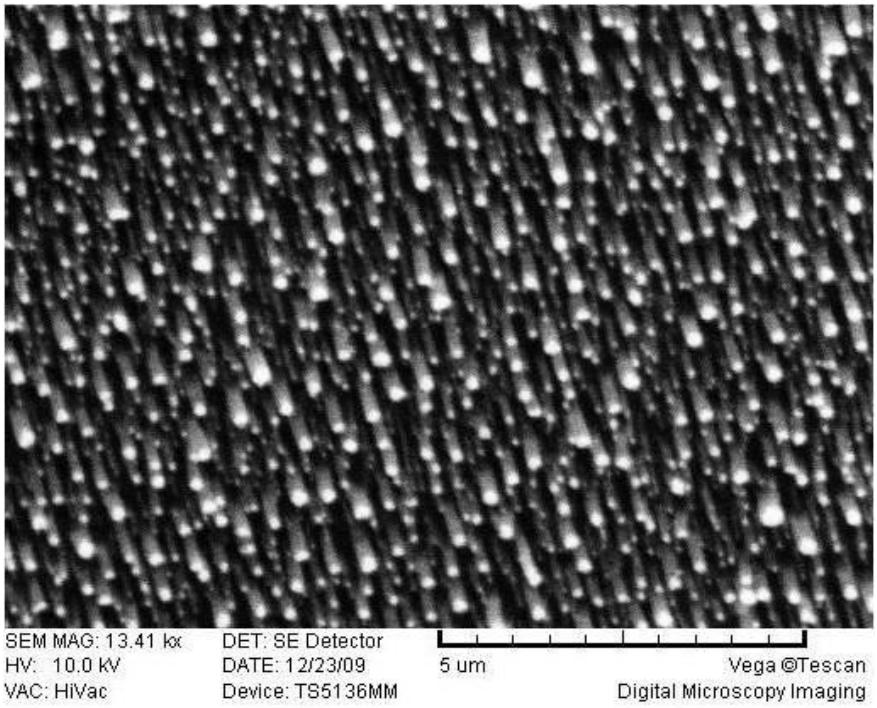

Figure 6.7 SEM Image of CNTs using Ni as catalyst. The CNTs have been grown through DC-PECVD.

The SEM image shows that CNTs are well aligned as shown in figure 6.7. This confirms that well aligned CNTs can be grown under stable plasma conditions at the applied power of about 44W. From the SEM image [figure 6.7] it is clear that it is a tip growth process with Ni particles at the tips. The sample has CNTs with a range of diameters, which is believed to be due to the particle size distribution[226,227]. The sample was treated ultrasonically in IPA to remove some of the CNTs and put a drop of it on a TEM copper grid to make a sample for TEM studies, as shown in figure 6.8a & b.

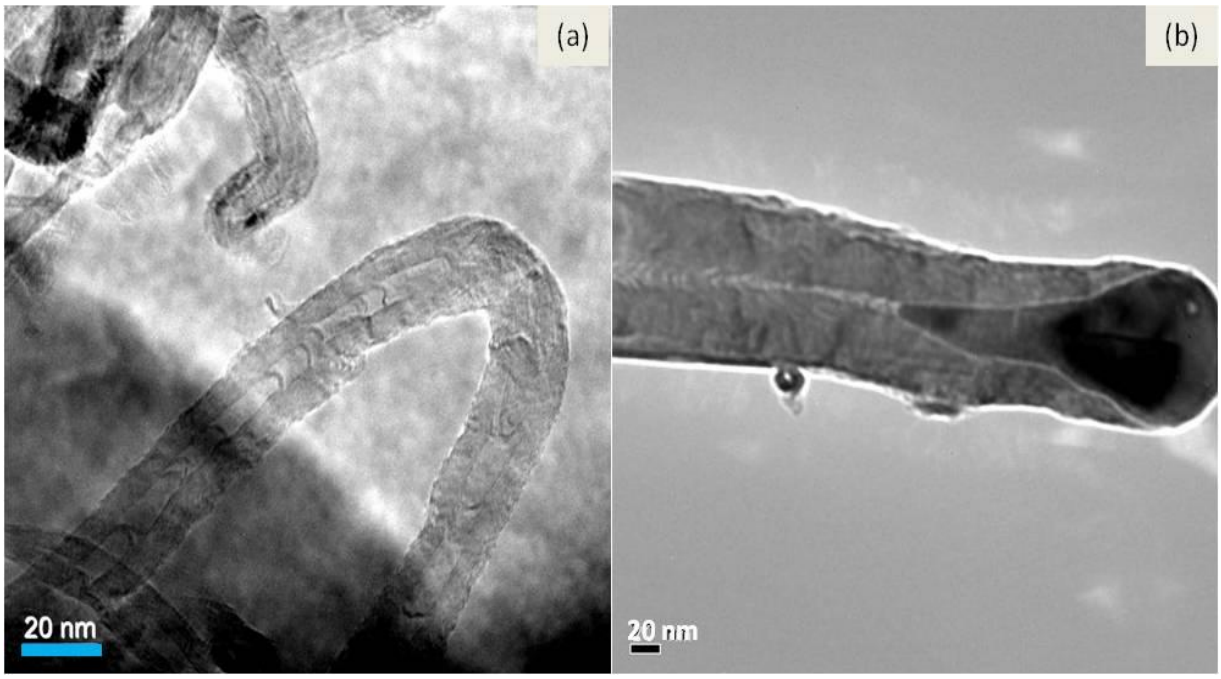

Figure 6.8 TEM Images using Ni as catalyst (a); bamboo type CNT (b); carbon nano-fibre (CNF)

The TEM images show that there are bamboo shaped CNTs and herringbone type filaments as shown in figure 6.8 a & b respectively. Figure 6.8a is a bamboo type multiwall CNT, with the walls parallel to the tube axis. A small curvature at the tip is supposed to be due to the addition of pentagons or heptagons to the hexagonal network. During the growth process the carbon atoms accumulate on the surface of the catalyst particle and then start diffusing through the catalyst surface to gives rise to a CNT formation. The production of herringbone filaments is due to the surface morphology of the catalyst particle, the relative composition of the carbon source gas and that of the etchant gas and the growth temperature[238]. According to Merckulov et al[239]; if the growth conditions such as the relative combination of the gases and the growth temperature are kept constant then this will give rise to one form of graphitic carbon, i.e. either CNT or carbon nano-fibre (CNF). But besides this the catalyst morphology plays a critical role in defining the structure of CNTs or CNFs, because in this study it has been observed that CNTs and CNFs grow in the same sample while keeping the growth conditions constant. This confirms that growth conditions like (chamber pressure, temperature flow rate of different gasses and plasma power) are not the only parameters that control the transition of CNTs to CNFs or vice versa.

6.5): Growth of CNTs using CuZnO as Catalyst

The substrate was cleaned in the clean room according to the procedure discussed in section (4.3.3). After the evaporation of the Cu/ZnO pellet on the Si substrates these were loaded into the CVD chamber to grow CNTs upon the surface of the substrate. The temperature was kept at 550C with nitrogen at a flow rate of 100sccm and acetylene (C_2H_2) as the carbon source with a flow rate of 20sccm. The chamber pressure was kept at 2500mTorr and the process was deactivated after 15min. Before starting the process the chamber was evacuated to a base pressure of ~5×10^{-6} mtorr. After the growth was completed the chamber was allowed to cool down to 100C in nitrogen atmosphere and after that the chamber was left under low pressure overnight. The samples were then taken out and inspected in the SEM as shown in figure 6.9.

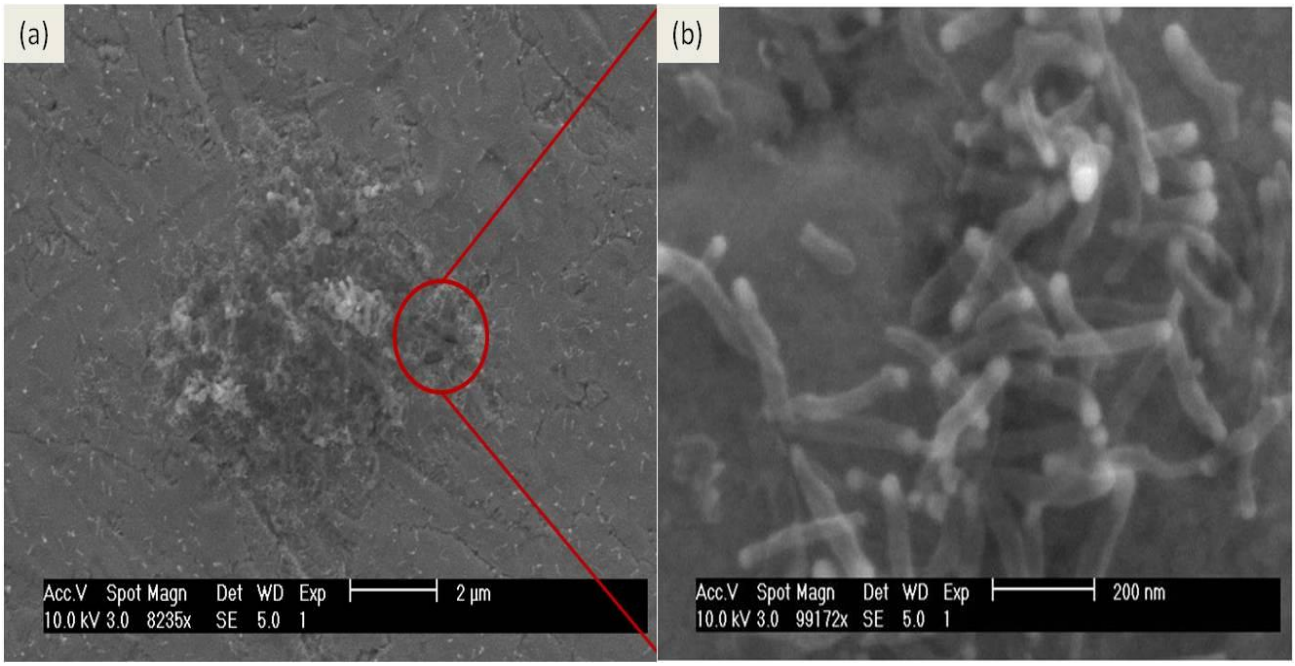

Figure 6.9 (a); Low magnification SEM Image of CNTs using $Cu_{0.05}$ $(ZnO)_{0.95}$ as catalysts through CVD . (b); High magnification SEM image, showing the CNTs are quite uniform in size and diameter, which correspond to the uniform size distribution of catalyst nanoparticles.

The SEM images of figure 6.9 show that all the CNTs are multi-wall and are quite uniform in size and in diameter, which is attributed to the uniform composition and narrow

distribution of the catalyst particle sizes[230]. Additionally it is quite clear from figure 6.9 that it is a tip growth process and all the observed CNTs have a particle at the tip. This clearly confirms that either all the catalyst nanoparticles have a weak interaction with the support[80] (substrate) or have the same chemical state[101], which gives rise to uniform lattice strain. The chemical state of the catalyst nanoparticles seems to be a dominant factor that defines the growth mechanism. It has been observed in the preceding sections [section (6.7) and (6.8)] that the catalyst nanoparticles with different dopant concentrations will give rise to CNTs with different morphologies, which is attributed to the difference in lattice strains. For uniform growth all the catalyst nanoparticles must have the same lattice strain and any change in the lattice strain will affect the diffusion of carbon atoms, which results in non-uniform growth.

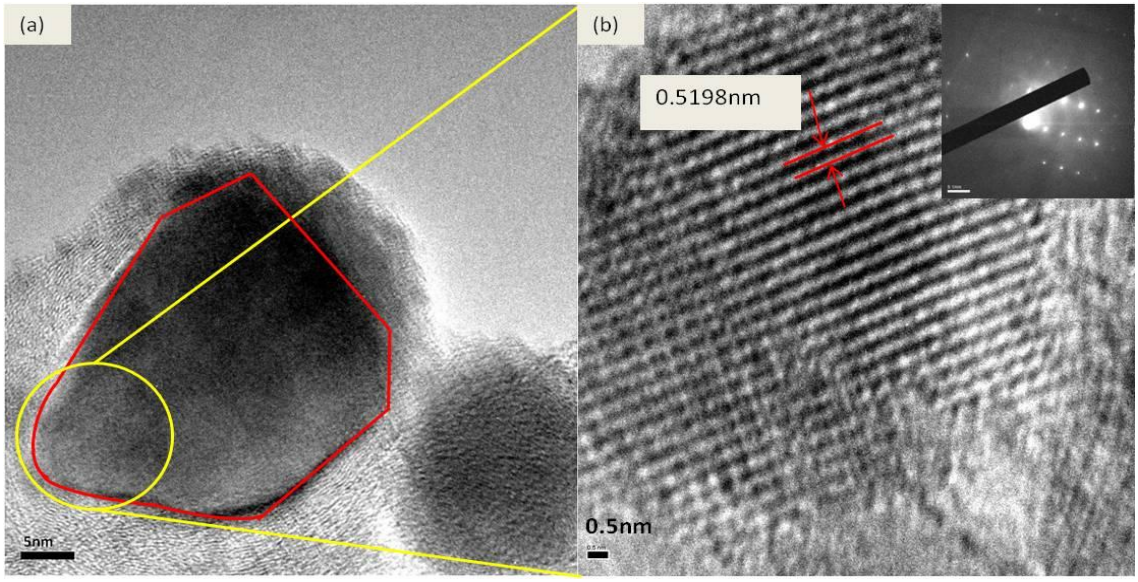

Figure 6.10 (a): TEM image of a CNT, (b): High resolution image of the particle at the tip of CNT. The scale bar of "a" is 5nm and that of "b" is 0.5nm.

The sample was investigated through a JEOL 2011 TEM to see the morphology of the CNTs. It was observed that almost all the CNTs show the same morphology and size as observed through the SEM in figure 6.9. It is believed that the size, shape and composition of the catalyst nanoparticles affect the CNTs growth, which seem to be dominant factors in the growth of CNTs. From the SEM and TEM images it is clear that the needle like structure

(observed in figure 4.7 section 4.4) do not contribute to the CNTs formation. All the CNTs are of the order of 10nm to 25nm in diameter. The majority of CNTs are quite cylindrical but there were a few that have very narrow compartments, which make them like a bamboo structure CNTs, which usually happens because of the composition[230] and morphology of the catalyst nanoparticles. During restructuring of the catalyst nanoparticles one of its edges is deformed as shown in figure 6.10a. According to Lee et al[240] the bamboo structure is because of the bulk diffusion of carbon through the catalyst nanoparticles that occurs in hot reaction zones. But for smaller nanoparticles in the range of 10 to 25nm diameter, it seems unlikely that a temperature gradient will occur on the surface of the catalyst nanoparticles. In this study it is believed that the main driving force for the carbon diffusion is the lattice strain across edge dislocations that give rise to surface diffusion of carbon through the catalyst particle. This is because the edge dislocations give rise to low activation energy due to higher strain[224].

The CNTs in figure 6.11 are quite crystalline but are surrounded by amorphous carbon (as shown by an arrow figure 6.11b). The high resolution TEM image show that the CNTs are quite straight with no helicity and curling. Catalytically grown CNTs usually have a low degree of graphitization but the CuZnO grown CNTs are highly graphitised. The graphitic layers are surrounded by some amorphous carbon, which might be because of the low etching effect of nitrogen.

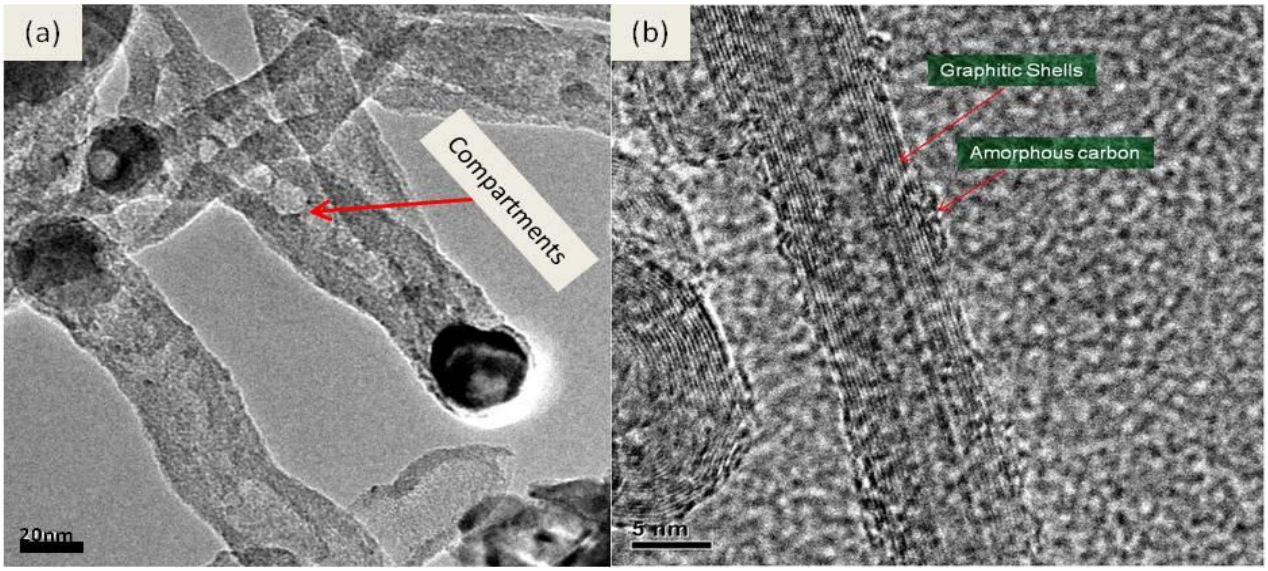

Figure 6.11 (a); (a); low magnification Image showing small compartments (b) High resolution TEM Image of the CNT showing graphitization and the amorphous carbon around the CNT.

The TEM images show that the CNTs have quite large inner diameter indicating that surface diffusion is dominant over bulk diffusion. The surface diffusion is more favourable because the diffusion of carbon through the catalyst takes place at the grain boundaries and edge dislocations because of the higher strain[241]. This study shows that CuZnO nanoparticles are highly active in dissociating the C_2H_2 at 550C and carbon diffusion occurs through the grain boundaries parallel to the c-axis of the catalyst nanoparticles. The CuZnO nanoparticles can accommodate electrons more easily than holes because of the increased resistivity and it has been observed that Cu as a dopant in the ZnO matrix increases the resistivity[242] of the nanostructure and hence the electron acceptance nature. Also the foremost requirement for the catalyst to grow CNTs is to make bonds with the hydrocarbon by accepting electrons.

To observe the effect of chemical composition of catalyst and the charge transfer phenomenon on the growth of CNTs, two separate samples were prepared. One sample was made of just the ZnO nanoparticles and the other was prepared by thermally evaporating the CuZnO pellet. It is worth noting that a charge transfer transition has been observed in the sample of CuZnO through XPS as discussed in section (4.7). Additionally the crystallographic and surface composition has been observed through XRD and XPS as discussed in section (4.6) & (4.7) respectively. The XPS analysis of the thermally evaporated CuZnO sample has confirmed that the thermal evaporation has not reduced the nanoparticles and the oxygen corresponds to the lattice oxygen and not the adsorbed one, which happens upon exposure to air. Both the samples were put in the MPS1400 with the same environment. After the process it was observed that copper doped ZnO can easily catalyse the growth at 550C while only amorphous carbon was observed on the ZnO sample. It could be concluded from the process that surface defects of the catalyst are not the only reason of the CNTs growth. According to Helveg[19] and Ajayan[91], the mono-atomic steps (vacancies or any defects) on the surface of catalyst nanoparticles help nucleate the CNTs growth, which is only possible if there is a charge transfer mechanism otherwise the trapped electrons will recombine and the surface will relax with a photon emission as happens in pure ZnO nanostructures[243].

Since the doping of ZnO with Cu make it more p-type[242] and causes a fast electron transfer process to occur[243]. This hinders the way of recombination of carriers and provides additional relaxation channels for the carriers. The charge transfer process helps dissociating the hydrocarbon molecules through back donation of electrons to the anti-bonding orbitals of

the hydrocarbon molecules. Xing et al[243] observed the charge transfer dynamics in copper doped ZnO nanowires using time resolved photoluminescence and transient absorption spectroscopy and showed that in undoped ZnO nanowires the carriers either undergo radiative recombination or become trapped at the defect states. The trapped carriers again then recombine and give rise to photon emission, while in copper doped ZnO a charge transfer process occurs, which competes with the trapped carriers and provide additional relaxation pathways for the trapped carriers.

Particles at the tip of the CNTs are having proper hexagonal geometry like that of wurtzite structure and are also slightly elongated in the direction of CNTs. This is because of the restructuring of the catalyst particles that undergo during adsorption of the carbon containing gas. According to Baker et al[244] this restructuring of the catalyst nanoparticles produce faces that cause the decomposition of carbon containing gas and other faces that favour the diffusion of the carbon atoms.

The selected area diffraction patterns (SAED) taken from the catalyst particle at the tip of the CNT (in the inset of fig 6.10b) unveils the crystal details of the catalyst particle. The pattern shows that the particle is single crystal that corresponds to the wurtzite structure of ZnO. The high resolution TEM image of the catalyst particle [figure 6.10b] shows the details of the lattice spacing, which is equal to 0.5198nm, which corresponds to the ZnO crystal structure with perfect wurtzite geometry.

6.6): Growth of CNTs using NiZnO as Catalyst

The Ni doped ZnO pellets prepared through solid state reaction were thermally evaporated on Cr coated W substrate and was placed in the MPS1400. This sample was characterised through XPS and XRD, SEM and TEM prior to use for CNTs growth to see the doping condition and crystalline nature of the particles as discussed in chapter 5. The reactor chamber was evacuated below 5×10^{-6} mTorr to remove all residual gases. After that the heater was switched on and the temperature was fixed to 650C under nitrogen atmosphere keeping the chamber pressure at 2500mTorr. As soon as the desired growth temperature of 650C was achieved, acetylene was allowed in the chamber at flow rate of 25sccm. The process was continued for about 15min. The process was then deactivated and the chamber to

cool at 2500mTorr until the temperature comes down to 100C. After that the nitrogen flow was stopped and left the chamber overnight. The sample was then inspected in the SEM for any CNTs growth. It was observed that Ni doped ZnO can actively grow CNTs as shown in figure 6.12.

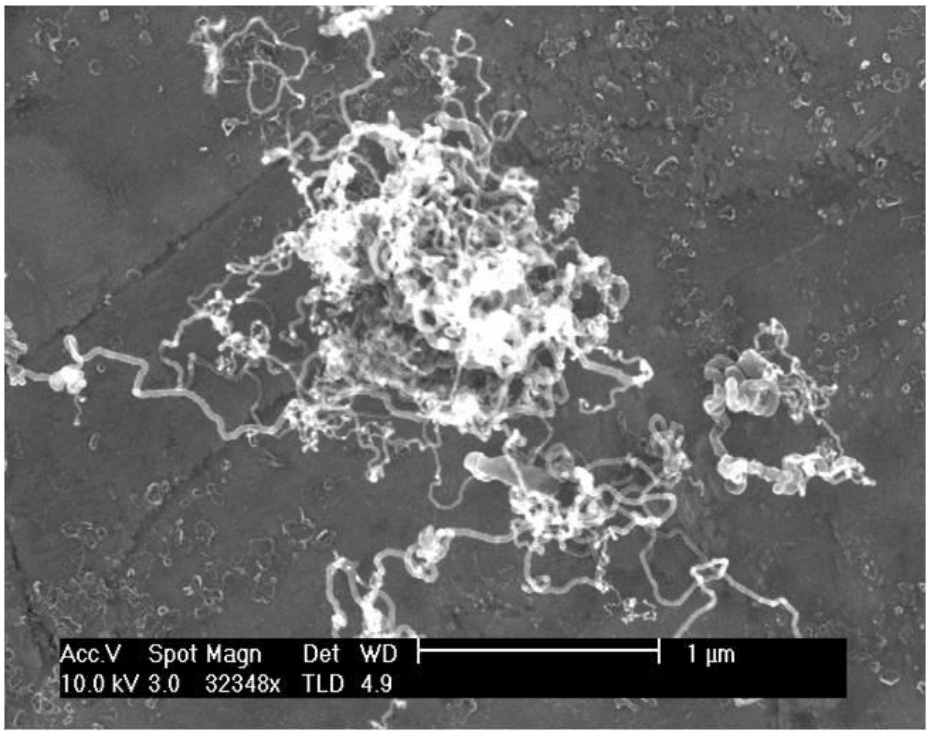

Figure 6.12 SEM Images of the NiZnO grown CNTs

It is clear from the SEM image that there is a wide range of CNTs with varied lengths and diameters. This indicates that there is a wide range of particle size distribution with a wide range of elemental composition as well. The growth process is also a mixture of growth processes, where some of the CNTs grow through the tip growth while some of the CNTs grow through the base growth process, which strongly depends upon the chemical state of the catalyst particles and the angle of the catalyst to the substrate.

The sample was then scratched using plastic tweezers to transfer the CNTs onto the copper grid for further investigation in the TEM. It is clear from the TEM analysis that there are two types of CNTs, one type corresponds to the tubular CNTs and the other corresponds to the bamboo shaped CNTs. The bamboo shaped CNT seem more crystalline than the tubular CNT. There are some irregularly arrange graphitic layers around. It has been

observed through XPS analysis [section 4.6] of the Ni doped ZnO nanoparticles that Ni exists in the mixed oxidation state in the ZnO matrix and it is believed that Ni in the +3 oxidation state act as an electron acceptor[234]. The acceptance of an electron from acetylene molecule is the pre-requisite for CNTs growth. Additionally the mixed oxidation states of the Ni ions gives rise to intra-granular charge transfer transition from ligand to metal, which helps dissociating the hydrocarbon molecules.

It has been observed in all the CNTs (using transition metal and rare earth doped ZnO grown) that the graphitisation decreases from outer to the inner side. It seems to be due to the higher diffusion of carbon atoms along the edge dislocations of the catalyst particle. The edge dislocations produce higher lattice strain that gives rise to low activation energy[224].

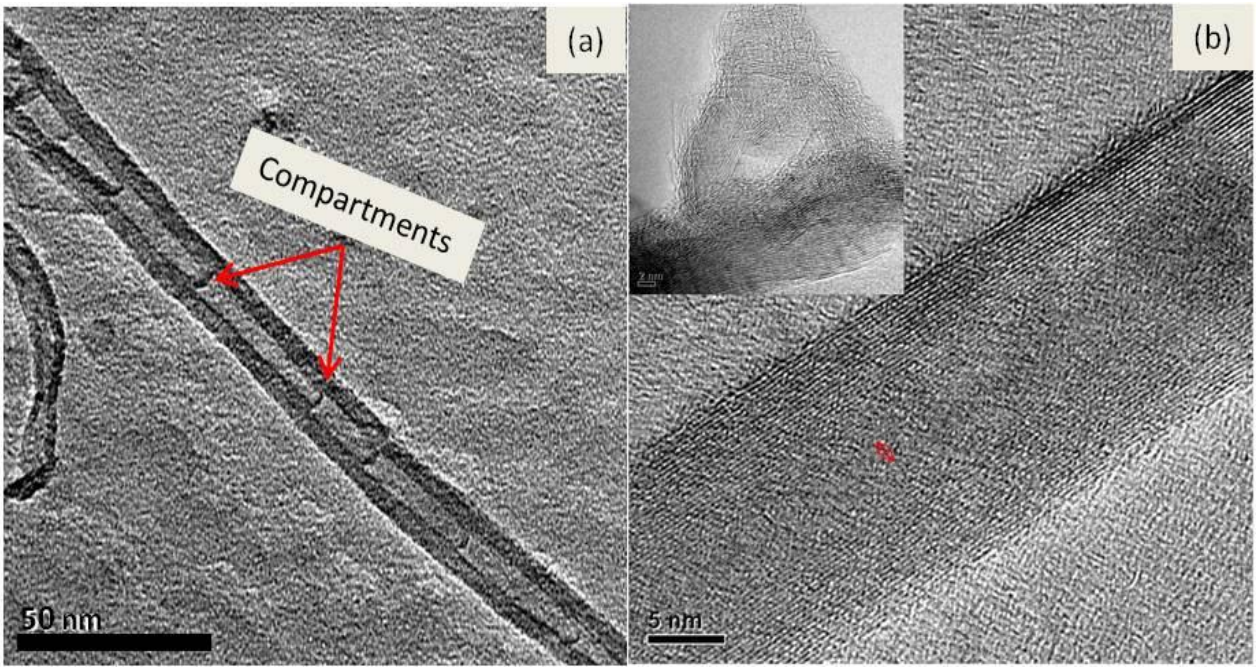

Figure 6.13 (a) TEM image of the bamboo shaped CNT (b) HRTEM of a tubular CNT showing the graphitic shells that are getting amorphous as goes from outer to the inner side of the CNT. The red arrow shows the inner diameter of the tube. In the inset some irregularly arranged graphitic layers are shown.

The growth of CNTs using NiZnO catalysts was confirmed through the ultra high resolution image of a particle at the tip of a CNT in figure 6.14b. it was observed that the stacking sequence of the follow the ABAB.....order which corresponds to the ZnO wurtzite structure.

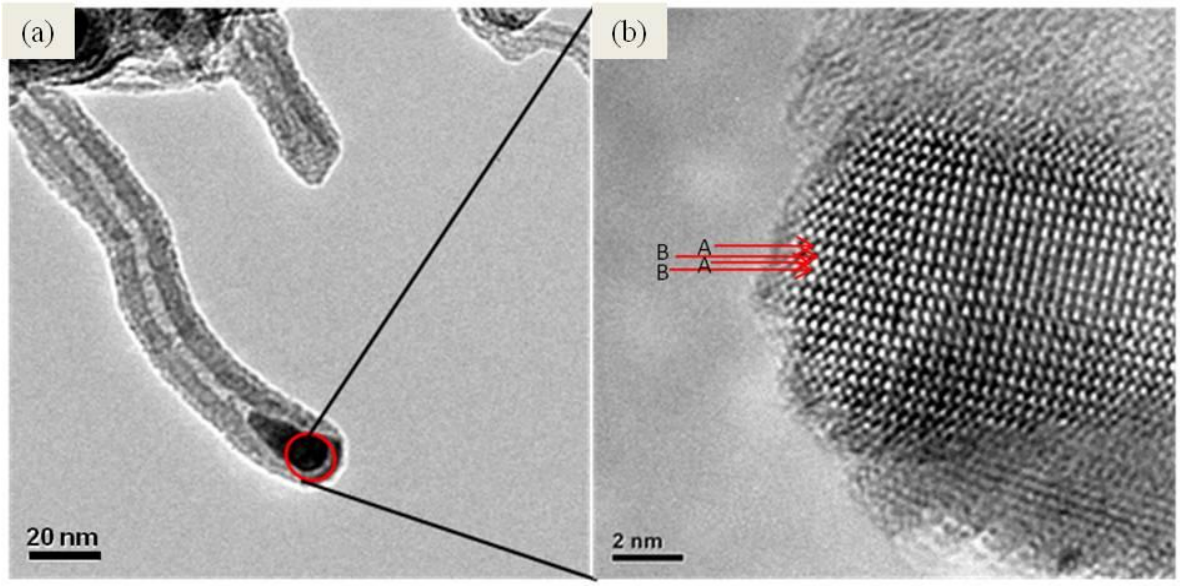

Figure 6.14 (a): TEM Images of the NiZnO grown CNTs (b): the ultra high resolution image of the particle at the tip of the CNT confirms the wurtzite crystal structure with the staking sequence as ABABAB.....

The yield of the Ni doped ZnO grown CNTs is pretty low. There might the two reasons for this, one is that it might be due to the low electron acceptance nature of the Ni doped ZnO. It has been observed by earlier studies[245,246] that Ni doping of ZnO make it more n-type. It is because the d-states of Ni appear near the Fermi level. The t2g orbitals overlap with the p-orbital of oxygen, which causes further splitting into bonding and anti-bonding orbitals. The bonding orbitals have lower energy so remain localized, while the anti-bonding orbital have higher energy and contain itinerant electrons. These itinerant electrons lie near the bottom of the conduction band thus giving rise to the higher conductivity. Secondly it is possible for the Ni^{+3} ions in the excited state to transfer their excitation energy to the nearby (few lattice sites away) trapped electron[247], which eventually causes recombination and gives rise to photon emission, thereby decreasing the charge transfer strength.

6.7): Growth of CNTs using Tb doped ZnO as Catalyst:

After the evaporation of the TbZnO pellet sintered at various temperatures upon the W substrates with Cr over layer, the samples were named after the sintering temperature as

TW1000, TW1050, TW1150 and TW1200. These were then placed in the CVD chamber to grow CNTs. The temperature was kept at 550C with nitrogen at flow rate of 100sccm and acetylene C_2H_2 as a carbon source with flow rate of 20sccm. The chamber pressure was kept at 2500mTorr and the process was deactivated after 15min. Before starting the process the chamber was evacuated below 5×10^{-6} mTorr to remove all the residual gasses. After the growth was completed the chamber was cooled down to 100C in nitrogen atmosphere and then left under vacuum overnight. The samples were then taken out and were inspected under the SEM. The SEM images show that all the CNTs are multi-wall with diameters in the range of 20nm to 40nm as shown in figure 6.15.

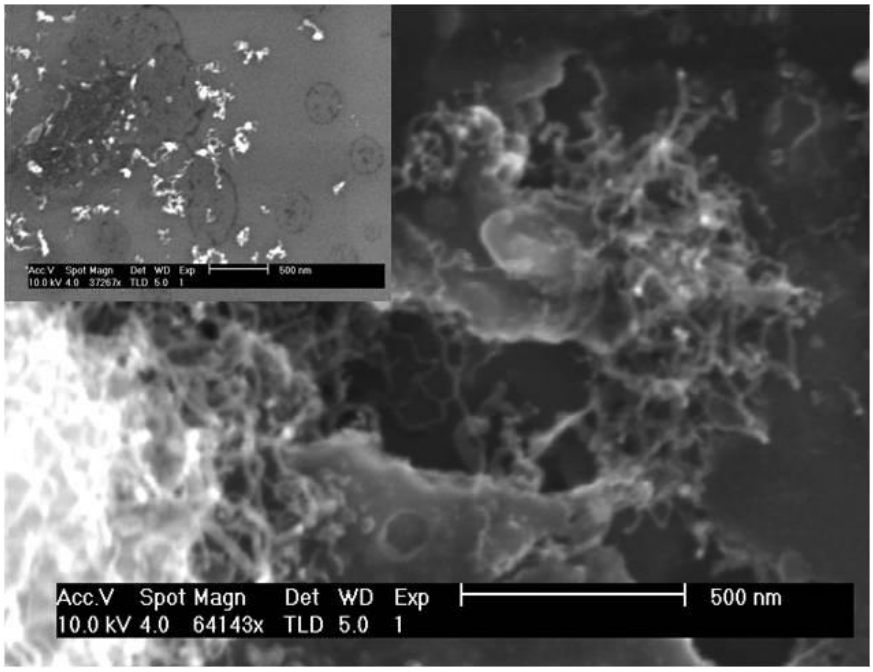

Figure 6.15 SEM images of TbZnO-CNTs. In the inset is the SEM image showing that almost every catalyst is nucleating a CNT.

From figure 6.15 it is clear that there is a range of diameters of the CNTs, which are attributed to the particle size distribution, because for uniform growth it is essential that all the catalyst nanoparticles should catalyse the hydrocarbon molecules at the same time and same amount. If the particles are not uniformly doped then there will be an anomaly in the growth which will give rise to CNTs with different morphologies and heights because of the catalyst composition[230]. The SEM image also shows that there is a mixture of growth modes

where some of the CNTs have grown through tip growth mode while others are through the base growth mode. This indicates that all the catalyst nanoparticles are not uniformly doped and that there is a difference in the composition of the dopant in the grains[230].

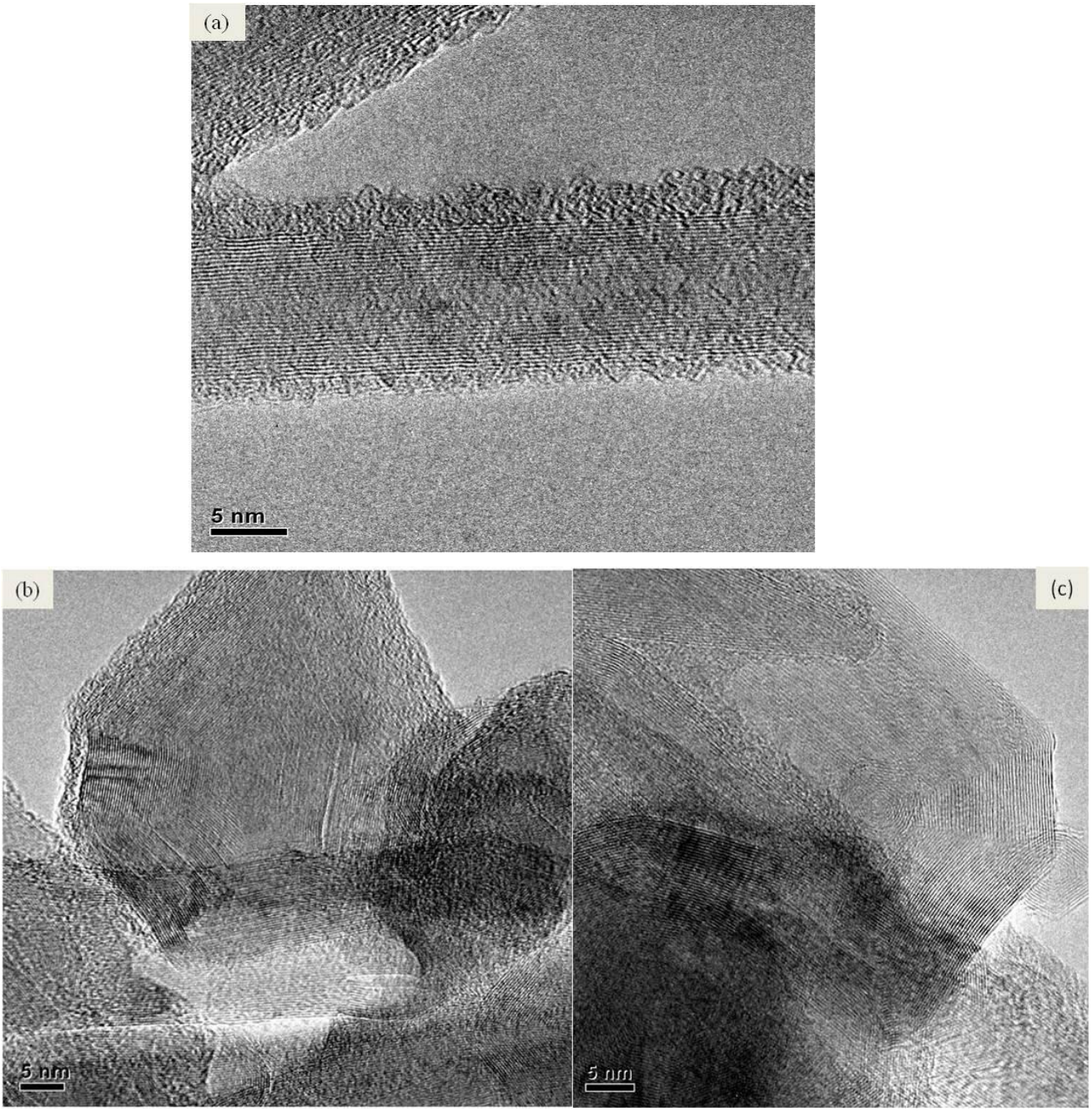

Figure 6.16 (a): HRTEM images of TW1000 grown CNTs showing the tubular and the graphitic nature of CNTs. (b): TW1150 grown CNTs showing the large number of graphitic shells with hexagonal geometry, (c): TW1150 grown CNTs with large number of graphitic shells. All the three images also show that the graphitisation decreases towards the inner side of CNTs.

It has been observed from the TEM images that the two parameters are quite prominent, one is the graphitisation and the other is the ratio of inner diameter of CNTs to the outer one. Both the parameters seem to be a function of lattice strain. The lattice strain at the edge dislocations remains higher than the centre of the particles[224]. The graphitisation of CNTs decrease from the outside to the inner side of the tube as shown in figure 6.16a & b. Additionally there is a reversible trend in the ratio of inner diameter of CNTs to the outer diameter, which exactly follows the trend of the lattice strain in the catalyst nanoparticles as observed from table 5.2 section (5.4) in the previous chapter. It has been observed in this study that the CNTs grown through the sample TW1000 have comparatively larger average inner diameter with few graphitic shells as shown in figure 6.16a, while CNTs grown through the sample TW1150C have a large amount of graphitic shells with a very small inner diameter as shown in figure 6.16b and 6.16c. This trend reverses for the sample TW1200C. The carbon diffusion through the catalyst particle increases with lattice strain, it might be because the lattice strain gradient is believed to be responsible for the drift velocity of diffusing material[228] and additionally it also reduces the activation energy[224]. The change in the inner diameter of CNTs do not follow the change in the lattice parameter, therefore it is believed that it might be because of the defect mediated strain. The lattice strain that arises from the surface defects (vacancies, ionic deficiency or impurity ions) of the catalyst nanoparticles controls the diffusion of carbon through the catalyst. The inner diameter of CNTs as a function of sintering temperature is shown in the figure 6.17.

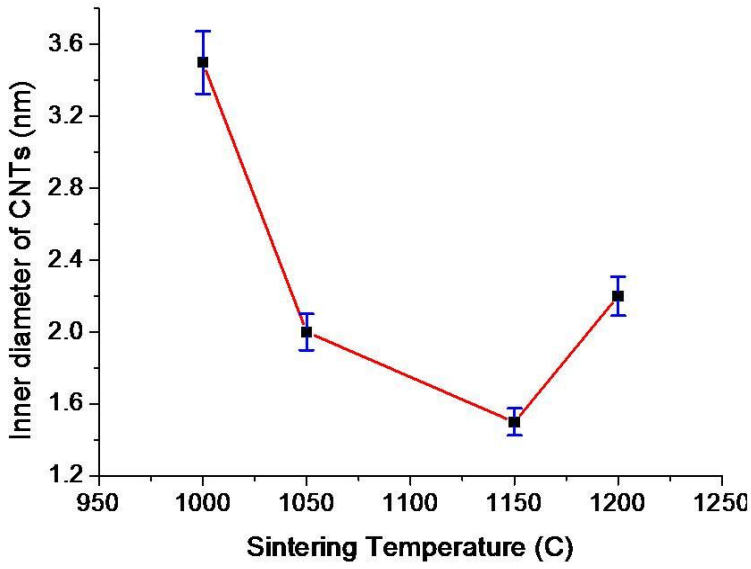

Figure 6.17 graph representing the inner diameter of CNTs as a function of sintering temperature of pellets. The change in inner diameter is because of the change in lattice strain.

The stress gradient, dislocation and vacancies give rise to higher diffusion of carbon through the catalyst[248], the mechanism was first proposed for stress dependent diffusion through Si by Laudon et al[249] . In this study strain dependent diffusion is proposed. On the one side of any dislocation the lattice is compressed and on the other side the lattice is stretched. This stretched side of the lattice is what gives rise to lattice strain and seems to be responsible of the adsorption of carbon atoms. According to Quyang et al[250] the lattice strain and compressive and thermal stresses are responsible for the mechanical behaviour of nanoparticles. The compressive stresses are considered responsible for the modulation of lattice parameter by changing the energy level of the bonding electron, while the lattice strain is responsible for the change in surface or interface free energy of the catalyst nanoparticles[251,252]. The lattice strain remains higher on the edge dislocations because it stabilizes the energy difference arising from the electronic coupling of adsorbates with the catalyst surface. The diffusion of carbon through the edge dislocations is highly favoured because of the enhanced adsorption energy[241]. Therefore it is strongly believed that it is the lattice strain that controls the carbon diffusion through the catalyst nanoparticles.

In so far as the morphology of CNTs is concerned the TEM analysis of the samples indicates that it consists of various structures, like straight long CNTs and just graphitic layers with hexagonal geometries which are hollow at the centres as shown in figure 6.16. The growth of CNTs through CVD is a continuous process, where a CNT will continue to grow until the carbon supply is stopped. It is believed that the graphitic layers with hexagonal geometry figure 6.16b are caused by the simultaneous decomposition of C_2H_2 molecule on the whole surface of Tb doped ZnO nanoparticles, which covers completely the outer surface of the catalyst and hinders the further supply of carbon to the catalyst particle, which results in yielding a hexagonally arranged graphitic layers without nucleating CNTs[230]. The presence of mixed valence cations in doped oxides gives rise to a charge transfer effect where the conversion of Tb^{+3} to Tb^{+4} ion produces an extra electron, which can be trapped by the local defect density of states on the surface[174]. The presence of mixed valence cations has been observed in section (5.3) through the XPS analysis of Tb doped ZnO. This clearly indicates that the stronger the charge transfer effect with higher lattice strain will give rise to higher decomposition rate of C_2H_2 molecules with higher diffusion of carbon. It is in accordance with the earlier study[230] , where the onion like structure has been attributed to the difference in composition of catalyst and faster decomposition rate of the carbon containing gas on the

whole surface of the catalyst particle. The change in the lattice strain as a function of sintering temperature has been observed from the XRD pattern discussed in section (5.4).

The elemental composition of the particle at the tip of a CNT (shown in figure 6.18) was investigated through EDS in the TEM and was observed the presence of five elements. The existence of copper is believed to be because of the copper grid and the carbon is because of the graphitic layers around the particle. This analysis confirms that the particle at the tip of a CNT belongs to TbZnO material, which confirms the active catalytic nature of Tb doped ZnO nanoparticles towards CNTs growth.

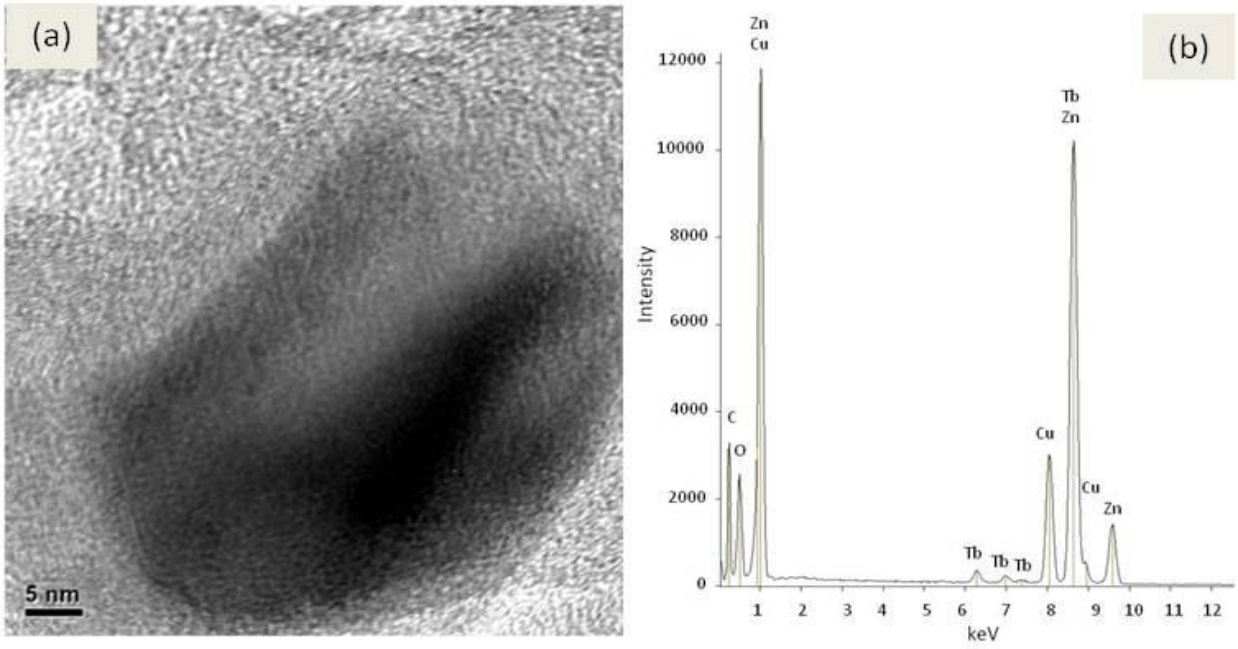

Figure 6.18 (a) TEM images of Tb/ZnO-CNTs (b) the corresponding EDS of the catalyst particle at the tip of the CNT.

6.8): Growth of CNTs using Ho doped ZnO as Catalyst:

In this section the growth of CNTs using Ho doped ZnO as catalyst is discussed. The sample was prepared through solid state reaction as discussed in section (4.2) by adding 5wt% Ho to ZnO. After thermal evaporation the samples were put in MPS1400 to grow CNTs. By using the growth temperature of 650C it was observed that Ho doped ZnO did not

catalyse the growth. When the temperature was increased to 750C growth was obtained. This is because temperature is believed to be the most important parameter affecting the kinematics and dynamics of the charge transfer[253]. The sample was then characterised through SEM to see the growth mechanism. It was observed from the SEM image that some of the CNTs grow through the base growth and some of the CNTs follow the tip growth mechanism as shown in figure 6.19.

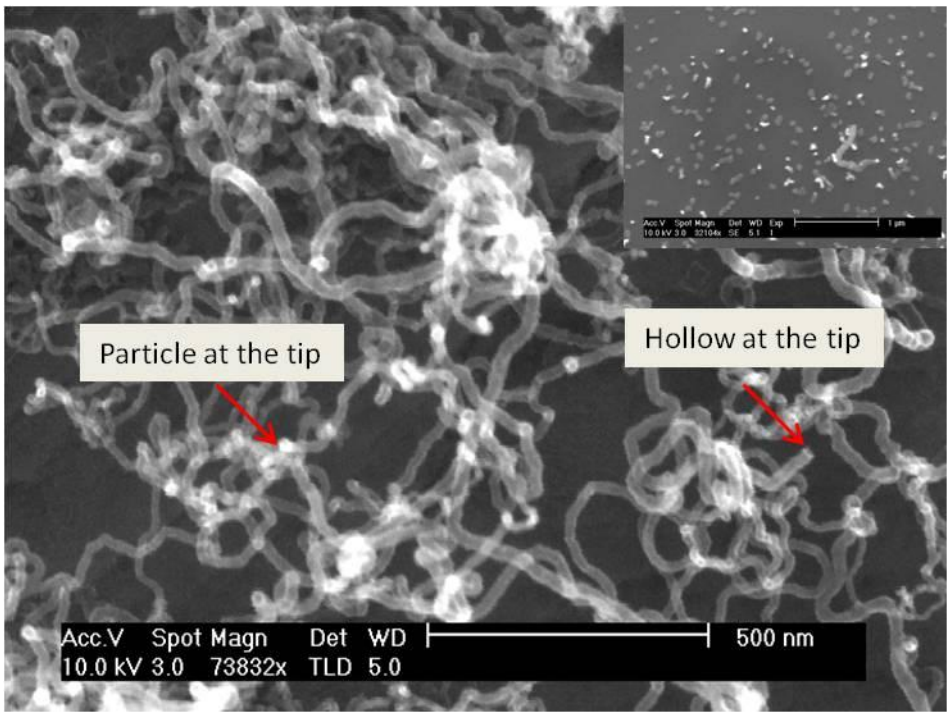

Figure 6.19 SEM image of Ho doped ZnO grown CNTs with particles at the tip and without catalyst particle at the tip of CNTs as shown by arrows. The image in the inset shows that CNTs have just started nucleating at 650C.

The SEM image shows that there is a very narrow distribution of CNTs diameters, which is because of the narrow particle size distribution. After thermal evaporation of the pellet the size and shape of the particles were quite uniform as has been discussed in section (5.8). Two types of CNTs have been observed that correspond to the two different growth mechanisms. One type of CNTs have are quite tabular with a particle at the tip indicating the tip growth process and the other is bamboo shaped CNTs with the compartments directed towards the tip indicating the base growth process[229] as shown in the figure 6.20, which implies that some of the grains are tightly bonded with the substrate and some have a weak

interaction with the substrate. Additionally the two different growth mechanisms might be caused by the two different chemical states of the catalyst particles[101].

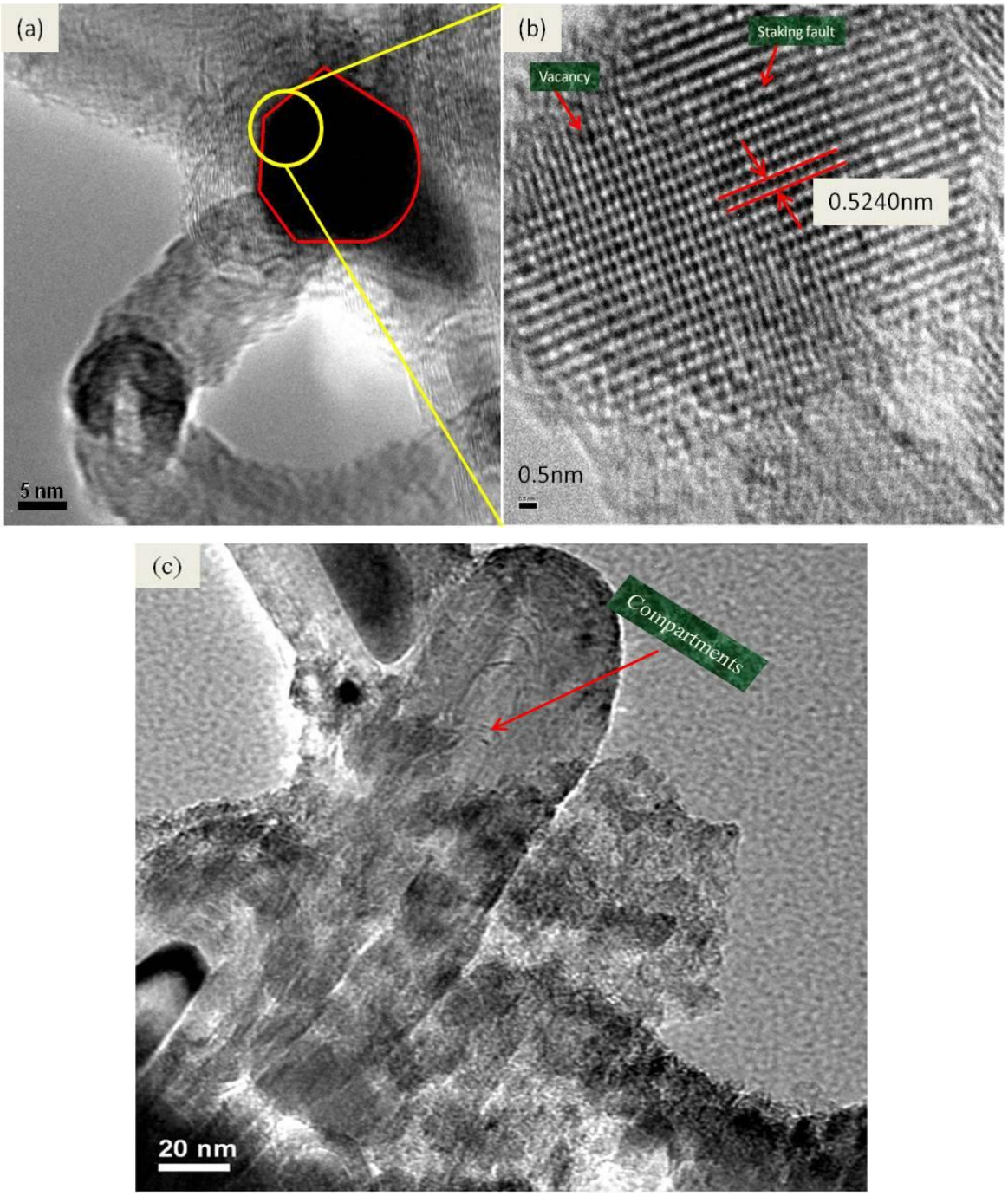

Figure 6.20 (a): HRTEM image of CNTs with particle at the tip showing hexagonal geometry; (b): HRTEM image of the particle at the tip of the CNT (c): low magnification TEM image showing the bamboo structure and the compartments (shown by arrow) are directed towards the tip of the CNT showing base growth process.

In catalyst support interaction the contact angle of the catalyst particle with the substrate defines the interaction. For larger contact angles the catalyst nanoparticles show weak interaction with the support and in this case the particle goes up and remains at the tip of the growing CNTs. While for smaller contact angles the catalyst nanoparticles remain attached to the substrate and the particle does not go up with the growing CNTs[254]. This may happen during the thermal evaporation of the pellet. In addition, the grains with varying chemical states give rise to different growth modes[101]. It has been observed through XPS [section (5.9)] that the dopant ions have mixed oxidation states in the ZnO matrix, which might affect the chemical state of the catalyst nanoparticles.

The TEM analysis of CNTs shows that the inner diameter and the number of graphitic shells of CNTs changes with lattice strain. The lattice strain plays an important role in tailoring the catalytic activity of the catalyst[225]. Shu et al[255] has pointed out that with increasing lattice strain the density of states becomes increasingly smooth at the valence band region and ultimately lead to a charge transfer between the two ions. Additionally the presence of mixed dopant ions in the ZnO matrix gives rise to charge transfer transition [either from metal to ligand or from ligand to metal] and is believed the main source of dissociating the acetylene molecule on the surface of catalyst nanoparticles and gives rise to CNTs growth upon diffusion through the catalyst.

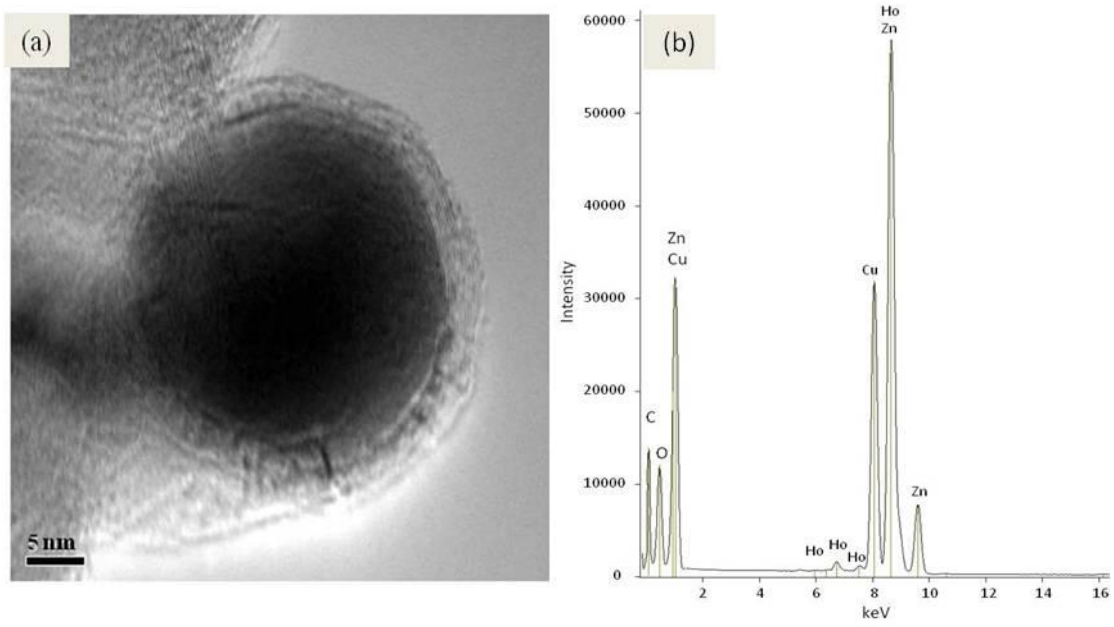

Figure 6.21 (a): TEM image of a CNT with the catalyst particle at the tip using HoZnO as catalyst. (b): the corresponding EDS spectrum of the particle at the tip.

The elemental composition of the particle at the tip of CNTs (shown in figure 6.21) was confirmed using two techniques; first the high resolution TEM image (in figure 6.20b) of the particle at the tip confirms that the lattice parameter of 0.5240nm corresponds to ZnO crystal structure, second the elemental composition analysis of the particle shown in figure (6.21b) was carried out through EDS in the TEM, which confirmed the existence of Ho, Zn and O.

6.9): Growth of CNTs using Sm doped ZnO as catalyst.

Samarium doped ZnO pellets were prepared through solid state reaction over a range of temperatures and were thermally evaporated on Si substrates using Cr as over-layer. The sample was then put in the CVD chamber to grow CNTs using these Sm doped ZnO grains. It was observed that the process was unsuccessful regarding the growth of CNTs. the process was repeated for various growth temperatures like 650C, 750C and that 850C for various sample sintered at different temperatures.

In the doped metal oxides the charge transfer mechanism remains ineffective if dopant cations remain in their minimum or maximum oxidation state[174]. This is because the energy gain for the local density of states is less than the amount of energy required to transfer an electron from Sm^{+3} ions. Since in this study it has been observed through the XPS analysis of Sm doped ZnO (section 6.6) that the dopant ions remains in the +3 oxidation state (which is the maximum oxidation state of Sm) in the ZnO host material and there is no Sm in +2 oxidation state. Therefore there will be no charge transfer process and hence no dissociation of hydrocarbon molecules.

6.10): Catalyst Free growth of CNTs:

Catalyst free growth of CNTs was carried out on a tungsten substrate. The substrate was first etched using hydrofluoric acid (HF) for about thirty minutes. It was observed that some parts of the sample have been etched successfully. Usually HF is used to remove the native oxides from a metallic surface. The dangling bonds on the surface are more reactive and quickly react with other species like hydrogen (H_2)[256]. The sample was then rinsed in DI

water and was placed in the CVD chamber. The chamber was cleaned properly, in a sense to avoid any chances of any other metals especially the presence of transition metals like Ni, Fe and Co and was heated to 700C in the presence of ammonia (NH_3). After the chamber gains the temperature the carbon containing gas acetylene (C_2H_2) was allowed into the chamber for the growth of CNTs. The process was deactivated after 25min. The chamber was left to cool down to room temperature and then the sample was taken for further investigation through SEM.

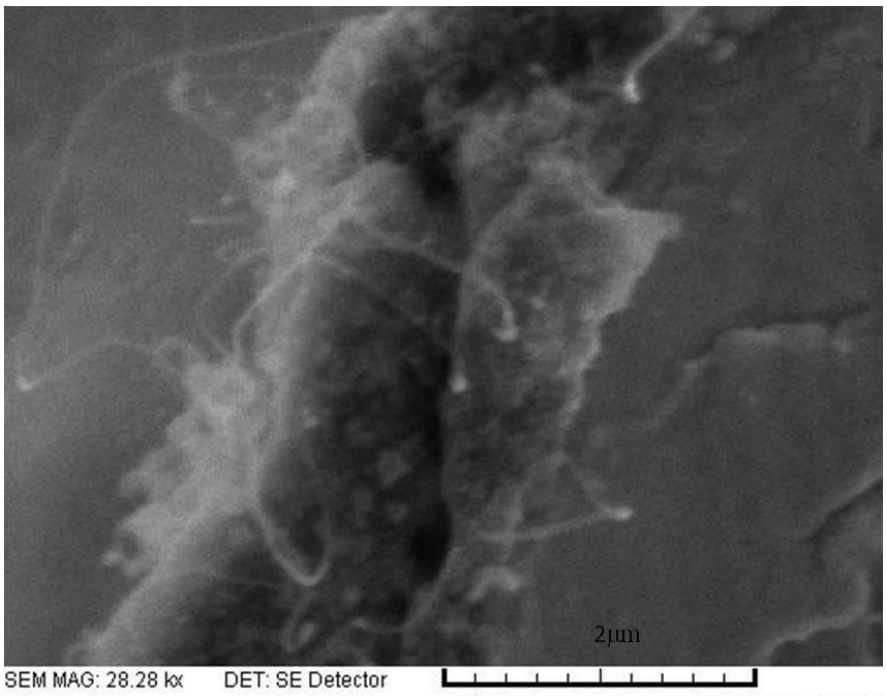

Figure 6.22 catalyst free growth of CNT on tungsten substrate

It is very clear from the figure 6.22 that CNTs have been grown in the split area of the sample, which is believed to be a high lattice strain area because the slip steps appear on the surface because of the higher lattice strain[257]. The lattice strain is believed to broaden the width of the density of states and with increasing strain the density of states is becoming smoother and leads to a charge transfer between the two ions[258]. This charge transfer dissociates the hydrocarbon molecule and because of the higher lattice strain the carbon atoms start diffusing through the surface and gives rise to CNTs growth.

6.11): Conclusion:

This chapter describes the growth of CNTs using Ni, NiO and doped (Cu, Ni, Sm, Tb, & Ho) ZnO catalysts through DC-PECVD and thermal CVD. It was observed that stable DC plasma with power of about 44W promoted the alignment of CNTs. In addition, novel metal oxide catalysts were used for the growth of CNTs through CVD. Those catalyst nanoparticles where the dopant ions were in mixed oxidation state, gave rise to CNTs growth, which was attributed to the intragrannular charge transfer transition between the metal and ligand ions. This charge transfer process seems to be responsible for back donation of electrons to the antibonding orbitals of acetylene molecule and dissociate it. Furthermore the lattice strain of the catalyst nanoparticles helps diffusion of carbon atoms through the nanoparticles and gives rise to CNTs growth. The lattice strain of the individual catalyst nanoparticles seems responsible for the morphology of CNTs. It has been observed that higher the lattice strain the higher will be the diffusion of carbon atoms through the catalyst nanoparticles, which in turn will affect the inner diameter and the number of graphitic shells around the CNTs. A new growth mechanism has been proposed for the growth of CNTs using metal oxide nanoparticles as catalysts and for catalyst free growth of CNTs.

7.1): Introduction:

Field emission is a quantum mechanical phenomenon where the electrons are extracted from the solid through electric field. CNTs are considered an excellent field emitter because of low threshold electric field and high brightness. In this chapter the current-voltage (I/V) characteristics of CNTs grown by using a range of catalyst have been discussed. The emission current stability is measured as a function of time. The field emission patterns are collected on a yttrium aluminium garnet (YAG) scintillator in a triode configuration.

7.2): Field Emission Set Up:

For field emission experiments it is necessary to have a system that is capable of achieving ultra-high vacuum conditions. The intense electric field may cause ionization of the existing gas molecules that might lead to an arc that might cause to damage the sample. To obtain field emission from carbon nanotubes a vacuum in the range of 10^{-8} to 10^{-11} mbar is needed[259].

The system consists of a stainless steel chamber with two pumps (rotary and turbo pumps) and a baking unit. The rotary pump is used to create vacuum of the order of 10^{-5} mbar and the turbo pump takes the vacuum down to 10^{-9} mbar. The field emission pattern is observed through a glass window that is fixed in the UHV system as shown in figure 7.1.

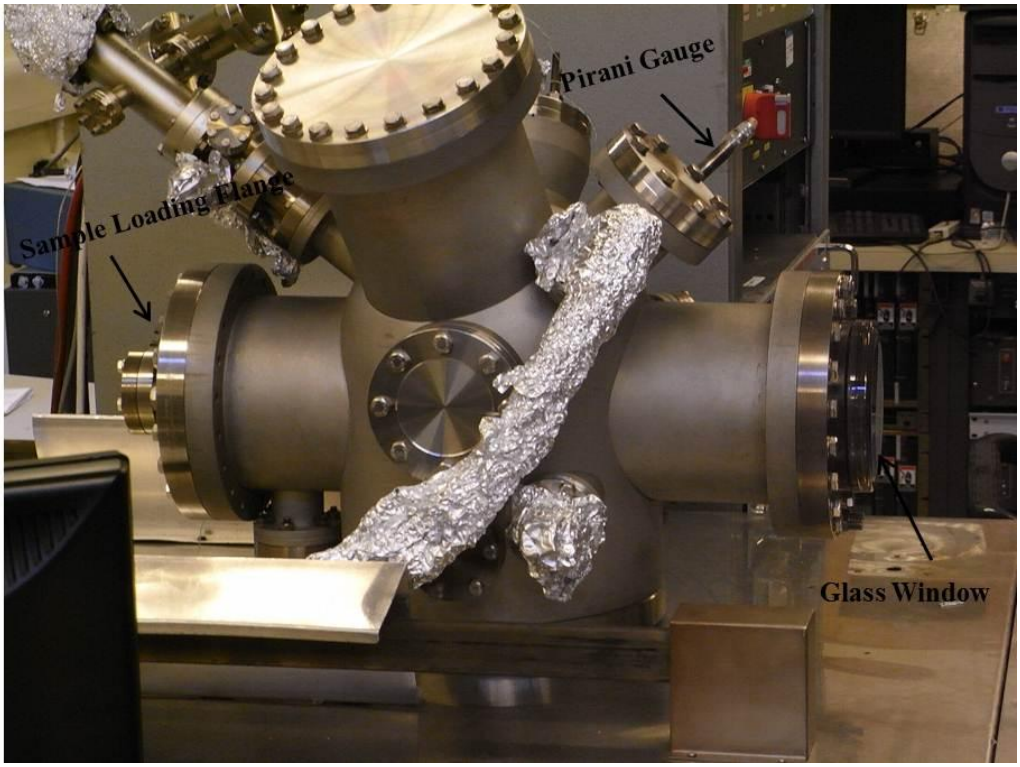

Figure 7.1 a photo of the chamber which was used for field emission experiments.

An ion gauge and pirani gauge are used for pressure measurement in the main vacuum chamber. The chamber is baked at 160C for 24 to 30 hours. The baking temperature is controlled through a thermocouple attached at the outside of the chamber. The baking of the chamber helps in removing the humidity and accelerates the removal of the gases from the chamber.

7.3): Design and Fabrication of Field Emission Setup (Triode Configuration)

Carbon nanotubes are considered to be an electron emission source with high brightness and small energy spread[119]. The CNTs grown sample is mounted on the sample holder and is kept at negative potential. A copper grid is separated from the sample holder through 250µm thick PEEK (poly ether ether ketone) sheet. The copper grid is kept at ground

potential to be used as extractor. A Yttrium Aluminium Garnet (YAG) is used as the screen for observing the field emission pattern and is kept at positive potential. The YAG screen is separated from the extractor through peek sheets of thickness of the order of about 1mm as shown in figure 7.2.

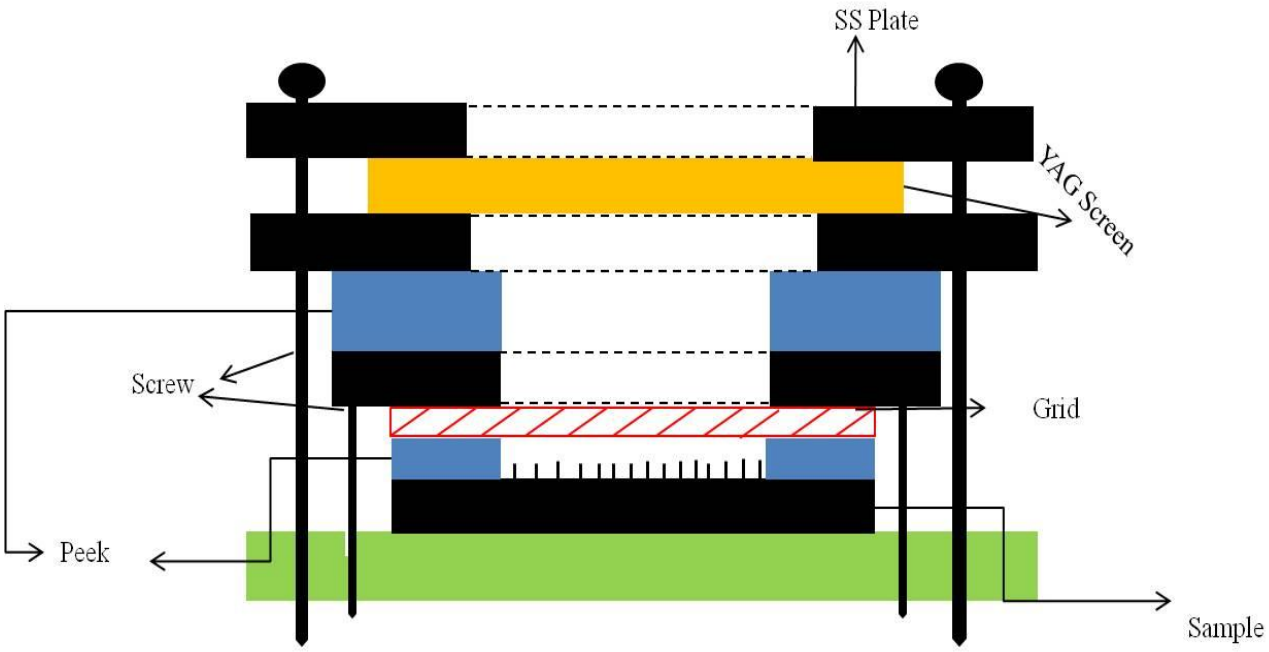

Figure 7.2 Schematic of the triode configuration for field emission, showing how the field emission pattern is observed on the YAG scintillator.

The sample holder consists of a stainless steel (SS) plate with two pieces of tungsten plate of about 50µm thickness is spot welded on each side of the SS plate to hold the sample as shown in figure 7.3. The purpose of the triode configuration is to achieve a relatively low control voltage. Grids of different material and density were used to find out the best value of anode current. Since the electric field is a function of the applied voltage and that of the distance between the electrodes therefore the applied electric field will not be smooth and uniform if a grid is used as an extractor. The field non-uniformity will be greater for stainless steel (SS) woven grid and will be less for copper grid. This is due to the higher surface uniformity of the copper mesh than the SS one. Additionally because of the non-uniform surface, the exact width of the gap between the SS wires cannot be determined accurately.

The width of the SS wire is about 100µm and the gap is 160 µm so the transparency for the emitted electrons is nearly 60% for SS grid.

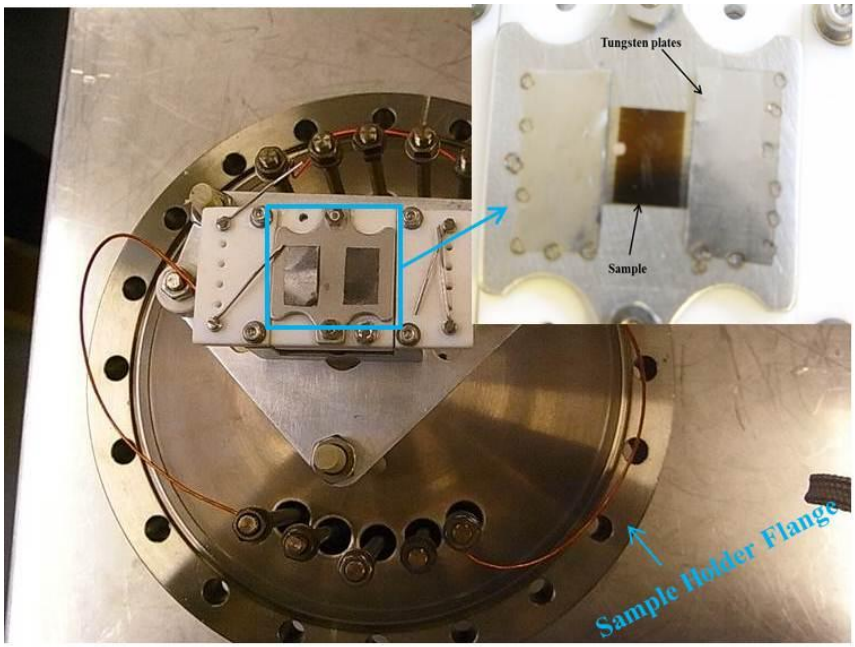

Figure 7.3 Photo of the flange with sample holder assembly, in the inset the sample is held in between the two tungsten plates

The sample loading and unloading involves the opening of the chamber to the atmosphere and is carried out by using the liquid nitrogen. Since the nitrogen is an inert gas therefore it is used to reduce the adsorption of water vapours on the walls of the chamber. After opening the chamber the sample holding assembly is separated and the flange is fitted again to reduce the chances of chamber contamination.

7.4): Current–Voltage characteristics of the transition metal (Cu and Ni) doped ZnO grown CNTs

The CNTs were characterised for their emission characteristics in the ultra high vacuum chamber described in figure 7.1. The emission current as a function of extraction voltage was then analysed through the Fowler-Nordheim (FN) plot.

$$\frac{I}{V^2} = A \times 1.42 \times 10^{-6} \frac{F^2}{d^2 \phi} \beta^2 \exp\left(\frac{10.4}{\phi^{1/2}}\right) \exp\left(\frac{-6.44 \times 10^7 \phi^{3/2} d}{\beta V}\right) \qquad (7.1)$$

The plot of 1/V vs ln(I/V^2) ideally gives a straight line. The field enhancement factor β can easily be calculated from the slope of the straight line, if the distance between the two electrodes and the emitting area A is accurately measured. In this experiment the emission current of 110nA was recorded at 1050V. It was observed that at each increase in voltage there was an abrupt increase in the emission current. Initially the voltage-current characteristics of the sample were measured only up-to 1.75kV. Further increase in applied voltage causes break-down and the huge amount of current limits the power supply. The emission current as a function of applied voltage of the first experiment with the corresponding FN plot is shown in the figure 7.4.

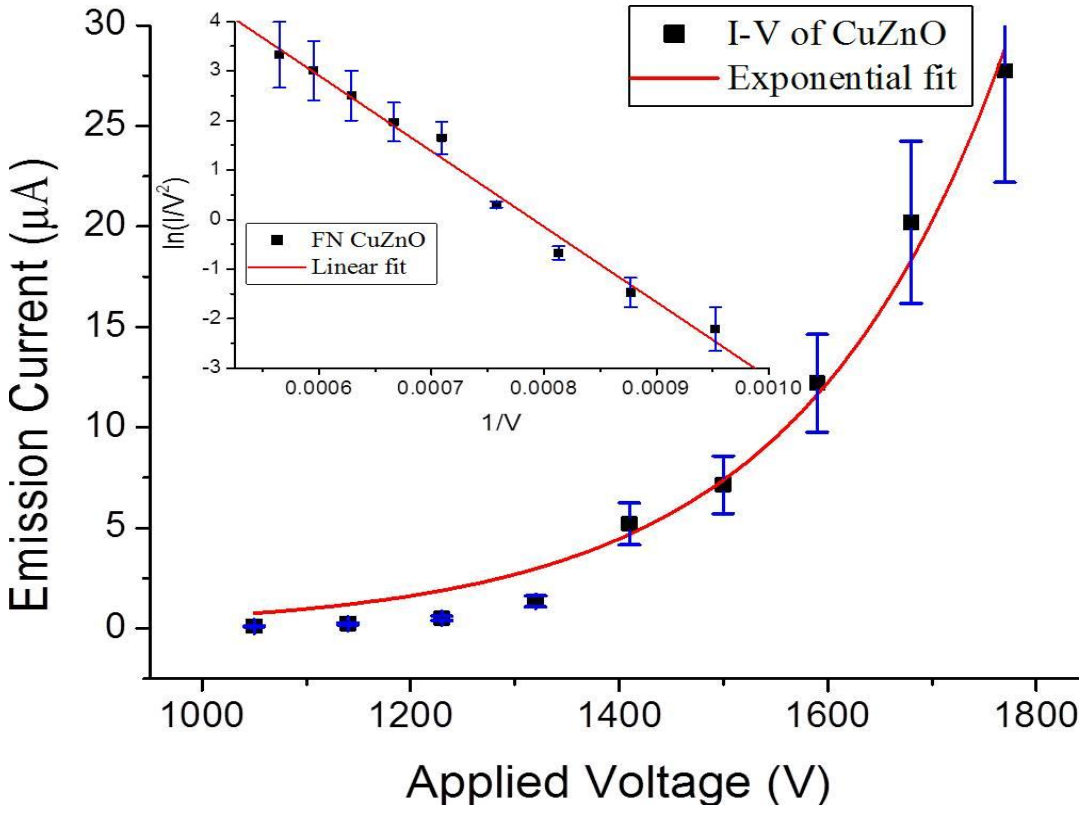

Figure 7.4 the first I/V characteristics of the CuZnO grown CNTs, where at low voltage high and very unstable emission current is observed. In the inset is the corresponding FN plot.

The first measurement of I-V characteristics of the CuZnO grown CNTs shows that the increase in emission current is quite high with a small increase in voltage. The turn on voltage for the first measurement is 1053V with 110nA emission current that seems reasonable but the rise in emission current with each applied voltage was quite unstable. The more likely reasons for this behaviour are the effect of adsorbates and the effect of the catalyst-support interaction[260].

In field emission experiments, the emission current is very sensitive to the cathode surface, where the adsorbates play an important role in the stability and the amount of emission current. Vacuum break down occurs in strong electric field and the field emission process is considered an important factor that initiates it. The following two are the more likely reasons for the soft break down in this study.

i): If the applied voltage is increased, an over-current followed by resistive heating on weakly contacted electrodes may result in thermal destruction of the materials to break off, and evaporate into vacuum[264], The evaporated particles (Impurities either on the grid or on the cathode) become charged and accelerated toward the anode to induce serious vacuum breakdowns or vacuum discharge.

ii): The CNTs might get heated due to self heating process by high emissive current and may gives rise to structural deformation[264]. The high emissive current at low voltage can cause a high electron bombardment on the anode (Grid) and cause evaporation of the material on the substrate and the scintillator[262].

After successive operations of the field emission system and soft breakdowns the adsorbates were mostly eliminated from the surface and the emission current became stabilised. This time higher voltage was required for the same emission current. The applied voltage across the sample was increased systematically with a step of 60V and observed the current for each increase. The data for the emission current as a function of applied voltage for the CuZnO grown CNTs is shown in the table 7.1. The I-V plot of the sample is quite symmetric and there is no sudden drop or rise in the emission current with the increase of applied voltage. This is a good indication towards the removal of adsorbates. The corresponding F-N plot is a straight line, which confirms the field emission.

The field emission characteristics from NiZnO grown CNTs was a bit different from that of the CuZnO grown CNTs in the sense that there was no abrupt increase in emission current. The emission current increases exponentially with each step of voltage. There is very

small deviation from an ideal linearity in the middle of the line. This is similar to that of CuZnO grown CNTs and is attributed to the thermal evaporation of CNTs and the subsequent increase is attributed to the adsorbates effects that lower the work function of the emission sites and causes to increase in the emission current.

It has been observed by Dean et al[261] that some of the species like H_2, H_2O, CO and CO_2 exist in the vacuum chamber during the field emission process. These adsorbed gas molecules are attracted towards the tip of CNTs and form stable complexes with the carbon atoms of CNTs that causes reduction in the work function. This decrease in the work function results in high emission current in the low voltage region like 1.374kV to 1.435kV. As the voltage increases above 1.5kV a soft breakdown occurs that limits the power supply for current measurement. This soft breakdown is used to clean the surface of the sample from different adsorbates[262].

The two most important parameters are taken into account to see the field emission characteristics of both the samples (CuZnO and NiZnO grown CNTs). One is the turn on field and the other is the emission current stability. The emission current density is an important parameter of the field emission, but cannot be estimated in this study because of the following two reasons.

i): One is that the CNTs are randomly oriented and the number of CNTs per unit area cannot be correctly estimated, additionally the adsorbates effect cannot be eliminated therefore the true current density cannot be calculated. Additionally all the CNTs in the sample do not have the same structure.

ii): Although it is believed that most of the adsorbates have been removed during the soft breakdown but it seems improbable to remove all of them completely.

The turn on fields for both the samples was calculated from the applied voltage and the distance between the electrodes. Since the distance between the electrodes is 300μm therefore the turn on field is 3.63V/ μm and 3.66V/ μm for CuZnO and NiZnO grown CNTs respectively. The emission current as a function of applied voltage and the corresponding FN data for both the samples are given in table 7.1.

CuZnO (CNTs)				NiZnO (CNTs)			
Applied Voltage (V)	Emission current (μA)	1/V	$In(I/V^2)$	Applied Voltage (V)	Emission current (μA)	1/V	$In(I/V^2)$
1090	0.022	0.00092	-3.81671	1100	0.011	0.00091	-4.5099
1150	0.035	0.00087	-3.35241	1150	0.026	0.00087	-3.6497
1210	0.062	0.00083	-2.78062	1200	0.035	0.00083	-3.3524
1270	0.095	0.00079	-2.35388	1250	0.059	0.0008	-2.8302
1330	0.19	0.00075	-1.66073	1300	0.098	0.00077	-2.3228
1390	0.35	0.00072	-1.04982	1350	0.165	0.00074	-1.8018
1450	0.5	0.00069	-0.69315	1400	0.243	0.00071	-1.4147
1510	0.73	0.00066	-0.31471	1450	0.294	0.00069	-1.2242
1570	0.95	0.00064	-0.05129	1500	0.45	0.00067	-0.7985
1630	1.8	0.00061	0.587787	1550	0.716	0.00065	-0.3341
1690	2.7	0.00059	0.993252	1600	0.97	0.00063	-0.0305
1750	4.3	0.00057	1.458615	1650	1.34	0.00061	0.2927
1810	7.2	0.00055	1.974081	1700	2.28	0.00059	0.8242
1890	12.5	0.00053	2.525729	1750	3.65	0.00057	1.2947
				1800	5.32	0.00056	1.6715
				1850	7.64	0.00054	2.0334
				1900	9.58	0.00053	2.2597
				1950	12.16	0.00051	2.4982
				2000	13.95	0.0005	2.6355

Table 7.1 the emission current as a function of applied voltage obtained from both the CuZnO and NiZnO grown CNTs through field emission.

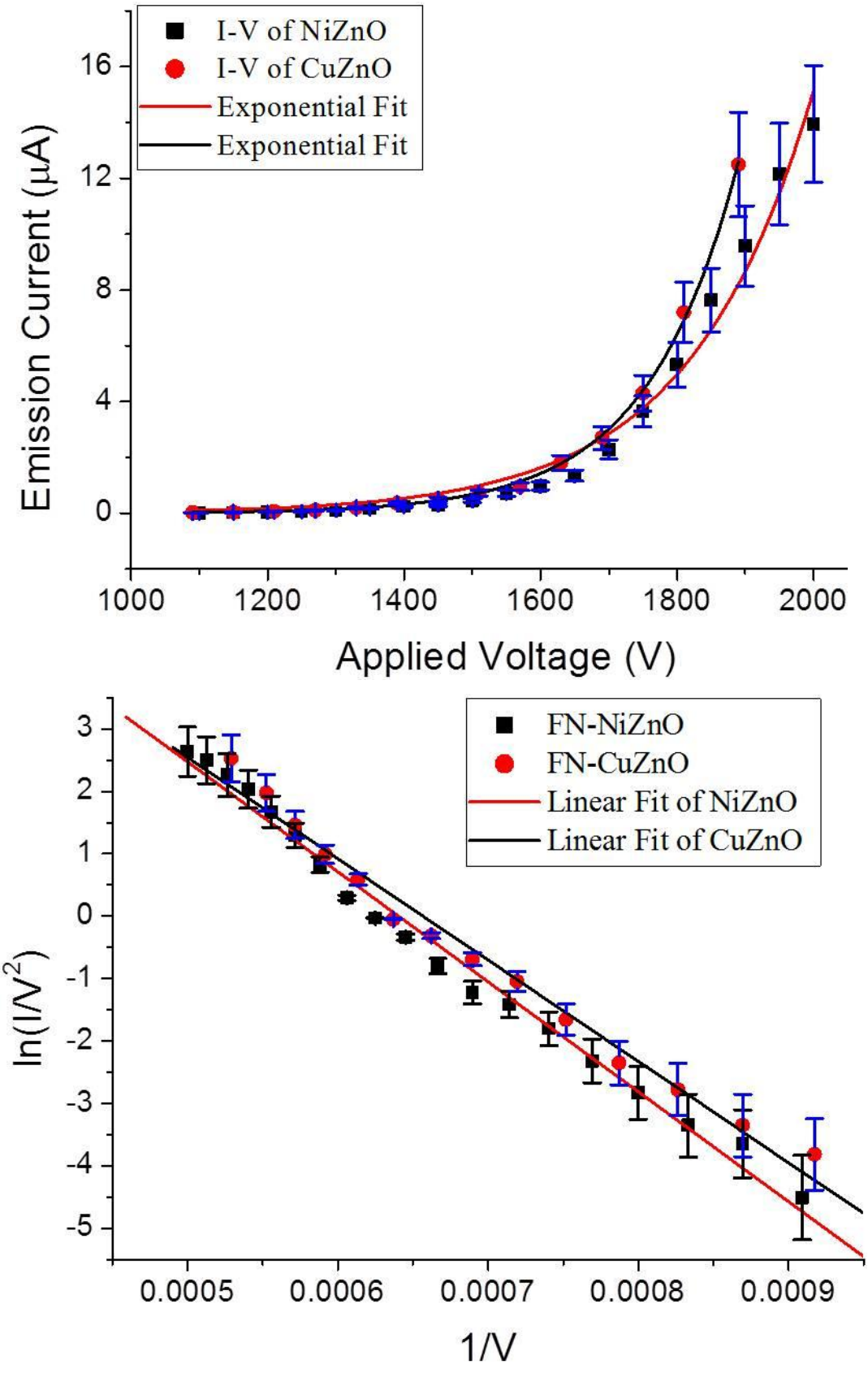

Figure 7.5 (a) The I-V of CuZnO and NiZnO grown CNTs (b); The corresponding FN plots

After the field emission process was completed the sample was checked under the SEM for any possible CNTs destruction. It was observed that some of the CNTs were peeled off from the substrate. It is because the chemical bond strength between the substrate and CNTs is lower than the bond strength between carbon molecules. Therefore it seems more probable that the resistivity at the joints between the substrate and CNTs will be higher than that of between the carbon atoms. Similarly the temperature will be higher at high resistance zones and hence causing to peeling off the CNTs from the substrate, which is known as a thermal run-away mechanism and is considered responsible for the initiation of vacuum breakdown[263]. This might be the possible reason for the vacuum breakdown that happened in the measurement of I/V characteristics of the samples for field emission.

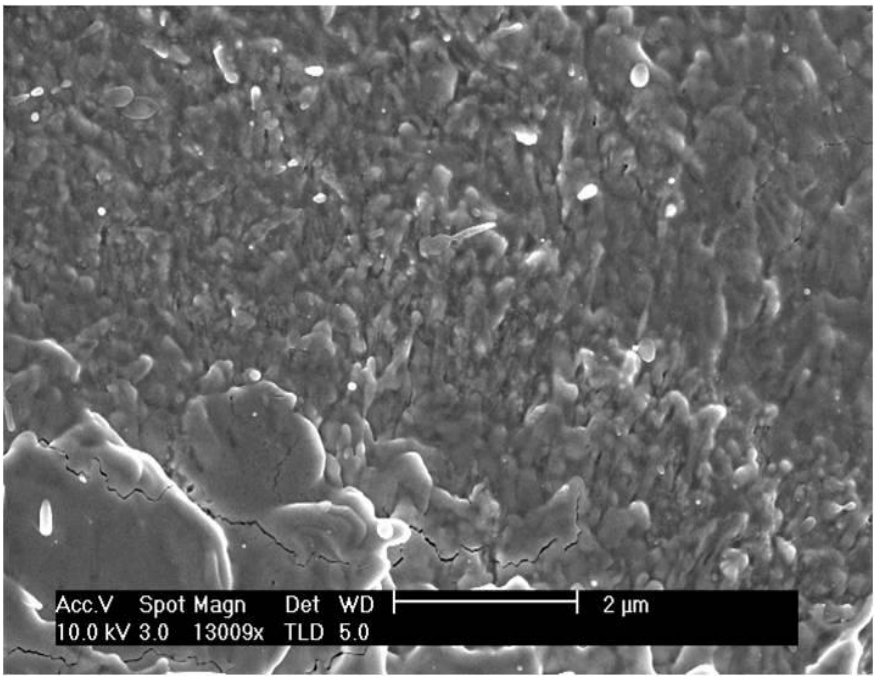

Figure 7.6 location where CNTs have been peeled off from the substrate during field emission.

The high electron emission from the CNTs increases the local temperature and causes burning the emitter[264] and may cause evaporation of some of the carbon and other adsorbate molecules. These molecules are then ionised by high temperature and the electric field. These ions cause a charge build-up in the gap between the two electrodes (sample and the grid) and eventually cause a breakdown[265]. It is also believed that electric field can induce structural damage to CNTs, like a very high electric field of the order of 100V/µm opens the tip of

CNTs and shortens them[266,267]. In this study the field strength ranges from 3V/ µm to 5.5V/ µm, which is very low for inducing any structural damage in CNTs, but its effect regarding the ionisation of carbon or any other residual molecules cannot be excluded.

7.4.1): Field emission patterns from transition metal doped ZnO grown CNTs

The field emission patterns from the CNTs using CuZnO and NiZnO as a catalyst were obtained on a YAG scintillator. The CNTs were grown using the CVD process as discussed in section (6.5 & 6.6). The low magnification SEM image of the sample is given in figure 7.7. The sample was then loaded on the sample holder. The whole assembly was then put in the UHV system. The system was baked for about 12 hours. Field emission experiment was carried out when the pressure came down to 2×10^{-9} mbar.

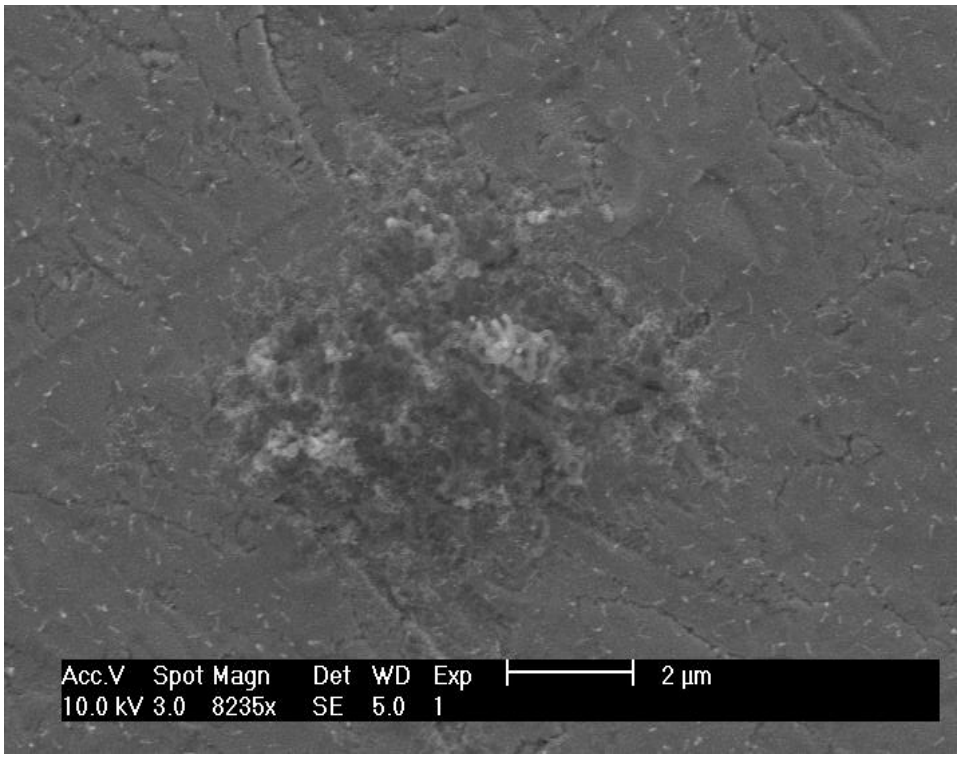

Figure 7.7 Low magnification SEM image of the CuZnO grown CNTs, showing a bunch of CNTs and the CNTs scattered around the sample.

The patterns were captured by a digital camera through a glass window in the UHV chamber. The first spot appeared on the YAG screen at 1090V with a current of about 22nA. It was observed that with the increase of the applied voltage, the emission current was increasing and many spots start appearing on the screen. These spots were getting intense and broadened with increasing applied voltage until the breakdown occurred. Since the CNTs of CuZnO are quit weakly attached to the substrate therefore in addition to the adsorbate effect, the peeling of CNTs from the substrate with the applied field also seems to be a factor of breakdown occurrence. After few soft breakdowns most of the adsorbates were removed from the surface of the sample and the field emission became stable. The emission patterns after the stabilised field emission are given in figure 7.8.

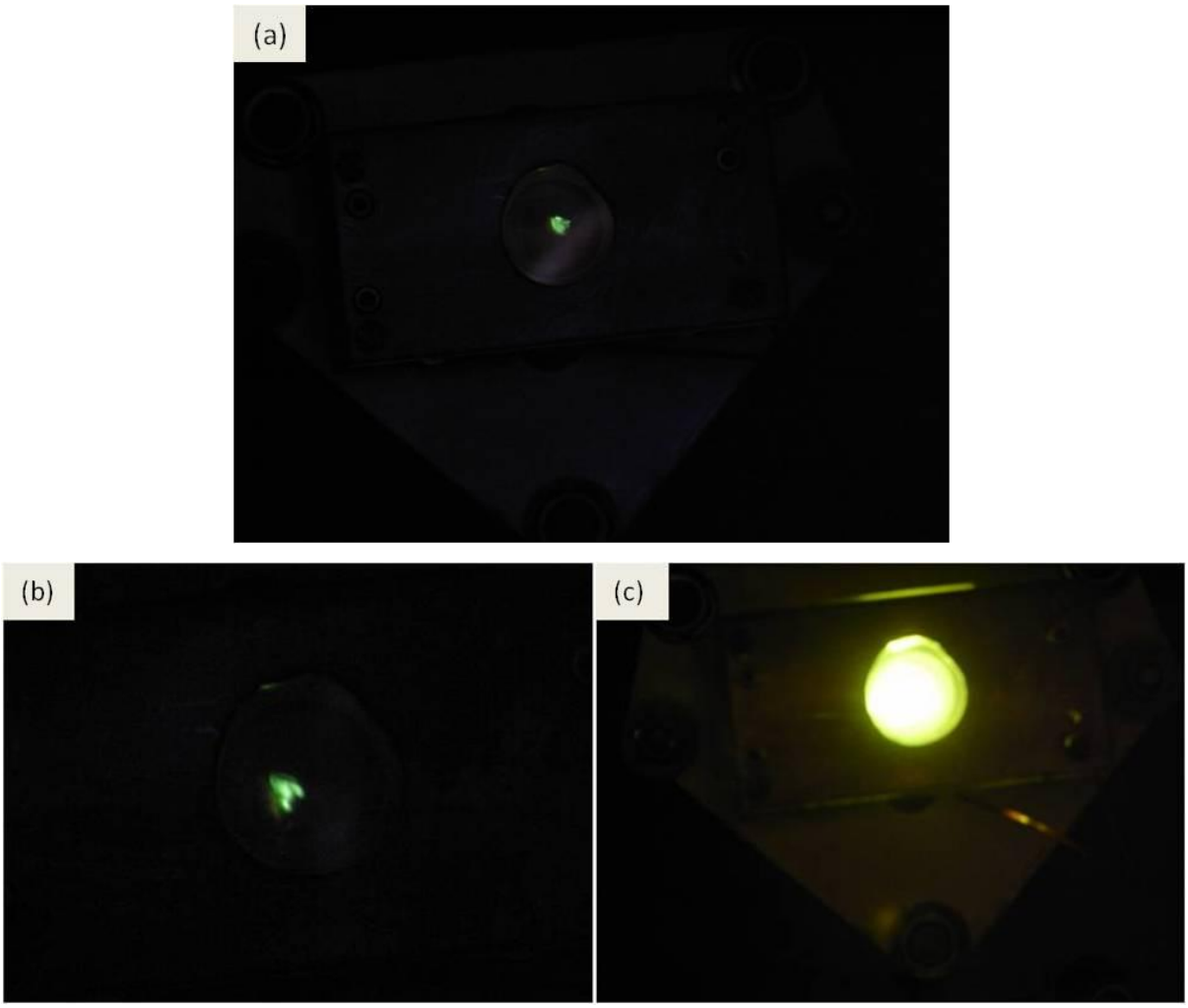

Figure 7.8 Field emission patterns of CNTs on Tungsten substrate using CuZnO as a catalyst with Cr as buffer layer. The patterns show the emission current as a function of increasing voltage: (a): 1.090kV, (b): 1.5kV and (c): Breakdowns flash at 2kV.

The field emission patterns from Ni doped ZnO grown CNTs were obtained through the same process as that for the Cu doped ZnO grown CNTs. It was observed that NiZnO grown CNTs produces less amount of adsorbates and have a very strong interaction with the substrate. These CNTs do not come off the substrate at the applied voltage of 2kV. The emission current obtained from the NiZnO CNTs is about 14μA at 2kV. The low magnification SEM image [figure 7.9] of the CNTs was taken to make correspondence with the emission pattern shown in figure 7.10.

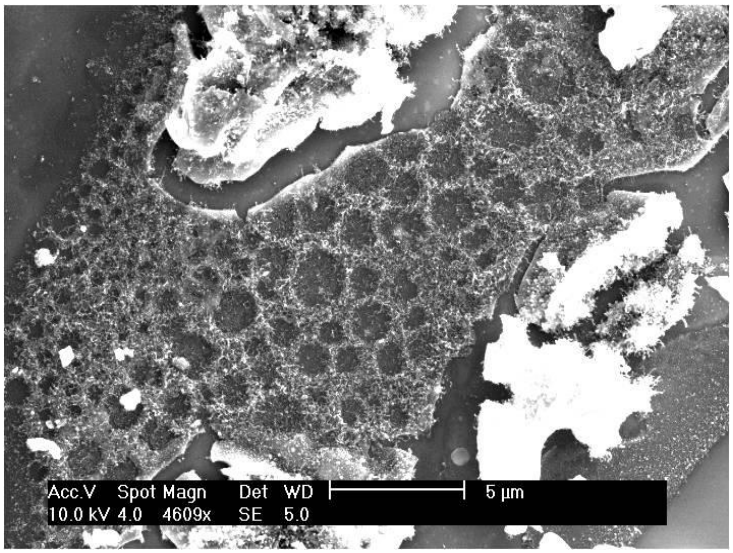

Figure 7.9 Low magnification SEM image of NiZnO grown CNTs, showing an area in the sample used for fields emission.

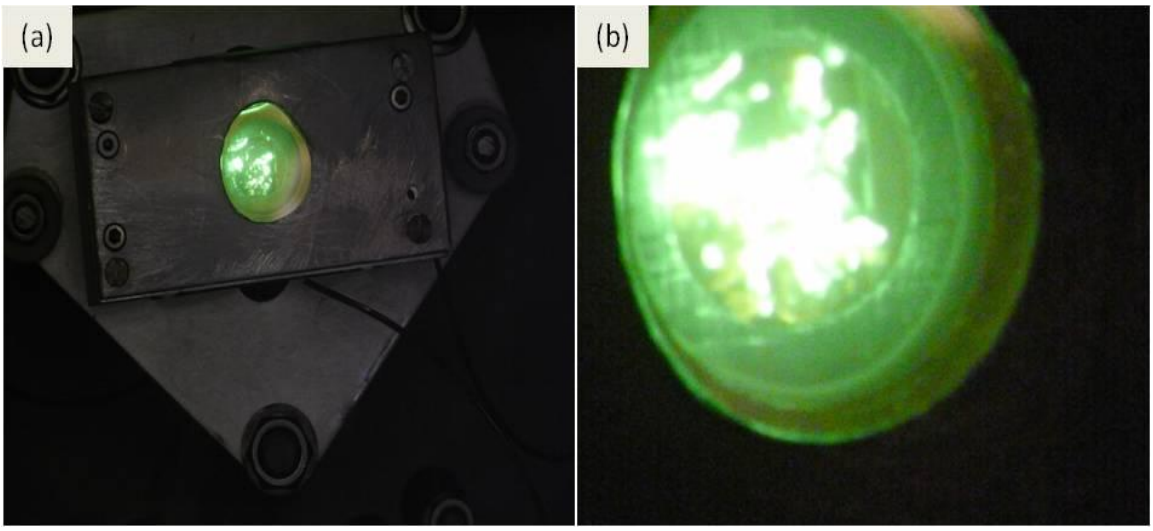

Figure 7.10 The field emission patterns obtained from the sample of figure (7.9) at (a): 1.5kV (b): 2.0kV

7.5): Current–Voltage characteristics of the rare earth doped ZnO grown CNTs

The CNTs were grown using CVD with Tb and Ho doped ZnO as the catalysts on Cr coated Si substrate. The Cr was evaporated thermally to make a conducting path to the CNTs on the surface. To observe the field emission from the CNTs using rare earth doped ZnO the sample was placed in the UHV chamber and baked the system for about 12 hours. After the system was cooled down, the emission current was observed as function of applied voltage. A range of voltages were applied to see the emission current characteristics of the sample. The voltage was applied from an external source and the current was observed through a pico-ameter. The first spot was observed at 1050volts with emission current of 13nA. After that the emission current used to increase with increasing applied voltage. The voltage was increased with a step of 50V and recorded the current at each step.

The CNTs grown from Tb and Ho doped ZnO exhibit excellent emission characteristics. It might be because most of the CNT have either open tips or closed tips with catalyst particles at the bottom. The open and closed tip CNTs have higher density of states near the Fermi level, which causes high emission current at low fields[268,269]. The turn on voltage was found to be 1000V and 1050V for Ho and Tb doped ZnO respectively. The respective emission current was recorded as 17nA and 13nA for both the samples respectively. The corresponding field emission patterns are shown in figure 7.14a and 7.16a for HoZnO and TbZnO respectively. Since the field enhancement factor for the non-aligned CNTs is negligibly small[270] and cannot be taken into account therefore the estimated turn on field is 3.3V/μm and 3.5 V/μm for the Ho and Tb doped ZnO CNTs respectively. Additionally the vacuum breakdown for TbZnO sample occurs at very low voltage in comparison to that of the HoZnO sample. Although both types of catalysts produce the same type of CNTs (with regards to structure i.e open tip and closed cap) with the same mixed growth mechanism (tip + base growth), however there seems to be a small difference in the emission characteristics of both the samples. The difference in the emission characteristics might be because of the following three possible reasons,

i): One possible reason might be the different amount of amorphous carbon[271] around the CNTs that have been grown using two different catalysts.

ii): The second is that those CNTs that have been grown through the tip growth process with different geometry and composition of the catalyst particle might affect the emission characteristics.

iii): The third possible reason is that the catalyst particle at the base of CNTs produces different electrical resistance, which has a strong effect upon the emission phenomenon[268,269].

From the I-V characteristics of both the sample it has been observed that the emission current increases with the applied voltage exponentially as shown in the figure 7.11a.

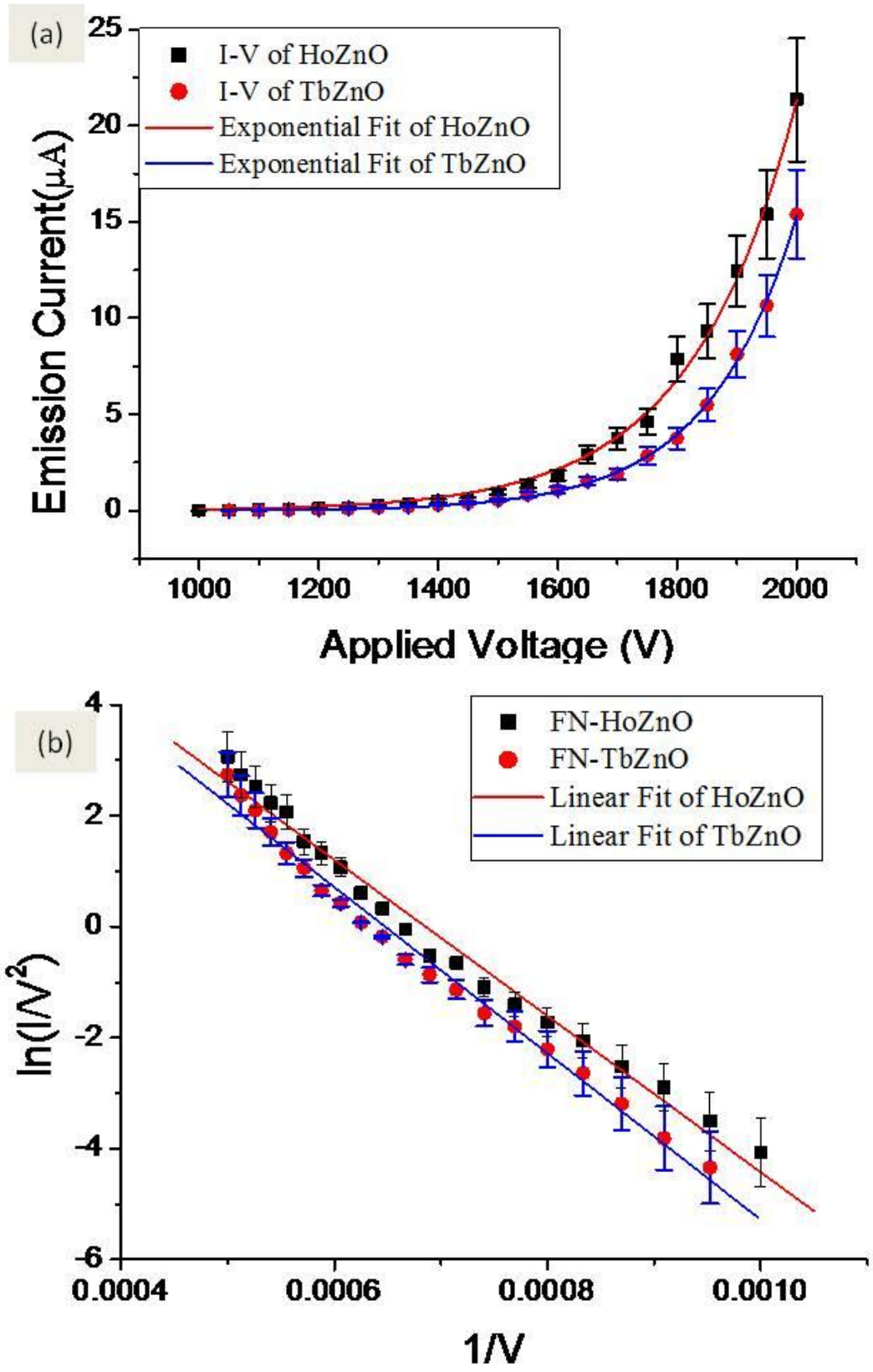

Figure 7.11 (a); The I-V characteristics of HoZnO and TbZnO grown CNTs (b); the corresponding FN-plots

The field emission phenomenon was confirmed by the Fowler-Nordheim plot. Ideally it should give a straight line, but there is a little deviation from the linearity in the F-N plot of both the samples. It is seen that there is a decrease in the slope in the middle of the line as shown in the figure 7.11b. This decrease in the slope has been attributed to various reasons like structure of CNTs, different catalyst particles at the tip of CNTs and because of the amorphous carbon[271]. It has been observed in section (6.7 and 6.8) that TbZnO grown CNTs are less crystalline and have more amorphous carbon around the CNTs in comparison to the HoZnO grown CNTs. Additionally both type of CNTs have been grown through both tip and base growth modes. Therefore it seems more likely that the deviation of the FN plots from linearity is because of the saturation sites of CNTs. Since both types of CNTs are randomly oriented with different sizes and diameters giving rise to different emission sites therefore as the applied voltage is increased more and more sites start emitting and the emission current increases with each step. Above a certain level of applied voltage some of the CNTs will get saturated, which slows down the increase in emission current, which results in the decrease in the slope in the middle of the line. The subsequent increase in the slope might be caused by the adsorbates that sit on the CNTs emission sites and decrease its work function. Additionally different species have been found like H_2, H_2O, CO and CO_2 as observed by Dean et al[261] and these are considered responsible for affecting the field emission process. The one difference that could be observed from the FN plot in figure 7.11b is that the subsequent increase in the emission current in TbZnO is higher than that of the HoZnO grown CNTs. It might be because the TbZnO catalysts react quickly with some of species like H_2, H_2O, CO and CO_2 etc the adsorbates rather than the HoZnO, which reduces its work function and causes an increased emission.

After the field emission process both the samples were checked under the SEM to see the after effect of field emission on CNTs. It was observed that the TbZnO sample was greatly affected by the field emission, while the HoZnO sample the CNTs have been affected but still exist on the substrate as shown in the figure 7.12a, b. After continuous operation of field emission, the resistive heating causes the destruction of more and more emission sites. It can be seen very clearly from the figure 7.12a that the CNTs have been cut into pieces showing the structural instability of CNTs as observed by Wang et al[264]. Since the TbZnO grown CNTs have more graphitic shells therefore expected to have more structural defects. Theses defects have electrostatic charge and causes soft breakdown.

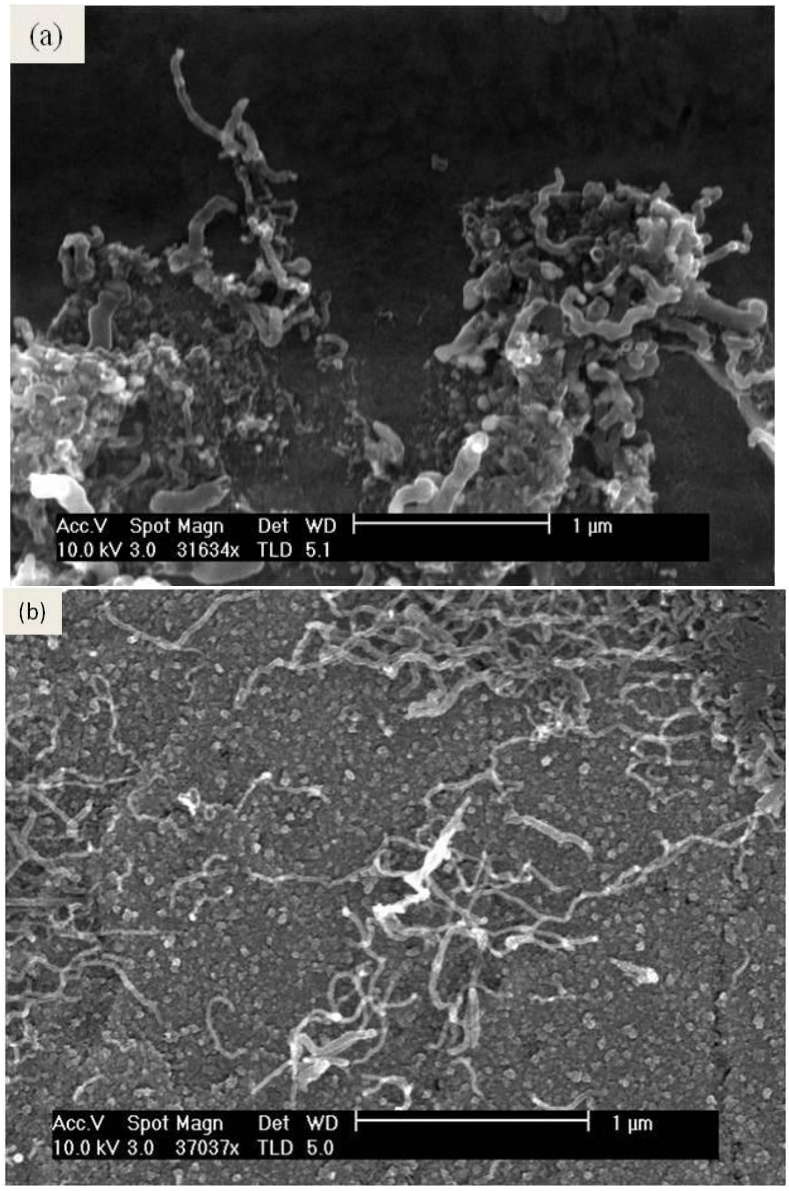

Figure 7.12 (a); The SEM image of TbZnO grown after field emission showing the evaporation and breaking of CNTs and (b) SEM image of HoZnO grown CNTs after field emission.

The CNTs in figure 7.12b has been affected by the field emission, which seems to be because of the ion bombardment (although it needs an experimental evidence), but has a very small effect upon the field emission characteristics. Additionally the damage of HoZnO grown CNTs is different from that of the TbZnO grown CNTs. The damage of the HoZnO grown CNTs is more like that of unravelling process as was first proposed by Rinzler et al[272].

According to which the CNTs are damaged through the string by string removal of carbon atoms along the circumference of the tube.

It seems quite evident from the above discussion that beside the CNTs structure the role catalyst composition and catalyst support interaction cannot be under estimated in defining the field emission properties of CNTs. The reaction of catalysts with the adsorbates and the amorphous carbon around the CNTs are also important parameters for stable field emission.

7.5.1): Field Emission Patterns from Rare Earth doped ZnO Grown CNTs:

Two samples of HoZnO and TbZnO were used to grow CNTs through CVD. The samples were then put in the UHV system to observe the field emission patterns. The growth of CNTs was confirmed through the SEM. The low magnification SEM images [as shown in figure 7.13] were obtained for further correspondence with the field emission patterns. The field emission patterns were collected through digital camera for various applied voltages as shown in figure 7.14.

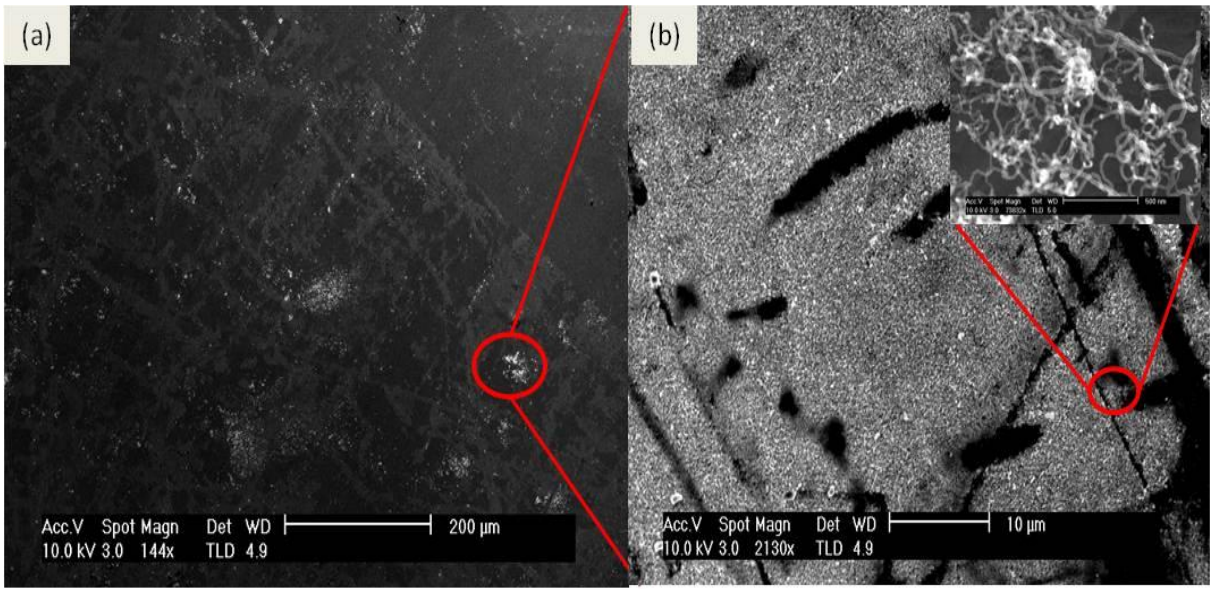

Figure 7.13 (a): Low magnification SEM image of HoZnO grown CNTs, which is the representative FE patterns. (b): Higher magnification SEM image of red circled area in figure 7.13a, in the inset is the high magnification image of the red circled area in figure 7.13b.

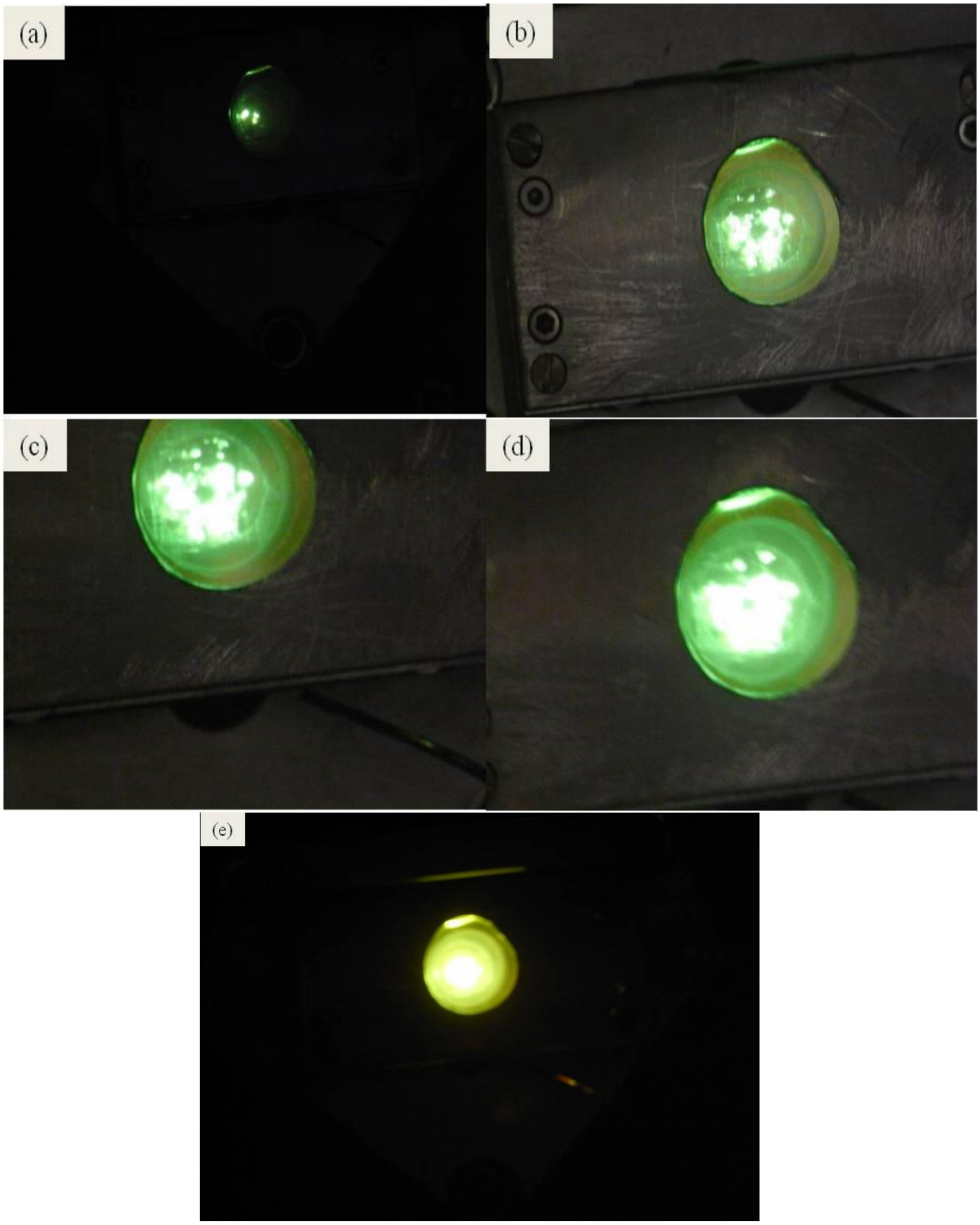

Figure 7.14 Field emission patterns as a function of increasing applied voltage from CNTs using Ho doped ZnO as catalyst. The CNTs were grown on W substrate using Cr as buffer layer. (a): 1.0kV with corresponding emission current of 17nA, (b)1.5kV with emission current of 948nA, (c): 1.8kV with emission current of 7.86µA (d): 2.0kV with emission current of 21.35µA (e): breakdown at 2.3kV

The first two very strong spots were obtained at applied voltage of 1050V for the Ho doped ZnO CNTs. As can be seen from figure (7.14a, b, c, and d) that the spots became brighter and larger as the applied voltage increased. When the applied voltage was increased above 2kV, a breakdown occurred and the emission current limited the power supply.

Field emission patterns from the Tb doped ZnO were obtained using the same vacuum system with the same triode configuration. It was observed that breakdown occurs at very low emission current in comparison to the Ho doped ZnO sample. There might be two reasons for that,

i): One is that it might be because of the amount of amorphous carbon around the CNTs in the Tb doped ZnO samples. The amorphous carbon is a good insulator[271] and gives rise to charge build up, which can lead to a vacuum breakdown.

ii): it might be because of the electrical resistance between the nanoparticles and the interface, because many of the CNTs have been grown through the base growth mechanism. This might cause the high rate of heat dissipation, which causes the catalyst interface degradation[273]. This results in peeling the CNTs off the substrate and causes breakdown.

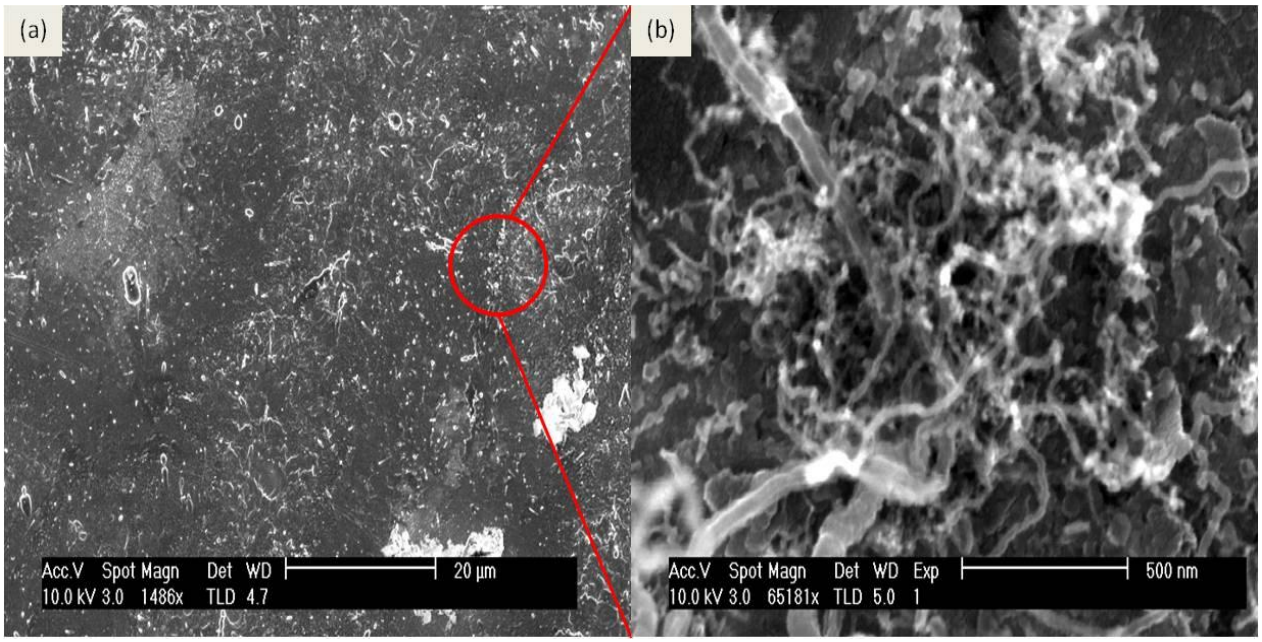

Figure 7.15 (a): Low magnification SEM image of TbZnO grown CNTs used for field emission (b): Higher magnification SEM image of the red circles area in the image (a).

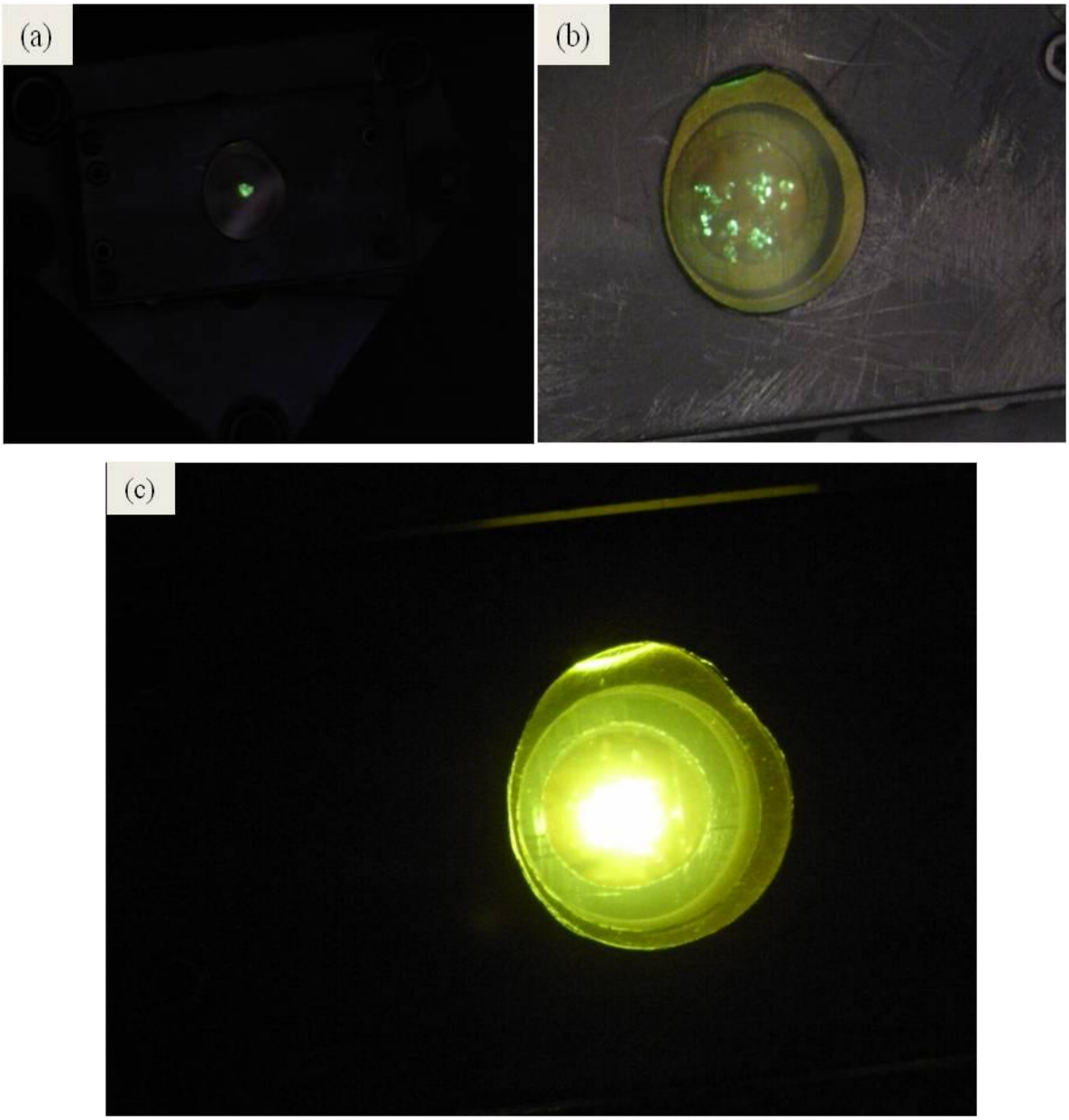

Figure 7.16 Field emission patterns as a function of increasing applied voltage from CNTs using Tb doped ZnO as catalyst. The CNTs were grown on W substrate using Cr as buffer layer. (a): 1.050kV with corresponding emission current of 13nA, (b)1.5kV with emission current of 550nA, (c): breakdown at 2kV

7.6): Emission current stability:

The emission current stability test was carried out for the sample of CNTs using CuZnO as catalyst using a chart recorder. The chart recorder has a voltage input so it was connected in parallel with a 10MΩ resistor, which converts the voltage input into a current signal and records the data as a function of time. The field emission performance of CuZnO grown CNTs regarding the emission current stability is not very attractive. There is a higher fluctuation of emission current at a fixed anode voltage. Long term emission current stability is an important factor for practical applications. The field emission started at 1.053kV in the first measurement of the I-V characteristics of the sample, which was quite unstable. From figure 6.9b [section (6.5)], it is quite evident that the CNTs are loosely attached to the support, which could easily be peeled off the substrate at high voltage and causes breakdown. Additionally from figure 6.11 it is clear that there exists some amorphous carbon around the CNTs, which might cause instability. After successive soft breakdowns at fixed voltage of 1.4kV it was observed that most of the adsorbates were removed and the emission current stability improved to some extent.

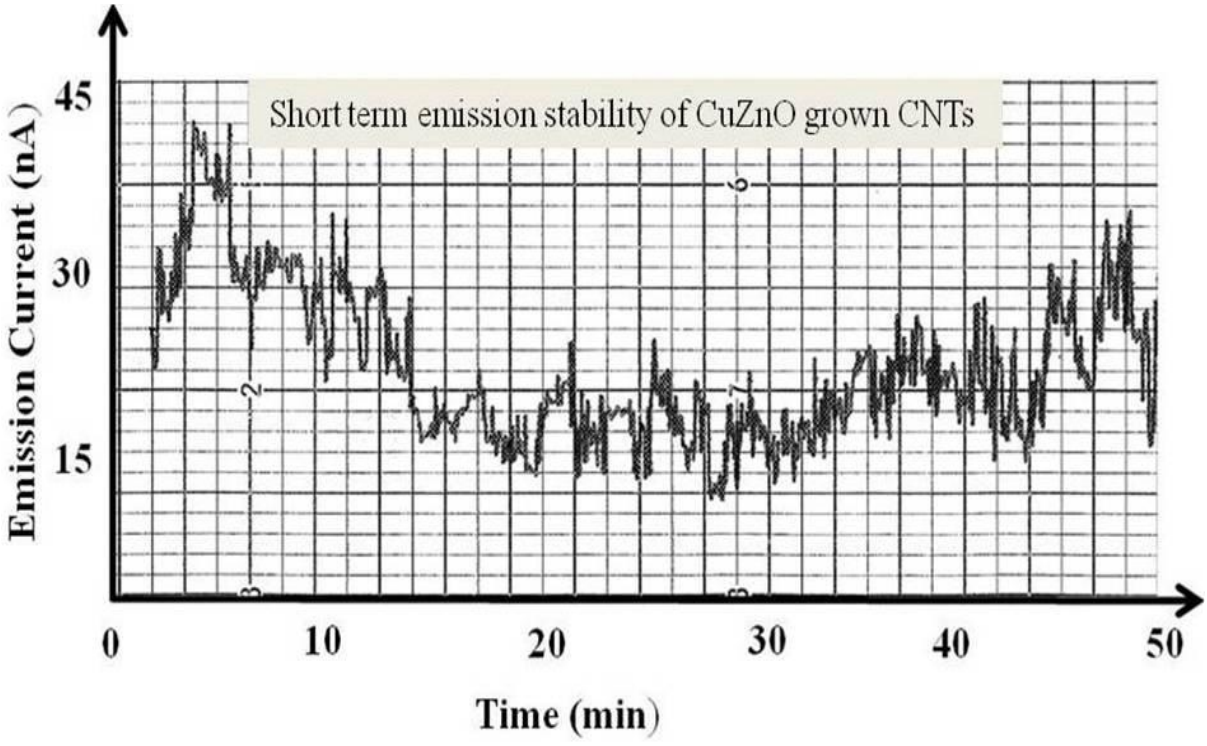

Figure 7.17 the emission current as a function of time.

The stability curve for the first 50 minutes at fixed voltage of 1.2kV was measured and it was observed that the emission first increases and then starts decaying exponentially. After the 20 to 25min continuous decay it starts rising again. There are two processes that are believed to be responsible for the decay. One is that proposed by Dean et al[274], that adsorbates occupy the enhanced tunnelling states, which gives rise to saturation current. At high applied field the adsorbates are completely removed and the enhanced tunnelling states are completely lost. At low applied field the adsorbates re-occupy the enhanced tunnelling states and gives rise high emission current. The current saturation mechanism is the level where the adsorbates are displaced through applied field and emission current to an extent to reduce the enhance tunnelling. This is a reversible phenomenon and is completely different from the etching process. This seems more likely to have happened in this experiment. The other possibility is the Joule heating. This effect can happen at two points of CNTs, one at the tip and the other is at the bottom of a CNT. It has been observed through field emission electron spectroscopy study that the emission current of 1μA from a single multi wall CNT can induce a temperature of 2000K at the tip during the field emission[275,276]. However the Joule heating at the tip of a CNT seems quite unlikely, because the emission current is not high enough to cause high temperature at the emission sites that eventually results in carbon evaporation. The Joule heating at the bottom of a CNT is produced by the difference in the electrical resistance of two different materials (catalyst and substrate). In addition, the doping of ZnO with Cu makes it more p-type and increase the resistivity of the CuZnO nanoparticles[242] therefore this seems to be the probable case, which gives rise to a voltage drop that causes decay in the emission current[277]. This is an indicative of the importance of the catalyst-support interaction. It has been observed by Moon et al[278] that adhesion of CNTs with the substrate plays a critical role in emission stability. It is necessary to have a strong CNT-support interaction to get an acceptable life time of CNTs. The strong electrostatic force can peel the CNTs off the substrate that causes a decrease in the emission current and also a vacuum breakdown.

The field emission results show that CNTs grown using CuZnO as catalyst have very poor adhesion to the substrate, while NiZnO grown CNTs show relatively good adhesion characteristics. The field emission stability of the NiZnO grown CNTs was measured for 13hours. It was observed that at low applied voltage it gives stability with almost 20% - 25% current fluctuation. The current fluctuation is measured as

$$Fluctuation = \left(\frac{I_{max} - I_{min}}{I_{av}}\right) \times 100 \qquad (7.2)$$

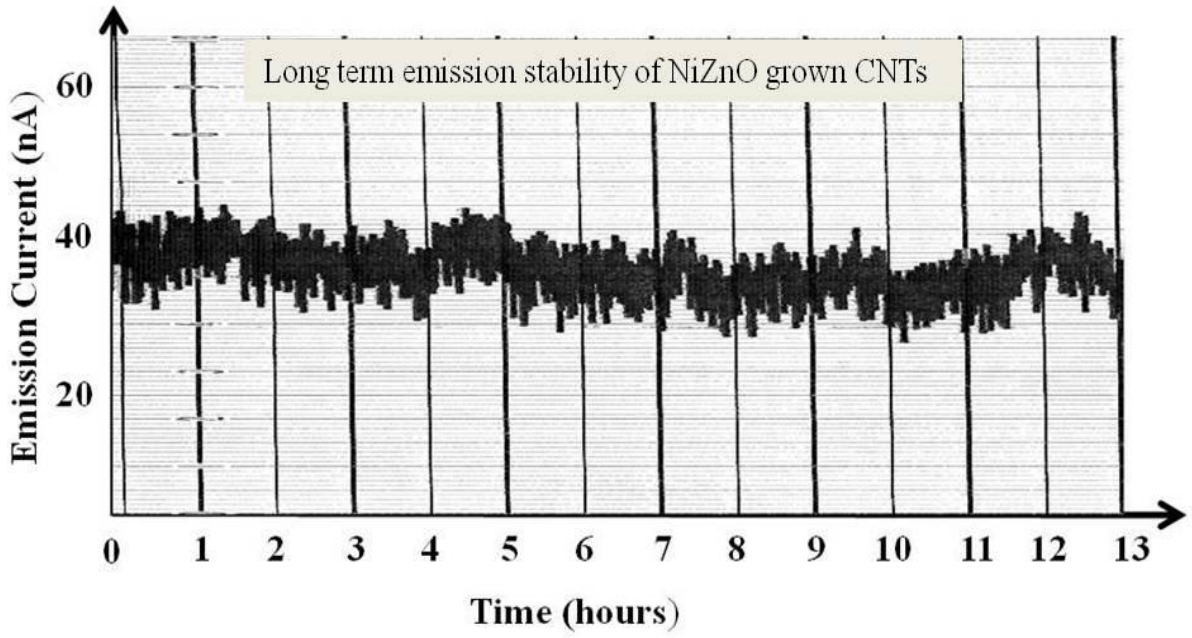

Figure 7.18 the plot showing the emission current as a function of time.

It has been observed in this study that NiZnO grown CNTs have two shortcomings in comparison to CuZnO grown CNTs.

i): The yield of NiZnO grown CNTs is very low in comparison to all other catalytically grown CNTs.

ii): since the NiZnO grown CNTs have large amount of graphitic shells than CuZnO grown CNTs therefore it is likely to have higher defect density[279] than CuZnO CNTs.

Besides these two shortcomings the NiZnO CNTs show better long term emission stability, this indicates that strong catalyst support interaction plays a key role in the emission stability, which favours the results by Moon et al[278]. Stronger the adhesion can add towards a better stability.

The emission stability from the rare earth doped ZnO grown CNTs was observed at the same constant voltage of 1.2kV, as was measured for the transition metal doped ZnO grown CNTs using the same chart recorder. It was observed that the stability for the first 100

minutes of HoZnO grown CNTs consists of many spikes and quite unstable, while after few hours the sample cleans itself and the stability improves. The long term emission stability of the HoZnO grown CNTs behaves quite well in comparison to all other CNTs grown by using other catalysts used in this study. The short and long term stability of Ho doped ZnO grown CNTs is given in figures (7.19 a & b) respectively.

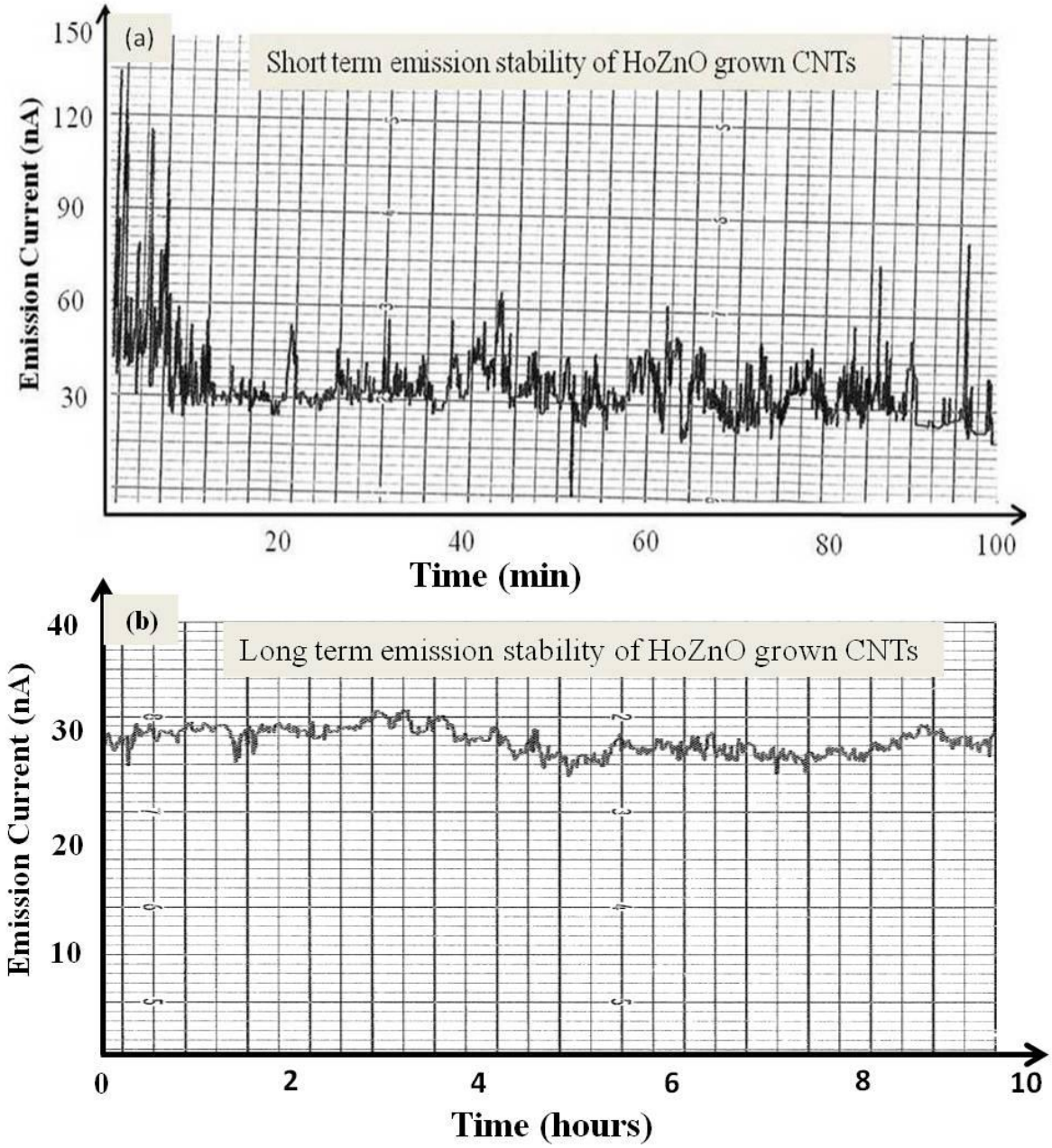

Figure 7.19 (a & b); The emission current as a function of time. This shows that adsorbates affect the work function and causes instability. After the evaporation of adsorbates the emission current becomes stable. Additionally it seems that the HoZnO catalysts do not react quickly with the adsorbates.

In the case of TbZnO grown CNTs, the emission current does not persist for long time and causes vacuum breakdown. It might be because of the Joule heating effect that causes to evaporate the adsorbate molecules and the applied field causes to ionise these molecules. After ionisation there is a charge build up between the two plates, which eventually results in vacuum breakdown[265]. It can be observed from figure 6.16 [section (6.7)] that these CNTs have higher amount of amorphous carbon around, which is a good insulator and might cause charge build up and results in vacuum breakdown. Additionally the TbZnO grown CNTs have a larger amount of graphitic shells than the other catalyst grown CNTs (in this study), therefore it is expected to have large amount of defects. These structural defects might cause instability[279]. The short term stability curve for the TbZnO grown CNTs is given in the figure 7.20.

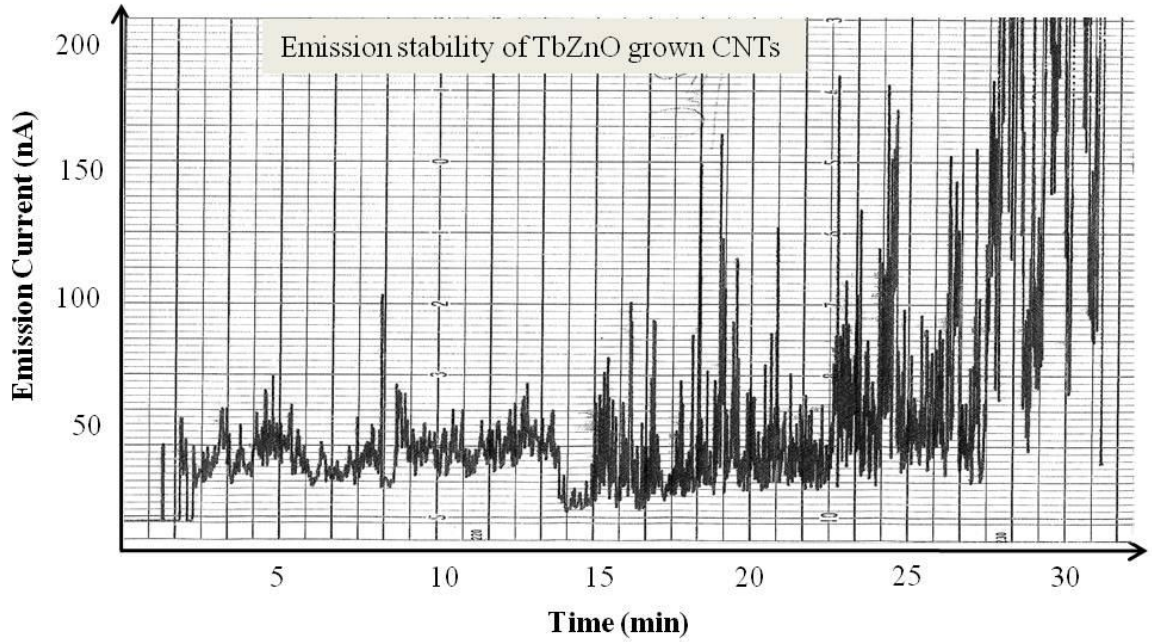

Figure 7.20 The emission current as a function of time.

The catalyst support interaction seems to be a dominant factor in defining the stability of the rare earth doped ZnO grown CNTs. It has been discussed in section (6.7 & 6.8) that both types of catalysts (TbZnO and HoZnO) give rise to CNTs growth through tip growth and base growth processes. In both samples, it was found that there exists both open and closed cap CNTs. But besides these two similarities both the samples behave differently regarding the emission stability. There seem to be two possible explanations for this.

i): The large amount of graphitic shells that are expected to have higher defects[279]

ii): The amount of amorphous carbon around the CNTs causing a charge build up and results in vacuum breakdown.

In summary, the study of short and long term emission stability of transition metal (Cu, Ni) and rare earth (Tb, Ho) doped ZnO grown CNTs shows that the following factors cause fluctuation in the emission current.

i): Adsorption and desorption of different gas molecules is the main problem in theses CNTs that affects the fluctuation of the emission current, because these adsorbates lower the work function and causes an increased emission current, which results in emission current instability.

ii): The joule heating, which is produced by the difference in electrical resistance of the catalyst and support.

iii): The structural differences also are believed to have a great impact on the emission stability. The CNTs with large amount of graphitic shells are believed to have large amount of defects, which gives rise to emission current instability.

7.7): Current–Voltage characteristics of the nickel oxide grown CNTs

Field emission studies were carried out for the CNTs grown on Si substrate using Cr as buffer layer and NiO as the catalyst. Since it is believed that catalysts have a great impact on CNTs morphologies[280] and hence on the field emission. The sample size is 4mm× 5mm. Field emission was observed by keeping the sample at negative potential. The applied voltage was increased from the negative power supply and the emission current was recorded. An observed current of 0.25 μA was recorded by pico-ameter at an applied voltage of 1.2kV in the first measurement of the I-V characteristics for the sample. The emission current appeared on the phosphor screen as a small dot and was observed that it increases as the applied voltage is increased. The emission current as a function of applied voltage and the corresponding for F-N plot is given in the figure 7.21. The FN plot is not ideally straight, which shows that with increasing applied voltage more and more sites have started emitting.

Since the CNTs in the sample are not uniform in length and diameter it is therefore according to the expectation that there will be a deviation from linearity of the FN plot with increasing applied voltage. The low turn on voltage is due to the high density and good alignment of CNTs.

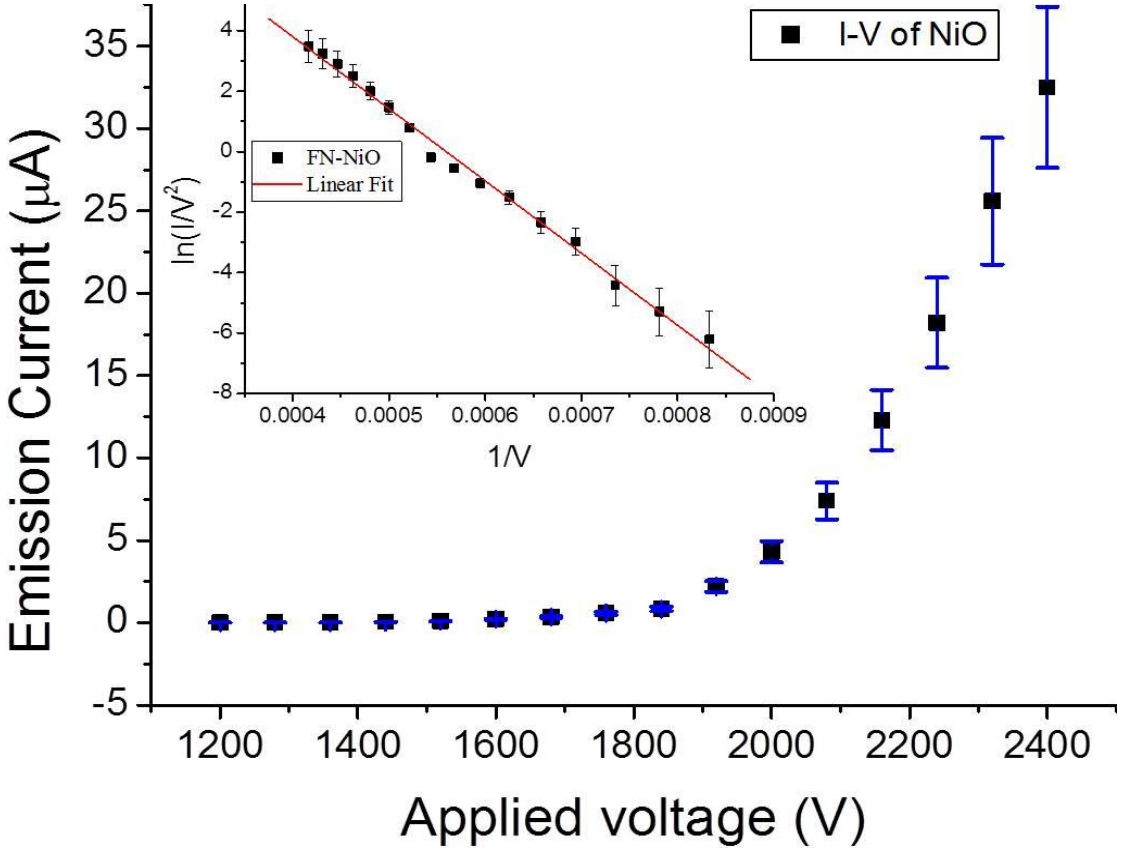

Figure 7.21 the I-V characteristics and the corresponding FN-plot (in the inset) of NiO grown CNTs

7.7.1): Emission Patterns of nickel oxide grown CNTs:

The field emission patterns from NiO grown CNTs were obtained in the UHV system through a diode configuration. The phosphor screen was made by thermally evaporating the phosphors on the gold coated glass. The sample and the phosphor screen were separated by 300μm thick PEEK sheet. It was observed that with increasing applied voltage the more and

more sites start to emit and gives rise to high emission current. The emission pattern is shown in figure 7.22

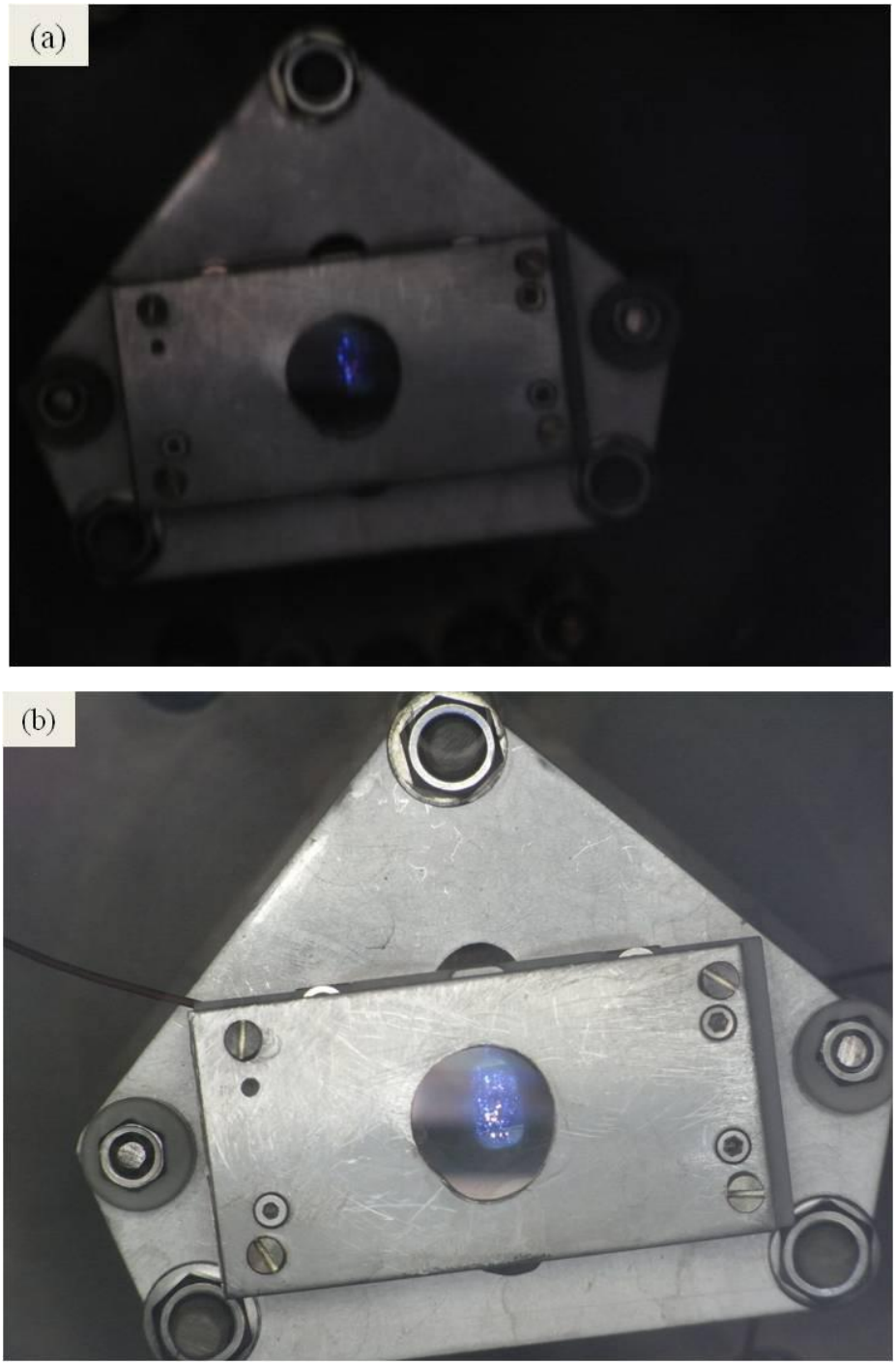

Figure 7.22 the field emission patterns (a): at 1.44kV with emission current as 31nA and (b)2.4kV with emission current as 22.5μA.

7.8): Emission Current Stability from NiO grown CNTs:

In the previous section a field emission pattern has been observed from NiO grown CNTs. In this regard emission stability for short and long time has been measured at applied voltage of 1.6kV at the pressure about 5×10^{-9} mbar. It was observed that at 1.6kV the emission current remains stable and after 3 minutes there is a sudden increase in the emission current. After this sudden increase the emission current decays exponentially. It is quite evident from figure 7.23 that the decay is quite stable with very less fluctuations, but as time increases the fluctuation increases. This increase in fluctuations indicates that the field emissions sites are constantly absorbing and desorbing species that constantly change the work function of CNTs which gives rise to unstable emission.

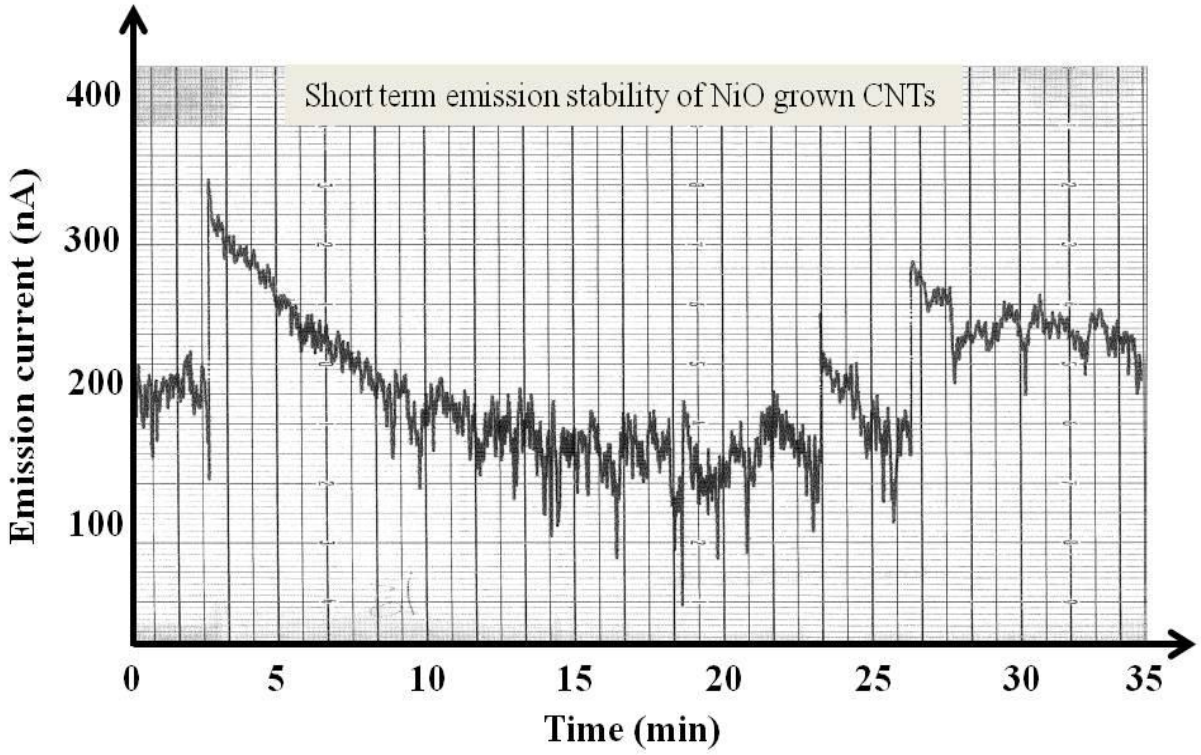

Figure 7.23 The emission current as a function of time.

For long term stability the emission current was measured at a constant voltage of 1.6kV as shown in figure 7.24. The stability of the first 5 hours shows several very sharp spikes, which means that the emission current is quite unstable. These spikes are clearly

because of the adsorption and desorption of some species that constantly alter the work function of the emission sites that causes the emission current instability. After 5 hours of constant emission the current becomes stable. There could be two possible reasons for this.

i): It seems quite reasonable that this instability is due to the adsorbates, because it is more likely that some molecules in the vacuum may reach the tip of CNTs through surface diffusion and affect the work function. It has been observed by Patra et al[281]; that the adsorption of H_2O molecules by CNTs can reduce the effective work function that causes an increase in the emission current. The spikes in the emission current show that the adsorbates are constantly removed by the field emission and upto the first six hours the sample cleans itself. From the figure 7.24, it is quite evident that the sample is passing through the self cleaning process in the first six hours. After the first five hours the spikes are getting depressed and the stability improves.

ii): the second possibility regarding the instability is the presence of a range of CNTs with different structure in one sample. It has been observed in section (6.3) that the sample consists of tubular and bamboo shaped CNTs. Since the emission current stability is dependent on the individual type of CNT[282] therefore it could be expected that the emission current from a sample with different CNTs structures have different emission stabilities and hence the total emission remains unstable.

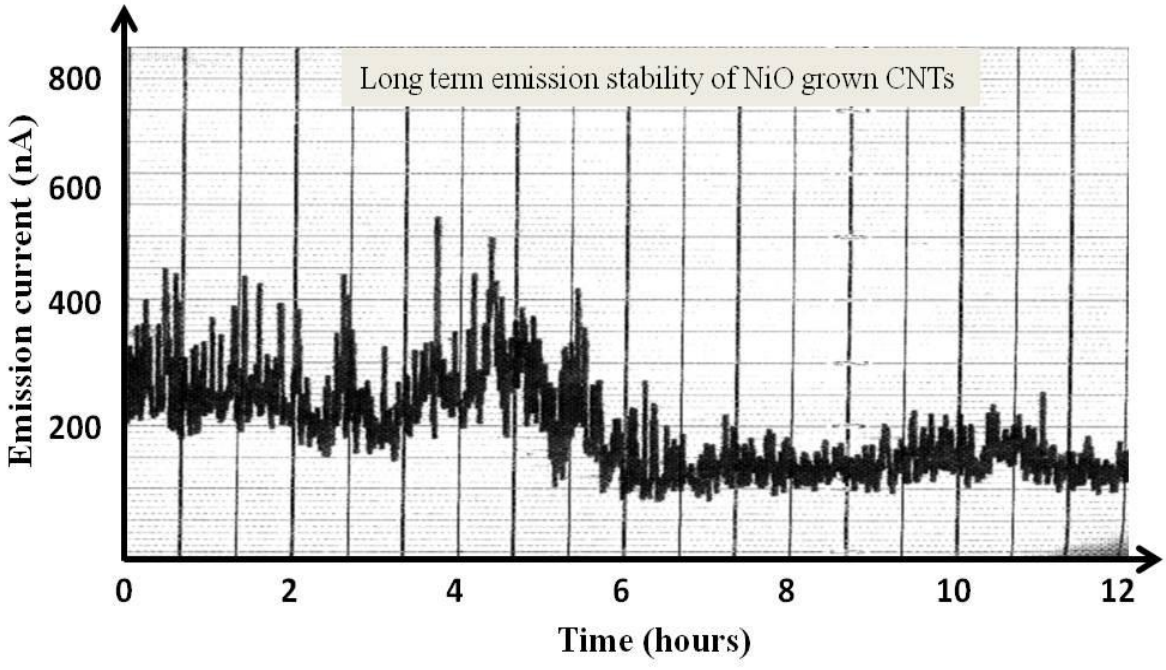

Figure 7.24 The emission current as a function of time.

7.9): Summary of the field emission studies of CNTs.

Field emission properties of CNTs grown through CVD using a range of novel oxide catalysts were carried out in a ultra high vacuum (UHV) system. Field emission patterns were obtained using a triode and diode configurations. It was observed that those samples where the CNTs have a strong interaction with the substrate and with low amorphous carbon give rise to high emission current and high stability. The Ho doped ZnO grown CNTs show an excellent long term stability at low applied voltage in comparison to all the rest of the samples, while the NiO grown CNTs gives rise to high emission current density but have comparatively low long term emission stability than HoZnO sample. One expected reason could be the reactivity of the NiO nanoparticles with different species present in the chamber during the field emission. The other possible reason could be that the HoZnO CNTs are grown through CVD, while the NiO CNTs are DC-PECVD grown. Since the CVD grown CNTs are curled and randomly aligned therefore experiencing a larger shielding effect from the neighbouring CNTs than the DC-PECVD grown CNTs, which are usually aligned and free standing.

The long term emission current stability of HoZnO sample is better than all the other CNTs investigated. The emission current stability of the NiO grown CNTs improves after a long time (nearly 6 hours in this study) operation. The main reasons that are affecting the stability seem to be the formation of residues during the growth, non-uniform CNTs emission and the catalyst support interaction.

8.1): Summary

In this work CNTs have been successfully grown using CVD with metal oxides (doped and undoped) as catalysts. The results of this research show that conventional thinking about the metal oxides as catalysts for the growth of CNTs and growth mechanism was somewhat misleading. Although very recently it has been observed that metal oxides can catalyse the growth but the growth mechanism is still unclear.

The initial studies carried out here focused on the characterisation of bulk and nanoparticles of ZnO doped with transition metals (Cu & Ni) and rare earths (Sm, Tb & Ho). The material behaves differently in bulk and in nanoparticles. The thermal evaporation of bulk (pellets) helps to completely incorporate dopants in the ZnO matrix. For uniform CNTs growth it is desirable to have a narrow size and shape distribution of catalyst nanoparticles. For this purpose Al, Cr and SiO_2 are used as buffer layers and it was observed that a Cr buffer layer gives rise to a very narrow size and shape distribution of grains.

It has been observed through the SEM that the thermal evaporation of pellets does not make a continuous film like that of Ni or Fe, but deposits on the substrate in the form of grains (nanoparticles). The size and shape of the grains strongly depend upon the nature of the substrate and the dopant material, because ZnO powder doped with various dopants exhibit different properties and hence gives rise to different lattice strain. The lattice strain, which arises from the dislocations and imperfections causes to distort the shape of the grains and gives rise to an anisotropic growth. The elemental composition of pellets and the grain on the substrate were confirmed through the EDS in the SEM. Additionally the elemental composition of individual nanoparticles was confirmed through the EDS in the TEM. The EDS confirms the existence of host (ZnO) and the dopants (transition metals and rare earths) in all the samples.

The XRD analysis of grounded pellets (powder) show that powders of all the samples are crystalline and some of the dopants make their own clusters at some specific temperature and do not go into the ZnO matrix completely. In this study it has been observed that ionic radii are not the only factor that restricts the ions to go into the ZnO matrix. It is because Ni has smaller ionic radius than Tb but at 1200C sintering temperature Tb goes into the ZnO matrix completely while Ni does not. The ions with higher ionic radii produce larger lattice

strain than smaller ones if used as dopants. After thermal evaporation it has been observed through XPS and TEM that dopants have been successfully incorporated into the ZnO matrix. The incorporation of dopant ions into the ZnO matrix could clearly be observed from the O1s core level spectra. The oxygen bonding to different metal atoms corresponds to different binding energies, which help in analysing the behaviour of the material. The doping behaviour could also be understood from the Zn2p core level spectra. Especially in the case of Sm and Ni where some of the Ni and Sm ions have been bonded with Zn and appears on the lower bonding energy side of the Zn2p core level spectra.

The XPS analysis of the thermally evaporated samples show that the grains are properly doped and the dopants have mixed oxidation states in the ZnO matrix except Sm doped ZnO where Sm remain in the +3 oxidation state only. It has been observed that the presence of mixed oxidation states of dopants in the ZnO matrix gives rise to charge transfer phenomenon that plays a key role in dissociating the hydrocarbon molecule (C_2H_2). The charge transfer transition does not occur in Sm doped ZnO and therefore does not catalyse the CNTs growth. It has been observed through the XRD that the oxidation state of dopants control the crystallite size and lattice strain. The lattice strain is responsible for the carbon diffusion through the catalyst nanoparticles and hence gives rise to CNTs growth. The higher the lattice strain the higher the diffusion of carbon through the catalyst.

CNTs have successfully been grown through DC-PECVD and CVD using NiO and doped ZnO respectively as catalysts. The NiO grown CNTs are well aligned and quite straight with the majority of CNTs having catalyst particles at the tip. The CNTs have a large distribution of diameters and length, which is because of the large size and shape distribution of the catalyst nanoparticles. The closed tip CNTs have been grown through the base growth process. The growth behaviour of both Ni and NiO grown CNTs seems pretty same, but the only difference is that in Ni all the CNTs have grown through the tip growth mechanism while some of the NiO grown CNTs have been grown through the base growth mechanism with the tip of the CNT closed. This shows that NiO nanoparticles do not have a uniform chemical state.

The CNTs grown through the CVD are curled and randomly oriented. The CNTs were grown through mixed growth process showing that the chemical state of the individual particle plays a main role in defining the growth process. Additionally the size and composition of the individual nanoparticle plays a main role in defining the diameter and

length of CNTs. Because some of the nanoparticles just gives rise to graphitic shells and does not nucleate CNTs. It has been observed that different dopants have different effect upon the CNTs morphologies. The catalyst nanoparticles with higher lattice strain gives rise to large amount of graphitic shells and smaller inner diameter and as the lattice strain decreases the ratio of inner diameter to outer diameter increases. This confirms that the lattice strain is responsible for the diffusivity of carbon atoms through the catalyst nanoparticles. Another interesting behaviour that has been observed is the decrease in crystallinity of graphitic shells towards the inner diameter. Since the lattice strain near the edge dislocations is very high in comparison to the inner surface, it is highly probable that sufficient amounts of carbon atoms diffuses near the edge and gives rise to well crystalline graphitic layers, while an insufficient amount of carbon atoms diffuse through the inner surface and hence the atoms are randomly arranged with some breaks, which gives rise to amorphicity. The crystallinity of HoZnO grown CNTs is far better than all the other catalysts (used in this study) grown CNTs. This might be because of the HoZnO nanoparticles need higher temperature for CNTs growth in comparison to the other catalysts (used in this study).

The growth of CNTs regarding the specific catalyst was confirmed from the particle at the tip of CNTs through EDS in the TEM. The high resolution images of the catalyst particle confirm the wurtzite structure of ZnO and EDS confirms the elemental composition of the catalyst particles.

Field emission properties of CNTs grown through CVD using all the novel oxide catalysts were carried out in an ultra high vacuum (UHV) system. Field emission patterns from all the transition metal (Cu, Ni) and rare earth (Tb, Ho) doped ZnO grown CNTs were obtained through a triode configuration setup, while from NiO the field emission patterns were obtained using diode configuration. It was observed that CNTs with a strong interaction with the support and with low amorphous carbon give rise to high emission current and high stability. Since the HoZnO grown CNTs have high crystallinity, they therefore show excellent long term stability at low applied voltage in comparison to all the rest of the samples, while the NiO grown CNTs gives rise to high emission current density but have comparatively low long term emission stability than HoZnO sample. One expected reason, could be the reactivity of the NiO nanoparticles with different species present in the chamber during the field emission. The other possible reason could be that the HoZnO CNTs are grown using CVD, while the NiO CNTs are DC-PECVD grown. Since the CVD grown

CNTs are curled and randomly aligned, the shielding effect of the neighbouring CNTs is more pronounced than the DC-PECVD grown CNTs, which are usually aligned and free standing. Additionally the NiO grown CNTs have higher density than HoZnO therefore it is very likely to have higher emission current than HoZnO grown CNTs at some specific applied voltage.

The long term stability of HoZnO sample is better than all the other CNTs. The emission current stability of the NiO grown CNTs improves after a long time (nearly 6 hours in this study) operation. The main reasons that affect the stability seem to be the formation of residues during the growth, non-uniform CNTs emission and the catalyst support interaction.

(8.2): Future Work:

Although NiO and doped ZnO (transition metal and rare earth) are used for the first time to explore its catalytic activity in the synthesis of CNTs, there is still a considerable amount of understanding to be gained from further exploring this material. In particular, the critical level of doping to control the ratio of the inner diameter to number of graphitic shells. Since the doping gives rise to the lattice strain and hence the diffusion of carbon through the catalyst nanoparticles, it is of the utmost importance to have proper control over the doping process. Additionally, since the Fermi level changes with the charge transfer process, the theoretical consideration of the position of Fermi level with charge transfer transition will help control the dissociation of carbon containing gas and will help reduce the amount of amorphous carbon.

Although the thermal evaporation of pellets help in complete doping of the grains, but it also gives rise to other adsorbates like amorphous carbon and hydrogen and hydroxyl (OH) ions. This amorphous carbon might poison the catalyst and lose the potential of the catalyst nanoparticles to dissociate the hydrocarbon and gives rise to CNTs growth. Therefore alternative deposition methods like molecular beam epitaxy (MBE) may be a better choice. Additionally since it has been observed in this study that the substrate and buffer layer have a great impact on the grain size and shape, the selection of a more suitable substrate or buffer layer will help control the size and shape of the grains and hence the diameter of CNTs.

It has been proposed by Lee et al[283] that the nano-composite of CNTs and NiO could be used as electrode for super-capacitors. Because of the high resistivity, NiO has very poor energy and power density. Additionally it has very low specific capacitance because of the low surface area. On the other hand CNTs have a very high conductivity and large surface to volume ratio[284,285] and it has been shown that the nano-composite of both NiO and CNTs can enhance the performance of NiO as an electrode for super-capacitors. But NiO grown CNTs is believed to be the easiest way to make the NiO/CNTs nano-composite.

The most important work regarding the growth of CNTs from either NiO or doped ZnO could be done by growing an individual vertically aligned CNT on a tip to use the CNT as a field emitter. Since the diameter of CNTs could be controlled by controlling the size of the grains, which could be controlled by selecting more appropriate substrate and buffer layers, the proper optimisation of growth conditions and growth setup can help in growing an individual CNT on a tip.

The field emission characteristics of CNTs in this study show that none of the catalysts produced CNTs that could be used for practical applications like flat panel field emission displays. To make CNTs suitable for field emission there are few steps that must be addressed.

i): catalyst support interaction
ii): suitable arrangements for the removal of residues adsorbed on the substrates or on the surface of CNTs.
iii): uniform CNTs structure, diameter and length.

The catalyst support interaction is important because the CNTs in some of the samples were weakly attached to the substrate and caused voltage breakdown during field emission. The field emission characteristics were studied through the diode and triode configuration. The problem with the triode configuration is the spacer (peek sheet), which is an insulating material that gives rise to charge build up which can affect the field emission process and might cause vacuum breakdown. Additionally the observed field emission characteristics are the average of all the CNTs with a range of lengths, diameters and structure. The field emission properties of an individual oxide grown CNT can provide an insight into the understanding of the field emission mechanisms.

Chapter: 8; Summary and Future Work

Electron beams are used in a variety of applications from electro-optical analytical instruments to synchrotron storage rings, visual displays[286] etc and the analysis of magnetic nanostructures. To analyse the magnetic nanostructures the incident beam must be spin polarised, because it gives rise to spin dependent scattering, which gives a complete description of the spin effects, while in conventional scattering the incident and oriented spins are random and the results for all the spin dependent phenomena are averaged**.** Increased polarisation from CNTs in comparison to the existing sources is possible because of the one dimensional quantum confinement[287]. In addition to increased polarisation than the existing sources, the magnetic particle at the tip may make it easy to select the spin polarisation direction by magnetising the particles in specific direction. Therefore it is believed that CNTs could be a possible spin polarised electron source. If a spin polarised source could be developed for scanning low energy electron microscope (SLEEM), then one can realise a new imaging electron microscope i.e. SP-SLEEM. Such a technique or imaging tool can be used to gain information about the domain structure and the direction of magnetisation. SP-SLEEM, if it could exist, would be used in many labs, since it could be inexpensive. The information obtained from the SP-SLEEM would be similar to that of the SPLEEM which provides magnetisation direction, having high spatial resolution below 10nm and could have a higher polarisation limit than the existing sources.

Spintronic devices have a range of applications, with spin field effect transistors and spin q-bits[288,289] as leading candidates. The challenge for realising these devices is the requirement for efficient spin polarised carrier injection and transport. To-date the current conventional ferromagnetic metals show no compatibility towards the existing semiconductor technologies. Diluted magnetic semiconductor (DMS) materials have the potential to inject electrons with a well defined spin and to control the same spin properties in the adjacent non-magnetic semiconductors[290]. The CNTs have a weak spin-orbit coupling therefore they have a large spin diffusion length[291]. Therefore it is expected that the hetrostructure of DMS and CNTs could be a possible way towards realising spin field effect transistors and the spin q-bit.

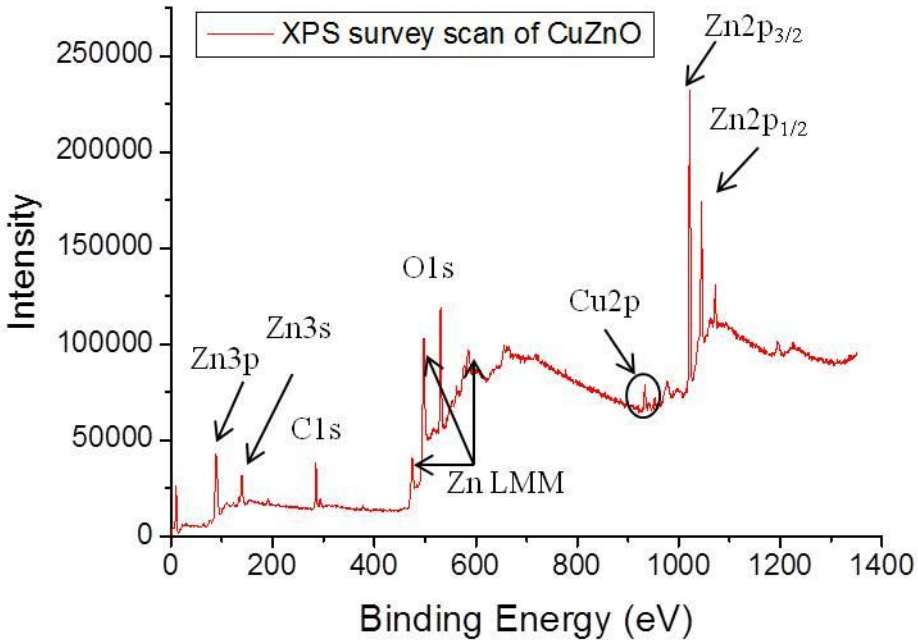
XPS survey scan of CuZnO
Zn2p3/2
Zn2p1/2
O1s
Cu2p
Zn3s
Zn3p
C1s
Zn LMM
Intensity
Binding Energy (eV)
250000
200000
150000
100000
50000
0
0
200
400
600
800
1000
1200
1400

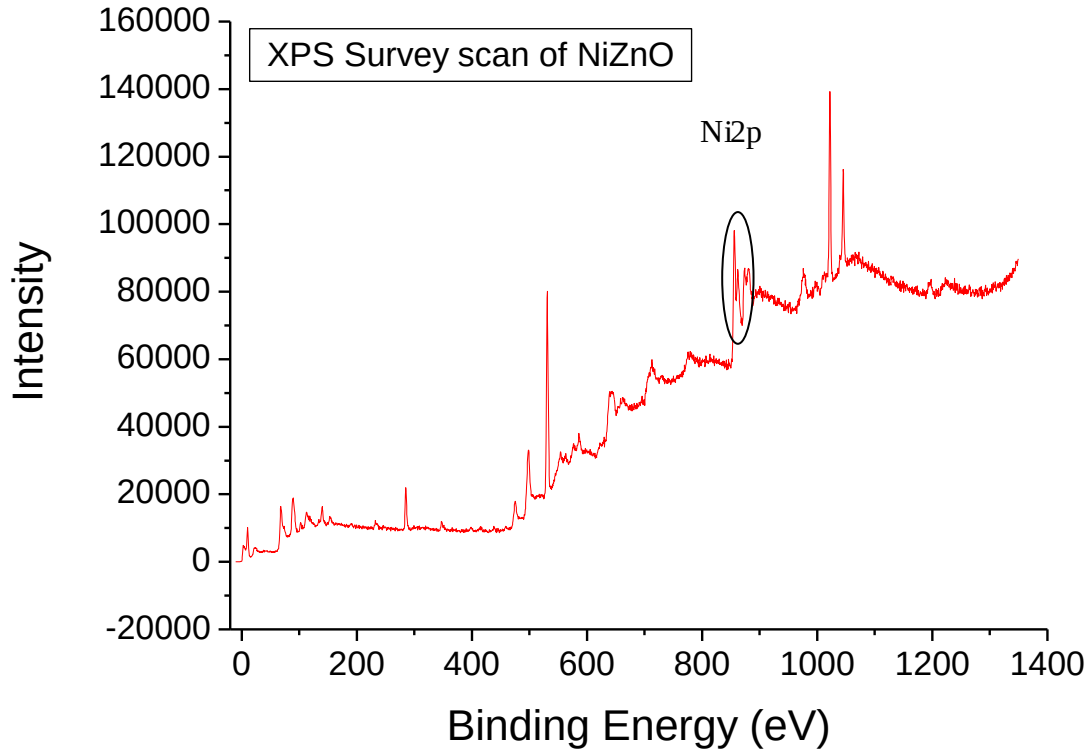
XPS Survey scan of NiZnO
Ni2p
Intensity
Binding Energy (eV)
160000
140000
120000
100000
80000
60000
40000
20000
0
-20000
0
200
400
600
800
1000
1200
1400

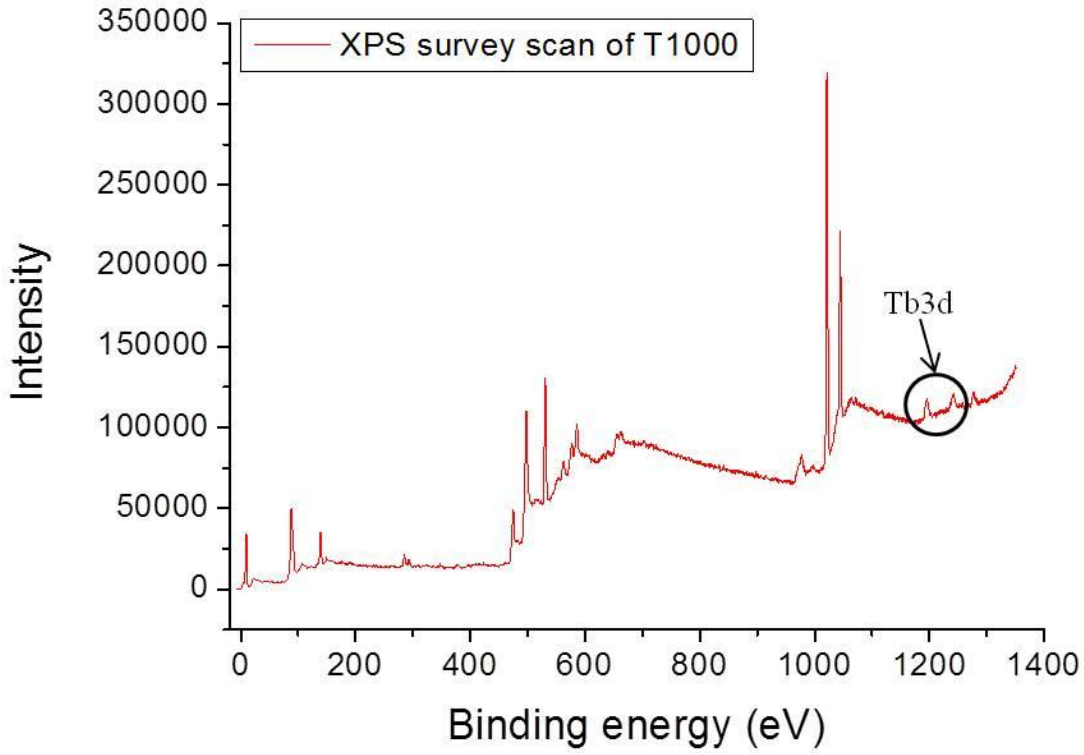
XPS survey scan of T1000
Intensity
Binding energy (eV)
Tb3d
350000
300000
250000
200000
150000
100000
50000
0
0
200
400
600
800
1000
1200
1400

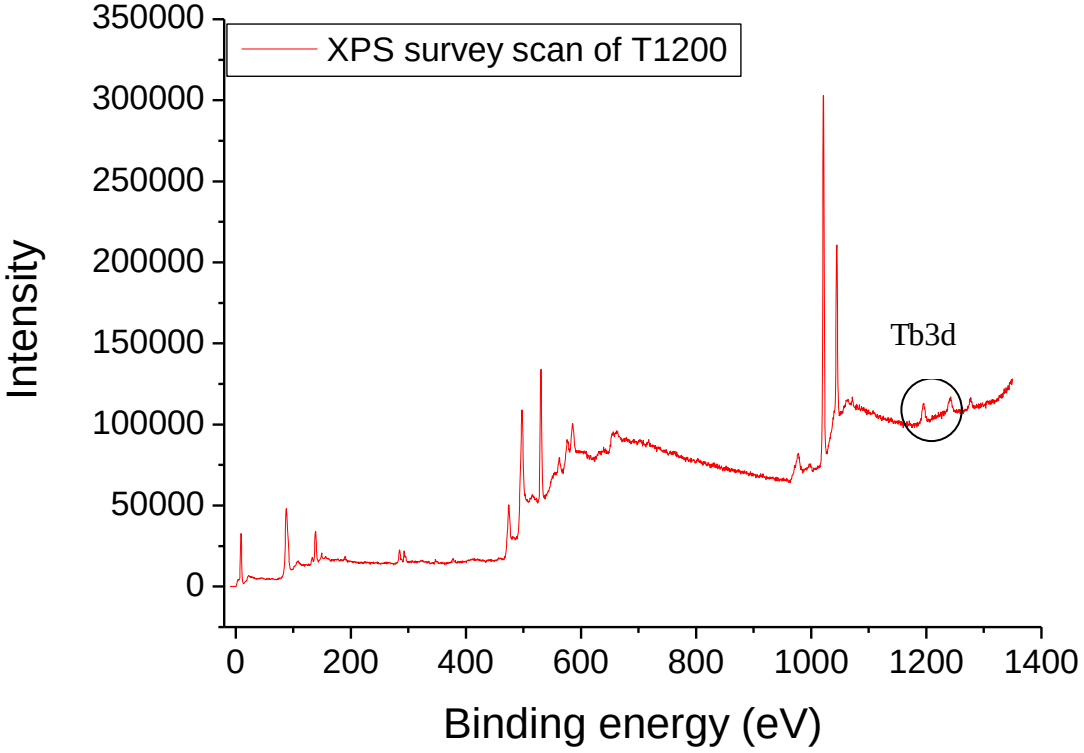
XPS survey scan of T1200
Intensity
Binding energy (eV)
Tb3d
350000
300000
250000
200000
150000
100000
50000
0
0
200
400
600
800
1000
1200
1400

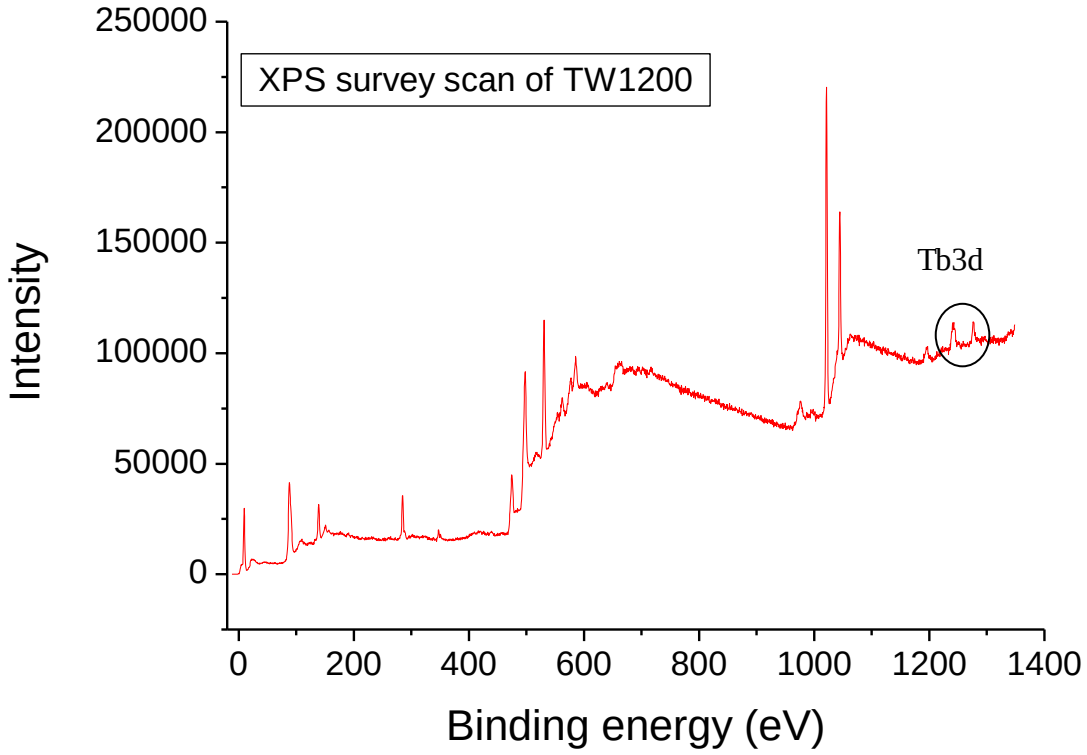
XPS survey scan of TW1200
Tb3d
Intensity
Binding energy (eV)
250000
200000
150000
100000
50000
0
0
200
400
600
800
1000
1200
1400

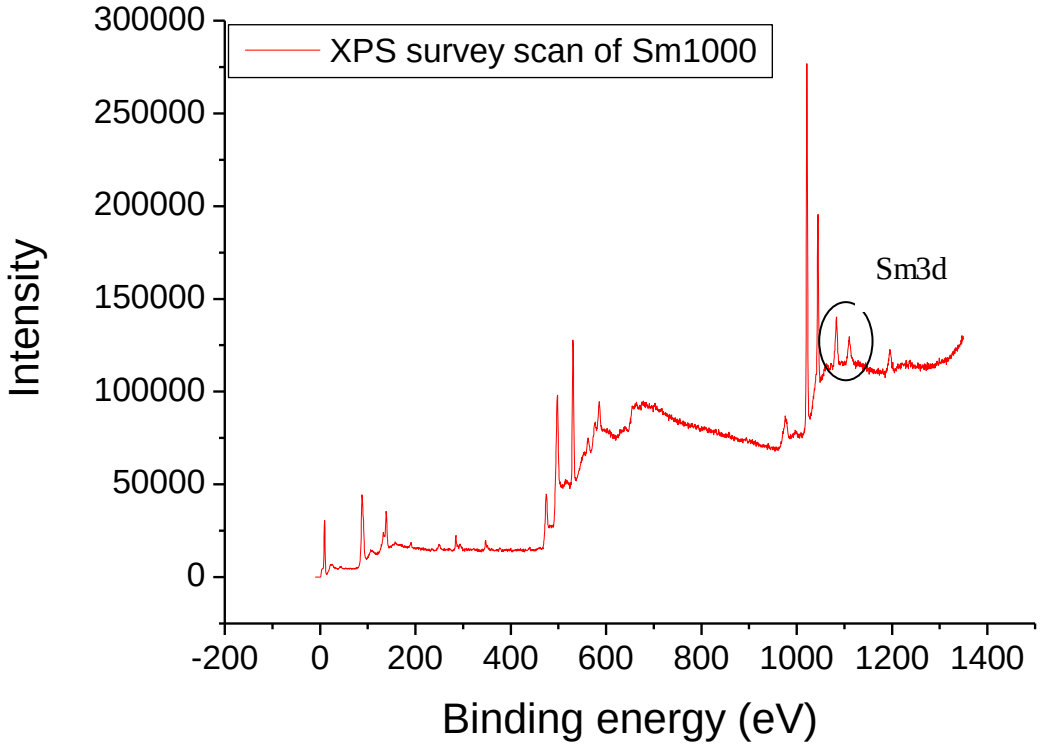
XPS survey scan of Sm1000
Sm3d
Intensity
Binding energy (eV)
300000
250000
200000
150000
100000
50000
0
-200
0
200
400
600
800
1000
1200
1400

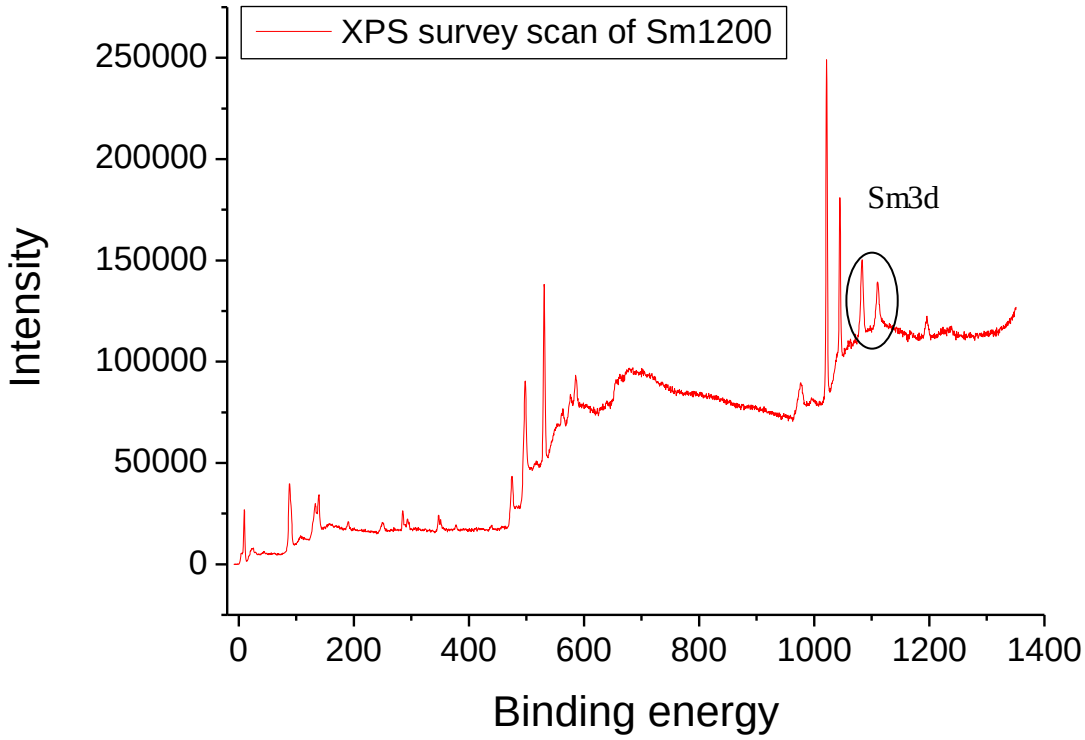
XPS survey scan of Sm1200
Sm3d
Intensity
Binding energy
0
50000
100000
150000
200000
250000
0
200
400
600
800
1000
1200
1400

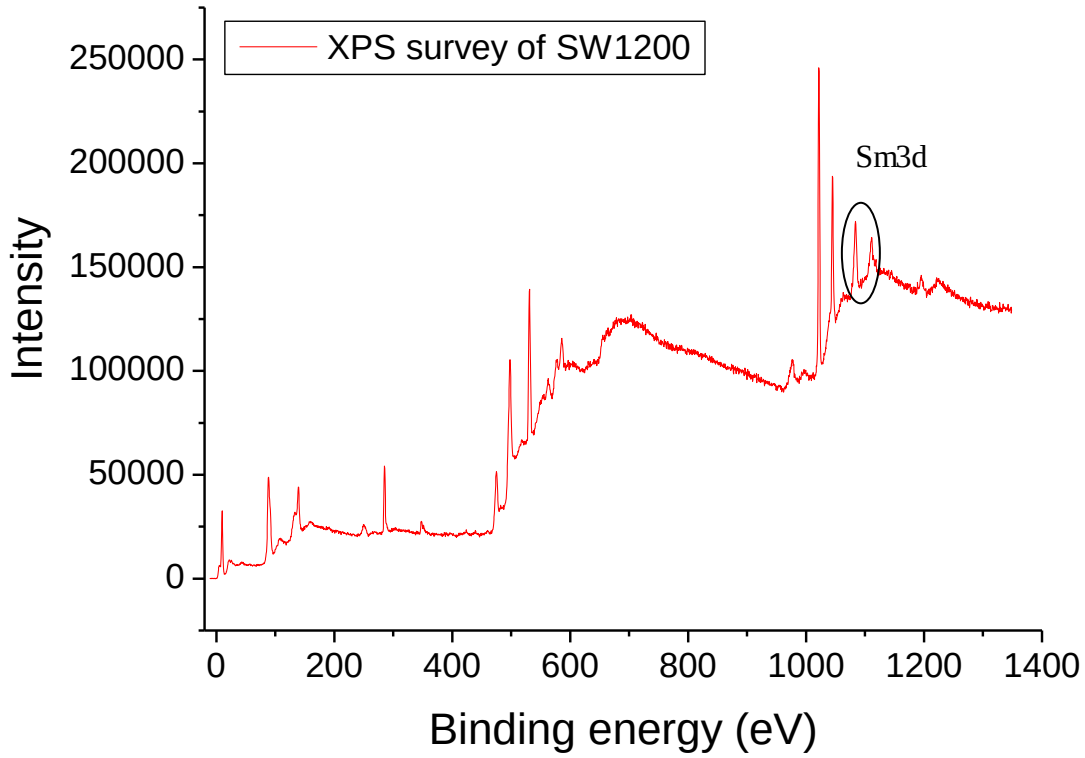
XPS survey of SW1200
Sm3d
Intensity
Binding energy (eV)
0
50000
100000
150000
200000
250000
0
200
400
600
800
1000
1200
1400

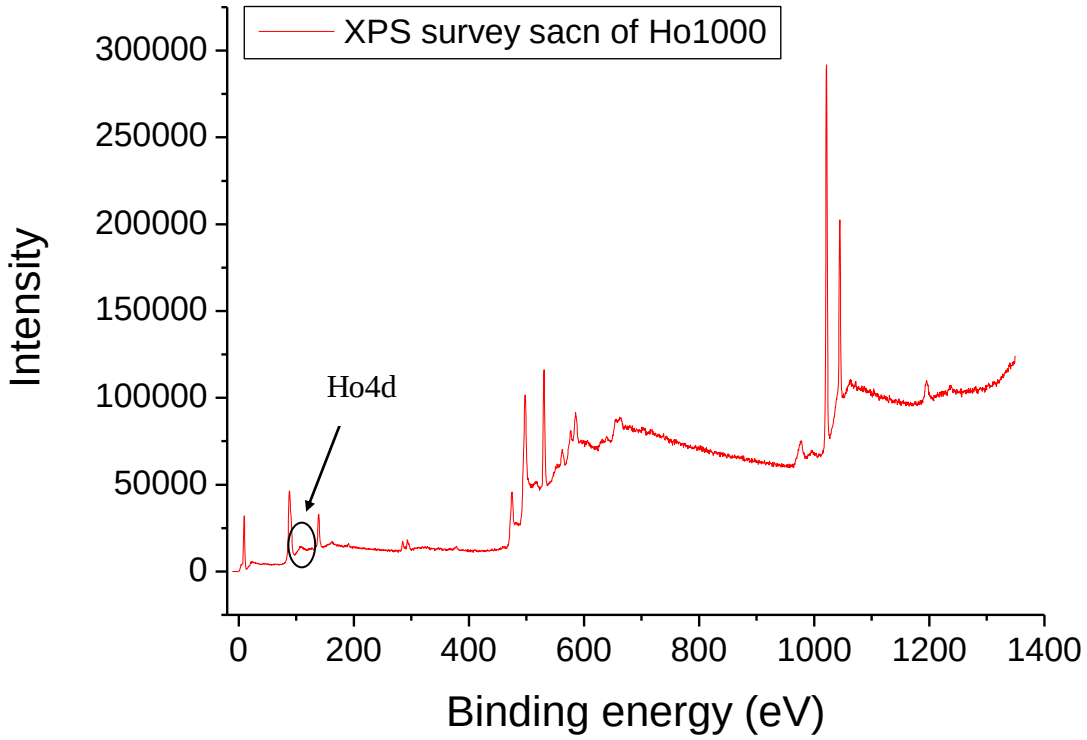
XPS survey sacn of Ho1000
Intensity
300000
250000
200000
150000
100000
50000
0
Ho4d
0
200
400
600
800
1000
1200
1400
Binding energy (eV)

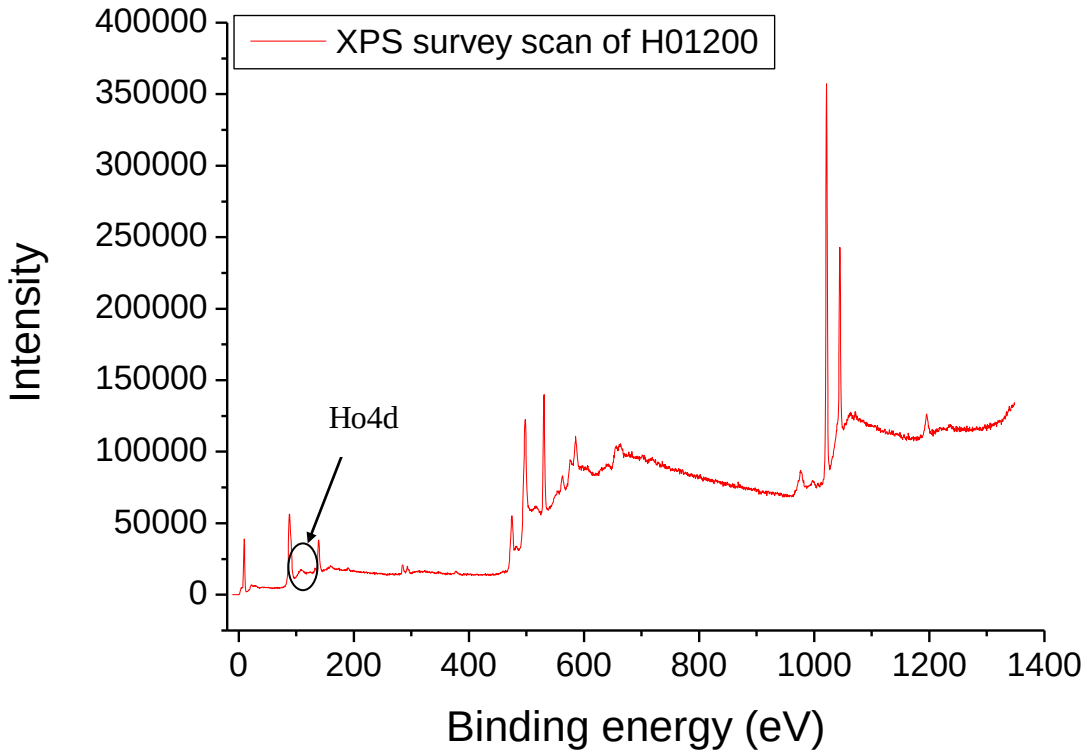
XPS survey scan of H01200
Intensity
400000
350000
300000
250000
200000
150000
100000
50000
0
Ho4d
0
200
400
600
800
1000
1200
1400
Binding energy (eV)

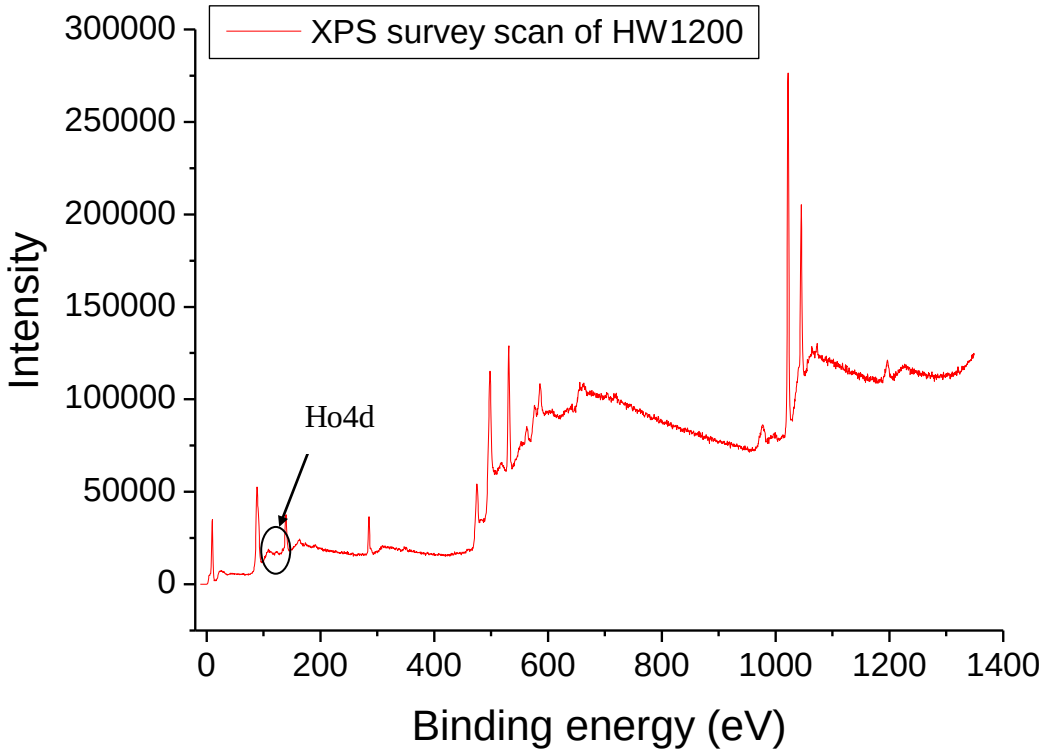
XPS survey scan of HW1200
Intensity
300000
250000
200000
150000
100000
50000
0
Ho4d
0
200
400
600
800
1000
1200
1400
Binding energy (eV)

References

[1] H. W. Kroto, J. R. Heath, S. C. O'Brien, R. E. Curl and R. E. Smally: Nature; 318, 162 (1985)

[2] Iijima et al: Nature. 354, 56 (1991)

[3] A. K. Geim & K. S. Novoselov: Nature Materials 6, 183 (2007)

[4] R. E. Smally: Carbon nanotubes; Synthesis, Structure, Properties and applications: Springer. (2001)

[5] R. Saito, G. Dresselhaus and M. S. Dresselhaus: Physical properties of carbon nanotubes; Theory and Applications. London: Imperial college press, 1998, and references therein.

[6] Meyyappan. M, Yamada. T, Sarrazin. P, and Li, J. (2005). Carbon Nanotubes: Science and Applications, CRC Press.

[7] Cheng H. M, Li S. F, Pan G, Pan H. Y, He L. L, Sun X: Appl Phys Lett; 72, 3282 (1998).

[8] Botti, S., Ciardi, R., Terranova, M. L., Piccirillo, S., Sessa, V., Rossi, M. & Vittori-Antisari, M., Appl. Phys. Lett. 80: 1441 (2002).

[9] Kusonoki, M., Rokkak, M. & Suzuki, T. Appl. Phys. Lett. 71: 2620. (1997)

[10] Kukovecz A,Ko´nya Z,Nagaraju N, Willems I,Tama´si A,Fonseca A: Phys. Chem. Chem Phys; 2, 3071 (2000)

[11] Pe´rez-Cabero M,Rodri´guez-Ramos I, Guerrero-Rui´z A: J Catal; 215, 305 (2003)

[12] Kim MS,Rodriguez NM,Baker RTK: J Catal 1992;134:253–68

[13] Randall L. Vander Wal. Thomas M. Ticich and V. E. Curtis; Carbon; 39, 2277 (2001)

[14] Baker RTK: Carbon; 27, 315 (1989).

[15] Kanzow H, Ding A: Phys Rev B; 60, 11180 (1999)

[16] R. S. Wagner and W. C. Ellis: Appl. Phys. Lett; 4, 89 (1964)

[17] Tibbetts GG: J Cryst Growth; 66, 632 (1984)

[18] Rostrup-Nielsen JR, Trimm DL: J Catal; 48, 155 (1977)

[19] Helveg S, Lo´pez-Cartes C, Sehested J, Hansen PL, Clausen BS, Rostrup-Nielsen JR, Nature 427, 426 (2004)

[20] P. Buffat and J.-P. Borel: Phys. Rev. A. 13, 2287 (1976)

[21] Q.S. Mei and K. Lu: Progr. Mater. Sci; 52, 1175 (2007)

[22] Dai H, Rinzler AG, Nikolaev P, Thess A, Colbert DT, Smalley RE. Chem Phys Lett; 260, 471 (1996).

[23] Uchino, T., Ayre, G. N., Smith, D. C., Hutchison, J. L., de Groot, C. H. & Ashburn, P: J. Electrochem. Soc. 156: K144–K148 (2009)

[24] Uchino, T., Bourdakos, K. N., de Groot, C. H., Ashburn, P., Kiziroglou, M. E., Dilliway, G. D. & Smith, D. C : Appl. Phys. Lett. 86: 233110 (2005b)

[25] Ivanov V,Nagy JB,Lambin P,Lucas A,Zhang XF,Bernaerts D: Chem Phys Lett; 223, 329 (1994)

[26] Durbach et al: Carbon 47 6, 35 (2009)

[27] W. Zhou, Z. Han, J. Wang, Y. Zhang, Z. Jin, X. Sun, Y. Zhang, C. Yan and Y. Li: Nano Lett: 6, 2987 (2006)

[28] Lee, S. Y, Yamada, M. & Miyake, M:. Carbon; 43, 2654 (2005)

[29] Mattevi, C.; Wirth, C. T.; Hofmann, S.; Blume, R.; Cantoro, M.; Ducati, C.; Cepek, C.; Knop-Gericke, A.; Milne, S.; Castellarin-Cudia, C.; Dolafi, S.; Goldoni, A.; Schloegl, R.; Robertson, J. J. Phys. Chem. C, 112, 12207 (2008)

References

[30] Hofmann, S.; Blume, R.; Wirth, C. T.; Cantoro, M.; Sharma, R.; Ducati, C.; Haevecker, M.; Zafeiratos, S.; Schnoerch, P.; Oestereich, A.; Teschner, D.; Albrecht, M.; Knop-Gericke, A.; Schloegl, R.; Robertson, J. J. Phys. Chem. C 2009, 113, 1648.

[31] Fonseca A, Hernadi K, Nagy, J. B, Bernaerts D, Lucas A. A; J . Mol. Catal A: Chem, 107,159(1996)

[32] Hernadi K ,Fonsec A, Nagy JB, Siska A, Kiricsi I; Appl Catal A 2000;199:245–55

[33] Klinke C, Bonard J-M, Kern K; Surf Sci 2001;492:195–201

[34] A. C. Dupuis; Progress in Materials Science 50 (2005) 929–961

[35] Y. T. Wong: J. Chem. Soc. Faraday. Trans; 86 (3), 553 (1990)

[36] H. Liu. , D. Tagaki, S. Chiashi, T. Chokan and Y. Homma: J. Nanosci Nanotechnol: 10, 4068 (2010)

[37] S. A. Steiner, T. F. Baumann, B. C. Bayer, R. Blume, M. A. Worsley, W. J. MoberlyChan, E. L. Shaw, R. Schlögl, A. J. Hart, S. Hofmann and B. L. Wardle: J. AM. CHEM. SOC, 131, 12144 (2009)

[38]B. Liu , D. M. Tang, C. Sun, C. Liu, W. Ren, F. Li, Wan-Jing Yu, Li-Chang Yin, L. Zhang, C. Jiang, and H. M. Cheng: J. AM. CHEM. SOC., 133, 197 (2011)

[39] M. H. Ru¨mmeli, F. Scha¨ ffel1, A. Bachmatiuk1, G. Trotter, D. Adebimpe, G.Simha-Martynkova, D.Placha, B. Rellinghaus, P. McCormick, E. Borowiak-Palen, P. Ayala, T. Pichler, R. Klingeler, M. Knupfer, and B. Buchner: Phys. Status Solidi B. 246, 2530 (2009)

[40] M. S. Dresselhaus, G. Dresselhaus and R. Ssito: Carbon; 33, 883 (1995)

[41] Redushkevich and Lukenovich: Zurn Fisic Chim. 26, 88 (1952)

[42] Saito, M. Fujita, G. Dresselhaus and M. S. Dresselhaus: Appl. Phys. Lett; 60, 2204 (1992)

[43] [http://sina.sharif.edu/~k1/nano.html].

[44] Benedek G, Milani P, Ralchenko VG, editors. Nanostructured Carbon for Advanced Applications. Dordrecht, The Netherlands: Kluwer Academic Publishers; 2001.

[45] Birò LP, Bernardo CA, Tibbetts GG, Larnbin PH, editors. Carbon Filaments and Nanotubes: Common Origins, Differing, Applications?. Dordrecht, The Netherlands: Kluwer Academic

[46] S, J. Tans, A. R. M. Verschueren & C. Dekker: Nature, 393, 49 (1998).

[47] N. Aoki, J.Takayama, M.Kida, K.Horiuchi, S.Yamada, T.Ida, K.Ishibashi and Y. Ochiai: J. J. Appl. Phy, 42, 2419 (2003).

[48] O. Lourie, D. M. Cox, and H. D. Wagner: Phys. Rev. Lett; 81, 1638 (1998)

[49]J. P. Lu: Phys. Rev. Lett. 79, 1297 (1997)

[50] A.Sears and R. C. Batra: Phys. Rev. B; 69, 235406 (2004)

[51] M. F. Yu, O. Louriel, M. J. Dyer, K. Moloni, T. F. Kelly and R. S. Ruoffl: Science; 287, 637 (2000)

[52] Salvetat, J.-M. Bonard, N.H. Thomson, A.J. Kulik, L. Forr´o, W. Benoit, L. Zuppiroliet al: Appl. Phys. A 69, 255 (1999)

[53] N. de Jonge, M. Allioux, J. T. Oostveen, K. B. K. Teo,and W. I. Milne: Phil. Trans. R. Soc. London. A. 362, 2239(2004)

[54] N. M. Gabor, Z. Zhong, K. Bosnick, J. Park, P. L. McEuen; Science 310, 1171 (2005)

[55] P. Kim, L. Shi, A. Majumdar, and P. L. McEuen: Phys. Rev. Lett. 87, 215502 (2001)

[56] L. G. C. Rego and George Kirczenow: Phys. Rev. Lett. 81, 232 (1998)

[57] C. W. Chang, D. Okawa, A. Majumdar, A. Zett: Science. 314, 1121 (2006)

References

[58]Q. Xiao, X. Zhou: Electrochimica Acta 48, 575 (2003)

[59] Hot nanotube sheets produce music on demand, New Scientists News, 31 October 2008

[60] C. Lui, Y. Y. Fan, M. Lui, H. T. Cong, H. M. Chemg and M. S. Dresselhaus; Science, 286, 1127 (1999)

[61] J. Cong, N. R. Frankline, C. Zhou, M. G. Chapline, S. Peng, K. Cho and H. Dai: Science. 287, 622 (2000)

[62] T. Guo, P. Nikolaev, A. Thess, D.T. Colbert, R.E. Smalley: Chem. Phys. Lett, 243, 49 (1995)

[63] J. Kong, H. T. Soh, A. M. Cassell, C. F. Quate & H. Dai

[64] S. Iijima and T. Ichihashi: Nature. 363, 603 (1993)

[65] D. S. Bethune, C. H. Klang, M. S. de Vries, G. Gorman, R. Savoy, J. Vazquez and R. Beyers: Nature. 363, 605 (1993)

[66] S. Seraphin: J. electrochem. Soc, 142, 290 (1994)

[67] S. Subramoney, R.S. Ruoff, D.C. Lorents and R. Maihotra, Nature 366, 637 (1993).

[68] D. Zhou, S. Seraphin and S. Wang, Appl. Phys. Letters 65, 1593 (1994).

[69] Ebbesen and Ajayan: Annu. Rev. Mater. Sci, 24, 235 (1994)

[70] T.W. Ebbesen, H. Hiura, J. Fujita, Y. Ochiai, S. Matsui and IL Tanigaki: Chem. Phys. Lett. 209, 83 (1993)

[71] G.H. Taylor a J.D. Fitz Gerald a L. Pang b and M.A. Wilson: J. Cryst. Growth. 135, 157 (1994)

[72] C. D. Scott, S. Arepalli, P. Nikolaev and R. E. Smalley: Applied Physics A: Materials Science & Processing 72, 573 (2001)

[73] A. Koshio, M. Yudasaka, S. Iijima: Chemical Physics Letters 356, 595 (2002)

[74] T. Koyama, M.Endo and Y. Onuma: Jpn. J. Appl. Phys. 11, 445 (1972).

[75] C. P. Deck and K. Vecchio: Carbon, 44, 267 (2007)

[76] Yazyev, O. V. & Pasquarello, A: Phys. Rev. Lett; 100: 156102 (2008)

[77] A Jungen, C Stampfer, L Durrer, T Helbling and C Hierold: Nanotechnology 18, 075603 (2007)

[78] H. Dai : Acc. Chem. Res: 35, 1035 (2002)

[79] C. L. Tsai, C. F. Chen, and L. K. Wu: Appl. Phys. Lett. 81, 721 (2002)

[80] C. Bower, W. Zhu, S. Jin and Otto Zhou: Appl. Phys. Lett; 77, 830, (2000)

[81] L. Delzeit, I. McAninch, B.A. Cruden, D. Hash, B. Chen, J.Han, and M. Meyyappanc: J. Appl. Phys. 91. 6027 (2002)

[82] V. I. Merkulov, D. H. Lowndes, Y. Y. Wei, and G. Eres and E. Voelkl: Appl. Phys. Lett. 76, 3555 (2000)

[83] K. B. K. Teo, M. Chhowalla, G. A. J. Amaratunga, W. I. Milne, D. G. Hasko, G. Pirio, P. Legagneux, F. Wyczisk, and D. Pribat: Appl. Phys. Lett, 79, 1534 (2001)

[84] S. M. Rossnagel, J. J. Cuomo, W. D. Westwood. "Handbook of Plasma processing Technology (2002).

[85] Z. Machala, E. Marode, C. O. Laux, and C. H. Kruger, J. Adv. Oxid. Technol. Vol. 7, No. 2, (2004)

[86] M. Tanemura,a) K. Iwata, K. Takahashi, Y. Fujimoto, and F. Okuyama, H. Sugie and V. Filip: J. Appl. Phys. 90, 1529 (2001)

[87] http://mysite.du.edu/~jcalvert/phys/dischg.htm

[88] R.T.K. Baker, M.A. Barber, P.S. Harris, F.S. Feates, R.J. Waite: Journal of Catalysis : 26, 51 (1972)

[89] R. Seidel, G. S. Duesberg, E. Unger, A. P. Graham, M. Liebau, and F. Kreupl: J. Phys. Chem. B. 108, 1888 (2004)

[90] T. Baird, J. R. Fryer, and B. Grands: Carbon. 12, 591 (1974)

References

[91] P. M. Ajayan: Nature, 427, 402 (2004)

[92] R. S. Wagner and W. C. Ellis: Appl. Phys. Lett; 4, 89 (1964)

[93] R. S. Wagner, C. J. Doherty, and W. C. Ellis: J. of Metals; 16, 761 (1964)

[94] Y. Saito, M. Okuda, M. Tomita, T. Hayashi: Chem. Phys. Lett; 236, 419 (1995)

[95] P. Buffat and J. P. Borel: Phys. Rev. A. 13, 2287 (1976)

[96] Q.S. Mei and K. Lu: Progr. Mater. Sci; 52, 1175 (2007)

[97] A. Moisala, A. G Nasibulin and E. I Kauppinen: J. Phys. Condens. Matter; 15, S3011 (2003)

[98] S. M. Huang: Nano letters. 4, 1025 (2004)

[99] A. Gohier, C. P. Ewels, T.M. Minea, M.A. Djouadi: Carbon. 46, 1331 (2008)

[100] King D A, Woodruff D P, editors. Growth and properties of ultrathin epitaxial layers,8. Elsevier;1997. p. 1–45.

[101] J. Dijon, P. D. Szkutnik, A. Fournier, T. G. de Monsabert, H. Okuno, E.Quesnel, V. Muffato, E. De Vito, N. Bendiab, A. Bogner, and N. Bernier: Carbon. 48, 3953 (2010)

[102] P. Hawks: Appl. Geometrical optics. Academic press ltd. 1989

[103] M. Prutten and M. El Gomalti, Scanning Auger Electron Microscopy. P-59

[104] Vacuum Electron Sources and their Materials and Technologies p-432: by G. Gaertner and H. W. P. Koops:

[105] Richardson et al: "Some applications of the electron theory of matter", Phill Mag, Series 6, issue 23, 136, 594 (1912)

[106] J. Goldstein, D. Newbury, D. Joy, C. Layman, P. Echlin, E. Lifshin, L. Sawyer and J. Michael: Scanning Electron Microscopy and x-ray microanalysis: 3rd Edition p-30.

[107] R. Nishitani, M. Aono, T. Tanaka, C. Oshima, S. Kawai, H. Iwasaki, S. Nakamura: Surface Science 93 (1980) 535-549

[108] N. A. de- Bruyne: Proc. Roy. Soc. A 120, 423 (1928)

[109] D.W. Truggle and L.W. Swanson : J. Vac. Sci. Technol: B, 3, 220 (1985)

[110] H. S. Kim, M. L. Yu, M. G. R. Thomson, E. Kratschmer, and T. H. P. Chang: J. Appl. Phys. 81, 461 (1997)

[111] L. Swanson and L. Crouser: Phys. Rev. 163, 622 (1967)

[112] Handbook of charged particle optics p-80, "by Jon Orloff"

[113] Philippe Sarrazin: Carbon nanotube Science & Applications, Ch-8, P-196

[114] F. Rohrbach. CERN report 1971; 71-5/TC-L

[115] R .H. Fowler and L. Nordheim, Proceedings of the royal society London, A119, 173 (1928).

[116] J. M. Bonard, H. Kind, T. Stöckli, and L. O. Nilsson: Solid state electronics, 45, 893 (2001)

[117] Luzhang thesis

[118] S. Han and J. Ihm : Phys. Rev. B. 61, 9986 (2000)

[119] H. Schmid and H. W. Fink: Appl. Phys. Lett. 70, 2679 (1997)

[120] N. de-Jonge, Y. Lamy, K. Shoots and T. H. Oosterkamp: Nature. 420, 393 (2002)

[121] K. A. Dean et and B. R. Chalamala: J. Appl. Phys. 85, 3832 (1999)

[122] L. Nilson, O. Groenning, C. Emmenegger, O. Kuettel, E. Schaller, L. Schlapbach, H. Kind, J. M. Bonard and K. Kern: Appl. Phys. Lett. 76, 2071 (2000)

[123] J. M. Bonard, J. P. Salvetate, T. Stöckli, L. Forró and A. Châtlain: Appl. Phys. A. 69, 245 (1999)

References

[124] S. Fujii S. I. Honda, H. Machida, H. Kawai, K. Ishida, M. Katayama,H. Furuta, T. Hirao and K. Oura : Appl. Phys. Lett. 90,153108 (2000)

[125] C.W. Baik, J. Lee, D. S. Chung, S. C. Jun, J. H.Choi, B. K. Song, M. J. Bae, T. W. Jeong, J. N.Heo, Y. W. Jin, J.M. Kim, S. Yu, K.-H. Jang, and G.S. Park,: IEEE TRANSACTIONS ON ELECTRON DEVICES, 54, 2392 (2007)

[126] E. H. Kisi and M. M. Elcombe: Acta Cryst.. C45, 1867(1989)

[127] H. Karzel, W. Potzel, M. Köfferlein, W. Schiessl, M. Steiner, U. Hiller, G. M. Kalvius, D. W. Mitchell T. P. Das, P. Blaha K. Schwarz and M. P. Pasternak: Phys. Rev. B 53, 11425 (1996)

[128] S. Desgreniers: Phys. Rev. B 58, 14102 (1998)

[129] Y. Catti, Y. Noel and R. Dovesi : Phys. Chem. Solids 64, 2183 (2003)

[130] T. Kogure and Y. Bando: J. Electron Microsc. 47, 7903 (1993)

[131] J. E. Jaffe and A. C. Hess: Phys. Rev. B 48, 7903 (1993)

[132] J. M. Recio and M. A. Blanco and V. Luaña: Phys. Rev. B 58, 8949 (1998)

[133] C. H. Bates, W. B. White, and R. Roy, Science 137, 993 (1962)

[134] L. Gerward, J. S. Olsen: J. Synchrotron Radiat. 2, 233 (1995)

[135] T. Minami, H. Sato, H. Nanto, and S. Takata: Jpn. J. Appl. Phys., Part 2, Vol; 24, L781 (1985)

[136] S. W. Jung, S.-J. An, Gyu-Chul Yi, C. U. Jung, Sung-Ik Lee, and Sunglae Cho: , Appl. Phys. Lett. 80, 4561 (2002)

[137] P. Sharma, K. Sreenivas, and K. V. Rao: J. Appl. Phys. 93, 3963 (2003)

[138] C. Liu, F. Yun and H. Morkoc: J. Material Science: Materials in Electronics.16, 555 (2005)

[139] C. H. Chien, S. H. Chiou, G.Y. Guo and Yeong-Der Yao. Journal of Magnetism and Magnetic Materials 282, 275 (2004)

[140] J. K. Furdyna: J. Appl. Phys: 64, R29 (1988)

[141] J. Kong, A. M. Cassell and H. Dai: Chem Phys Lett 292, 567 (1998)

[142] Chapman, S. K. (1986). Maintaining and Monitoring the Transmission Electron Microscope. Royal Microscopical Society Microscopy Handbooks. 08. Oxford University Press. ISBN 0198564074.

[143] Introduction to solid state physics by Kittel Chap: 2 and p-19

[144] Young Ah Jeon et al. METALS AND MATERIALS International, Vol. 9, No. 4, pp. 383(2003)

[145] M. N. Rahaman and R. Manalert : Journal of the European Ceramic Society 18, 1063 (1998)

[146] R. J. Brook: Proc, Brit Ceram. Soc. 32, 7 (1982)

[147] X, Guo , W, Sigle, J, Fleig, J, Maier: Solid State Ionics: Vol (154– 155), 555 (2002)

[148] S.J Bennison and M. P Harmer; J. Am. Ceram. Soc. 68 (1) C22-C24 (1985)

[149] J. S. Park, S. K. Hong, T. Minegishi, S. H. Park, I. H. Im, T. Hanada, M. W. Cho, T. Yao, J. W. Lee, and J. Y. Lee : Appl. Phys. Lett, 90, 201907 (2007)

[150] D. Ricci, A. Bongiorno, G. Pacchioni and U. Landman: Phys. Rev. Lett. 97, 036106 (2006)

[151] U. Landman, Proc. Natl. Acad. Sci. U.S.A. **102**, 6671 (2005).

[152] H. C. Gatos: J. Appl. Phys. **32**, 1232 (1961)

[153] A. N. Mariano and R. E. Hanneman ; J. Appl. Phys. 34, 384 (1963)

[154] I. Constant, F. Tardif and J. Derrien; Semicond. Sci. Technol. 15 (2000) 61–66.

[155] M. Kakazey, M. Vlasova, M. Dominguez-patiño, G. Dominguez-patiño. Y. E. Méndez, M. C. R. Gonzalez, T. Tomila, M. Ristic and M. V. Nikolic; Powder Technology. 193, 130 (2009)

[156] X. J. Liu, C. Song, F. Zeng, F. Pan, B. He, and W. S. Yan. J. Appl. Phys. 103, 093911 (2008)

[157] S. Bayan, U. Das, and D. Mohanta; Phys. Status Solidi A 207, 1859 (2010)

[158] G. K. Williamson and W. H. Hall, Acta Metall. 1, 22 (1953).

[159]J. Ghijsen, L. H. Tjeng, J. van Elp, H. Eskes, J. Westerink, and G. A. Sawatzky: Phys. ReV. B, 38, 11322 (1988)

[160] D. Chakraborti, J. Narayan, and J. T. Prater: Appl. Phys. Lett. 90, 062504 (2007)

[161] K. S. Kim: Journal of Electron Spectroscopy and Related Phenomena, 3, 217 (1974)

[162] Marion A. Brisk and A. D. Baker; Journal of Electron Spectroscopy and Related Phenomena, 7, 197 (1975)

[163] G. Xing, M. Li, E. J. Sie, D. Wang, A. Sulistio, Q-lin Ye, C. H. A. Huan, T. Wu, and T.C. Sum: Appl. Phys. Lett; 98, 102105 (2011)

[164] A. Hartmann, M. K. Puchert and R. N. Lamb: surface and interface analysis, Vol. 24, 671 (1996).

[165] T. Novakov: Phys. Rev. B. 3, 2693 (1971).

[166] K. Hirokawa, F. Honda, and M. Oku, J. Electron. Spectrosc. 6, 333 (1975)

[167] B. J. Coppa, R. F. Davis, and R. J. Nemanich: Appl. Phys. Lett. 82, 400 (2003)

[168]J. C. C. Fan, J. B. Goodenough: J. Appl. Phys. 48 3524 (1977).

[169] R. K. Singhal, S. C. Sharma, P. Kumari, Sudhish Kumar, Y. T. Xing, U. P. Deshpande, T. Shripathi, and Elisa Saitovitch: J. Appl. Phys. 109, 063907 (2011)

[170]M. N. Islam, T.B. Ghosh, K.L. Chopra, H.N. Acharya. Thin Solid Films 280, 20 (1996)

[171] X. Huang, G. Li, L. Duan, L. Li, X. Dou, and L. Zhang, Scr. Mater. 60, 984 (2009).

[172] A. M. Venezia, A. Rossi, D. Duca, A. Martorana and G. Deganello, Appl. Catal., A, 125, 113 (1995)

[173] C. D. Wagner, W. M. Riggs, L. E. Davis, and J. F. Moulder, Handbook of X-ray Photoelectron Spectroscopy (Perkin, Elmer, Eden Prairie, 1979), p.81.

[174] J. M. D. Coey, K. Wongsaprom, J. Alaria and M. Venkstesan: J. Appl. Phys. D: Appl. Phys; 41, 134012 (2008)

[175] R. K. Singhal, A. Samariya, Y. T. Xing, S. Kumar, S. N. Dolia, T. Shripathi,U. P. Deshpande, and E. Saitovitch, J. Alloys Compd. 496, 324 (2010).

[176] R. K Singhal, M. Dhawan, S. K Gaur, S. N. Dolia, S. Kumar, T. Shripathi, U. P. Deshpande, Y. Xing, E. Saitovitch, and K. B. Garg, J. Alloys Compd. 477, 379 (2009).

[177] S. Major, S. Kumar, M. Bhatnagar, K.L. Chopra, Appl. Phys. Lett. 40. 394 (1986)

[178] P. Yang, C. M. Lieber, J. Mater, Res, 12, 2981 (1997)

[179] S. S. Pitale, V. Kumar, I. M. Nagpure, O. M. Ntwaeaborwa, E. Coetsee, and H. C. Swart: J. Appl. Phys. 109, 013105 (2011)

[180] D. Sarma and C N R Rao: Journul of Electron Spectroscopy and Related Phenomena, 20, 25 (1980)

[181]G. Blanco, J. M. Pintado, S. Bernal, M. A. Cauqui, M. P. Corchado, A. Galtayries, J. Ghijsen, R. Sporken, T. Eickhoff and W. Drube : Surf, Interface anal. 34, 120 (2002)

[182] L. Yang, Y. Tang, A. Hu, X. Chen, K. Liang and L. Zhang: Physica. B. 403, 2230 (2008)

[183] Rodrigo. M. P, Fredrik. S, Anna. K, Anke. S, marc. A. F, Natalia. A, Linnea. S, Per-Olov. K, Maria. E and

Kajsa. U, J. Phys. Chem. C. 113, 6913 (2009)

[184] G. R. Li, X. H. Lu, C. Y. Su, and Y. X. Tong: J. Phys. Chem. C; 112, 2927 (2008)

[185] B.D. Padalia, W.C. Lang, P.R. Norris, L.M. Watson, D.J. Fabian, Proc. R. Soc. A 354 (1977) 269.

[186] Tiekun J. Weimin W, Fei L, Hao W, Qingjie Z, Material Science and Engineering B, 162, 179 (2009)

[187] D. J, Kim; J. of Am. Ceram. Soc; 72, 1415 (1989)

[188] Cheng F., Jia J., Xu Z., Zhou B., Liao C., Yan C., Chen L.,and Zhao H; J. Appl. Phys; 86, 2727 (1999).

[189] J Zhang, S H Liou and D J Sellmyer; J. Phys.: Condens. Matter 17, 3137 (2005)

[190] Ü. Özgür, Ya. I. Alivov, C. Liu, A. Teke, M. A. Reshchikov, S. Doğan, V. Avrutin, S.-J. Cho, and H. Morkoç: J. Appl. Phys. 98, 041301 (2005)

[191] S. Karamat, S. Mahmood, J. J. Lin, Z. Y. Pan, P. Lee, T. L. Tan, S. V. Springham, R. V. Ramanujan and R. S. Rawat; Appl. Surf. Sci; 254, 7285 (2008)

[192] George. K. C, Karien. S, Mathew. J: J. Nanosci Nanotechnol; 7, 2016 (2007)

[193] L. A. Xu; PhD thesis ; University of Leeds (1987)

[194] F. Yakuphanoglu, S. Ilican, M. Caglar, Y. Caglar; J. Optoelectron. Adv. Mater. 9, 2180 (2007)

[195] Y. Mori and S. Tanemura: appl. Surface Science, 253, 3856 (2007)

[196] S. Kačiulis, A. Latišenka and A. Plešanovas; Surface Science, 251, 330 (1991)

[197] W. C. lang, B. D. Padalia, D. J. Fabian and L. M. Watson: J. Electron. Spectry. 5, 207 (1974)

[198] E. J. Chao; Journal of the Korean Physical Society, 51,1331 (2007)

[199] G. Dufour, R. C. karnatak, J. M. Mariot, C. Bonnelle, Chem. Phys. Lett, 42, 433 (1976)

[200] M. G. Mason, S. T. Lee, G. Apai, R. F. Davis, D. A. Shirley, A. Franciosi and J. H. Weaver; Phys. Rev. Lett; 47, 730 (1981)

[201] G. K. Wertheim and G. Grecelius; Phys. Rev. Lett; 40, 813 (1978)

[202] P. Burroughs, A. Hamnett, A. F. Orchard and G. Thornton; J. Chem. Soc. Dalton Trans. 1686 (1976)

[203]W. O. Milligan, D. F. Mullica, H. O. Perkins and C. K. C. Lok; J. Phys. Chemistry; 87, 5411 (1983)

[204] G. Crecelius, G. K. Werdeim and D. N. E. Buchanan; Pys. Rev. B. 18, 6519 (1978)

[205] T. D. Nguyen, D. Mrabet, and Trong-On Do: J. Phys. Chem. C ; 112, 15226 (2008)

[206] Y Zhang, Y L Chen, Y J Cui, C H Cheng, H Zhang and Y Zhao; Supercond. Sci. Technol. 22, 015007 (2009)

[207] http://www.standnes.no/chemix/periodictable/electronegativity-chart.htm

[208] P Singh, A. B. Mandale and S. badrinarayanan. J of Less Common Metals; 141, 1 (1988)

[209] S. P. Kowalczyk, N. Edelstein, F. R. McFeely, L. Ley and D. A. Shirley; Chem. Phys. Lett. 29, 491 (1974)

[210] A. Kotani; J. Electron. Spectrosc. Relat. Phenom, 100, 75 (1999)

[211] Hongxia Li, Hong Liu, Jiyang Wang, Shushan Yao, Xiufeng Cheng, R.I. Boughton; Materials Letters 58, 3630 (2004)

[212] G. Litsardakis, I, Manolakis, C, Serletis and K. G. Efthimiadis: J. Magn. Magn. Meter; 316, 170 (2007)

[213] C. Cheng, Z.J. Jiang, C.Y. Liu, J. Photoch, Photobiol A: Chem. 195, 151 (2008).

[214] D. J. Digiovanni, T. F. Morse and J. W. Cippolla. Jr.; Journal of light wave technology, 7, 1967 (1989)

[215] Hofmann, S.; Blume, R.; Wirth, C. T.; Cantoro, M.; Sharma, R.; Ducati, C.; Haevecker, M.; Zafeiratos, S. Schnoerch, P.; Oestereich, A.; Teschner, D.; Albrecht, M.; Knop-Gericke, A.; Schloegl, R.; Robertson, J. Phys. Chem. C 2009, 113, 1648.

References

[216] Sun H, Zhang Q-F, Wu J-L: Nanotechnology;17, 2271 (2006)

[217] Huang MH, Mao S, Feick H, Yan H, Wu Y, Kind H: Science;292,1897 (2001)

[218] T. Jiang, T. Xie, Y. Zhang, L. Chen, L. Peng, H. Li and D. Wang; Phys: Chem. Chem. Phys; 12, 15476 (2010)

[219] X. Y. Zeng, J. L. Yuan, Z. Y. Wang, and L. D. Zhang, Adv. Mater. 19,4510 (2007)

[220] M. Wang, C. Huang, Z. Huang, W. Guo, J. Huang, H. He, H. Wang, Y.Cao, Q. Liu, and J. Liang, Opt. Mater. 31, 1502 (2009)

[221] W. G. Frenkenburg; Advances in catalysis and related subjects p-72

[222] Y. A. Berlin, G. R. Hutchison, P. Rampala, M. A. RanterJ. J. Michl; Phys. Chem. A. 107, 3970 (2003)

[223] M. Bixon, and J. Jortner; Adv. Chem. Phys; 106, 35 (1999)

[224] H. Grönbeck: Phys. Rev. B; 84, 052301 (2011)

[225] M. Mavrikakis, B. Hammer, and J. K. Nørskov;: Phys. Rev. Lett: 81, 2819 (1998)

[226]I. Levchenko and K. Ostrikov: Nanotechnology 19, 335703 (2008)

[227]L. Tsakadze, I. Levchenko, K. Ostrikov, and S. Xu: Carbon 45 2022 (2007)

[228] G. Frohberg. Phys. State Sol. B; 48, 243 (1971)

[229] C. J. Lee and J. Park; Carbon 39, 1891 (2001)

[230] X. Z. Liao, A. Serquis, Q. X. Jia, D. E. Peterson, Y. T. Zhu and H. F. Xu; Appl. Phys. Lett: 82, 2694 (2003)

[231] J. B. Fernandas : Electrolysis Department of Chemistry University of Goa, Goa

[232] K. W. Blazy; Physica. B. 89, 47 (1977)

[233] Wikipedia

[234] F. A. Kröger: J. Phys. Chem. Solids. 29, 1889 (1968)

[235] W. G. Frenkenburg; Advances in catalysis and related subjects p-72

[236] A. Serquis et al: Appl. Phys. Let; 79, 4399 (2001)

[237] J. A. S. Ikeda, Y.-M. Chiang, A. J. G. Reed, and J. B. V. Sande: J. Am. Ceram. Soc: 76, 2447 (1993)

[238] Zavarukhin and G. G. Kuvshinov. Appl. Catalysis A. 272, 219 (2004)

[239] V.I. Merkulov. M.A.Guillorn. D.H. Loowndes, M. L. Simpson and E. Voelkl. Appl. Phys. Lett. 79, 1178 (2001)

[240] C. J. Lee, J. H. Park and J. Park: Chem. Phys. Lett. 323, 560 (2000)

[241] J. Wintterlin, T. Zembelli, J. Trust, J. Greeley and M. Mavrikakis: Angew. Chem. Int. Ed; 42, 2849 (2003)

[242] X. B. Wang, D. M. Li, F. Zeng and F. Pan: J. Appl. Phys. D; 38, 4104 (2005)

[243] G. Xing, Guichuan Xing, M. Li, E. J. Sie, D. Wang, A. Sulistio, Q. Ye, C. H. A. Huan, T. Wu, and T. C. Sum: Appl. Phys. Lett; 98, 102105 (2011)

[244] R.T.K. Baker and and R. J. Waite : J. catalysis : 37, 101 (1975)

[245] S. Ghosh, P. Srivastava. B. Pandey, M. Saurav, P. Bharadwaj, D.K. Avasthi, D. Kabiraj, S.M. Shivaprasad: Appl.Phys. A. 90, 765 (2008)

[246] S.Singh, N. Rama and M. S. R. Rao: Appl. Phys. Lett, 88, 222111 (2006)

[247] M. L. Renolds, W. E. Hagston and G. F. J. Garlick: Phys. State. Sol; 33, 579 (1969)

[248] V. I. Merkulov, A. V. Melechko, M. A. Guillorn, D. H. Lowndes, and M. L. Simpson; Appl. Phys. Lett; 79, 2970 (2001)

[249] M. Laudon, N. N. Carlson, M.l P. Masquelier, M. S. Daw and W. Windl; Appl. Phys. Lett: 78, 201 (2001)

References

[250] G. Quyang, X. Tan, W. G. Zhu, C. Q. Sun, Z. M. Zhu and S. Z. Liao: Phys. Chem. Chem. Phys: 12, 1543 (2010)

[251] G. Quyang, X. Tan and G. Yang: Phys. Rev. B. Cond. Matter. Mater. Phys. 53, 1827 (2005)

[252] G. Quyang, G. Yang, C. Sun and W. Zhu: Small; 4, 1359 (2008)

[253] G. Li, M. Josowicz, J. Janata and S. Semancik; Apply. Phys. Lett; 85, 1187 (2004)

[254] M. Chhowalla, K. B. K. Teo, C. Ducati, N. L. Rupesinghe, G. A. J. Amaratunga, A. C. Ferrari, D. Roy, J. Robertson, and W. I. Milne : J. Appl. Phys. 90, 5308 (2001)

[255] H. B. Shu: J. Phys. Condens. Matter; 19, 276213 (2007

[256] Handbook of compound semiconductors: By P. H. Holloway and G. E. McGuire p-273 and the references therein.

[257] http://www.doitpoms.ac.uk/tlplib/slip/printall.php

[258] H B Shu, G C Zhou, X L Zhong, L Z Sun, JBWang, X S Chen and Y C Zhou: J. Phys.: Condens. Matter; 19, 276213 (2007)

[259] A Chambers. R. K. Fitch, B. S. Holliday. Basic vacuum Technology. Adam higher imprint by IOP Publishing ltd; 1991

[260] C. Dong, M. C. Gupta. Appl. Phys. Lett. 83, 159 (2003)

[261] K. A. Dean, P. V. Allmen and B. R. Chalamala. J. Vac. Sci. Technol. B. 17, 1959 (1999)

[262] C. Baik, J. Lee, D. Chung, J.Choi, In-Taek Han, H. Kim, S. Park,S.Kim, Y. Jin, J. Kim, S. Yu, K. Jang, and G.Park: IEEE Transactions on Nanotechnology,. 6, 727 (2007)

[263] N. Y. Huang, J. C. She, J. Chen, S. Z. Deng, N. S. Xu, H. Bishop, S. E. Huq, L. Wang, D. Y. Zhong, E. G. Wang, and D. M. Chen, Phys.Rev. Lett. 93, 075501 _2004_.

[264] Z. L. Wang, R. P. Gao, W. A. de Heer, P. Poncharal: Appl. Phys. Lett., 80, 856 (2002)

[265] A. Von Hippel, E. P. Gross, J. G. Jelatis and M. Geller; Phys. Rev. 91, 568 (1953)

[266] M. S. Wang, J. Y. Wang, and L. M. Peng, Appl. Phys. Lett. 88, 243108 (2006).

[267] M. S. Wang, Q. Chen, and L. M. Peng, Small 4, 1907 (2008)

[268] G. Zhang, W. Duan and B. Gu: Appl. Phys. Lett; 80, 2589 (2002)

[269] H.L. Sun, J. F. Jia, D. Zhong, Q. T. Shen, M. Sun, Q.K. Xue, and E. G. Wang: Phys. Rev. B; 66 085423 (2002)

[270]T. Ikuno, S.Honda, H. Furuta, K. Aoki, T. Hirao , K. Oura and M. Katayama: Jpn J Appl Phys;44:1655 (2005)

[271]H. Tanaka, S. Akita, L. Pan and Y. Nakayama: J. J. Appl. Phys. 43, 864 (2004)

[272] A. G. Rinzler, J. H. Hafner, P. Nikolaev, L. Lou, S. G. Kim, D. Tomanek, P. Nordlander, D. T. Colbert, and R. E. Smalley, Science **269**, 1550 (1995)

[273] I. Lahiri, R. Seelaboyina, J. Y. Hwang, R. Benerjee and W. Choi: Carbon: 48, 1531 (2010)

[274] K. A. Dean and B. A. Chalamala: Appl. Phys. Lett; 76, 375 (2000)

[275] S. T. Purcell, S. T. Purcell, P. Vincent, C. Journet, and V. T. Binh; Phys. Rev. Lett; 88, 105502 (2002)

[276] P. Vincent, P. Vincent, S. T. Purcell, C. Journet, and V. T. Binh; Phys. Rev. B; 66, 075406 (2002)

[277]E. Minoux, O. Groening, K. B. K. Teo, S. H. Dalal, L. Gangloff, J. P. Schnell, L. Hudanski, I. Y. Y. Bu, P. Vincent, P. Legagneux, G. A. J. Amaratunga, and W. I. Milne, Nano Lett;5(11):2135 (2005)

[278] J. S. Moon, P. S. Alegaonkar, J. H. Han, T. Y. Lee, J. B. Yoo, and J. M. Kim: J. Appl Phys;100:104303 (2006)

[279] J. M Bonard, H. Kind, T. Stöckli and L. O. Nilsson : Solid State Electron; 45, 893 (2001).

[280]G. Luo, Z Li, F Wei, L Xiang, X Deng, Y Jin. Physica B 323, 314 (2002)

[281] S. K. Patra and G. M. Rao: J. Appl. Phys. 100, 024319 (2006)

[282] B. Ulmen, B. Ulmen, V. K. Kayastha, A. DeConinck, J. Wang, Y. K. Yap : Diamond Related Mater; 15, 212 (2005)

[283] J. Y. Lee, K. Liang, K. H. An and Y. H. Lee; Synthetic metals; 150, 153 (2005)

[284] Niu, E.K. Sichel, R. Hoch, D. Moy, H. Tennent, Appl. Phys. Lett. 70, 1480 (1997).

[285] G. Arabale, D. Wagh, M. Kulkarni, I.S. Mulla, S.P. Vernekar, K.Vijayamohanan, A.M. Rao: Chem. Phys. Lett. 376, 207 (2003).

[286] Y. Saito, S. Uemura, K. Hamaguchi; Jpn. J. Appl. Phys. 37, L346 (1998).

[287]R. Dingle, A. C. Gossard, and W. Wiegmann: Phys. Rev. Lett. 34, 1327 (1975)

[288] S. Data and B. Dass; Apply. Phys. Lett; 56, 665 (1990)

[289] G. Burkard, D. Loss and D. P. DiVicenzo. Phys. Rev. B. 59, 2070 (1999)

[290] M. W. Wu, J. H. Jiang and M. Q. Weng: Physics Reports; 493, 61 (2010)

[291] L. E. Hueso, J. M. Pruneda, V. Ferrari, G. Burnell1, J. P. Valde´s-Herrera, B. D. Simons, P. B. Littlewood, E. Artacho, A. Fert & N. D. Mathur1: Nature (London) 445, 410 (2007)